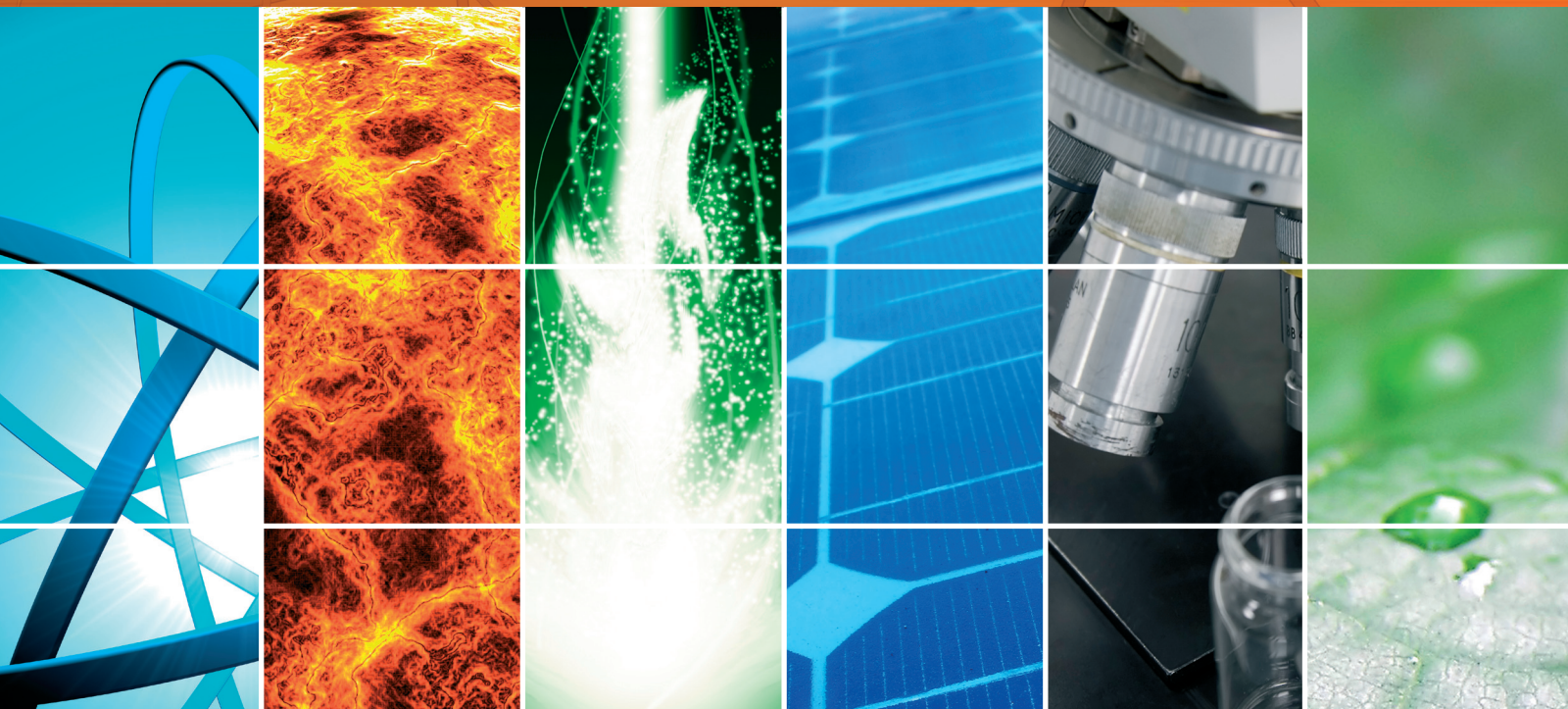


Dye-Sensitized Solar Cells: From Materials to Devices

Guest Editors: Tianxin Wei and Theodoros Dimopoulos





Dye-Sensitized Solar Cells: From Materials to Devices

International Journal of Photoenergy

**Dye-Sensitized Solar Cells:
From Materials to Devices**

Guest Editors: Tianxin Wei and Theodoros Dimopolos



Copyright © 2013 Hindawi Publishing Corporation. All rights reserved.

This is a special issue published in "International Journal of Photoenergy." All articles are open access articles distributed under the Creative Commons Attribution License, which permits unrestricted use, distribution, and reproduction in any medium, provided the original work is properly cited.

Editorial Board

M. Abdel-Mottaleb, Egypt
Nihal Ahmad, USA
N. Alonso-Vante, France
Wayne A. Anderson, USA
Vincenzo Augugliaro, Italy
D. W. Bahnemann, Germany
M. A. Behnajady, Iran
Ignazio R. Bellobono, Italy
Raghu N. Bhattacharya, USA
Pramod H. Borse, India
G. Calzaferri, Switzerland
Adriana G. Casas, Argentina
Wonyong Choi, Korea
Vra Cimrova, Czech Republic
Vikram Dalal, USA
D. (Dion) D. Dionysiou, USA
Mahmoud M. El-Nahass, Egypt
Ahmed Ennaoui, Germany
Chris Ferekides, USA
Beverley Glass, Australia
Shinya Higashimoto, Japan
Yadong Jiang, China
Chun-Sheng Jiang, USA

Shahed Khan, USA
Cooper H. Langford, Canada
Yuexiang Li, China
Stefan Lis, Poland
Niyaz M. Mahmoodi, Iran
D. Mantzavinos, Greece
Ugo Mazzucato, Italy
Jacek Miller, Poland
Jarugu N. Moorthy, India
Franca Morazzoni, Italy
F. Morlet-Savary, France
E. B. Namdas, Australia
M. da Graça Neves, Portugal
Leonidas Palilis, Greece
Leonardo Palmisano, Italy
Ravindra K. Pandey, USA
D. Lee Phillips, Hong Kong
Pierre Pichat, France
Gianluca Li Puma, UK
Xie Quan, China
Tijana Rajh, USA
Peter Robertson, UK
Avigdor Scherz, Israel

L. Schmidt-Mende, Germany
P. Smirniotis, USA
Zofia Stasicka, Poland
Juliusz Sworakowski, Poland
Nobuyuki Tamaoki, Japan
Gopal N. Tiwari, India
N. V. Tkachenko, Finland
Veronica Vaida, USA
Roel van De Krol, Germany
M. van Der Auweraer, Belgium
Ezequiel Wolcan, Argentina
Man Shing Wong, Hong Kong
David Worrall, UK
F. Yakuphanoglu, Turkey
Minjoong Yoon, Korea
Hongtao Yu, USA
Jimmy C. Yu, Hong Kong
Jun-Ho Yum, Switzerland
K. Zachariasse, Germany
Lizhi Zhang, China
Jincai Zhao, China

Contents

Dye-Sensitized Solar Cells: From Materials to Devices, Tianxin Wei and Theodoros Dimopolos
Volume 2013, Article ID 789801, 2 pages

Glass Frit Dissolution Influenced by Material Composition and the Water Content in Iodide/Triiodide Electrolyte of Dye-Sensitized Solar Cells, Katrine Flarup Jensen, Md. Mahbubur Rahman, Welmoed Veurman, Henning Brandt, Chan Im, Jürgen Wilde, Andreas Hinsch, and Jae-Joon Lee
Volume 2013, Article ID 696052, 8 pages

Ultradurable Dye-Sensitized Solar Cells under 120°C Using Cross-Linkage Dye and Ionic-Liquid Electrolyte, Seigo Ito, Kaoru Takahashi, Shin-ichi Yusa, Masayuki Saito, and Toshiyuki Shigetomi
Volume 2013, Article ID 501868, 9 pages

Alignment of TiO₂ (Anatase) Crystal of Dye-Sensitized Solar Cells by External Magnetic Field, Na-Yeong Hong, Hyunwoong Seo, Min-Kyu Son, Soo-Kyoung Kim, Song-Yi Park, Kandasamy Prabakar, and Hee-Je Kim
Volume 2013, Article ID 638105, 6 pages

Natural Dye-Sensitized Solar Cells Based on Highly Ordered TiO₂ Nanotube Arrays, Na Li, Nengqian Pan, Danhong Li, and Shiwei Lin
Volume 2013, Article ID 598753, 5 pages

Particle Size Effects of TiO₂ Layers on the Solar Efficiency of Dye-Sensitized Solar Cells, Ming-Jer Jeng, Yi-Lun Wung, Liann-Be Chang, and Lee Chow
Volume 2013, Article ID 563897, 9 pages

Integration of High-Performance Nanocrystalline TiO₂ Photoelectrodes for N719-Sensitized Solar Cells, Ke-Jian Jiang, Jin-Ming Zhou, Kazuhiro Manseki, Qi-Sheng Liu, Jin-Hua Huang, Yan-lin Song, and Shozo Yanagida
Volume 2013, Article ID 807931, 6 pages

A Facile Synthesis of Granular ZnO Nanostructures for Dye-Sensitized Solar Cells, Md. Mahbubur Rahman, Narayan Chandra Deb Nath, Kwang-Mo Noh, Jaecheon Kim, and Jae-Joon Lee
Volume 2013, Article ID 563170, 6 pages

DFT Study of Binding and Electron Transfer from a Metal-Free Dye with Carboxyl, Hydroxyl, and Sulfonic Anchors to a Titanium Dioxide Nanocluster, Corneliu I. Oprea, Petre Panait, Jeanina Lungu, Daniela Stamate, Anca Dumbravă, Fanica Cimpoesu, and Mihai A. Gîrțu
Volume 2013, Article ID 893850, 15 pages

Theoretical Study of Copper Complexes: Molecular Structure, Properties, and Its Application to Solar Cells, Jesus Baldenebro-Lopez, Norma Flores-Holguin, Jose Castorena-Gonzalez, Jorge Almaral-Sanchez, and Daniel Glossman-Mitnik
Volume 2013, Article ID 613064, 7 pages

Computational Nanochemistry Study of the Molecular Structure and Properties of Chlorophyll a, Mónica Alvarado-González, Norma Flores-Holguín, and Daniel Glossman-Mitnik
Volume 2013, Article ID 424620, 8 pages

Editorial

Dye-Sensitized Solar Cells: From Materials to Devices

Tianxin Wei¹ and Theodoros Dimopoulos²

¹ School of Chemistry, Beijing Institute of Technology, Beijing 100081, China

² Energy Department, Electric Energy Systems, Austrian Institute of Technology AIT, 1210 Vienna, Austria

Correspondence should be addressed to Tianxin Wei; txwei@bit.edu.cn
and Theodoros Dimopoulos; theodoros.dimopoulos@ait.ac.at

Received 29 August 2013; Accepted 29 August 2013

Copyright © 2013 T. Wei and T. Dimopoulos. This is an open access article distributed under the Creative Commons Attribution License, which permits unrestricted use, distribution, and reproduction in any medium, provided the original work is properly cited.

The need to replace fossil fuels with renewable and sustainable energy sources is more exigent than ever, in order to reduce CO₂ emissions causing climatic change and guarantee the further development of mankind in harmony with our natural environment. Photovoltaics (PV) is considered as one of the most reliable platforms for green energy production. To convert sunlight into electricity, the majority of PV technologies rely on semiconductor p-n junctions. An alternative attractive strategy is the development of photoelectrochemical solar cells, the function of which is based on the photosensitization process.

In photosensitization, a molecule called photosensitizer (or simply sensitizer), absorbs light, is lifted to an excited electronic state, and transfers the charge to an acceptor, giving rise to a chain of chemical reactions. The sensitizer usually returns to its original state by receiving electrons from another source. In natural photosynthesis, plants use the chlorophyll pigment in the chloroplasts as sensitizer that captures sunlight and donates electrons to a series of molecular intermediates, resulting in the production of chemical energy.

In technology, photosensitization was firstly demonstrated in 1873 by Hermann Wilhelm Vogel [1], who mixed dyes of different colors in photographic emulsions to render silver halide photographic plates sensitive to different parts of the light spectrum. The underlying physical mechanism is the injection of electrons from the photoexcited dye to the silver halide, with the subsequent formation of metallic silver.

In the 1960s and 70s, semiconductor electrodes were sensitized with organic pigments in electrochemical cells, converting the electronic photoexcitation of the pigment into electric energy [2, 3], albeit with very low efficiency.

Efforts towards electricity production led to a breakthrough in 1991, when the first dye-sensitized solar cell (DSSC) with photovoltaic properties competitive to the conventional silicon-based technology was presented by B. O'Regan and M. Grätzel [4]. Their success relied on the use of a mesoporous TiO₂ film with a very large internal surface area for sensitization and the employment of a Ru-based, metallorganic dye with optimized spectral characteristics for light harvesting. The operation principle of the DSSC is based on the injection of electrons from the photoexcited dye to the TiO₂, the transport of electrons towards the conducting glass substrate, and the regeneration of the dye by electron transfer from a redox electrolyte, which is then reduced at the counter electrode.

Since this ground-breaking work, a series of energy conversion efficiency records were marked, bringing the current state of the art close to 15%, through the employment of newly developed perovskite dyes and sensitization recipes [5]. This efficiency is amongst the highest for solution processed PV. Research in all material components of the DSSC, that is, dyes, nanostructured electrodes, electrolytes, and encapsulation, is intensified continuously, bringing the DSSC very close to widespread application.

Sensitizer development is an important issue, targeting materials which combine absorption matched to the solar spectrum, easy chemisorption onto the semiconductor surface, efficient electron injection into the semiconductor's conduction band, low cost, and environmental sustainability. In particular regarding the last points, natural pigments, stemming from plants, and flowers, could provide a viable alternative to expensive synthetic dyes, although the maximum

achieved efficiency of 1.7% [6] is still very low. In this special issue of the Journal of Photoenergy, a number of papers deal with the sensitizer, covering both computational studies of their molecular structure and properties and experimental investigations of natural and synthetic dyes employed in solar cells.

Another important aspect of the DSSC is the nanostructured semiconductor electrode, which has to provide the necessary large internal surface area, as well as promoting easy electron transfer from the dye and efficient electron transport. This special issue contains advances in the development of nanostructured semiconductor photoanodes, such as TiO₂ nanocrystalline films and nanotube arrays or ZnO nanostructures. Last but not the least, investigations on the interaction of the redox electrolyte with the other DSSC components are included.

We hope that the reader will find in this issue many interesting information on the materials and DSSC device development.

Tianxin Wei
Theodoros Dimopoulos

References

- [1] W. West, "Proceedings of vogel centennial symposium," *Photographic Science and Engineering*, pp. 18–35, 1974.
- [2] H. Gerischer and H. Tributsch, "Elektrochemische Untersuchungen über den Mechanismus der Sensibilisierung und Übersensibilisierung an ZnO-Einkristallen," *Berichte der Bunsengesellschaft für Physikalische Chemie*, vol. 73, pp. 251–260, 1969.
- [3] H. Tributsch and M. Calvin, "Electrochemistry of excited molecules: photoelectrochemical reactions of chlorophylls," *Photochemistry and Photobiology*, vol. 14, pp. 95–112, 1971.
- [4] B. O'Regan and M. Grätzel, "A low-cost, high-efficiency solar cell based on dye-sensitized colloidal TiO₂ films," *Nature*, vol. 353, no. 6346, pp. 737–740, 1991.
- [5] J. Burschka, N. Pellet, S. J. Moon et al., "Sequential deposition as a route to high-performance perovskite-sensitized solar cells," *Nature*, vol. 499, no. 7458, pp. 316–319, 2013.
- [6] G. Calogero, G. Di Marco, S. Cazzanti et al., "Efficient dye-sensitized solar cells using red turnip and purple wild Sicilian prickly pear fruits," *International Journal of Molecular Sciences*, vol. 11, no. 1, pp. 254–267, 2010.

Research Article

Glass Frit Dissolution Influenced by Material Composition and the Water Content in Iodide/Triiodide Electrolyte of Dye-Sensitized Solar Cells

Katrine Flarup Jensen,^{1,2} Md. Mahbubur Rahman,³ Welmoed Veurman,¹ Henning Brandt,¹ Chan Im,² Jürgen Wilde,⁴ Andreas Hinsch,¹ and Jae-Joon Lee^{2,3,5}

¹ Fraunhofer Institute for Solar Energy Systems (ISE), HeidenhofstraBe 2, 79110 Freiburg, Germany

² Konkuk University-Fraunhofer Next Generation Solar Cell Research Center (KFnSC), 120 Neungdong-ro, Gwangjin-gu, Seoul 143-701, Republic of Korea

³ Department of Advanced Technology Fusion, Konkuk University, 120 Neungdong-ro, Gwangjin-gu, Seoul 143-701, Republic of Korea

⁴ Department of Microsystems Engineering-IMTEK, University of Freiburg, Georges-Köhler-Allee 103, 79110 Freiburg, Germany

⁵ Nanotechnology Research Center and Department of Applied Chemistry, Konkuk University, 268 Chungwondaero, Chungju 380-701, Republic of Korea

Correspondence should be addressed to Andreas Hinsch; andreas.hinsch@ise.fraunhofer.de and Jae-Joon Lee; jjlee@kku.ac.kr

Received 6 February 2013; Revised 11 June 2013; Accepted 11 June 2013

Academic Editor: Theodoros Dimopoulos

Copyright © 2013 Katrine Flarup Jensen et al. This is an open access article distributed under the Creative Commons Attribution License, which permits unrestricted use, distribution, and reproduction in any medium, provided the original work is properly cited.

To ensure long-term stable dye-sensitized solar cells (DSCs) and modules, a hermetic sealing is required. This research investigates the chemical stability of I^-/I_3^- redox electrolyte and four different glass frits (GFs). Sintered GF layers were openly exposed to nonaqueous redox electrolyte and redox electrolyte with 1, 5, and 10 wt% H_2O in thin, encapsulated cells. The change in I_3^- absorbance was assigned to a reaction between the GF and I^-/I_3^- electrolyte and was used to evaluate the chemical stability of the different GFs. The I_3^- absorbance change was monitored over 100 days. Two out of the four GFs were unstable when H_2O was added to the redox electrolyte. The H_2O caused metal ion leaching which was determined from EDX analysis of the inorganic remains of electrolyte samples. A GF based on $Bi_2O_3-SiO_2-B_2O_3$ with low bond strength leached bismuth into electrolyte and formed the BiI_4^- complex. A $ZnO-SiO_2-Al_2O_3$ -based GF also became unstable when H_2O was added to the redox electrolyte. Leaching of zinc ions due to exchange with H^+ resulted in the formation of a zinc-iodine compound which caused I_3^- depletion. By applying the test design to different types of GFs, the material suitability in the DSC working environment was investigated.

1. Introduction

The dye-sensitized solar cell (DSC) is a photoelectrochemical cell which imitates nature's photosynthesis [1]. In its classical configuration, see Figure 1, the cell consists of 2 glass substrates coated with transparent conductive oxide (TCO) (usually $SnO_2:F$ on soda-lime glass) on which the electrodes are deposited. The photoelectrode consists of a mesoporous layer of semiconductive TiO_2 with a monolayer of chemically adsorbed dye. The transparent counter electrode is coated with a very thin catalytic layer of platinum. A liquid redox electrolyte containing the redox couple iodide/triiodide

(I^-/I_3^-) is encapsulated between the two electrodes by a sealant agent, resulting in a plate distance of 20–50 μm . When light strikes the solar cell, the photon is absorbed by the dye. The excited dye injects an electron into the TiO_2 conduction band which diffuses through the TiO_2 network. The electron enters the external circuit through the TCO and is transferred to the counter electrode. The photo-oxidized dye injects an electronic hole into the electrolyte which, in the form of I_3^- diffuses to the counter electrode. At the counter electrode, I_3^- is reduced back to I^- .

In order to make the DSC attractive to the building industry, long-term stable, large modules on single substrates

have to be realized. A thermally and chemically stable sealant is inevitably required to avoid degradation of the DSC. The degradation of the DSC can be caused either by intrinsic instability of the cell components or mechanically by electrolyte leakage or intrusion of H_2O or O_2 from the outside environment [2, 3].

To achieve long-term stable DSCs, H_2O in the electrolyte should be prevented. Although H_2O in electrolyte can create an initial increase in photovoltage [4], faster device degradation has been reported [4]. This is assumed to be due to loss of iodine when H_2O is present in the electrolyte [4] as well as dye detachment from the TiO_2 [5].

Many materials have been explored as sealant material such as thermoplastic hotmelt foils like Surlyn 1702 (DuPont) and Bynel 4702 (Dupont), UV curable glues, and glass frit (GF) [6, 7]. GF is used as sealing material at Fraunhofer ISE. GF is believed to be a strong candidate as sealant material in glass-based DSC modules as it possesses the same properties as the substrates [8–10], is nonpermeable, and is UV- and temperature stable in the temperature range which can occur in hot climates. But it is not trivial to find a suited Pb-free [11] GF with low melting temperature that is chemically stable against the oxidative redox electrolyte. It has previously been reported that GF was seen to leach elements into electrolyte [12, 13], which caused depletion of I_3^- and electrochemical degradation of the DSC.

The present work investigates the chemical stability of four low-temperature melting GFs in I^-/I_3^- redox electrolyte. The stability of the GFs were investigated individually in nonaqueous I^-/I_3^- redox electrolyte and in I^-/I_3^- redox electrolyte containing 1, 5, and 10 wt% H_2O . The design of experiments will be helpful to evaluate a GF for its compatibility and stability in the DSC environment.

2. Materials and Methods

2.1. Materials. The redox electrolyte contained 0.1M iodine (Sigma-Aldrich), 0.1M guanidine thiocyanate (Sigma-Aldrich), and 0.50 M n-butyl-1H benzimidazole (NBB) (Merck, Germany) dissolved in 1-methyl-3-propylimidazolium iodide (PMIM-I) (Merck, Germany) with 11 wt% acetonitrile (Sigma-Aldrich). Demineralized water was used throughout the experiments to create redox electrolytes with 1, 5, and 10 wt% H_2O . Due to the great excess of I^- , all I_2 is expected to have reacted to I_3^- by the following reaction,



The diffusion coefficient of I_3^- , $D[\text{I}_3^-]$ was experimentally determined by cyclic voltammetry as described elsewhere [13]. $D[\text{I}_3^-]$ in the electrolyte with 10 wt% H_2O was determined to be $1.5 \cdot 10^{-6} \text{ cm}^2/\text{s}$ at 25°C .

Soda-lime glass with a transparent conductive oxide ($\text{SnO}_2:\text{F}$, $8 \Omega/\square$) was purchased from Pilkington.

The GFs were used as received from the manufacturers, and the main compositional elements of the GFs are given in Table 1. The melting temperature, T_m , was experimentally determined by heating the GF paste to various temperatures

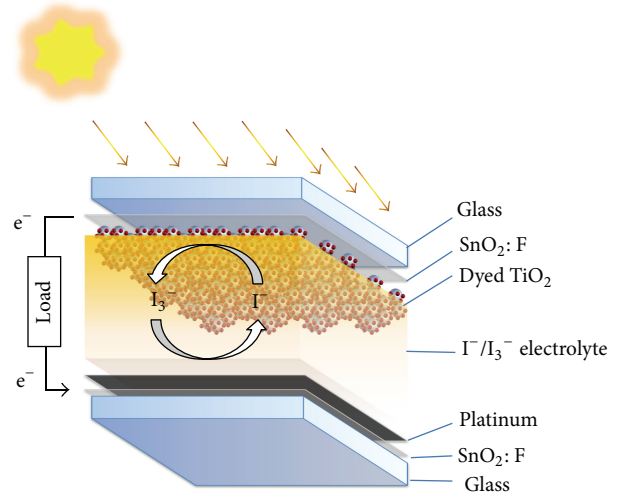


FIGURE 1: Working principle and device structure of a dye-sensitized solar cell (DSC). An organic electrolyte with the redox couple I^-/I_3^- transports the positive charge between the mesoscopic photoelectrode and the counter electrode.

TABLE 1: Main composition of glass frits for sealing.

	Composition	T_m ($^\circ\text{C}$)
GF1	$\text{Bi}_2\text{O}_3\text{-SiO}_2\text{-B}_2\text{O}_3$	470
GF2	$\text{Bi}_2\text{O}_3\text{-SiO}_2\text{-B}_2\text{O}_3$	400
GF3	$\text{ZnO-SiO}_2\text{-Al}_2\text{O}_3$	500–520
GF4	$\text{SiO}_2\text{-ZnO-Al}_2\text{O}_3$	530

T_m : temperature where glass powder initiates to melt.

and by investigating the particles by SEM. The onset of melting was determined as T_m .

2.2. The Test Cell. In the working DSC, the sealing material will only be exposed to the electrolyte at the typically $20\text{--}50 \mu\text{m}$ high cell edges. But with the aim to perform accelerated testing, we created a system with a larger (approx. 30 times) openly exposed GF area. The total cell area was $5 \text{ cm} \times 0.6 \text{ cm}$. An area of $2 \text{ cm} \times 0.4 \text{ cm}$ GF was doctor bladed on one TCO glass (Pilkington TEC-8) and dried in a convection furnace at 150°C for about 10 min. The samples were sintered with the manufacturer's recommended sintering profile. An intermediate step in the heating curve assured that the organic binder was burnt out of the paste, before melting of the glass particles [2, 9]. The peak sintering temperature T_{max} was approximately 50°C higher than T_m (given in Table 1). The GF layer had a height of $12 \mu\text{m}$ after sintering. This TCO glass was sealed with another TCO glass by a Surlyn gasket ($45 \mu\text{m}$) as described in [7], creating encapsulated cells with a plate distance of $20 \mu\text{m}$; see Figure 2. The widely used Surlyn is chemically stable, but it has a softening point of 65°C , so it is not suitable for tests exceeding 60°C [7]. Surlyn was used as encapsulation to isolate the effect of GF on the confined area inside the cell and was suitable as the storage and exposure temperatures of the cells were mild (room temperature). The cells were filled with electrolyte, and the filling holes were

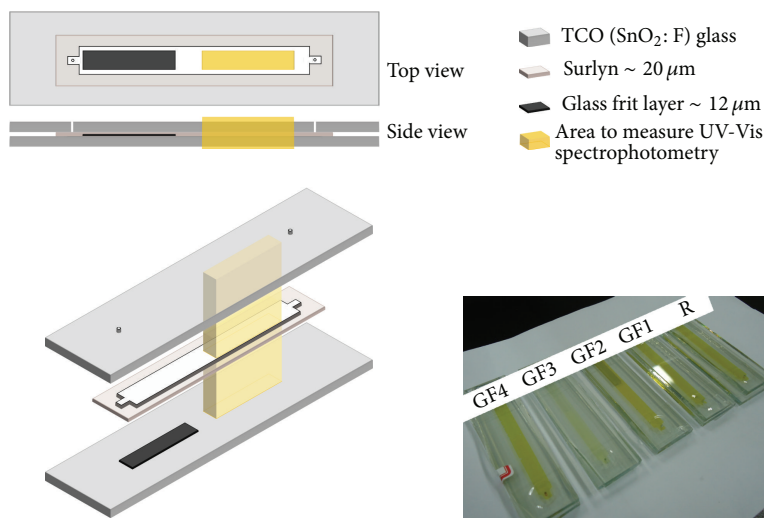


FIGURE 2: Cell design for investigating the accelerated influence of GF and H_2O in the DSC electrolyte. Restricted area with a thin layer of GF and an area for absorbance measurements through the cell. The photo displays the test cells with 10 wt% H_2O in the redox electrolyte after 100 days. *R* indicates the reference cell (no GF).

sealed with Surlyn and a thin slide glass. The reference cells did not contain a GF layer.

2.3. SEM and EDX Sample Preparation. After 100 days, the electrolyte samples were extracted from the cells and placed on a TCO ($\text{SnO}_2:\text{F}$) glass, which is classified as chemically inert and thermally stable up to 600°C [14]. Solvents were evaporated, and the organic iodide salt was burnt out at 350°C , so precipitated residues from the electrolyte could be examined with SEM and EDX. The samples were sputtered with Au to enhance the conductivity.

2.4. Instrumentation. UV-visible measurements were carried out with a spectrophotometer (Scinco UV-Vis spectrophotometer, Neosys 2000) with a detection limitation for transmittance lower than 10^{-2} . Absorbance of the electrolyte inside the cell was measured from 350 nm to 500 nm. The baseline was taken with a test cell containing H_2O .

A scanning electron microscope, SEM, and energy dispersive X-ray analysis, EDX, (FESEM JSM 6700F) were used to investigate the morphology and analyze the leached GF elements.

The GF layer thickness was determined with a Dektak profilometer.

3. Results

3.1. Absorbance Spectrum of I_3^- . The absorbance spectrum of I_3^- in acetonitrile has specific absorbance peaks at around 290 nm and 360 nm [15]. I_3^- absorbs until approximately 500 nm. Calibration measurements with known I_3^- concentration in redox electrolyte showed a slight red-shift of the absorbance peak to 366 nm, Figure 3(a), due to the difference in polarity of the ionic liquid PMIM-I compared with acetonitrile [16]. A good linear dependence between absorbance and I_3^- concentration according to Beer-Lambert's law [17]

was observed at 366 nm as well as 430 nm, Figure 3(b). The linearity at 430 nm will be used to correlate the glass frit interaction with I_3^- loss since the test cells showed absorbance saturation at 366 nm.

3.2. Detection of I_3^- Change in Electrolyte by UV-Vis Spectrophotometry. Absorbance measurements on the test cells were performed during 100 days. The absorbance spectra of the cells with redox electrolyte were saturated for most samples. This was due to the high triiodide concentration in the electrolyte. Therefore, the absorbance value at 366 nm could not be determined.

The absorbance spectra for the reference cell (no GF) and the test cells with GF1–GF4 containing redox electrolyte with 5 and 10 wt% H_2O are shown in Figures 4(a)–4(e). Only selected representative data are shown. The largest change in absorbance over time was seen for the cells containing GF2 and GF3 when H_2O was added to electrolyte.

Figure 4(a) displays the initial absorbance spectra of the reference cell (no GF) with water-containing electrolyte initially and after 99 days. No changes in the spectra are seen. This was also the case for the test cells with GF1, Figure 4(b), and GF4, Figure 4(e), which showed constant absorbance spectra over time. Therefore, a long-term reaction between H_2O and I_3^- under the mild storage conditions (dark, room temperature) can be excluded. Figures 4(c) and 4(d) clearly show that the I_3^- concentration decreases over time in the test cells with GF2 and GF3. The reason for I_3^- depletion can thus be assigned to the GF material and the addition of H_2O in the system.

The absorbance spectra for the cell with GF2 changed over time and displayed a new absorbance peak at 475 nm, Figure 4(c). This will be further discussed in Section 4.1.

For the cells with GF3 and H_2O -containing electrolyte, a continuous decrease of the absorbance was seen. After 71 days, the characteristic absorbance peak of I_3^- at 366 nm

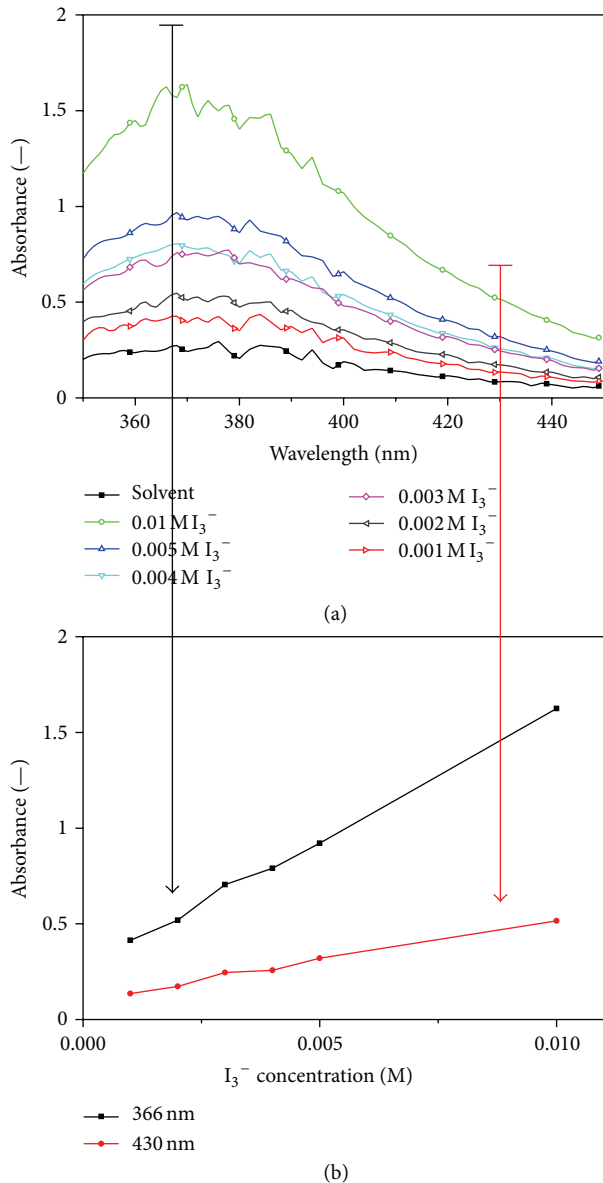


FIGURE 3: (a) Absorbance spectra of I_3^- in PMIM-I at various concentrations. $45 \mu\text{m}$ light path length, H_2O as baseline. The absorbance peak of I_3^- is seen at 366 nm. (b) Linear dependence of I_3^- concentration with absorbance at, respectively, 366 nm and 430 nm. The linearity at 430 nm is important since the absorbance spectra for the test cells are saturated at 366 nm. Therefore, the decrease in absorbance at 430 nm for the test cells is correlated with the loss of I_3^- .

became visible due to the significant decrease in I_3^- concentration, Figure 4(d).

The linearity between I_3^- concentration and absorbance at 430 nm was shown in Figure 3(b). Due to measurement saturation at 366 nm, the absorbance at 430 nm as a function of time for the cells with GF2 and GF3 is shown in Figure 5.

As it can be seen from Figure 5(a), a decrease in I_3^- absorbance for the GF2-containing cell is already visible when 1 wt% H_2O is added to the redox electrolyte. The absorbance decrease, when respectively 5 wt% and 10 wt%

H_2O are added to electrolyte, follows a similar decay trend and becomes linear after approximately 70 days.

In Figure 5(b), the results for the cell with GF3 are shown. A decrease in absorbance is seen when respectively 5 and 10 wt% H_2O are added to the electrolyte, with a less strong decrease for the cell with 5 wt% H_2O in the electrolyte. The absorbance decrease for the cell with 10 wt% H_2O becomes linear after 70 days, as it was also observed for the cells with GF2.

3.3. Diffusion Limitation of I_3^- in the Cell Design. The decrease in I_3^- content of the cell with GF3 and aqueous electrolyte was clearly visible, as the electrolyte bleached rapidly in the area of the GF layer. The diffusion of I_3^- from the uncoated area to the area with GF, therefore, seems to be of importance for the depletion time of I_3^- .

The largest I_3^- concentration gradient will be from the end of the GF area to the end of the noncoated area ($\sim 3 \text{ cm}$). The relation between I_3^- diffusion coefficient $D[I_3^-]$ determined at room temperature, diffusion length L , and diffusion time τ ($\tau = L^2/D[I_3^-]$) gives a diffusion time $\tau \sim 70$ days, for $D[I_3^-] = 1.5 \cdot 10^{-6} \text{ cm}^2/\text{s}$ and $L = 3 \text{ cm}$. This is in good correspondence with the initiation of the observed linear decay in absorbance as seen in Figure 5.

3.4. EDX Investigation of Leached GF Elements in Redox Electrolyte with 10 wt% H_2O . After 100 days, the electrolyte was extracted from the cells, placed on a TCO glass, and heat treated. The leached GF elements could be determined by EDX. As the TCO consists of $\text{SnO}_2:\text{F}$, Sn and O elements were detected in all EDX spectra.

The EDX spectrum of the precipitate from the reference cell with nonaqueous redox electrolyte is displayed in Figure 6(a). The EDX analysis was performed on the area shown in the inserted SEM image. The detected Sn, O, and F originated from the TCO substrate, C and Na from trace amounts in the electrolyte [18], and Au from the Au sputtering for better conductivity. It should be noted that no iodine was detected, so the heat treatment had successfully burnt out the iodine from the redox electrolyte.

The EDX spectra from the remains of the aqueous electrolyte (10 wt% H_2O) in contact with GF2 and GF3 are shown in the Figures 6(b) and 6(c). The insets show the SEM images of the precipitate. The spectra were obtained by performing spot analysis on the precipitates.

The precipitate from the redox electrolyte with 10 wt% H_2O extracted from the test cell with GF2 contained bismuth and iodide. For the test cell with GF3, zinc and iodide were detected as the precipitate. In order to ensure that zinc was detected, the acceleration voltage was increased to 20 keV for the sample with GF3. This caused the electron beam to go through the precipitate and the TCO and reach the soda-lime substrate. Hence, silicon was further detected.

The detected metals originated from the GF, and the iodine was from the electrolyte. Since iodine was burnt out during the heating of electrolyte, the detected bismuth and iodine for the GF2 sample and the detected zinc and iodine for the GF3 sample were bound in a thermally stable form.

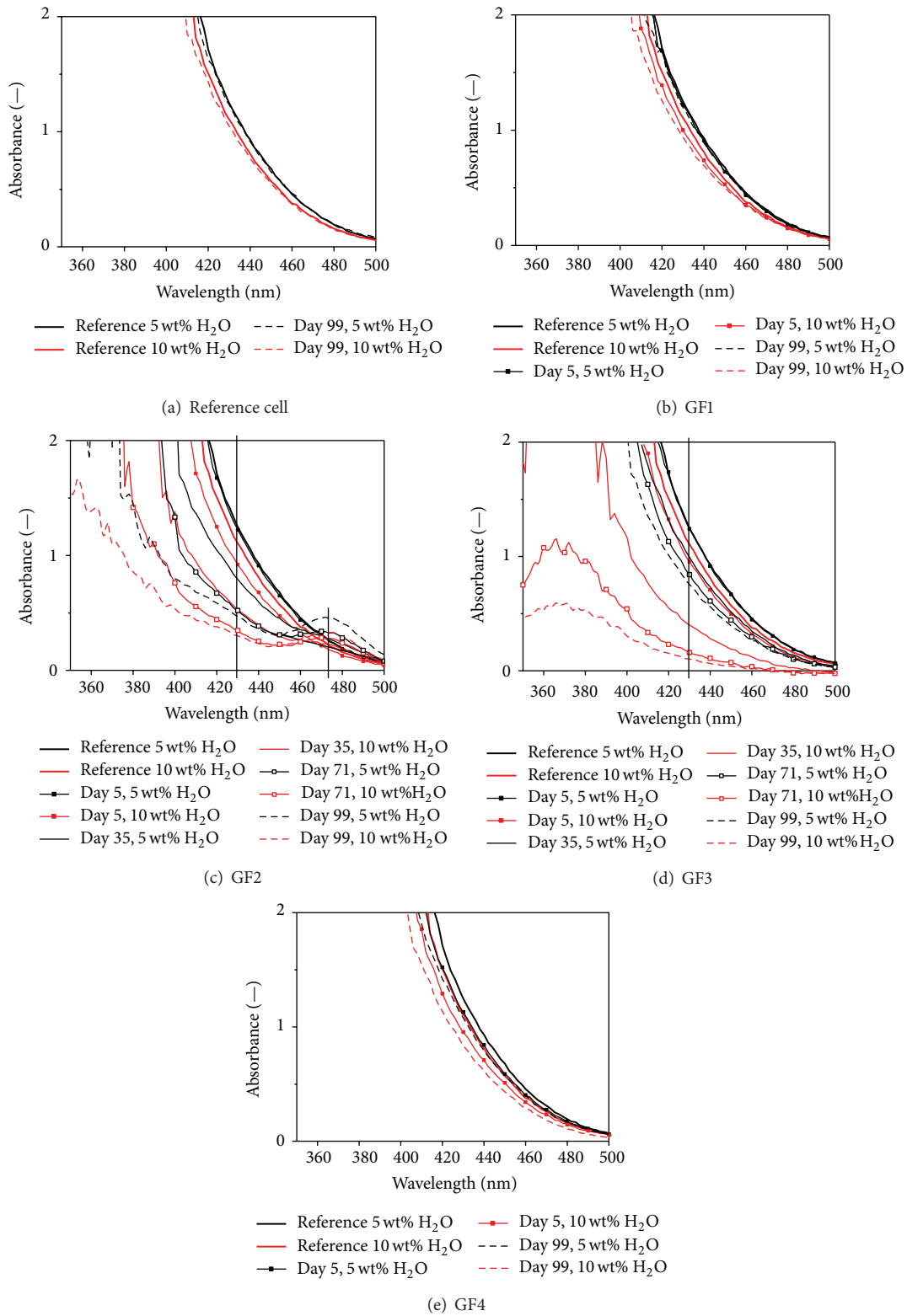


FIGURE 4: Development of absorbance spectra during ageing of the reference cell (no GF) and the test cells with 5 and 10 wt% H₂O added to the redox electrolyte. (a) Reference cell with no GF; no change in absorbance over time, (b) test cell with GF1 showing stable absorbance spectra over time, (c) test cell with GF2; notice the appearance of a new peak at 475 nm and the decrease in absorbance at lower wavelengths, (d) test cell with GF3 showing continuous decrease in absorbance over time, and (e) test cell with GF4 which is relatively stable over time.

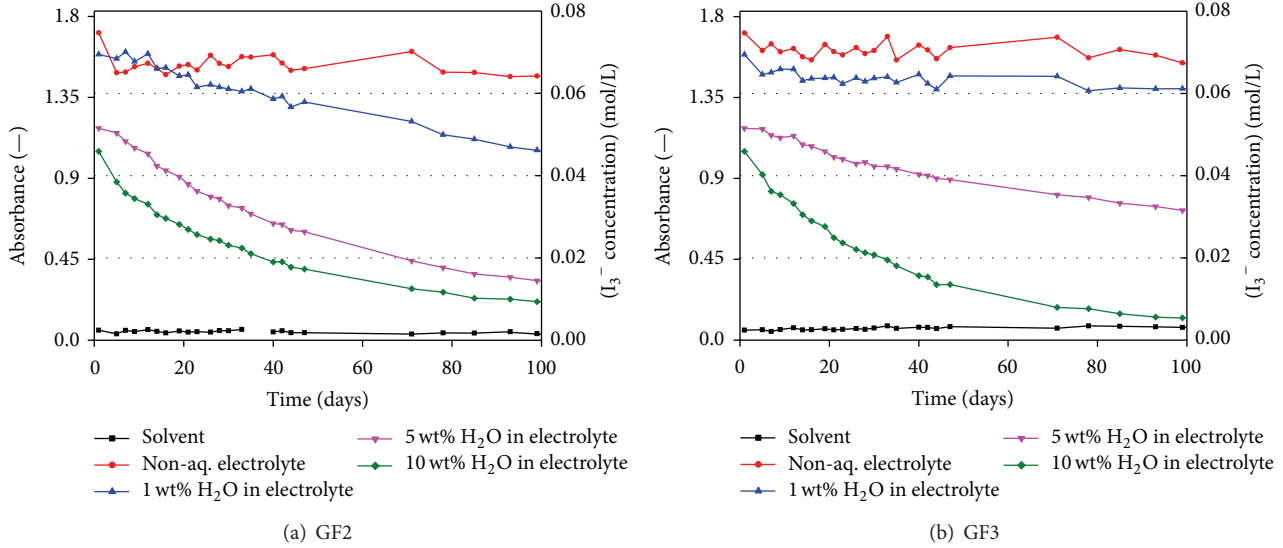


FIGURE 5: Absorbance at 430 nm as a function of time for the test cells filled with solvent, nonaqueous redox electrolyte, and redox electrolyte with 1, 5, and 10 wt% H_2O . (a) Test cell with GF2. Absorbance decreases over time for cells with 1, 5, and 10 wt% H_2O in electrolyte. (b) Test cell with GF3. Absorbance decreases over time for cells with 5 and 10 wt% H_2O in electrolyte.

4. Discussion

For DSC cells and modules, the I_3^- concentration is one of the possible current-limiting parameters. Therefore, significant I_3^- depletion will lead to a decrease in electrical performance [13].

4.1. Test Cell with GF2. The absorbance measurements revealed a significant decrease in I_3^- absorbance over time for the samples in contact with GF2 and aqueous redox electrolyte.

The EDX analysis of leached elements from GF2 revealed a precipitate of bismuth and iodine. Even though the absorbance measurements showed decaying absorbance at 430 nm over time (Figure 5(a)), the cells did not visually bleach, which can be explained by the occurrence of a new absorbance peak at 475 nm as seen in Figure 4(c). This peak could be assigned to the BiI_4^- formation in aqueous redox electrolyte, as the absorbance peak of BiI_4^- is reported at 460 nm in acetonitrile [19].

4.2. Test Cell with GF3. The GF3 test cells with 5 and 10 wt% H_2O -containing redox electrolyte showed significant decrease in I_3^- absorbance over time as seen in Figure 5(b). The electrolyte bleached due to I_3^- depletion.

EDX revealed that zinc was leached from the GF in aqueous redox electrolyte and formed a thermally stable compound with iodine. At present, the formed zinc-iodine complex is not known, but could be present in the form of $Zn(I_3)_2$ (aq), $[ZnI_3]^-$ (aq), or $[ZnI_3(H_2O)]^-$ (aq) [20]. The formed complex did not change the absorbance spectrum in the range of 350–500 nm over time. Despite the missing determination of the formed compound, the experimental results (Section 3.2) clearly showed a continuous decrease in

I_3^- absorbance over time. This will be detrimental for the DSC operation.

4.3. Influence of GF Composition on Stability. Glass dissolves by two mechanisms: selective leaching of glass modifier elements or complete glass dissolution [21]. It is known that soda-lime glass dissolves in H_2O with a dissolution rate in the order of 10^{-6} cm^2/s [21]. The process is controlled by the exchange of Na^+ ions with H^+ , which breaks up the glass matrix [22].

GF2 and GF3 became unstable when H_2O was added to the redox electrolyte. GF2 exhibited a low melting temperature compared with GF1, which consists of same major elements. Evidently the solubility of GF2 is higher than GF1. This can be the result of a low bond strength so it is easier to break up the glass structure. The effect of H_2O in electrolyte led to leaching of bismuth ions that reacted with iodide and formed the BiI_4^- complex, as detected by spectrophotometry.

The composition of GF3 has a high content of ZnO compared with SiO_2 and Al_2O_3 . As SiO_2 and Al_2O_3 have a strong tendency to form a tetrahedral structure which forms the glass matrix, ZnO will act as a glass modifier by obtaining interstitial positions in the glass structure. Zinc ions can then readily be exchanged with H^+ if present in the electrolyte, which leads to leaching of zinc ions [23].

GF3 contained the same major oxides as GF4, but GF4 had a higher melting temperature, which explains the higher chemical stability towards H_2O .

4.4. Accelerated Tests. In order to test different kinds of GFs, an accelerated test would be preferred. Based on the experiences with the experiment carried out, reflections are made towards applicability and design of accelerated testing.

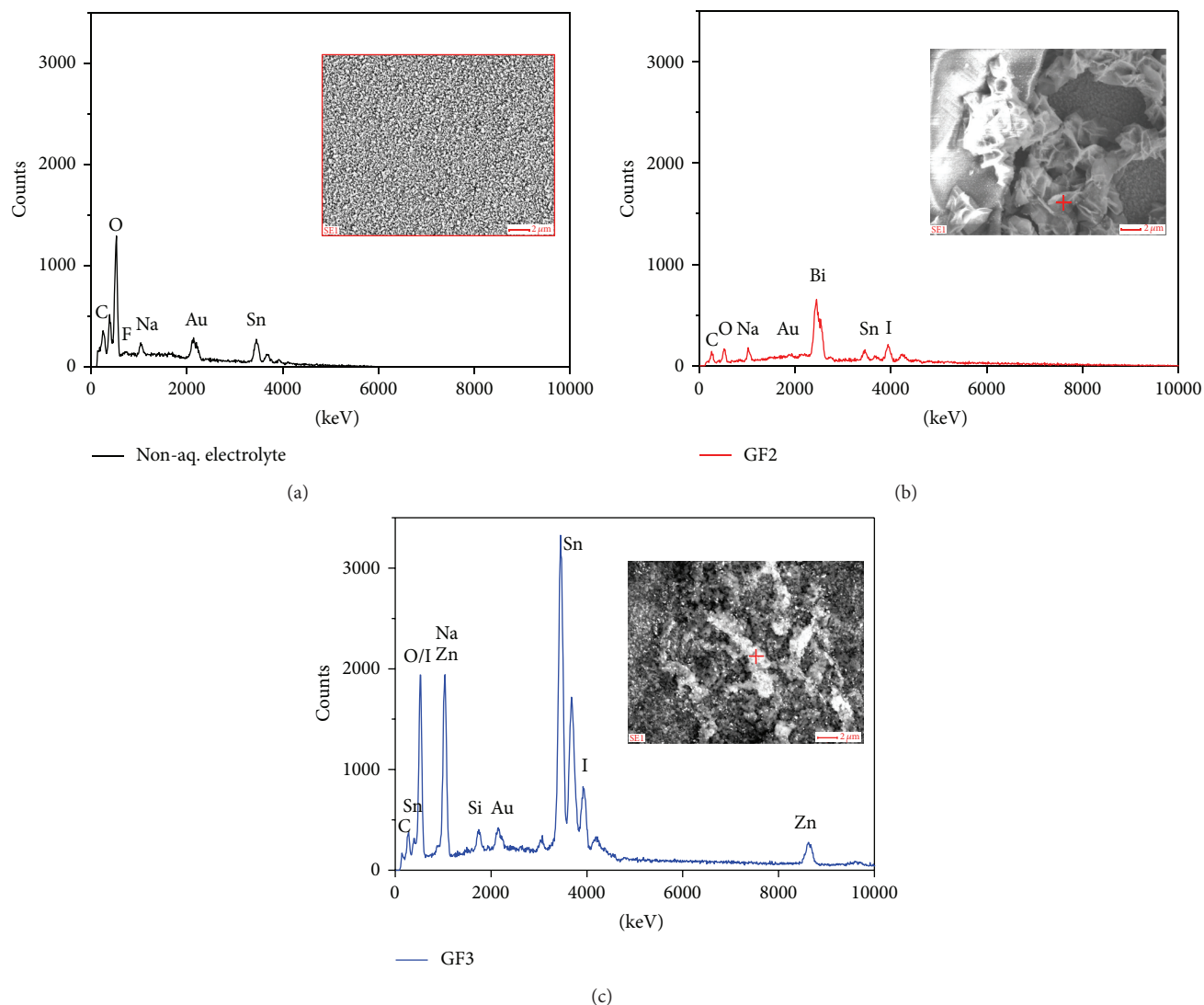


FIGURE 6: EDX spectra of precipitates on TCO after evaporation of electrolyte. Samples were sputtered with Au to increase conductivity. (a) Area analysis as indicated from the SEM inset of nonaqueous electrolyte precipitate. Sn, O, and F originate from the TCO substrate. C and Na are trace amounts from the electrolyte. (b) Spot analysis of precipitate from cell with 10 wt% H_2O -containing electrolyte in contact with GF2. Bi and I are detected due to GF2 and electrolyte interaction. (c) Spot analysis of precipitate from cell with 10 wt% H_2O -containing electrolyte in contact with GF3. Zn and I are detected due to GF3 and electrolyte interaction. Si is detected due to increased acceleration voltage, so the soda-lime glass was reached by the electron beam.

The ageing conditions of the samples were mild as the samples were stored at room temperature and in the dark. Interaction between GF and redox electrolyte with H_2O could be accelerated by using a cell design where diffusion-limitation of I_3^- is negligible. Furthermore, the storage temperature could be increased, but this would require a different hole- and cell sealing material than the present Surlyn.

In a GF-sealed DSC, the GF exposed to electrolyte is only present at the sealing edges compared with the investigated cells with an openly exposed GF layer. The GF area in these cells is approximately 30 times larger than in the case of a cell with a plate distance of $25\ \mu\text{m}$ sealed with GF, so the ratio between GF area and electrolyte volume is significantly larger, accelerating a possible reaction between the cell components.

5. Conclusions

In this work, interaction of glass frit (GF) with I^-/I_3^- electrolyte and H_2O present in the electrolyte was investigated for four different GFs. Thin cells with a confined layer of GF were fabricated to enable *in situ* monitoring of the I_3^- absorbance change of the redox electrolyte. The change in I_3^- absorbance was assigned to a reaction between the GF and the electrolyte and was used to evaluate the chemical stability of the different GFs.

All GFs were stable in nonaqueous redox electrolyte. When H_2O was added to the electrolyte, two of the investigated GFs became unstable. GF2 based on $\text{SiO}_2\text{-B}_2\text{O}_3\text{-Bi}_2\text{O}_3$ leached bismuth, and a bismuth iodide complex was formed. This was confirmed by the new absorbance peak assigned to BiI_4^- and the detection of bismuth in the electrolyte by EDX.

GF3, based on ZnO–SiO₂–Al₂O₃, became unstable when 5 and 10 wt% H₂O were added to the redox electrolyte. The instability was due to the high ZnO content, where the addition of H₂O in electrolyte caused zinc ion leaching. The leached zinc ions reacted with I₃[−] and caused gradual I₃[−] depletion. EDX analysis on the extracted electrolyte confirmed the formation of a compound containing zinc and iodine.

To maintain long-term electrical performance and stability of the dye-sensitized solar cell, a nonreactive and water-tight sealing is needed. The methodology of the study can be used to test various GF candidates in a system comparable with the working DSC.

Conflict of Interests

The authors declare that they have no conflict of interests.

Acknowledgments

This work is supported by Seoul Metropolitan Government in the Joint Project KU/Fraunhofer-ISE Next Generation Solar Cell Research Center (KFNSC) between Konkuk University, Republic of Korea, and Fraunhofer ISE, Germany (Seoul R&BD Program no. WR090671). The authors would like to thank Jutta Zielonka, Fraunhofer ISE, for the SEM and EDX analysis.

References

- [1] B. O'Regan and M. Grätzel, "A low-cost, high-efficiency solar cell based on dye-sensitized colloidal TiO₂ films," *Nature*, vol. 353, no. 6346, pp. 737–740, 1991.
- [2] A. Hinsch, W. Veurman, H. Brandt, R. A. Loayza, K. Bialecka, and K. F. Jensen, "Worldwide first fully up-scaled fabrication of 60 × 100 cm² dye solar module prototypes," *Progress in Photovoltaics*, vol. 20, no. 6, pp. 698–710, 2012.
- [3] R. Sastrawan, "Photovoltaic modules of dye solar cells," Dissertation, University Freiburg Freiburg, Germany, 2006 http://www.freidok.uni-freiburg.de/volltexte/2623/pdf/Sastrawan-Photovoltaic_modules_of_dye_solar_cells_Dissertation.pdf.
- [4] B. Macht, M. Turrión, A. Barkschat, P. Salvador, K. Ellmer, and H. Tributsch, "Patterns of efficiency and degradation in dye sensitization solar cells measured with imaging techniques," *Solar Energy Materials and Solar Cells*, vol. 73, no. 2, pp. 163–173, 2002.
- [5] Y.-S. Jung, B. Yoo, M. K. Lim, S. Y. Lee, and K.-J. Kim, "Effect of Triton X-100 in water-added electrolytes on the performance of dye-sensitized solar cells," *Electrochimica Acta*, vol. 54, no. 26, pp. 6286–6291, 2009.
- [6] A. Hagfeldt, G. Boschloo, L. Sun, L. Kloo, and H. Pettersson, "Dye-sensitized solar cells," *Chemical Reviews*, vol. 110, no. 11, pp. 6595–6663, 2010.
- [7] A. Hinsch, J. M. Kroon, R. Kern et al., "Long-term stability of dye-sensitized solar cells," *Progress in Photovoltaics*, vol. 9, no. 6, pp. 425–438, 2001.
- [8] A. Hinsch, S. Behrens, M. Berginc et al., "Material development for dye solar modules: results from an integrated approach," *Progress in Photovoltaics*, vol. 16, no. 6, pp. 489–501, 2008.
- [9] H. Chen, S. Wang, H. Lin, G. Wang, S. Wang, and G. Yang, "Stability of dye sensitized solar cells with glass frit sealant," *Key Engineering Materials*, vol. 512–515, pp. 1619–1624, 2012.
- [10] R. Sastrawan, J. Beier, U. Belledin et al., "A glass frit-sealed dye solar cell module with integrated series connections," *Solar Energy Materials and Solar Cells*, vol. 90, no. 11, pp. 1680–1691, 2006.
- [11] W. J. Lee, E. Ramasamy, D. Y. Lee, and J. S. Song, "Glass frit overcoated silver grid lines for nano-crystalline dye sensitized solar cells," *Journal of Photochemistry and Photobiology A*, vol. 183, no. 1–2, pp. 133–137, 2006.
- [12] T. Kitamura, K. Okada, H. Matsui, and N. Tanabe, "Durability of dye-sensitized solar cells and modules," *Journal of Solar Energy Engineering*, vol. 132, no. 2, pp. 0211051–0211057, 2010.
- [13] A. Hauch and A. Georg, "Diffusion in the electrolyte and charge-transfer reaction at the platinum electrode in dye-sensitized solar cells," *Electrochimica Acta*, vol. 46, no. 22, pp. 3457–3466, 2001.
- [14] P. Gerhardinger and D. Strickler, "Fluorine doped tin oxide coatings: over 50 years and going strong," *Key Engineering Materials*, vol. 380, pp. 169–178, 2008.
- [15] Z. Kebede and S.-E. Lindquist, "Donor-acceptor interaction between non-aqueous solvents and I₂ to generate I₃[−], and its implication in dye sensitized solar cells," *Solar Energy Materials and Solar Cells*, vol. 57, no. 3, pp. 259–275, 1999.
- [16] K. A. Fletcher, S. Pandey, I. K. Storey, A. E. Hendricks, and S. Pandey, "Selective fluorescence quenching of polycyclic aromatic hydrocarbons by nitromethane within room temperature ionic liquid 1-butyl-3-methylimidazolium hexafluorophosphate," *Analytica Chimica Acta*, vol. 453, no. 1, pp. 89–96, 2002.
- [17] J. D. J. Ingle and S. R. Crouch, *Spectrochemical Analysis*, Prentice Hall, New Jersey, NJ, USA, 1988.
- [18] I. Lee, S. Hwang, and H. Kim, "Reaction between oxide sealant and liquid electrolyte in dye-sensitized solar cells," *Solar Energy Materials and Solar Cells*, vol. 95, no. 1, pp. 315–317, 2011.
- [19] O. Horváth and I. Mikó, "Spectra, equilibrium and photoredox chemistry of iodobismuthate(III) complexes in acetonitrile," *Inorganica Chimica Acta*, vol. 304, no. 2, pp. 210–218, 2000.
- [20] H. Wakita, G. Johansson, M. Sandström, P. L. Goggin, and H. Ohtaki, "Structure determination of zinc iodide complexes formed in aqueous solution," *Journal of Solution Chemistry*, vol. 20, no. 7, pp. 643–668, 1991.
- [21] D. E. Clark and B. K. Zaitos, *Corrosion of Glass, Ceramics and Ceramic Superconductors: Principles, Testing, Characterization and Applications*, William Andrew, New Jersey, NJ, USA, 1993.
- [22] R. H. Do Remus, Y. Mehrotra, W. A. Lanford, and C. Burman, "Reaction of water with glass: influence of a transformed surface layer," *Journal of Materials Science*, vol. 18, no. 2, pp. 612–622, 1983.
- [23] A. A. Khedr and H. A. ElBatal, "Corrosion of zinc-containing cabal glasses by various leaching solutions," *Journal of the American Ceramic Society*, vol. 79, no. 3, pp. 733–741, 1996.

Research Article

Ultradurable Dye-Sensitized Solar Cells under 120°C Using Cross-Linkage Dye and Ionic-Liquid Electrolyte

Seigo Ito,¹ Kaoru Takahashi,¹ Shin-ichi Yusa,² Masayuki Saito,³ and Toshiyuki Shigetomi³

¹ Department of Electrical Engineering and Computer Sciences, Graduate School of Engineering, University of Hyogo, 2167 Shosha, Himeji, Hyogo 671-2280, Japan

² Department of Materials Science and Chemistry, Graduate School of Engineering, University of Hyogo, 2167 Shosha, Himeji, Hyogo 671-2280, Japan

³ Tanaka Kikinzoku Kogyo K.K., 22 Wadai, Tsukuba, Ibaraki 300-4247, Japan

Correspondence should be addressed to Seigo Ito; itou@eng.u-hyogo.ac.jp

Received 12 February 2013; Accepted 25 May 2013

Academic Editor: Tianxin Wei

Copyright © 2013 Seigo Ito et al. This is an open access article distributed under the Creative Commons Attribution License, which permits unrestricted use, distribution, and reproduction in any medium, provided the original work is properly cited.

A double-bond-edged Ru dye (code name: SG1051) has been studied as a novel sensitizing dye for ultradurable dye-sensitized solar cells (DSCs). The SG1051 Ru dye showed the quick dye-uptake time (1 h for the optimized condition: $\eta = 9.2\%$, using volatile electrolyte) and the strong adsorption strength compared with standard Ru dyes (N719 and Z907), which was checked by successive dipping of dye-adsorbed nanocrystalline-TiO₂ electrodes into NaOH aqueous solution and acetonitrile. The resulting DSCs using SG1051 Ru dye and ionic-liquid electrolyte survived the durability test at 120°C for 480 h, which can be the strong interest of the industrial groups.

1. Introduction

Although significant investigations have been performed for dye-sensitized solar cells (DSCs) in these two decades from the emerge [1–5], still DSCs have not been adopted to fully commercialized outdoor applications for the photovoltaic generation systems. In order to establish cost-effective outdoor solar photovoltaic generation systems by DSCs, the important points are (1) high efficiency, (2) low cost, and (3) high stability, which are summarized as follows.

(1) High efficiency: 11.4% [6] and 12.3% [7] conversion-efficiency DSCs have been reported as confirmed and in-house best results, respectively, which are still lower than other crystal-utilized solar cells (c-silicon (24.7%) [8], CuIn (Ga) Se₂ (20.3%) [9], GaInP/GaAs/GaInAs (tandem; 36.9%) [10], and so on). Although the DSC conversion efficiencies are lower than other solar cells, it can be acceptable if the production cost can be drastically lower than other solar cells.

(2) Low cost: DSCs, which can be fabricated using low-cost materials (TiO₂, dye, etc.) by a nonvacuum printing system, have attracted academic and industrial attention. The fabrication cost was estimated as 0.48–0.80 dollar per Watt [11], which can suggest that DSC can be one of the candidates for the further cost-effective solar cells.

(3) Stability: unfortunately, DSCs which presented above over 10% conversion efficiencies are not so stable under the outdoor conditions; the high-efficiency DSCs show the lower stability because of the utilization of volatile electrolyte (acetonitrile); on the other hand, the lower-efficiency DSCs show the higher stability [12]. One of the benchmark results is 8% conversion efficiency with 1000 h stability under 80°C in dark condition [13]. However, stability at much higher temperature has been required from the viewpoint of industrial companies, which have demanded the durability at 120°C for the commercialization as the outdoor applications (in private communications between industrial partners).

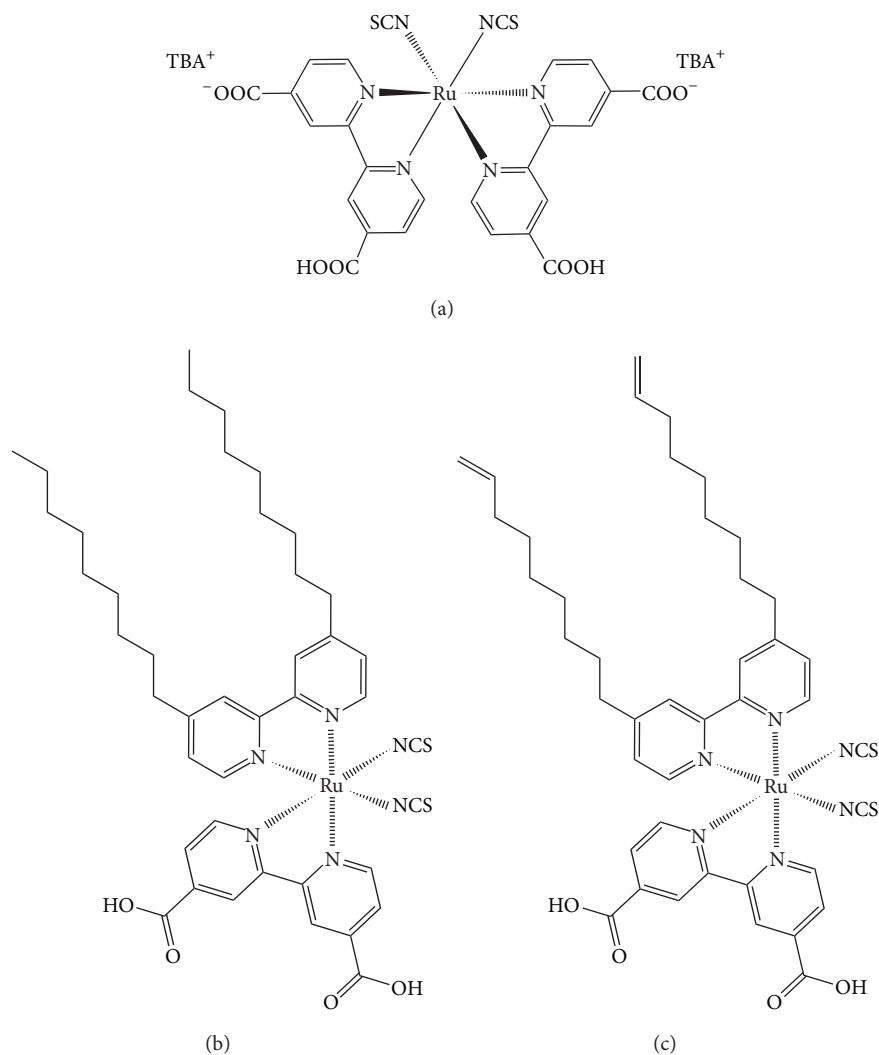


FIGURE 1: Structures of Ru dyes studied in this paper (N719 dye (a), Z907 dye (b), and double-bond-edged dye (c)).

In order to enhance the durability of DSCs, a number of dyes have been synthesized [12–21]. However, the thermal stability tests reported have been up to 85°C [12–27]. In order to check the much-higher temperature stability, we have tried thermal durability test using ionic-liquid electrolyte and Z907 dye from 80 to 110°C [28]. Although the electrolyte was not leaked out from the cells at 110°C, the photoenergy-conversion efficiency dropped to 6% of initial value in 80 h. It was confirmed that the reason of the deterioration of photoenergy-conversion efficiency against thermal stress is desorption of the sensitizing dyes from the surface of TiO₂ electrode into the electrolyte [12, 29, 30]. In order to prevent the dye desorption, the sensitizing dye was bonded by epoxy polymer [28]. However, the epoxy polymer coating on dye molecule did not work for the enhancement of thermal stability at 110°C (it was almost sudden death). Another idea was polymerization of dyes using cross-linkage ligand [31]. However, in the report, volatile electrolyte (acetonitrile) was utilized for the room temperature stability test (not for high temperature).

In this report, therefore, ultradurable DSCs have been fabricated. For the durable DSCs, we have synthesized a Ru dye with double-bond-edged alkyl chains (the same chain length with Z907, code name: SG1051, in Figure 1(c)) for cross-linkage between dyes on the TiO₂ surface [31]. Using ionic liquid and heating treatment, the resulting DSCs showed significant stability for the thermal effect. The DSCs using SG1051 dye performed the durability at 120°C for 480 h.

We have compared three ruthenium dyes for the sensitizers in DSCs. The first is a standard high-efficiency dye without alkyl chain (N719, Figure 1(a)), which has a record of 11.2% conversion efficiency [32]. The second is a standard high-stable dye with alkyl chain (Z907, Figure 1(b)), which has a record of 7.6% conversion efficiency with 1000 h durability at 80°C [14]. The third is the double-bond-edged ruthenium dye (named as SG1051, Figure 1(c)), which was synthesized using the same carbon chain length (C₉) with a standard stable ruthenium dye (Z907 [14–16]) for this report. In order to show the reason why the double-bond-edged alkyl chain is necessary for the durable DSCs, we have checked the

adsorption strength on TiO_2 surface against aqueous alkali solution (NaOH *aq.*) and organic solvent (acetonitrile) for the test case of thermal durability. It was confirmed that the side double-bond-edged alkyl chains of ruthenium dyes have strong effect on the dye alignment on nanocrystalline- TiO_2 surface and the adsorption strength, resulting in the durability of DSCs.

2. Experiments

For the preparations of stable DSCs, a double-bond-edged ruthenium dye [31] was synthesized using the carbon chain length (C_9). Z907 and N719 were purchased from Solaronix SA (Switzerland). For the preparation of the DSC working electrodes, FTO-glass plates (TEC 15 Ω/square , 2.2 mm thickness, Nippon Sheet Glass-Pilkington) were used. The details of the fabrication scheme are described in a previous report [33]. For the transparent ($t = 8.6 \mu\text{m}$) and light-scattering ($t = 6.3 \mu\text{m}$) layers, commercialized TiO_2 pastes (PST-30NRD and PST-400C, JGC-CCIC, Japan) were utilized, respectively. The porous double-layered TiO_2 electrodes were immersed in ruthenium dyes (SG1051, Z907, or N719). The dipping durations were 1 h for SG1051 and 20–24 h for Z907 and N719. The dye-uptake nanocrystalline- TiO_2 electrodes and platinized FTO counter electrodes were assembled using a hot-melt film glue (Bynel 4164, Du-Pont) at 250°C for 1 min, which became the dye-polymerization treatment to stabilize DSC thermally, at the same time. The ionic-liquid electrolyte for the stable DSCs was 0.3 M iodine in 1-propyl-3-methyl imidazolium iodide. The electrolyte for the high-efficiency DSCs was 0.3 M iodine, 0.1 M guanidinium thiocyanate, 0.5 M *tert*-butylpyridine, 0.05 M lithium iodide, and 1.0 M 1,3-dimethyl imidazolium iodide in acetonitrile. The end sealant was also the Bynel 4164 film glue. The power of an AM 1.5 solar simulator (100 mW cm^{-2}) was calibrated using a reference silicon photodiode equipped with an infrared cutoff filter in order to reduce the mismatch between the simulated light and AM 1.5 in the region of 350–700 nm to less than 2% [34]. The photo current-voltage curves are obtained by the application of an external bias to the cell and by measuring the generated photocurrent with a digital source meter. Masks made of black plastic tape were attached on the top to reduce the scattering of light [35].

3. Results and Discussion

In order to set optimized condition of the SG1051 dye (Figure 1(c)), at first, it was confirmed the DSC photovoltaic variations related to the dye-uptake time to nanocrystalline- TiO_2 electrodes (Figure 2). Up to 60 min, the short-circuit photocurrent density (J_{sc}) increased, the open-circuit photovoltage (V_{oc}) decreased, the fill factor (FF) slightly decreased, and the photoenergy-conversion efficiency (η) increased, resulting in the peak of η at 60 min. Keeping the dye-uptake for overnight, the η deteriorated to 0.1%. In contrast to N719 (Figure 1(a)) and Z907 (Figure 1(b)) which need 20–24 h for the optimized dye uptake, the double-bond-edged dye needs just 60 min for the saturation of conversion efficiency. For the

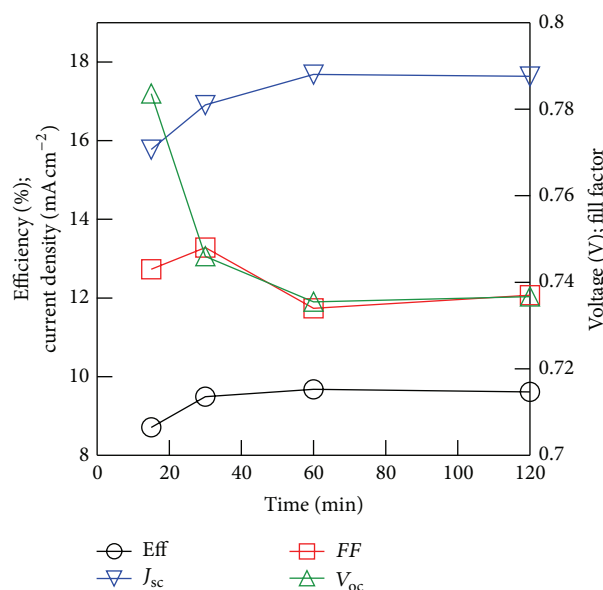


FIGURE 2: Variations of photovoltaic characteristics of SG1051 dye-sensitized solar cells related to the dye-uptake time. The electrolyte was acetonitrile-based electrolyte for high-efficiency DSCs.

experiments below, the dye-uptake time duration of 60 min has been utilized for SG1051 dye.

The difference between Z907 (Figure 1(b)) and SG1051 (Figure 1(c)) was just the double bonds on the edge of alkyl chain on the dye. Hence, this phenomenon is due to the π - π stacking between double-bond-edged dyes, which is verified by Bagnis et al. in the organic solar cells [36]; it was reported that double bonds on edges of alkyl chains changed the conformation of dye molecular aggregation forms and improved the photovoltaic effects in organic thin-film solar cells. Therefore, it was considered that the double-bond-edged dyes were aligned via π - π stacking side by side on the TiO_2 surface (as Figure 3(a)).

The stability tests were managed on DSCs using Z907 and SG1051 dyes and the ionic-liquid electrolyte, which were kept at 120°C in an oven (dark condition). Each V_{oc} was deteriorated 78–79% from the initial value in the first 30 h and became stable (Figure 4(a)). On the other hand, the behavior of J_{sc} showed the difference between Z907 and SG1051 (Figure 4(b)); after 480 h, J_{sc} of Z907 and SG1051 dropped to 7.3% and 69% from the initial value, respectively. Hence, SG1051 dye was relatively stable at 120°C . The variation of FF was differed between dyes (Figure 4(c)). However, the resulting FF after 480 hours became close each other, which is also close to the initial value. Hence, it was considered that FF did not vary the photoenergy-conversion efficiency between dyes. About the conversion efficiency (η) (Figure 4(d)), Z907 showed the huge drop during the thermal stability test (as reported [28]). On the other hand, although the conversion efficiency of SG1051 DSC decreased to 60% from the initial value due to the deterioration of J_{sc} and V_{oc} , the SG1051 DSC survived the thermal stability test at 120°C . Since the difference between Z907 and SG1051 was just the edge double

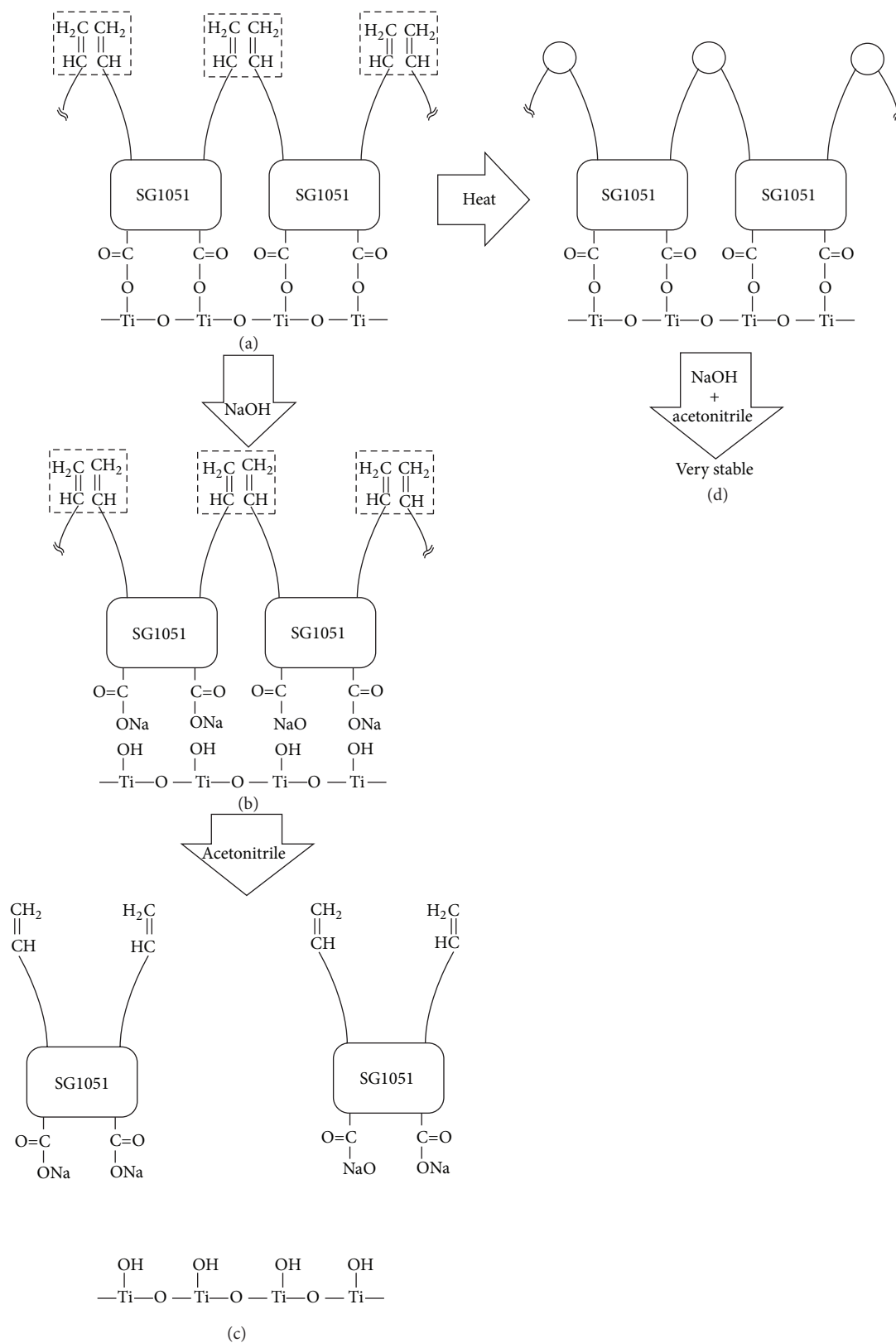


FIGURE 3: Images of double-bond-edged Ru dye on TiO₂ surface. The squares by broken line suggest π-π stacking bond.

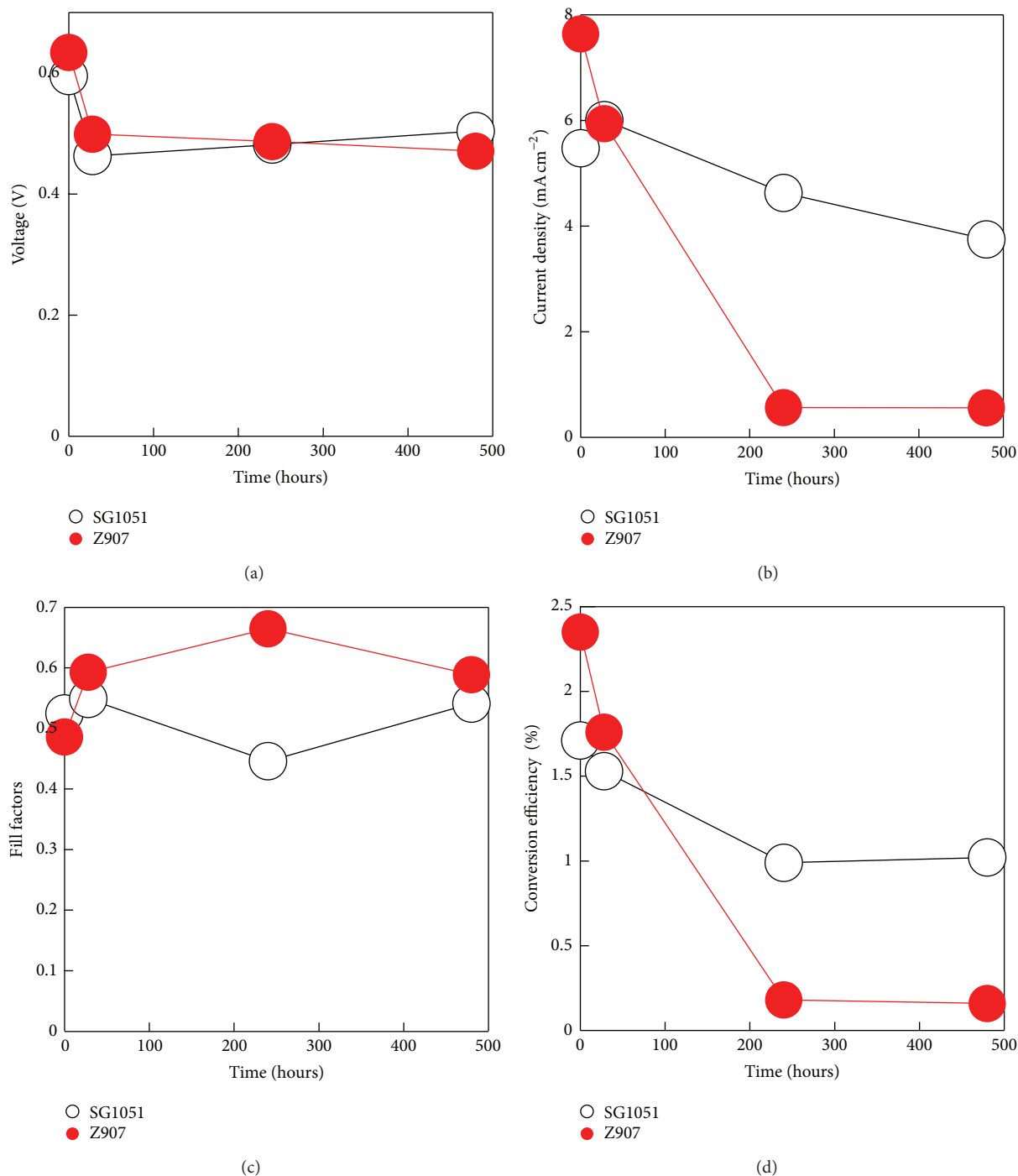


FIGURE 4: Variation of photovoltaic effects of dye-sensitized solar cells using ionic-liquid electrolyte and Z907 and double-bond-edged Ru dyes at 120°C: (a) open-circuit photovoltage, (b) short-circuit photocurrent density, (c) fill factor, and (d) conversion efficiency.

bond, the progress against such thermal stress test is due to the double bond.

In order to check the bonding stability between dye and TiO₂ surface, absorption spectra of dyed nanocrystalline-TiO₂ electrodes were measured before/after dipping NaOH aqueous solution and acetonitrile. Since NaOH removed N719 dye from the TiO₂ surface [32], the N719-adsorbed

TiO₂ lost the absorbance (Figure 5(a)). On the other hand, since the 47% of Z907 absorbance remained on the TiO₂ surface against the NaOH treatment, almost half of the Z907 molecules remained on the TiO₂ surface from the initial value (Figure 5(b)).

About SG1051 dye, the dipping of dyed-TiO₂ electrodes in NaOH aqueous solution, surprisingly, did not decrease the

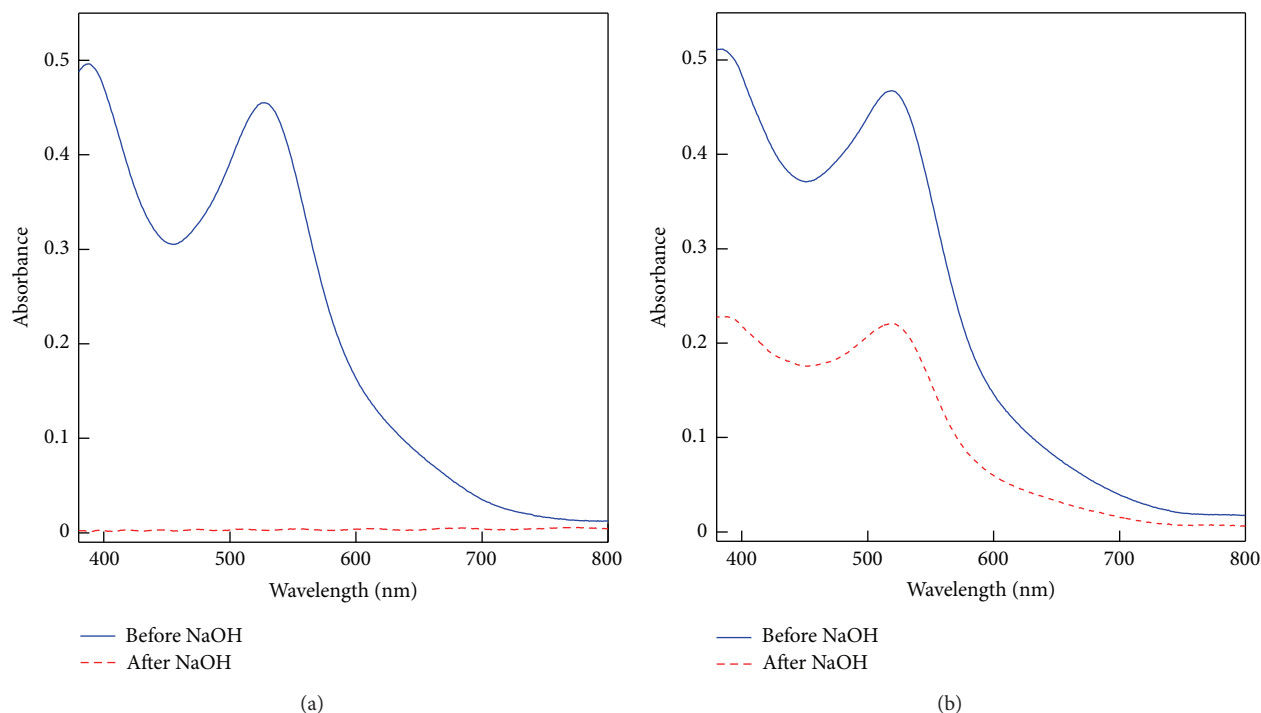


FIGURE 5: Absorption spectra of Ru-dye (N719 (a) and Z907 (b)) adsorbed TiO_2 nanocrystalline electrodes. Each dyed electrode was dipped in NaOH aq. , and the difference of absorbance was checked.

absorbance (Figure 6(a)), which is showing the more stable adsorption of the SG1051 dye onto the TiO_2 surface than N719 and Z907 Ru dyes. This phenomenon is due to the π - π stacking between SG1051 dyes. However, the successive dipping to NaOH aq. and acetonitrile removed the SG1051 dye from TiO_2 (Figure 6(a)). Therefore, it was considered that the double bonds did not make the bonding each other which are just the π - π stacking (as Figure 3(a)). The NaOH treatment attacked the connections between SG1051 anchors ($-\text{COO}-$) and TiO_2 (Figure 3(b)). Finally, SG1051 dyes were separated from each other by acetonitrile, and then, the SG1051 dye was removed from the TiO_2 surface (as Figure 3(c)).

In order to stabilize the dye adsorption strength, the dyed- TiO_2 electrodes were heated by a hot plate at 125°C and 250°C for 1 min, which were the same effects as the cell assembly procedure using hot-melt glue films (Surlyn 1702, sealed at 125°C [31], and Bynel 4164, sealed at 250°C), respectively. Although the heated nanocrystalline- TiO_2 electrodes with the SG1051 Ru dye kept the absorbance after the dipping in NaOH aq. solution as nonheated dyed- TiO_2 electrodes (Figures 6(b) and 6(c)), the dyed- TiO_2 electrode heated at 125°C lost the absorption after dipping in acetonitrile successively. On the other hand, the absorbance of the heated electrode at 250°C remained after the successive dipping in NaOH aq. and acetonitrile, which has not been observed on the TiO_2 electrodes using N719 and Z907 and on nonheated and 125°C -heated TiO_2 electrode using SG1051 dye. Hence, it was confirmed that the absorption strength of SG1051 dye on TiO_2 surface was stronger than N719 and Z907. This is the reason

why SG1051 DSC using Bynel 4164 (sealed at 250°C) had better thermal stability performance than Z907 (Figure 4). The improvement of the adsorption strength by heating at 250°C significantly may be due to the polymerization between the double-bond edges on alkyl chain (as Figure 3(d)).

In order to explain the heating effect on SG1051 dye, ATR FT-IR spectra were measured before and after heating. In Figure 7(a), the peaks observed at 2927 and 2856 cm^{-1} correspond to the asymmetric and symmetric stretching modes of the CH_2 -units of the aliphatic chains [14–16, 18, 31]. At room temperature, it was confirmed that $-\text{CH}=\text{CH}_2$ was existed due the small peak at 2956 cm^{-1} . Increasing the temperature, the peak at 2956 cm^{-1} was disappeared, suggesting a new structure fabricated from the $-\text{CH}=\text{CH}_2$.

Before annealing, in Figure 7(b), the large broad absorption from 1500 cm^{-1} to 1750 cm^{-1} is due to bipyridyl ring and $-\text{CH}=\text{CH}_2$ group. The apparent peak located at 1383 cm^{-1} for stretching mode of carboxylate groups [14–17]. With increasing the annealing temperature, the $-\text{CH}=\text{CH}_2$ group was decreased, and four peaks at 1434 , 1542 , 1616 , and 1730 cm^{-1} enhanced prominently. The peaks at 1434 and 1542 cm^{-1} are attributed to bipyridyl ring modes [14–17]. The peak at 1616 cm^{-1} is ascribed to stretching mode of carboxylate groups [14–17]. The peak at 1730 cm^{-1} is due to ester group which is synthesized from double-bond edges and oxygen by heating treatment.

In conclusion, double-bond-edged dye (SG1051) was found to be the best photosensitizer for use in ultra-durable DSCs which can survive at 120°C . When the film is sensitized

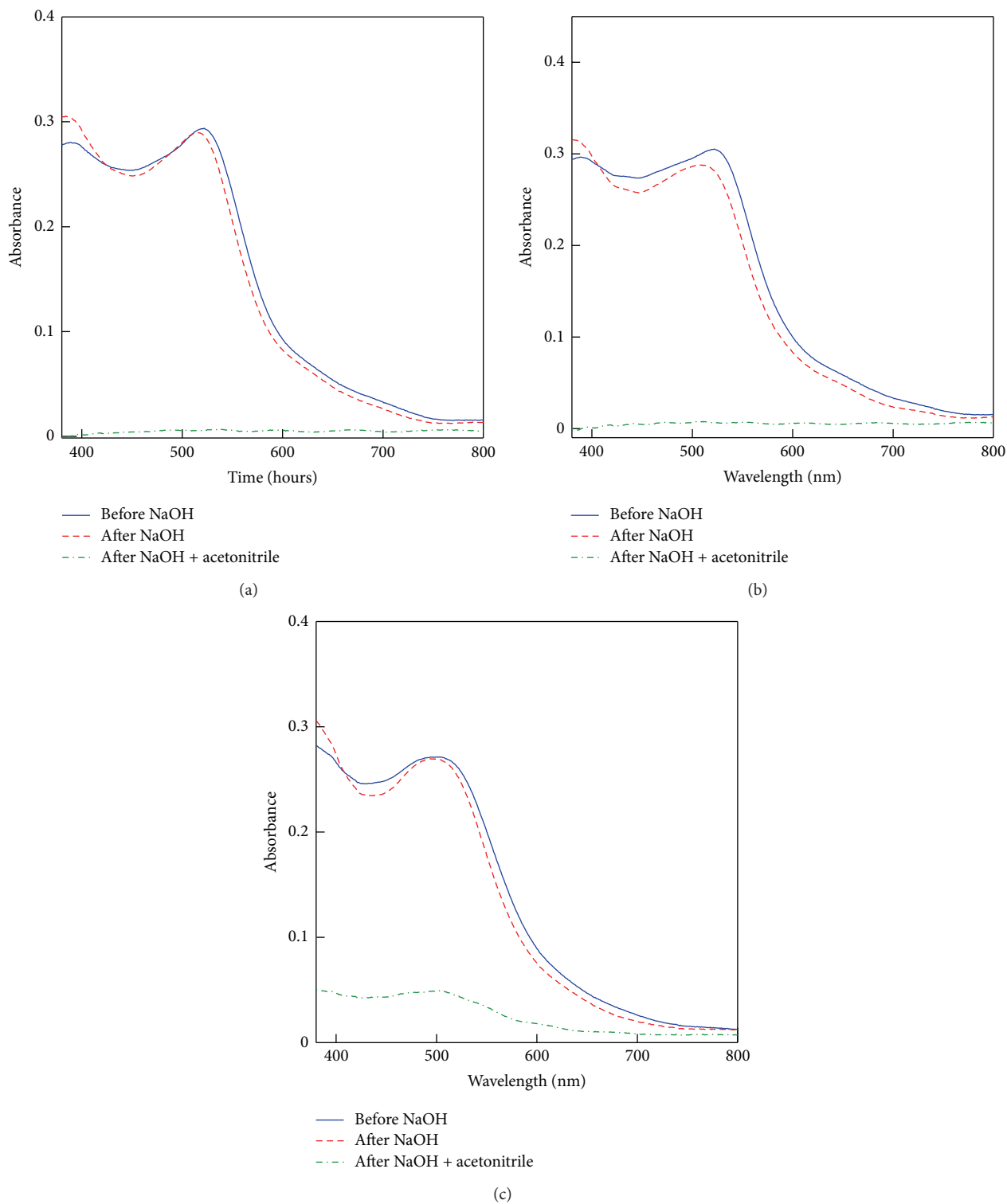


FIGURE 6: Absorption spectra of double-bond-edged Ru-dye (SG1051) adsorbed nanocrystalline-TiO₂ electrodes without heating (a) and after the heating on a hot plate at 125°C (b) and 250°C (c). Each dyed electrode was dipped in NaOH *aq.* and acetonitrile successively, and the difference of absorbance was checked.

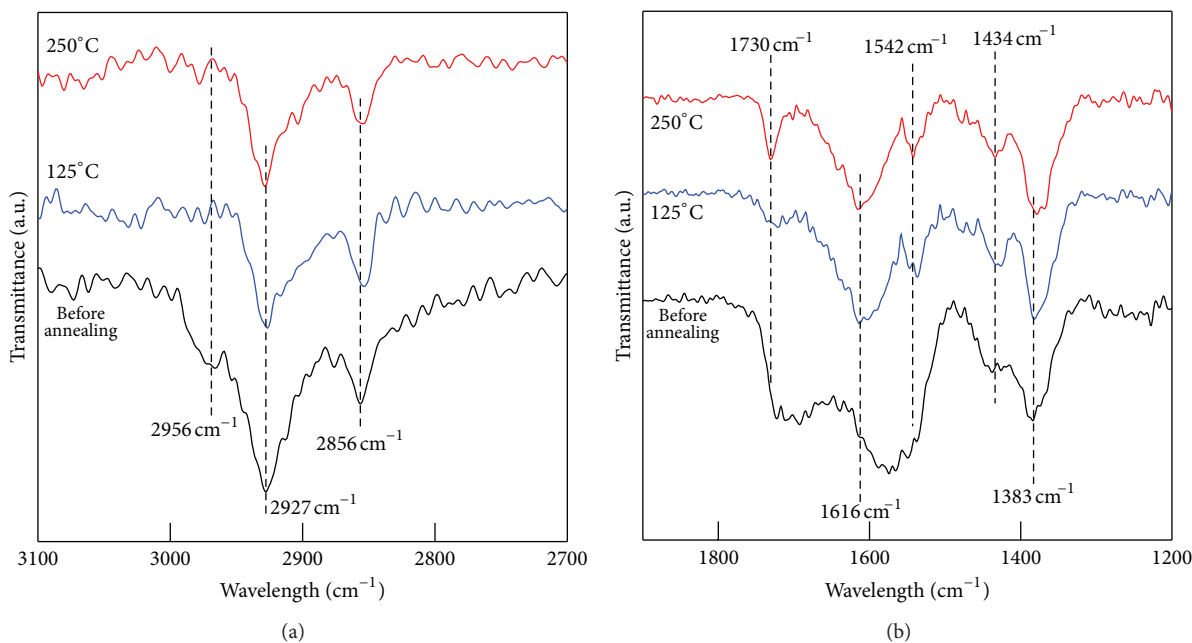


FIGURE 7: FT-IR measurements of double-bond-edged dye-adsorbed TiO_2 nanoparticles before and after annealing; (a) $2700\text{--}3100\text{ cm}^{-1}$ and (b) $1200\text{--}1900\text{ cm}^{-1}$.

without heating treatment at 250°C , the adsorption strength becomes weaker, which was checked as the test case using NaOH aq. and acetonitrile dipping. For treatment on the hot plate at 250°C , the double-bond-edged dye can be bound to the surface of the nanocrystalline- TiO_2 film with dye polymerization, facilitating the prohibition of dye desorption from the TiO_2 surface. Moreover, the double-bond edges are suitable for the dye to align on TiO_2 electrodes that exhibit high photovoltaic performance by the short dye-uptake time (for 1 h). Under the optimized conditions, the double-bond-edged-dye-sensitized cells showed energy conversion efficiency as high as 9.2% using volatile electrolyte. These results clearly show that the application of double-bond-edged dye to DSCs as a photosensitizer is promising for the realization of high stability cell performance and high-speed production. Specially, the double-bond-edged dye could be applied on outdoor buildings and cars. The further studies to improve the conversion efficiency emphasize the DSC industrialization.

Acknowledgments

The authors gratefully acknowledge Merck Co. Ltd. and EPFL-LPI group for providing samples of ionic liquid.

References

- [1] B. O'Regan and M. Grätzel, "A low-cost, high-efficiency solar cell based on dye-sensitized colloidal TiO_2 films," *Nature*, vol. 353, pp. 737–740, 1991.
- [2] M. Grätzel, "Photoelectrochemical cells," *Nature*, vol. 414, no. 6861, pp. 338–344, 2001.
- [3] Y. Bai, Y. Cao, J. Zhang et al., "High-performance dye-sensitized solar cells based on solvent-free electrolytes produced from eutectic melts," *Nature Materials*, vol. 7, pp. 626–630, 2008.
- [4] S. Ito, S. M. Zakeeruddin, P. Comte, P. Liska, D. Kuang, and M. Grätzel, "Bifacial dye-sensitized solar cells based on an ionic liquid electrolyte," *Nature Photonics*, vol. 2, no. 11, pp. 693–698, 2008.
- [5] J.-H. Yum, E. Baranoff, F. Kessler et al., "A cobalt complex redox shuttle for dye-sensitized solar cells with high open-circuit potentials," *Nature Communications*, 2012.
- [6] M. A. Green, K. Emery, Y. Hishikawa, W. Warta, and E. D. Dunlop, "NIMS sets a new world record for the highest conversion efficiency in dye-sensitized solar cells," *Progress in Photovoltaics*, vol. 20, pp. 12–20, 2012.
- [7] A. Yella, H.-W. Lee, H. N. Tsao et al., "Porphyrin-sensitized solar cells with cobalt (II/III)-based redox electrolyte exceed 12 percent efficiency," *Science*, vol. 334, no. 6056, pp. 629–634, 2011.
- [8] J. Zhao, A. Wang, and M. A. Green, "24.5% Efficiency silicon PERT cells on MCZ substrates and 24.7% efficiency PERL cells on FZ substrates," *Progress in Photovoltaics*, vol. 7, no. 6, pp. 471–474, 1999.
- [9] P. Jackson, D. Hariskos, E. Lotter et al., "New world record efficiency for $\text{Cu}(\text{In,Ga})\text{Se}_2$ thin-film solar cells beyond 20%," *Progress in Photovoltaics*, vol. 19, no. 7, pp. 894–897, 2011.
- [10] T. Agui, H. Juso, A. Yoshida, K. Nakaido, K. Sasaki, and T. Takamoto, "Design and fabrication of broadband anti-reflection sub-wavelength periodic structure for solar cells," in *Proceedings of the Renewable Energy, O-Pv-5-4*, Yokohama, Japan, 2010.
- [11] G. Smestad, C. Bignozzi, and R. Argazzi, "Testing of dye sensitized TiO_2 solar cells I: experimental photocurrent output and conversion efficiencies," *Solar Energy Materials and Solar Cells*, vol. 32, no. 3, pp. 259–272, 1994.
- [12] M. I. Asghar, K. Miettunen, J. Halme et al., "Review of stability for advanced dye solar cells," *Energy and Environmental Science*, vol. 3, no. 4, pp. 418–426, 2010.

- [13] P. Wang, C. Klein, R. Humphry-Baker, S. M. Zakeeruddin, and M. Grätzel, "Stable $\geq 8\%$ efficient nanocrystalline dye-sensitized solar cell based on an electrolyte of low volatility," *Applied Physics Letters*, vol. 86, no. 12, Article ID 123508, 2005.
- [14] P. Wang, S. M. Zakeeruddin, R. Humphry-Baker, J. E. Moser, and M. Grätzel, "Molecular-scale interface engineering of TiO_2 nanocrystals: improving the efficiency and stability of dye-sensitized solar cells," *Advanced Materials*, vol. 15, no. 24, pp. 2101–2104, 2003.
- [15] P. Wang, S. M. Zakeeruddin, P. Comte, R. Charvet, R. Humphry-Baker, and M. Grätzel, "Enhance the performance of dye-sensitized solar cells by co-grafting amphiphilic sensitizer and hexadecylmalonic acid on TiO_2 nanocrystals," *Journal of Physical Chemistry B*, vol. 107, no. 51, pp. 14336–14341, 2003.
- [16] P. Wang, B. Wenger, R. Humphry-Baker et al., "Charge separation and efficient light energy conversion in sensitized mesoscopic solar cells based on binary ionic liquids," *Journal of the American Chemical Society*, vol. 127, no. 18, pp. 6850–6856, 2005.
- [17] P. Wang, S. M. Zakeeruddin, J. E. Moser et al., "Stable new sensitizer with improved light harvesting for nanocrystalline dye-sensitized solar cells," *Advanced Materials*, vol. 16, no. 20, pp. 1806–1811, 2004.
- [18] P. Wang, C. Klein, J. Moser et al., "Amphiphilic ruthenium sensitizer with 4,4'-diphosphonic acid-2,2'-bipyridine as anchoring ligand for nanocrystalline dye sensitized solar cells," *Journal of Physical Chemistry B*, vol. 108, no. 45, pp. 17553–17559, 2004.
- [19] F. Gao, Y. Wang, D. Shi et al., "Enhance the optical absorptivity of nanocrystalline TiO_2 film with high molar extinction coefficient ruthenium sensitizers for high performance dye-sensitized solar cells," *Journal of the American Chemical Society*, vol. 130, no. 32, pp. 10720–10728, 2008.
- [20] Y. Cao, Y. Bai, Q. Yu et al., "Dye-sensitized solar cells with a high absorptivity ruthenium sensitizer featuring a 2-(hexylthio)thiophene conjugated bipyridine," *Journal of Physical Chemistry C*, vol. 113, no. 15, pp. 6290–6297, 2009.
- [21] A. Hagfeldt, G. Boschloo, L. Sun, L. Kloo, and H. Pettersson, "Dye-sensitized solar cells," *Chemical Reviews*, vol. 110, no. 11, pp. 6595–6663, 2010.
- [22] P. T. Nguyen, R. Degn, H. T. Nguyen, and T. Lund, "Thiocyanate ligand substitution kinetics of the solar cell dye Z-907 by 3-methoxypropionitrile and 4-tert-butylpyridine at elevated temperatures," *Solar Energy Materials and Solar Cells*, vol. 93, no. 11, pp. 1939–1945, 2009.
- [23] H. Matsui, K. Okada, T. Kitamura, and N. Tanabe, "Thermal stability of dye-sensitized solar cells with current collecting grid," *Solar Energy Materials and Solar Cells*, vol. 93, no. 6–7, pp. 1110–1115, 2009.
- [24] H. Arakawa, T. Yamaguchi, T. Sutou et al., "Efficient dye-sensitized solar cell sub-modules," *Current Applied Physics*, vol. 10, supplement 2, pp. S157–S160, 2010.
- [25] P. M. Sommeling, M. Späth, H. J. P. Smit, N. J. Bakker, and J. M. Kroon, "Long-term stability testing of dye-sensitized solar cells," *Journal of Photochemistry and Photobiology A*, vol. 164, no. 1–3, pp. 137–144, 2004.
- [26] A. Hinsch, J. M. Kroon, R. Kern et al., "Long-term stability of dye-sensitized solar cells," *Progress in Photovoltaics*, vol. 9, no. 6, pp. 425–438, 2001.
- [27] R. Sastrawan, J. Beier, U. Belledin et al., "New interdigital design for large area dye solar modules using a lead-free glass frit sealing," *Progress in Photovoltaics*, vol. 14, no. 8, pp. 697–709, 2006.
- [28] K. Tsujimoto, S. Ito, S. Yusa, and T. Imamura, *Environmental Science & Technology*, vol. 2, pp. 74–78, 2011.
- [29] T. Sekiguchi, S. Kambe, M. Tani, T. Kitagaki, and K. Takahama, *Panasonic Denko Giho*, vol. 56, pp. 87–92, 2008.
- [30] W. Kubo, S. Kambe, S. Nakade et al., "Photocurrent-determining processes in quasi-solid-state dye-sensitized solar cells using ionic gel electrolytes," *Journal of Physical Chemistry B*, vol. 107, no. 18, pp. 4374–4381, 2003.
- [31] K.-Y. Liu, C. Hsu, S.-H. Chang, J.-G. Chen, K.-C. Ho, and K.-F. Lin, "Synthesis and characterization of cross-linkable ruthenium complex dye and its application on dye-sensitized solar cells," *Journal of Polymer Science A*, vol. 48, no. 2, pp. 366–372, 2010.
- [32] M. K. Nazzerruddin, A. Kay, I. Rodicio et al., "Conversion of light to electricity by cis-X2bis(2,2'-bipyridyl-4,4'-dicarboxylate)ruthenium(II) charge-transfer sensitizers (X = Cl-, Br-, I-, CN-, and SCN-) on nanocrystalline titanium dioxide electrodes," *Journal of the American Chemical Society*, vol. 115, no. 14, pp. 6382–6390, 1993.
- [33] S. Ito, T. N. Murakami, P. Comte et al., "Fabrication of thin film dye sensitized solar cells with solar to electric power conversion efficiency over 10%," *Thin Solid Films*, vol. 516, no. 14, pp. 4613–4619, 2008.
- [34] S. Ito, H. Matsui, K. Okada et al., "Calibration of solar simulator for evaluation of dye-sensitized solar cells," *Solar Energy Materials and Solar Cells*, vol. 82, no. 3, pp. 421–429, 2004.
- [35] S. Ito, P. Liska, P. Comte et al., "Photovoltaic characterization of dye-sensitized solar cells: effect of device masking on conversion efficiency," *Progress in Photovoltaics*, vol. 14, no. 7, pp. 589–601, 2006.
- [36] D. Bagnis, L. Beverina, H. Huang et al., "Marked alkyl-Vs alkenyl-substituent effects on squaraine dye solid-state structure, carrier mobility, and bulk-heterojunction solar cell efficiency," *Journal of the American Chemical Society*, vol. 132, no. 12, pp. 4074–4075, 2010.

Research Article

Alignment of TiO₂ (Anatase) Crystal of Dye-Sensitized Solar Cells by External Magnetic Field

Na-Yeong Hong, Hyunwoong Seo, Min-Kyu Son, Soo-Kyoung Kim, Song-Yi Park, Kandasamy Prabakar, and Hee-Je Kim

Department of Electrical Engineering, Pusan National University, Pusan 609-735, Republic of Korea

Correspondence should be addressed to Hee-Je Kim; heeje@pusan.ac.kr

Received 6 February 2013; Revised 23 May 2013; Accepted 25 May 2013

Academic Editor: Tianxin Wei

Copyright © 2013 Na-Yeong Hong et al. This is an open access article distributed under the Creative Commons Attribution License, which permits unrestricted use, distribution, and reproduction in any medium, provided the original work is properly cited.

In this study, magnetic field (B) was applied on TiO₂ (anatase) of dye-sensitized solar cell (DSC) for alignment of crystal. Magnetic field was applied on TiO₂ when deposited TiO₂ on the fluorine tin oxide (FTO) was dried at 373 K for crystalline orientation. And applying time of B was varied 0~25 min. Characteristics of the magnetic field applied TiO₂ films were analyzed by X-ray diffraction (XRD), high resolution transmission electron microscopy (HRTEM), scanning electron microscopy (SEM), and electrochemical impedance spectroscopy (EIS). Current-voltage characteristics were also analyzed using solar simulator, and it was confirmed that the energy conversion efficiency of 41% was increased. Finally, it was identified that the magnetic field affected orientation of TiO₂, resulting in the enhancement of the performance of the DSC.

1. Introduction

DSC is one of the promising alternatives to conventional solar cells because of low fabrication cost and relatively simple production processes. A typical DSC is a sandwich structure which consists of a nanoporous TiO₂ film photoelectrode covered with a monolayer of the Ruthenium complex-based dye, a Pt counterelectrode, and a redox electrolyte of I⁻/I₃⁻ in an acetonitrile solution which is between two electrodes [1, 2].

Semiconductor of photoelectrode is important role in DSC performance, because electrons from dye molecules transport to conductive glass through semiconductor materials by hopping. To enhance dye absorption and accessibility to the hole-carrying electrolyte, a mesoporous structure is essential for the semiconductor film [3]. However, mesoporous films are of a nanocrystalline nature and contain numerous crystal defects in the grain boundaries. These defects impede electron transport and are harmful to cell performance [4–8]. The diffusion of electrons through the nanocrystalline network is several orders of magnitude slower than that in a single crystal [9]. Thus, how the crystal structure of nanocrystalline films affects electron transport is an important issue.

Among the semiconductor materials used in DSCs [10–12], TiO₂ has been proven to be the best semiconductor material for the DSC. TiO₂ has three crystallographic polymorphs, that is, rutile, anatase, and brookite, composed of Ti ions having octahedral coordination. Anatase is perceived as the more active phase of TiO₂ because of its surface chemistry and potentially higher conduction-band edge energy [13] and shows advantages in photocatalysis and energy conversion. The size, shape, crystallization, and morphology of anatase particles are important to the performance of the DSC, because this has a great effect on electron mobility and then energy conversion efficiency. Generally, TiO₂ in DSC has nanoporous structure. It is advantageous for dye absorbing but causes many losses of energy.

It has been reported that anatase has an orientation dependence of the reaction activity. Water reduction and photooxidation occur at more negative potentials for the anatase (0 0 1) surface than for the anatase (1 0 1) surface [14]. Orienting anatase nanocrystals with (0 0 1) preferred growth may improve the electron transport in the nanoporous structured dye-sensitized solar cells by changing structure of the photoelectrode [15].

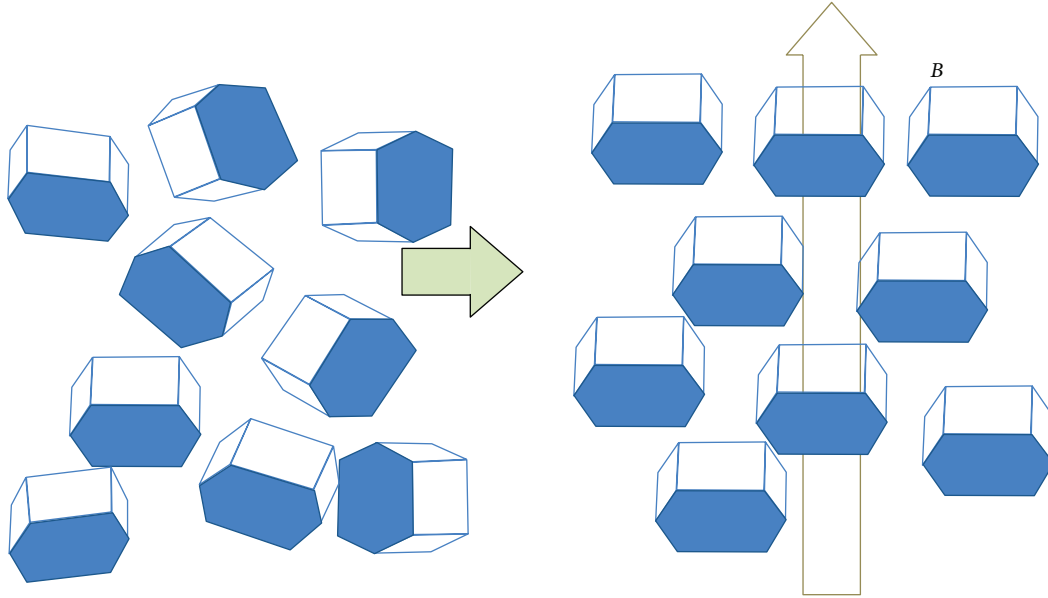


FIGURE 1: Concept of the well-aligned TiO₂ crystals in magnetic field.

Many materials including TiO₂ in asymmetric crystalline structures have anisotropic magnetic susceptibilities, associated with their crystal structures as in

$$\Delta\chi = \chi_{\parallel} - \chi_{\perp}, \quad (1)$$

where χ_{\parallel} and χ_{\perp} are the susceptibilities parallel and perpendicular to the magnetic principal axis, respectively.

The driving force of the magnetic alignment is the energy of the crystal anisotropy and is given as

$$\Delta E = \frac{\Delta\chi VB^2}{2\mu_0}, \quad (2)$$

where V is the volume of the material, B is the applied magnetic field, and μ_0 is the permeability in a vacuum [16]. Therefore, when a single crystal of anatase TiO₂ is placed in a magnetic field, the crystal is rotated, and the crystallographic axis of high χ is aligned in the direction of the magnetic field. A schematic illustration of the rotation of particles in a magnetic field is shown in Figure 1 [17]. It is expected that this property provides TiO₂ photoelectrode condition advantageous for electron transport.

In this study, we researched the alignment of TiO₂ (anatase) crystal in the DSC by applying the external magnetic field. Characteristics of the magnetic field applied TiO₂ films were analyzed by X-ray diffraction (XRD), high resolution transmission electron microscopy (HRTEM), scanning electron microscopy (SEM), UV-vis spectroscopy, and electrochemical impedance spectroscopy (EIS). And current-voltage characteristics were analyzed using solar simulator. As a result, it was confirmed that the energy conversion efficiency was enhanced by the well-aligned anatase TiO₂ crystal, resulting from the external magnetic field.

2. Experimental

2.1. Preparation of the Photoelectrode. TiO₂ paste (Ti-Nanoxide HT/SP, Solaronix) was deposited on FTO glass by the doctor-blade method (effective area = 0.29 cm²). And then, magnetic field was applied by setting the photoelectrode between two permanent Neodymium magnets when the paste was dried at 373 K. The magnetic flux density was 2.99 T measured by Gauss Meter (MG4D, WALKER). Applying time of magnetic field was varied 0, 5, 10, and 25 min. After that, the photoelectrodes were calcined at 723 K for 30 min to form porosity. It was immersed in 0.5 mM N719 dye (Ru(2,20-bipyridyl-4,40-dicarboxylate)₂(NCS)₂, Solaronix) solution for 24 h, so that dye molecules are attached to TiO₂. Then photoelectrode was rinsed with ethyl alcohol for the excess dye molecule elimination and dried.

2.2. DSC Fabrication. Pt counterelectrode was prepared with depositing Pt paste (Pt-Catalyst T/SP, Solaronix) by the doctor-blade method on the FTO glass which has predrilled pin holes to inject electrolyte and sintered at 723 K for 10 min. Prepared two electrodes were joined with thermoplastic hot-melt sheet (SX 1170-60, Solaronix). Electrolyte (0.5 M Lil, 0.05 M I₂, and 0.5 M 4-tert-butylpyridine) was injected between two electrodes, and holes were sealed with cover glass.

2.3. Characterizations. The morphology and the structure of the TiO₂ film were investigated by high resolution transmission electron microscopy (HRTEM, Jem 2011, Jeol Cop.), field emission scanning electron microscopy (FE-SEM, S-4200, Hitachi), and X-ray diffraction (XRD, PANalytical B.V.). The performances of cell were tested by recording the current-voltage curve with source meter (Model 2400, Keithley Instrument, Inc.) under standard illumination

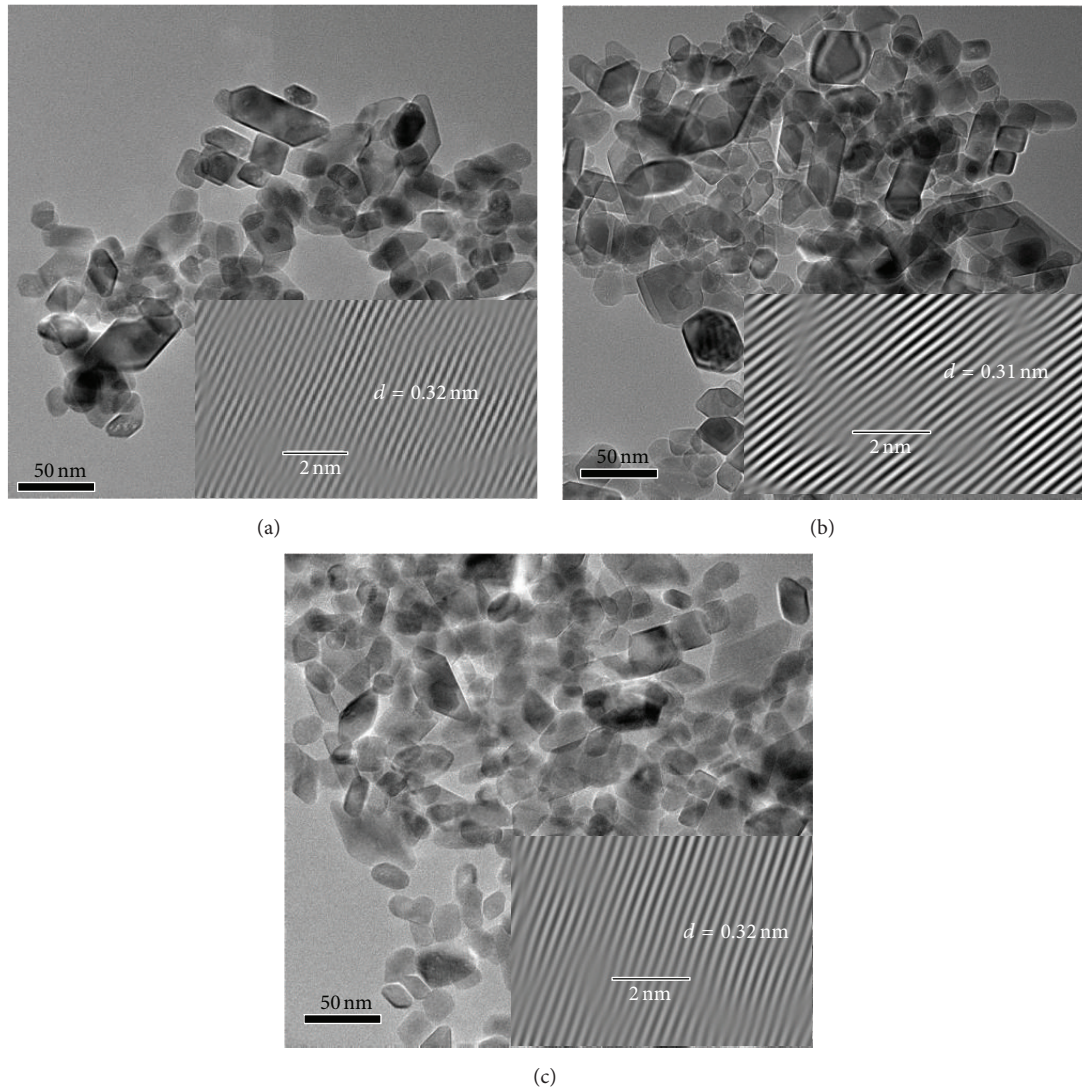


FIGURE 2: The HRTEM images of (a) the conventional TiO_2 , (b) the magnetic field applied TiO_2 after calcined at 723 K for 30 min, and (c) the magnetic field applied TiO_2 without sintering.

of 1 sun (100 mW/cm^2 , AM 1.5). The absorption spectra were obtained using a UV-vis spectrophotometer (Optizen 3220UV, Mecasys). Internal impedance of DSC was measured using electrochemical impedance spectroscopy (EIS, SP-150, Biologic SAS), with a frequency ranging $10^{-2} \text{ Hz} \sim 10^6 \text{ Hz}$.

3. Results and Discussion

3.1. Morphology and Structure of TiO_2 . The HRTEM images of the conventional TiO_2 (a), the magnetic field applied TiO_2 after calcined at 723 K for 30 min (b), and the magnetic field applied TiO_2 without sintering (c) were shown in Figure 2. The corresponding lattice fringes shown in the insets of all figures were clearly observed, indicating that TiO_2 nanoparticles formed with good crystallinity. The interplanar spacing was determined to be 0.32, 0.31, and 0.32 nm, respectively. There was no big difference; it means magnetic field could not affect the structure of crystal.

Figure 3 is XRD patterns of the conventional TiO_2 , the magnetic field applied TiO_2 after calcined at 723 K for 30 min, and the magnetic field applied TiO_2 without sintering. All shows anatase peaks. The diffraction peak of the (0 0 4) of both B applied anatase is stronger than that of conventional. This said that magnetic field made the (0 0 4) plane of anatase vertical to its direction. Anatase TiO_2 particle has a tetragonal crystalline structure and is very likely to be aligned with the direction of the magnetic field as explained with formulae (1) and (2). The c -axis of the anatase TiO_2 particle is aligned parallel to B in the suspension. This property is important for improving interparticle electrical contact and for transporting electrons at neck of interparticle connections [10]. Disordered crystals create defect states during nanoparticle necking into films. These defect states serve as electron trap states, retarding both the electron transport toward the FTO substrate and electron recombination with the electrolyte [4, 18]. And no difference between sintered

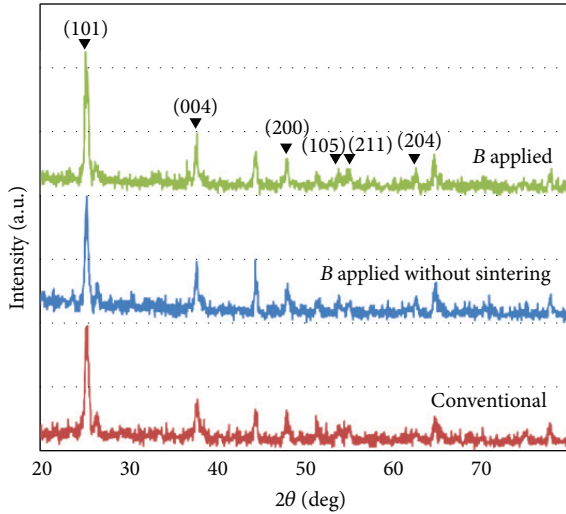


FIGURE 3: XRD patterns of conventional TiO_2 , B applied TiO_2 , and B applied TiO_2 without sintering.

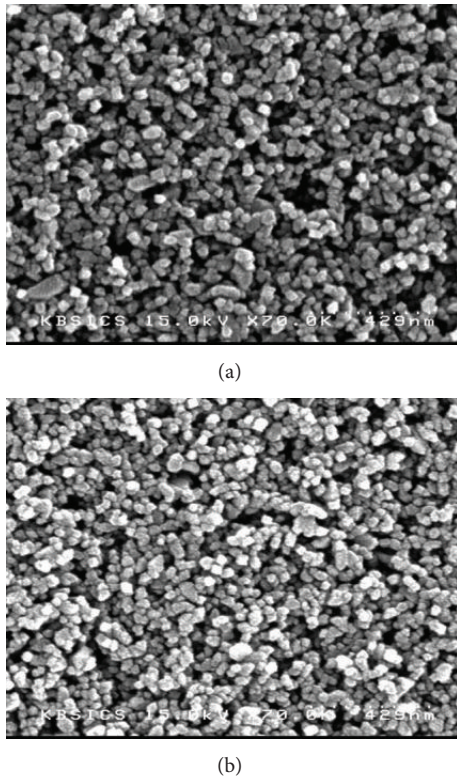


FIGURE 4: SEM images of reference TiO_2 (a) and magnetic field applied TiO_2 (b).

and not sintered B applied TiO_2 was considered no alignment transform of crystals by calcination.

Figure 4 shows SEM images of conventional TiO_2 and magnetic field applied TiO_2 nanoparticles deposited on the FTO glass after calcined at 723 K for 30 min, (a) and (b), respectively. The diameter of each particle is in range of 20~30 nm in both images. It means that magnetic field did not

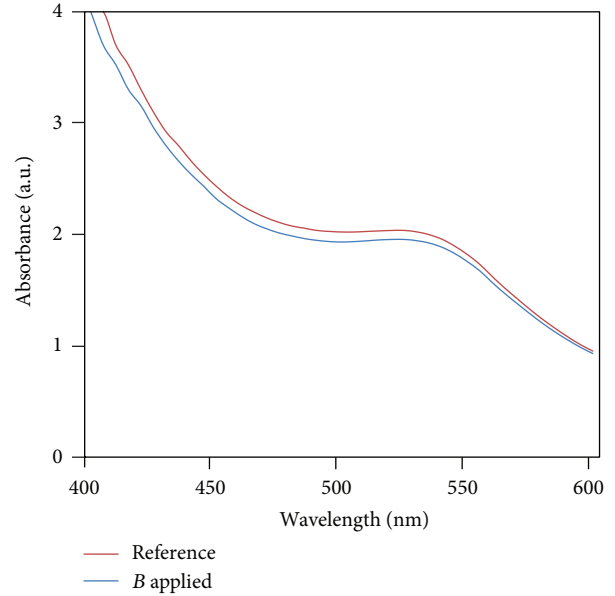


FIGURE 5: UV-vis absorption spectra of DSCs.

affect the size of particle. The morphology of conventional TiO_2 is roughly packed and uneven. Compare to conventional one, the TiO_2 film after crystallization assisted by magnetic field became more densely packed and flat. This shows that magnetic field aligned TiO_2 crystals well.

Figure 5 is UV-vis absorption spectra of magnetic field applied and not applied DSCs. Because both used N719 dye, similar shapes of absorption spectra are shown. Magnetic field applied cell was densely packed comparable to conventional, therefore a surface area of TiO_2 was decreased, and there were less voids to attach dye molecules. So the light absorption of B applied cell was decreased. Despite this, the photocurrent was increased by the well-oriented TiO_2 that is discussed later.

3.2. The Current-Voltage Behaviors. Under standard illumination of 1 sun, I - V curves of DSCs based on conventional and magnetic field applied TiO_2 were measured. They are shown in Figure 6, and the photovoltaic characteristics of these DSCs are summarized in Table 1. Photocurrent was increased as applying time of magnetic field rises, while the open circuit voltage did not change noticeably. Higher photocurrent is probably related to the amount of absorbed dye, light scattering, or interparticle electrical contact. Although the dye absorption was decreased as magnetic field applying, photocurrent was increased. Well-aligned nanoparticles improved electrical contact so that electron transport became faster (Figure 7). When the magnetic field applying time was increased, photocurrent of DSC was enhanced. It says that crystal orientation is better with longer magnetic field applied time on TiO_2 . As a result, the 7.50% efficiency of DSC with well-aligned TiO_2 crystal by applying magnetic field for 25 min was 41% higher than the 5.31% efficiency for conventional. After 25 min, the TiO_2 paste was fully dried,

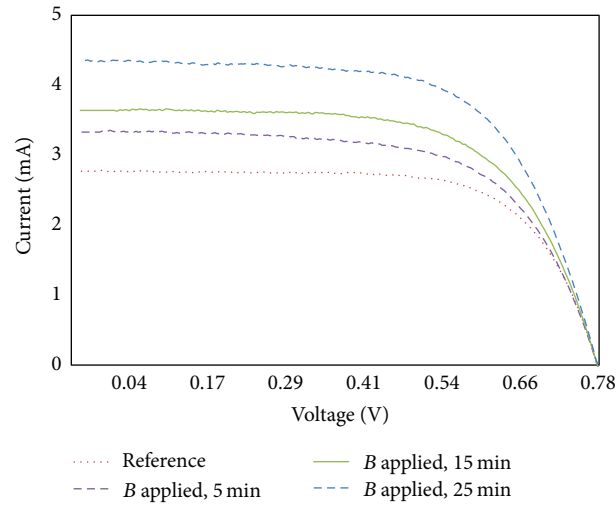


FIGURE 6: *I-V* curves of magnetic field applied DSCs with different applying times under standard illumination of 1 sun.

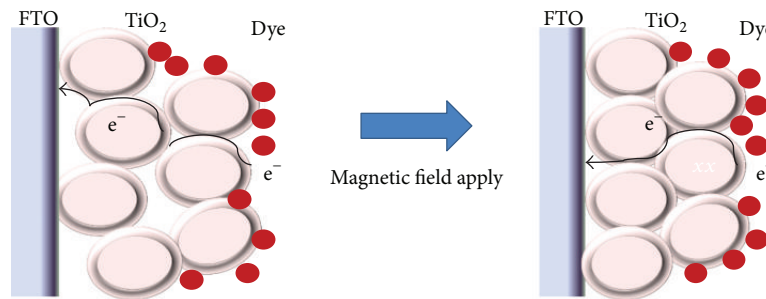


FIGURE 7: Schematic illustration of faster electron transportation in TiO_2 nanocrystals after magnetic field applied.

TABLE 1: *I-V* characteristics of magnetic field applied DSCs of different applying times.

Applied time (min)	V_{OC} (V)	I_{SC} (mA)	FF	Efficiency (%)
0	0.80	2.79	0.69	5.31
5	0.79	3.43	0.62	5.79
15	0.79	3.75	0.62	6.33
25	0.78	4.36	0.64	7.50

and additional magnetic field did not change orientation of TiO_2 particle. Therefore, additional B did not bring efficiency enhancement.

Electrochemical impedance spectra of magnetic field applied and not applied DSCs are shown in Figure 8. R_1 (real part of small semicircle) is the electron transfer resistances at Pt/electrolyte interface, and R_2 (real part of large semicircle) is at TiO_2 /dye/electrolyte interface [19]. While R_1 of two plots is similar, there is difference in R_2 . Resistance of TiO_2 /dye/electrolyte interface (R_2) was decreased from 44Ω to 39Ω by applying magnetic field onto TiO_2 . It implies that well-oriented TiO_2 nanoparticles by applying magnetic field improved electron conductivity. Consequently, overall performance of DSC was enhanced.

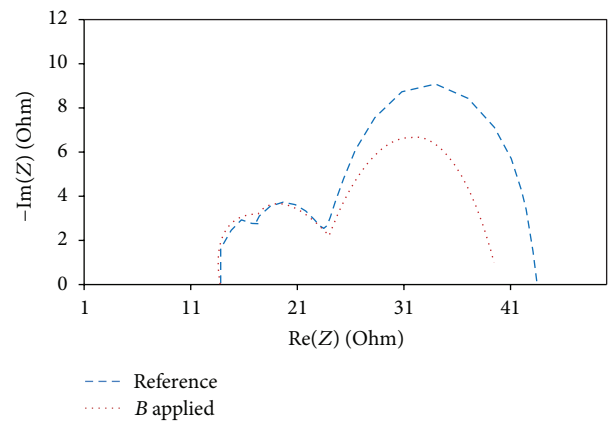


FIGURE 8: Internal resistances of the DSCs measured by EIS.

4. Conclusions

In this study, effect of the magnetic field on anatase TiO_2 crystal alignment of DSC was investigated. It was reported that the magnetic field arranges TiO_2 crystal to its direction

that has advantage for reaction activity. The *c*-axis of the anatase TiO₂ is aligned parallel to *B* in the suspension. This improved interparticle electrical contact and for transporting electrons at neck of interparticle connections. It was identified with EIS that resistance of TiO₂/dye/electrolyte interface (*R*₂) was decreased by applying magnetic field onto TiO₂. Consequently, it was demonstrated that energy conversion efficiency of TiO₂ particles arrangement was enhanced by an external magnetic field.

Conflict of Interests

The authors declare no conflict of interests.

Acknowledgment

This work no. 20110001295 was supported by Mid-Career Researcher Program through NRF grant funded by the MEST.

References

- [1] B. O'Regan and M. Gratzel, "A low-cost, high-efficiency solar cell based on dye-sensitized colloidal TiO₂ films," *Nature*, vol. 353, pp. 737–740, 1991.
- [2] A. Hagfeldt and M. Gratzel, "Light-induced redox reactions in nanocrystalline systems," *Chemical Reviews*, vol. 95, no. 1, pp. 49–68, 1995.
- [3] C. J. Barbé, F. Arendse, P. Comte et al., "Nanocrystalline titanium oxide electrodes for photovoltaic applications," *Journal of the American Ceramic Society*, vol. 80, no. 12, pp. 3157–3171, 1997.
- [4] M. J. Cass, A. B. Walker, D. Martinez, and L. M. Peter, "Grain morphology and trapping effects on electron transport in dye-sensitized nanocrystalline solar cells," *Journal of Physical Chemistry B*, vol. 109, no. 11, pp. 5100–5107, 2005.
- [5] T. Oekermann, D. Zhang, T. Yoshida, and H. Minoura, "Electron transport and back reaction in nanocrystalline TiO₂ films prepared by hydrothermal crystallization," *Journal of Physical Chemistry B*, vol. 108, no. 7, pp. 2227–2235, 2004.
- [6] S. Nakade, Y. Saito, W. Kubo, T. Kitamura, Y. Wada, and S. Yanagida, "Influence of TiO₂ nanoparticle size on electron diffusion and recombination in dye-sensitized TiO₂ solar cells," *Journal of Physical Chemistry B*, vol. 107, no. 33, pp. 8607–8611, 2003.
- [7] K. P. Wang and H. S. Teng, "Structure-intact TiO₂ nanoparticles for efficient electron transport in dye-sensitized solar cells," *Applied Physics Letters*, vol. 91, no. 17, Article ID 173102, 3 pages, 2007.
- [8] X. Fang, Y. Bando, U. K. Gautam, C. Ye, and D. Golberg, "Inorganic semiconductor nanostructures and their field-emission applications," *Journal of Materials Chemistry*, vol. 18, no. 5, pp. 509–522, 2008.
- [9] T. Dittrich, E. A. Lebedev, and J. Weidmann, "Electron drift mobility in porous TiO₂ (anatase)," *Physica Status Solidi (A)*, vol. 165, no. 2, pp. R5–R6, 1998.
- [10] M. Law, L. E. Greene, J. C. Johnson, R. Saykally, and P. Yang, "Nanowire dye-sensitized solar cells," *Nature Materials*, vol. 4, no. 6, pp. 455–459, 2005.
- [11] K. Sayama, H. Sugihara, and H. Arakawa, "Photoelectrochemical properties of a porous Nb₂O₅ electrode sensitized by a ruthenium dye," *Chemistry of Materials*, vol. 10, no. 12, pp. 3825–3832, 1998.
- [12] A. Wold, "Photocatalytic properties of titanium dioxide (TiO₂)," *Chemistry of Materials*, vol. 5, no. 3, pp. 280–283, 1993.
- [13] R. Hengerer, L. Kavan, P. Krtil, and M. Grätzel, "Orientation dependence of charge-transfer processes on TiO₂ (anatase) single crystals," *Journal of The Electrochemical Society*, vol. 147, no. 4, pp. 1467–1472, 2000.
- [14] H. Deng, H. Zhang, and Z. Lu, "Dye-sensitized anatase titanium dioxide nanocrystalline with (0 0 1) preferred orientation induced by Langmuir-Blodgett monolayer," *Chemical Physics Letters*, vol. 363, no. 5–6, pp. 509–514, 2002.
- [15] P. de Rango, M. Lees, P. Lejay et al., "Texturing of magnetic materials at high temperature by solidification in a magnetic field," *Nature*, vol. 349, no. 6312, pp. 770–772, 1991.
- [16] T. Uchikoshi, "Control of crystalline texture in polycrystalline TiO₂ (Anatase) by electrophoretic deposition in a strong magnetic field," *Journal of the European Ceramic Society*, vol. 26, no. 4–5, pp. 559–563, 2006.
- [17] P. Luo, H. Niu, G. Zheng, X. Bai, M. Zhang, and W. Wang, "Enhancement of photoelectric conversion by high-voltage electric field assisted crystallization of a novel ternary-encapsulated spherical TiO₂ aggregate for solar cells," *Electrochimica Acta*, vol. 55, no. 8, pp. 2697–2705, 2010.
- [18] P. T. Hsiao, Y. L. Tung, and H. Teng, "Electron transport patterns in TiO₂ nanocrystalline films of dye-sensitized solar cells," *Journal of Physical Chemistry C*, vol. 114, no. 14, pp. 6762–6769, 2010.
- [19] N. Koide, A. Islam, Y. Chiba, and L. Han, "Improvement of efficiency of dye-sensitized solar cells based on analysis of equivalent circuit," *Journal of Photochemistry and Photobiology A*, vol. 182, no. 3, pp. 296–305, 2006.

Research Article

Natural Dye-Sensitized Solar Cells Based on Highly Ordered TiO₂ Nanotube Arrays

Na Li, Nengqian Pan, Danhong Li, and Shiwei Lin

Key Laboratory of Ministry of Education for Advanced Materials in Tropical Island Resources, School of Materials and Chemical Engineering, Hainan University, Haikou 570228, China

Correspondence should be addressed to Shiwei Lin; linsw@hainu.edu.cn

Received 27 January 2013; Accepted 21 April 2013

Academic Editor: Theodoros Dimopoulos

Copyright © 2013 Na Li et al. This is an open access article distributed under the Creative Commons Attribution License, which permits unrestricted use, distribution, and reproduction in any medium, provided the original work is properly cited.

The dye-sensitized solar cells (DSSCs) have been fabricated using highly ordered TiO₂ nanotube arrays as photoelectrode and natural dyes as photosensitizers. The natural dyes were extracted from the abundant plants in the tropical region, such as *Tradescantia zebrina*, kapok, and pitaya. The dyes could chemically couple with TiO₂ nanotubes and effectively convert visible light into electricity in DSSCs. A power conversion efficiency could be achieved up to 0.3% in the solar cell sensitized by the extracts from kapok with a short-circuit current of 0.86 mA/cm². Furthermore, the influences of the crystal structure of TiO₂ nanotube arrays on the performance of the natural DSSCs were discussed.

1. Introduction

Photosensitized wide-band gap metal-oxide semiconductors are used to convert visible light into electricity [1, 2]. In most dye-sensitized solar cells (DSSCs), nanocrystalline TiO₂ films are used as photo-electrode due to their impressive properties when compared to other metal-oxide semiconductors. Most recently, different TiO₂ nanostructures (nanotubes, nanorods, nanowires, nanoparticles, etc.) are explored as dye carriers [3–8]. Compared to other nanostructures, TiO₂ nanotubes (TNTs) enhance much visible-light scattering and absorption due to their high length-to-diameter ratio and large surface area and facilitate electron transportation to the electrodes due to their unique geometry [9–12].

One of the key elements in DSSCs is photosensitizer. The most successful photo-induced electron transfer sensitizers employed so far in DSSCs are ruthenium (II) polypyridyl complexes. The ruthenium complexes in DSSCs have exhibited power conversion efficiencies up to 12% [13]. Due to the high cost of ruthenium complexes and the scarce availability of those noble metals, looking for cheaper, simpler, and safer sensitizers becomes a scientific challenging problem [14]. Natural pigments, including chlorophyll, anthocyanin, nasunin, and carotenoids, can fulfill those requirements, and sensitization of TiO₂ by natural pigments has been reported

[15–19]. Experimentally, natural dye-sensitized TiO₂ solar cells have reached an efficiency of 7.1% [17].

Natural pigments extracted from leaves, flowers, and fruits of plants have advantages over rare metal complexes and other organic dyes. The natural dyes are readily available, easy to extract, of less cost, and environmentally friendly. In this work, we have made an attempt to collect red pigments from *Tradescantia zebrina*, kapok, and pitaya, as these plants are abundant in Hainan, the tropical island of China. The natural dyes were used to sensitize the highly ordered TiO₂ nanotube arrays fabricated by chemical anodization technique. Then DSSCs were assembled, and the photoelectrical properties were investigated.

2. Experimental

2.1. Preparation of Natural Dye-Sensitized TiO₂ Solar Cells. Ti foils (0.5 mm thickness, 99.4% purity) were sequentially cleaned in acetone, ethanol, and deionized (DI) water. Anodization was then performed in a two-electrode configuration with titanium foil as the working electrode and a stainless steel foil as the counter electrode [11, 12, 20]. A direct current power supply was used as the voltage source to drive the anodization. The electrolyte consisted of 0.3 wt% NH₄F and 2 vol% H₂O in ethylene glycol. The anodization

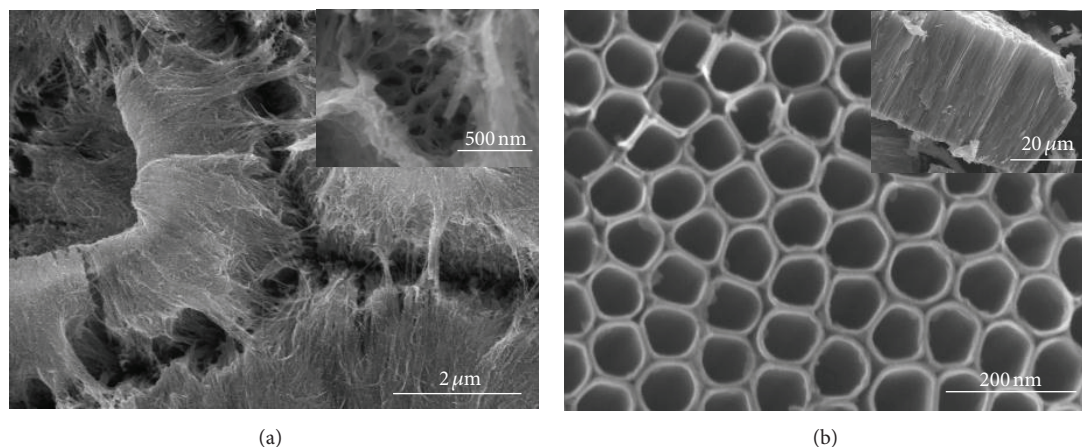


FIGURE 1: Top view SEM images of TiO_2 nanotube arrays (a) before and (b) after the ultrasonic treatment. The inset in (a) is the image with high magnification, while the inset in (b) shows the cross-sectional view of the nanotube arrays after ultrasonic treatment.

was conducted at 60 V for 2 h at room temperature. After anodization, the samples were annealed at 500°C or 600°C for 2 h in air with the temperature rising rate of $2^\circ\text{C}/\text{min}$.

All the fresh fruits and flowers were harvested in Hainan, the tropical island in China. The extracts of *Tradescantia zebrina*, kapok, and pitaya were obtained according to the similar steps as followed. The fresh fruits or flowers well cleaned (200 g) were crushed and soaked in 95% ethanol (50 mL) and then kept for 24 h in dark at room temperature. The residual parts were filtered. The clear solutions were centrifuged and diluted HCl was added to adjust the pH value. The solution with the extracts became red in color, and the natural dyes were ready to use as sensitizers in DSSCs.

TiO_2 nanotube array electrodes were immersed at room temperature for 12 h in dark in the solution with the extracts, respectively. To evaluate the photovoltaic performance, TiO_2 nanotube array electrode and Pt counter electrode were assembled to form a DSSC. The electrolyte was injected into the space between the two electrodes. The redox electrolyte with $[\text{I}^{3-}]/[\text{I}^-] = 1:9$ was prepared by dissolving 0.5 M LiI and 0.05 M I_2 in acetonitrile solution.

2.2. Characterization of Natural Dye-Sensitized TiO_2 Solar Cells. The morphology and crystal structure of TiO_2 nanotube-array electrode were characterized by field-emission scanning electronic microscopy (FESEM, Hitachi S4800, Japan) and X-ray diffraction technique (XRD, Bruker D8, Germany), respectively. The absorption spectrum of three kinds of natural extracts in solution and adsorbed onto TiO_2 photoanode were measured by UV-visible absorption spectra measurements (Persee, TU-1901). Photocurrent-photovoltage characteristics of the natural dye-sensitized solar cells were measured by the electrochemical workstation (Zahner 6.0, Germany) with a xenon source with intensity of $50 \text{ mW}/\text{cm}^2$. The effective cell area was 1.0 cm^2 .

3. Results and Discussion

3.1. Characteristics of TiO_2 Nanotube-Array Electrode. Figure 1(a) shows the SEM image of the sample without

ultrasonic treatment. The surface is covered with a layer of grassy residual and the nanotubes underneath are visible as shown in the inset of Figure 1(a). The grassy layer could block the infiltration of the dye and the redox electrolyte into the nanotubes. Thus it must be removed before the nanotubes are assembled into the DSSC [9]. Ultrasonic treatment can remove the grassy layer and expose the underneath nanotubes, as shown in Figure 1(b). The nanotubes are well defined. As the nanotubular structure provides a high specific surface area, the nanotubes can absorb more dyes on the electrode surface as compared with the planar film.

Before being assembled into DSSCs, the samples were annealed for crystallization of the TiO_2 , since a large number of localized states in the amorphous structure without annealing can act as traps and recombination centers [21]. Figure 2 shows the XRD patterns of TiO_2 nanotubes annealed at different temperatures. It is evidenced that TiO_2 transforms from amorphous phases to crystalline anatase phases and rutile phases after the annealing at 500°C . When the temperature increased to 600°C , the peaks relate to rutile phase increase.

3.2. Spectroscopic Characterization of Natural Photosensitizers. Figure 3(a) presents the absorption spectra of the red pigments in acid solutions, which were extracted from *Tradescantia zebrina*, kapok, and pitaya, respectively. The absorption peaks of the extracts from *Tradescantia zebrina* in visible-light region have maximums at 540 nm and 584 nm, which show typical absorption of anthocyanin [22]. For the extracts from kapok in solution, the maximum of the absorption intensity in visible-light region is located at 406 nm and 508 nm, which correspond to the absorption of carotenoid [18, 23] and anthocyanin, respectively. And the absorption peak obtained for extracts from pitaya in visible-light region is at 400 nm. As shown in Figure 3(a), these red pigments in solution have maximum absorption peaks at 350 nm and 380 nm in ultraviolet region. The same locations of the absorption peaks mean that they contain similar compounds.

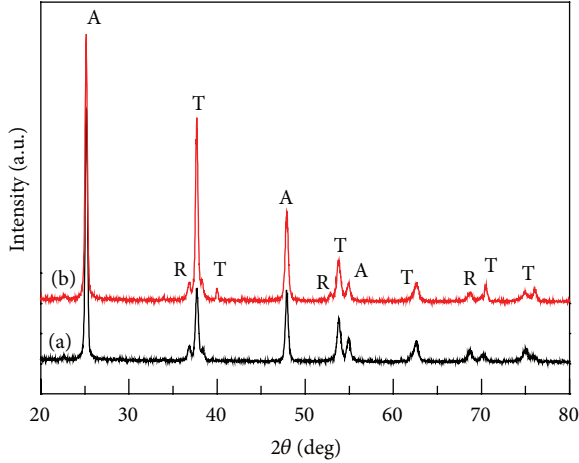


FIGURE 2: XRD patterns of (a) the TiO_2 nanotube arrays annealed at 500°C and (b) the TiO_2 nanotube arrays annealed at 600°C . A, R, and T represent anatase, rutile, and titanium, respectively.

Figure 3(b) shows the absorption spectra of the extracts adsorbed on TiO_2 electrodes, which were compared with that of TiO_2 electrode without any dye sensitization. The bare TiO_2 electrode cannot respond to the visible light due to its large band gap of 3.2 eV [24]. However, a broad absorption peak in visible-light region extending from 380 to 680 nm was observed for the electrodes sensitized with the extracts of tradescantia zebriza, kapok, and pitaya. The natural dye sensitizers are thus found to effectively increase the absorption of the visible light, which dominates the terrestrial solar spectrum.

A close look at Figure 3 could found that the UV-vis absorption peaks of the dyes adsorbed on TiO_2 electrodes are broadened and the peak positions are redshift, compared to those in solution. Such phenomenon can be explained as follows. Anthocyanin has a high absorption coefficient in the visible part of the solar spectrum. The binding between anthocyanin molecules and TiO_2 semiconductor takes place through the carbonyl and hydroxyl groups. The chemical attachment could affect the energy levels of the highest occupied molecular level and the lowest unoccupied molecular level of the anthocyanidin molecules [25], which eventually affects the band gap and results in a shift of the absorption peak in the absorption spectra. Besides, the redshift of the visible-light absorption peaks could also be due to the complexation with metal ions [15].

3.3. Photoelectrochemical Performance of DSSCs Sensitized with Natural Dyes. Figure 4 shows the photocurrent-photovoltage (J - V) characteristics of the DSSCs. The photoelectrochemical parameters evaluated from Figure 4 are summarized in Table 1. The photoenergy conversion efficiencies (η) of the DSSCs sensitized with tradescantia zebriza, kapok, and pitaya are 0.23%, 0.3%, and 0.17%, respectively, and the short-circuit photocurrent densities (J_{SC}) are 0.63 mA/cm^2 , 0.87 mA/cm^2 , and 0.50 mA/cm^2 , respectively. The values of η and J_{SC} after natural dye sensitization are effectively

TABLE 1: Photoelectrochemical parameters of DSSCs sensitized with three kinds of natural dyes, compared with the solar cell without dye sensitization.

Sensitizer	J_{SC} (mA/cm^2)	V_{OC} (V)	FF	η (%)
Without dye	0.023	0.3	0.494	0.006
<i>Tradescantia zebrina</i>	0.63	0.35	0.52	0.23
Kapok	0.87	0.36	0.49	0.3
Pitaya	0.50	0.33	0.52	0.17

TABLE 2: Photoelectrochemical parameters of DSSCs based on TiO_2 nanotube arrays annealed at different temperatures.

Annealing temperature	J_{SC} (mA/cm^2)	V_{OC} (V)	FF	η (%)
500°C	0.64	0.35	0.52	0.23
600°C	0.15	0.41	0.26	0.03

enhanced in comparison to that without dye sensitization with the value η of 0.006% and J_{SC} of 0.023 mA/cm^2 , while the open-circuit voltages and the fill factor are similar. This suggests that the chemical adsorption of the natural dye molecules on TiO_2 electrodes takes place. The hydroxyl and carboxyl groups on anthocyanin are easy to chelate with Ti (IV) on TiO_2 surface [25]. This helps the excited electron quickly transfer from anthocyanin molecules to the conduction band of TiO_2 .

It can be seen from Table 1 that the DSSC sensitized with the extracts from kapok exhibits the best value of η among the three kinds of dyes. This might be due to the higher intensity and broader range of the visible-light absorption of the extracts from kapok in comparison to the others as shown in Figure 3(b). Furthermore, stronger interaction between TiO_2 and the dye molecules of the extracts of kapok also might lead to charge transfer quickly.

The stability of the natural dyes was further studied by continuous irradiation in the sunshine for 2 h and no significant changes were observed.

3.4. Effect of TiO_2 Crystal Structure on the Performance of DSSCs. To further investigate the effect of TiO_2 nanotube crystal structure on the natural DSSCs, characteristics of DSSCs at different annealing temperature were measured. As shown in Figure 5 and Table 2, the values of J_{SC} and η for DSSCs based on TiO_2 annealed at 500°C outperformed those annealed at 600°C . According to Figure 2, TiO_2 nanotube arrays annealed at 500°C were major anatase phase with minor rutile ones. The electrode possesses the mixed crystal structure. When the temperature increased to 600°C , the sample has more obvious rutile peaks than the one annealed at 500°C . The results here suggest that the performance of DSSC based on TiO_2 nanotube arrays depends on the proportion of anatase to rutile for TiO_2 crystal structure. Besides the crystal structure, the geometric structure of TiO_2 nanotube arrays can affect the photoelectrical properties and thus the performance of the DSSCs [11], which requires further experimental investigation.

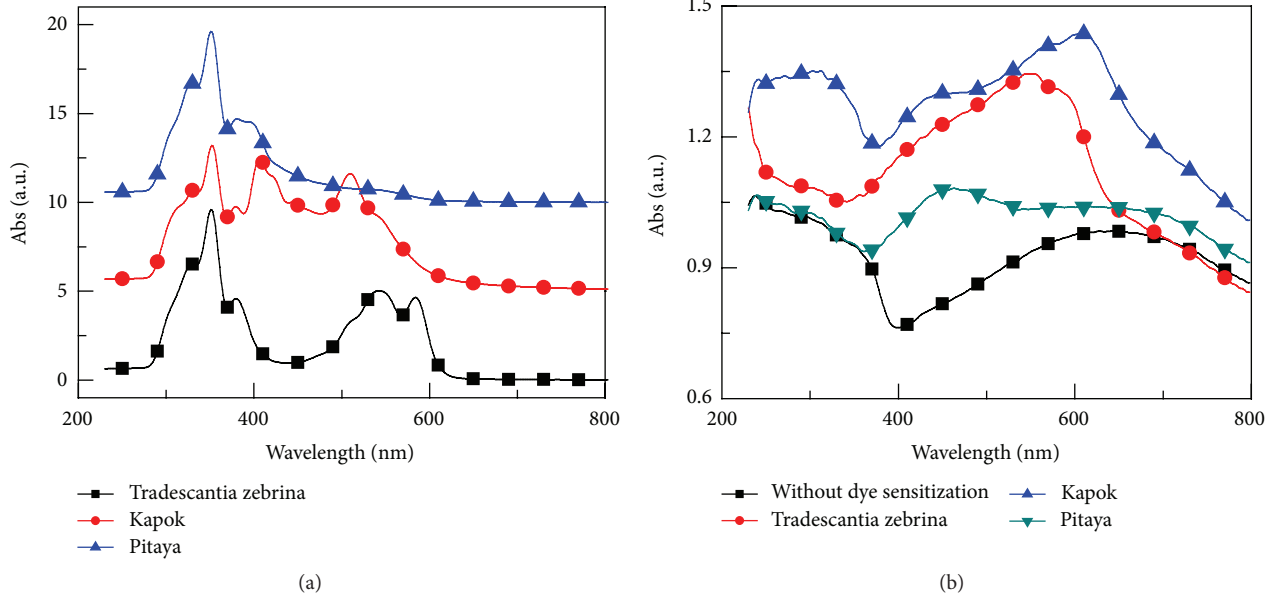


FIGURE 3: Comparison of the absorption spectra of the natural extracts: (a) in acid solution; (b) adsorbed on TiO_2 electrode.

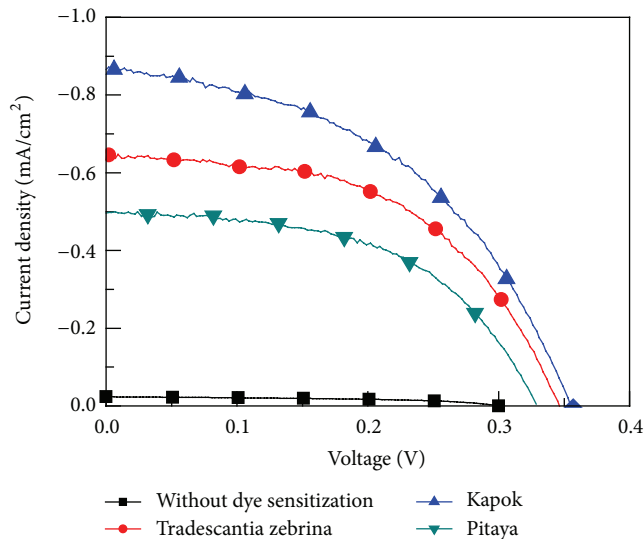


FIGURE 4: J - V characteristics of DSSCs sensitized with three kinds of natural dyes under illumination of $50 \text{ mW}/\text{cm}^2$, compared with the solar cell without dye sensitization.

4. Conclusions

The feasibility of assembling DSSCs with TiO_2 nanotube arrays sensitized with three kinds of natural dyes has been demonstrated. Successful conversion of visible light into electricity was achieved. The efficiencies of the solar cells sensitized with the extracts of Tradescantia zebrina, kapok, and pitaya skin were up to 0.23%, 0.3%, and 0.17%, respectively. Crystalline phases of TiO_2 significantly affect the photoenergy conversion parameters of DSSCs. Although our best values of DSSCs using kapok pigments are still lower than those obtained for the reference solar cells using the

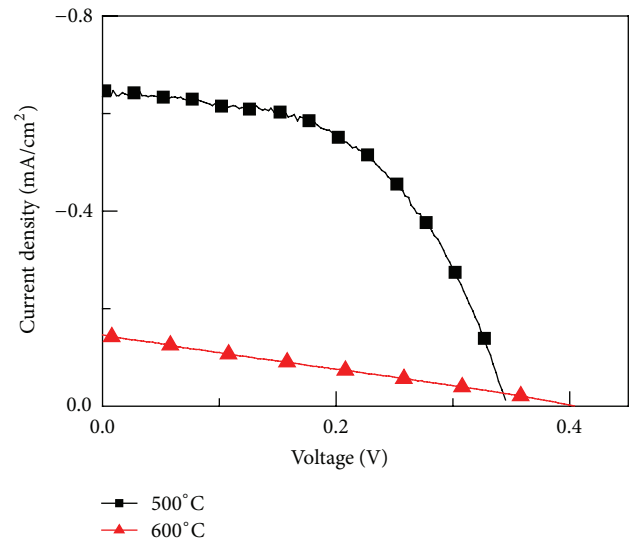


FIGURE 5: J - V characteristics of DSSCs sensitized with extracts of Tradescantia Zebrina based on TiO_2 nanotube arrays annealed at different temperatures.

chemical dye N719, the simple extraction procedure, low cost, wide availability, and environmentally friendly nature make natural dyes as the promising sources of sensitizers for DSSCs. Through improving extraction method, refining natural dyes, and optimizing the geometric and crystal structures of TiO_2 nanotube arrays, we believe that better results will be achieved.

Acknowledgments

This work was supported by Program for New Century Excellent Talents in University (NCET-09-0110), National

Nature Science Foundation of China (51202050), Hainan Natural Science Foundation (511110), and Hainan University Youth Foundation (qnjj1241).

References

- [1] B. O'Regan and M. Grätzel, "A low-cost, high-efficiency solar cell based on dye-sensitized colloidal TiO₂ films," *Nature*, vol. 353, no. 24, pp. 737–740, 1991.
- [2] M. Grätzel, "Solar energy conversion by dye-sensitized photo-voltaic cells," *Inorganic Chemistry*, vol. 44, no. 20, pp. 6841–6851, 2005.
- [3] J. R. Jennings, A. Ghicov, L. M. Peter, P. Schmuki, and A. B. Walker, "Dye-sensitized solar cells based on oriented TiO₂ nanotube arrays: transport, trapping, and transfer of electrons," *Journal of the American Chemical Society*, vol. 130, no. 40, pp. 13364–13372, 2008.
- [4] A. Ghicov, S. P. Albu, R. Hahn et al., "TiO₂ nanotubes in dye-sensitized solar cells: critical factors for the conversion efficiency," *Chemistry*, vol. 4, no. 4, pp. 520–525, 2009.
- [5] S. H. Kang, S. H. Choi, M. S. Kang et al., "Nanorod-Based dye-sensitized solar cells with improved charge collection efficiency," *Advanced Materials*, vol. 20, no. 1, pp. 54–58, 2008.
- [6] J. Jiu, S. Isoda, F. Wang, and M. Adachi, "Dye-sensitized solar cells based on a single-crystalline TiO₂ nanorod film," *The Journal of Physical Chemistry B*, vol. 110, no. 5, pp. 2087–2092, 2006.
- [7] B. Tan and Y. Wu, "Dye-sensitized solar cells based on anatase TiO₂ nanoparticle/nanowire composites," *The Journal of Physical Chemistry B*, vol. 110, no. 32, pp. 15932–15938, 2006.
- [8] P. Roy, D. Kim, I. Paramasivam, and P. Schmuki, "Improved efficiency of TiO₂ nanotubes in dye sensitized solar cells by decoration with TiO₂ nanoparticles," *Electrochemistry Communications*, vol. 11, no. 5, pp. 1001–1004, 2009.
- [9] G. K. Mor, K. Shankar, M. Paulose, O. K. Varghese, and C. A. Grimes, "Use of highly-ordered TiO₂ nanotube arrays in dye-sensitized solar cells," *Nano Letters*, vol. 6, no. 2, pp. 215–218, 2006.
- [10] K. Zhu, N. R. Neale, A. Miedaner, and A. J. Frank, "Enhanced charge-collection efficiencies and light scattering in dye-sensitized solar cells using oriented TiO₂ nanotubes arrays," *Nano Letters*, vol. 7, no. 1, pp. 69–74, 2007.
- [11] D. H. Li, S. W. Lin, S. P. Li et al., "Effects of geometric and crystal structures on the photoelectrical properties of highly-ordered TiO₂ nanotube arrays," *Journal of Materials Research*, vol. 27, no. 7, pp. 1029–1036, 2012.
- [12] S. P. Li, S. W. Lin, J. J. Liao et al., "Nitrogen-doped TiO₂ nanotube arrays with enhanced photoelectrochemical property," *International Journal of Photoenergy*, vol. 2012, Article ID 794207, 7 pages, 2012.
- [13] A. Yella, H. W. Lee, H. N. Tsao et al., "Porphyrin-sensitized solar cells with cobalt (II/III)-based redox electrolyte exceed 12 percent efficiency," *Science*, vol. 334, no. 6056, pp. 629–634, 2011.
- [14] W. M. Campbell, A. K. Burrell, D. L. Officer, and K. W. Jolley, "Porphyrins as light harvesters in the dye-sensitised TiO₂ solar cell," *Coordination Chemistry Reviews*, vol. 248, no. 13–14, pp. 1363–1379, 2004.
- [15] N. J. Cherepy, G. P. Smestad, M. Grätzel, and J. Z. Zhang, "Ultrafast electron injection: implications for a photoelectrochemical cell utilizing an anthocyanin dye-sensitized TiO₂ nanocrystalline electrode," *The Journal of Physical Chemistry B*, vol. 101, no. 45, pp. 9342–9351, 1997.
- [16] K. Wongcharee, V. Meeyoo, and S. Chavadej, "Dye-sensitized solar cell using natural dyes extracted from rosella and blue pea flowers," *Solar Energy Materials and Solar Cells*, vol. 91, no. 7, pp. 566–571, 2007.
- [17] G. Calogero and G. D. Marco, "Red Sicilian orange and purple eggplant fruits as natural sensitizers for dye-sensitized solar cells," *Solar Energy Materials and Solar Cells*, vol. 92, no. 11, pp. 1341–1346, 2008.
- [18] E. Yamazaki, M. Murayama, N. Nishikawa, N. Hashimoto, M. Shoyama, and O. Kurita, "Utilization of natural carotenoids as photosensitizers for dye-sensitized solar cells," *Solar Energy*, vol. 81, no. 4, pp. 512–516, 2007.
- [19] Q. Dai and J. Rabani, "Photosensitization of nanocrystalline TiO₂ films by pomegranate pigments with unusually high efficiency in aqueous medium," *Chemical Communications*, no. 20, pp. 2142–2143, 2001.
- [20] H. Omidvar, S. Goodarzi, A. Seif, and A. R. Azadmehr, "Influence of anodization parameters on the morphology of TiO₂ nanotube arrays," *Superlattices and Microstructures*, vol. 50, no. 1, pp. 26–39, 2011.
- [21] A. Ghicov and P. Schmuki, "Self-ordering electrochemistry: a review on growth and functionality of TiO₂ nanotubes and other self-aligned MOx structures," *Chemical Communications*, no. 20, pp. 2791–2808, 2009.
- [22] Q. Dai and J. Rabani, "Photosensitization of nanocrystalline TiO₂ films by anthocyanin dyes," *Journal of Photochemistry and Photobiology A: Chemistry*, vol. 148, no. 1–3, pp. 17–24, 2002.
- [23] F. G. Gao, A. J. Bard, and L. D. Kispert, "Photocurrent generated on a carotenoid-sensitized TiO₂ nanocrystalline mesoporous electrode," *Journal of Photochemistry and Photobiology A: Chemistry*, vol. 130, no. 1, pp. 49–56, 2000.
- [24] M. Grätzel, "Perspectives for dye-sensitized nanocrystalline solar cells," *Progress in Photovoltaics: Research and Applications*, vol. 8, no. 1, pp. 171–185, 2000.
- [25] S. Meng, J. Ren, and E. Kaxiras, "Natural dyes adsorbed on TiO₂ nanowire for photovoltaic applications: enhanced light absorption and ultrafast electron injection," *Nano Letters*, vol. 8, no. 10, pp. 3266–3272, 2008.

Research Article

Particle Size Effects of TiO₂ Layers on the Solar Efficiency of Dye-Sensitized Solar Cells

Ming-Jer Jeng,¹ Yi-Lun Wung,¹ Liann-Be Chang,¹ and Lee Chow²

¹ Department of Electronic Engineering and Green Technology Research Center, Chang-Gung University, Taoyuan 333, Taiwan

² Department of Physics, University of Central Florida, Orlando, FL 32816, USA

Correspondence should be addressed to Ming-Jer Jeng; mjjeng@mail.cgu.edu.tw

Received 11 October 2012; Accepted 22 March 2013

Academic Editor: Tianxin Wei

Copyright © 2013 Ming-Jer Jeng et al. This is an open access article distributed under the Creative Commons Attribution License, which permits unrestricted use, distribution, and reproduction in any medium, provided the original work is properly cited.

Large particle sizes having a strong light scattering lead to a significantly decreased surface area and small particle sizes having large surface area lack light-scattering effect. How to combine large and small particle sizes together is an interesting work for achieving higher solar efficiency. In this work, we investigate the solar performance influence of the dye-sensitized solar cells (DSSCs) by the multiple titanium oxide (TiO₂) layers with different particle sizes. It was found that the optimal TiO₂ thickness depends on the particle sizes of TiO₂ layers for achieving the maximum efficiency. The solar efficiency of DSSCs prepared by triple TiO₂ layers with different particle sizes is higher than that by double TiO₂ layers for the same TiO₂ thickness. The choice of particle size in the bottom layer is more important than that in the top layer for achieving higher solar efficiency. The choice of the particle sizes in the middle layer depends on the particle sizes in the bottom and top layers. The mixing of the particle sizes in the middle layer is a good choice for achieving higher solar efficiency.

1. Introduction

Dye-sensitized solar cells (DSSCs) have attracted much attention as good candidates for low-cost, good-stability, and high-efficiency solar cells [1, 2]. There are many innovations in this emerging technology like the new dyes which absorb a longer range of wavelengths and the proposed nanostructure titanium oxides (TiO₂) for increasing surface area and so forth [3–6]. The DSSCs with the nanostructure titanium oxide/porphyrins dye thin films on TCO glass can achieve a solar efficiency as high as with 13% [7]. The major improvement of the research is not only by introducing artificial synthesized dye as light harvesters instead of TiO₂ itself, but also by using the nanostructure layer to improve the absorption and collection efficiency. In principle, rapid electron transport and slow recombination will be better for obtaining high solar conversion efficiency. For conventional DSSCs, the mesoporous photoelectrode films composed of small-sized TiO₂ nanocrystalline particles have the advantages of providing a large surface for greater dye adsorption and facilitating electrolyte diffusion within their pores [8]. Therefore, optimizing the microstructure of the photoanode is vital for

developing high solar efficiency of DSSCs. Recently, the light-scattering effects of TiO₂ electrode have been proposed by using different particles in the TiO₂ layers, which can significantly improve the light harvest efficiency [9]. Ferber and Luther [10] and Rothenberger et al. [11] confirmed the light-scattering effect with the transport theory and the many-flux model, respectively. Except for the scattering abilities of TiO₂ layers, it is also important that the TiO₂ electrode has a larger surface area, which can increase the dye adsorption and then high photocurrent generation. Recently, many efforts have been focused on the development of multifunctional TiO₂ nanostructures for application in the DSSCs [12–19]. However, they lack a systematic study for particle size effects. It is known that the large particle size of TiO₂ layers can result in a strong light scattering ability and increase an optical absorption path. It indicates that it has higher short circuit current. However, the small nanoparticle size of TiO₂ layers has large contact area and low contact resistance. It means that it has higher open circuit voltage. How to combine large and small nanoparticle sizes together is an interesting work for achieving higher solar efficiency. In this work, we investigate the performance influence of DSSCs

prepared by multiple TiO₂ layers with different particle sizes systematically.

2. Experiments

The 2 cm × 1.5 cm fluorine-doped SnO₂ (FTO) electrodes (sheet resistance 8 Ω/square) were cleaned by acetone, isopropanol, and deionized water sequentially. TiO₂ solutions are prepared by mixing 3 g of TiO₂ powders with different particle sizes, 1 mL of TTIA, 0.5 g of polyethylene glycol (PEG), and 0.5 mL of Triton X-100 in 50 mL of isopropanol (IPA), and then ground and stirred by zirconia ball for 8 hours. It is known that the addition of TTIP in the solution can reduce the surface crack and that the PEG can make a porous thin film by annealing. The TiO₂ thin films were formed by spin-coating TiO₂ solutions on FTO glass and annealed at 500°C for one hour. Three structures of single, double, and triple TiO₂ layers with different particle sizes were prepared. The commercial TiO₂ powders with different particle sizes used in the experiments are listed in Table 1. For double or triple layers, their total thicknesses are controlled to be the same of 12 μm (not an optimal thickness). It is noted that the thickness of each layer of TiO₂ film can influence the results of solar performance parameters and EIS of DSSCs. We did our best to control the thickness of each layer of TiO₂ film to be about 6 and 4 μm, respectively, for double and triple layers. TiO₂ photoelectrodes were immersed for 24 hrs in anhydrous ethanol solution containing 3 × 10⁻⁴ M N719 dye. The liquid electrolyte consisted of 1 M lithium iodide (LiI), 0.1 M iodine (I₂), 0.5 M 4-tert-butylpyridine (TBP), and 0.6 M 1,2-dimethyl-3-propylimidazolium iodide (DMPII) in acetonitrile. The cathode electrode was made by FTO, which is coated by H₂PtCl₆ precursor and annealed at 450°C for 30 min. The cell was fabricated by applying Surlyn, with a thickness of 60 μm between the two electrodes, and the gap was fixed at 60 μm. Two FTO glasses were made with the Surlyn heated at 100°C. The electrolyte was injected into the space between the electrodes by capillarity. Finally, these two FTO glasses were sealed completely. The active area of cells is 0.25 cm². The photocurrent-voltage (I-V) characteristic curves were measured by Keithley 2420 under AM1.5G illumination. Light absorption was measured by a UV-vis spectrophotometer. In addition, electrochemical impedance spectroscopy (EIS) is used to analyze the charge transport resistance [20–24].

3. Results and Discussion

The strong back-scattering light due to the large particles near the conducting glass unavoidably results in a light loss. To reduce light loss due to the strong back-scattering light, multiple-layer structure of TiO₂ has been proposed to deposit the small particles first on the conducting glass for increasing contact area and then followed by the large particle layers for back-light scattering. To examine the particle size effect on the solar performance of DSSCs systemically, three structures of single, double, and triple TiO₂ layers with different particle sizes are investigated. For single TiO₂ layer, different particle sizes and thicknesses of TiO₂ are studied. Different particle

TABLE 1: The commercial TiO₂ particle sizes used in the experiments.

TiO ₂ powder	Average particle sizes (nm)		
Small particles	5	9 or 10	
Medium particles	21	40	
Large particles	100	200	400

sizes in the top, middle, and bottom layers are examined, respectively, for the double or triple TiO₂ layers.

Figure 1 shows the cross section and surface-view field emission scanning electron microscopy (FESEM) images of single TiO₂ layer with three different particle sizes of 21 nm, 100 nm, and 200 nm. The solar efficiency dependence on the thickness of TiO₂ layer with different particle sizes is shown in Figure 2. Clearly, the DSSCs with the large particle size of TiO₂ layer have lower solar efficiency than those with small particle size of TiO₂ layer under the same TiO₂ thickness. The lower solar efficiency in large particle sizes of TiO₂ layer can be attributed to a strong back-scattering light and can result in lower solar efficiency. It is known that the large particle size of TiO₂ layer has smaller surface area than the small one. The number of adsorbed dyes in large particle size of TiO₂ layer is less than that in small particle size of TiO₂ layer due to small surface area. Therefore, the photocurrent of the DSSCs with large particle size of TiO₂ layer is smaller than that with small particle size of TiO₂ layer and results in lower solar efficiency. It is also observed that the optimal TiO₂ thickness depends on the particle sizes of TiO₂ layer for achieving the maximum efficiency. The larger the particle sizes of TiO₂ layers, the shorter the optimal TiO₂ thickness due to a strong back-scattering light. The larger thickness of TiO₂ layers is expected to adsorb more dyes. But the generated electron in dyes cannot be injected to electrode effectively due to long distance when the thickness of TiO₂ layers is long enough. Thus, the optimal thickness of TiO₂ layers is different for each particle size due to different back-scattering lights and charge transport properties in the DSSCs. Dyes in the TiO₂ layers will build up with increasing thickness and hence increase the photocurrent. However, thicker TiO₂ layers will result in a decrease in the transmittance of TiO₂ layers and thus reduce the incident light intensity to dyes. In addition, the charge transfer resistance increases with the increasing thickness of TiO₂ layers. The charge recombination between electrons injected from the excited dye to the conduction band of TiO₂ and the I₃⁻ ions in the electrolyte will become more serious in thicker TiO₂ layers.

Figure 3 shows the schematic diagrams of double-layer structures with the different particle sizes in the top and bottom layers. The cross section FESEM images of double TiO₂ layers with (a) 400 nm/5 nm/FTO, (b) 400 nm/100 nm/FTO, (c) 400 nm/200 nm/FTO, (d) 100 nm/10 nm/FTO, (e) 200 nm/10 nm/FTO, and (f) 400 nm/10 nm/FTO are shown in Figure 4. It is clear to demonstrate the different particle sizes in the top and bottom layers. Figures 5(a) and 5(b) show the photocurrent-voltage curves of the DSSCs with double-layer structures of different TiO₂ particle sizes in the bottom and top layers, respectively. Clearly, the DSSCs

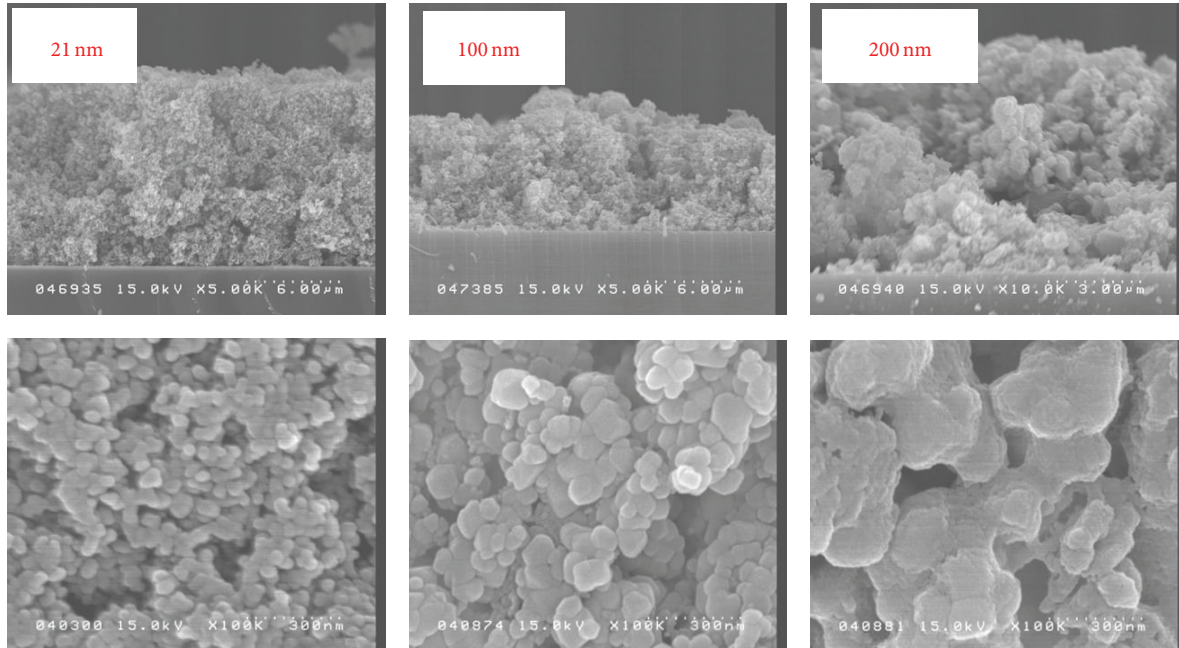


FIGURE 1: The cross section and surface-view field emission scanning electron microscopy (FESEM) images of a single TiO_2 layer with three different particle sizes of 21 nm, 100 nm, and 200 nm.

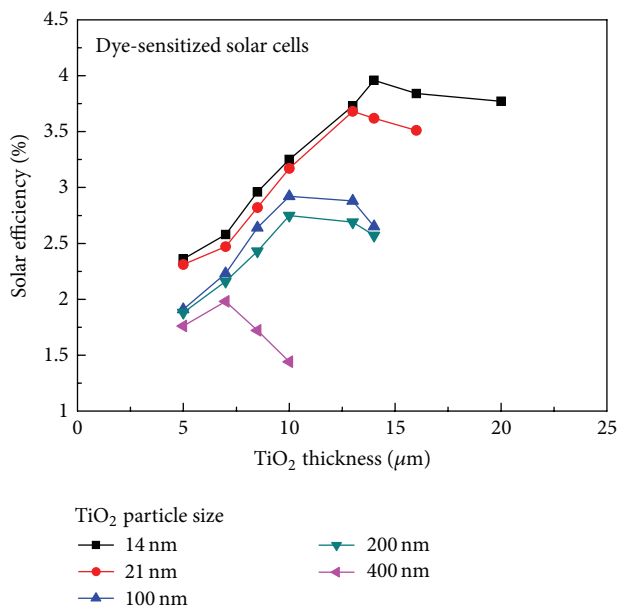


FIGURE 2: The solar efficiency dependence on the thickness of TiO_2 layers with different particle sizes.

with smaller particle size of 5 nm in the bottom have larger short-circuit current and efficiency than those with larger particle sizes of 100 and 200 nm, as shown in Figure 5(a). It is known that smaller particles of TiO_2 layers have large surface areas and adsorb more dyes. Hence, they have low contact resistance and high photocurrent. In addition, the strong back-scattering light due to large particle size of 400 nm

will also increase the reabsorption in the small particle size of TiO_2 layer. These smaller particle sizes in the bottom are beneficial to recapture the scattering light from the top scattering layer. The larger particle sizes of TiO_2 layers in the top can enhance the back-scattering light effectively and result in higher photocurrent, as shown in Figure 5(b). Thus, the combination of larger particle sizes of TiO_2 in the top and smaller particle sizes of TiO_2 in the bottom will be better for achieving higher solar efficiency. The solar performance parameters of the DSSCs with double-layer structure of different TiO_2 particle sizes in the bottom and top layers are listed in Table 2. Interestingly, the solar efficiency of DSSCs with 400 nm/10 nm/FTO, 200 nm/10 nm/FTO, or 100 nm/10 nm/FTO structure is much higher than that with 400 nm/100 nm/FTO or 400 nm/200 nm/FTO structure. It means that the choice of particle size in the bottom layer is more important than that in the top layer for achieving higher solar efficiency. Figures 6(a) and 6(b) show the light absorption of double-layer structures with different TiO_2 particle sizes in the bottom and top layers, respectively. The TiO_2 layers with smaller particle sizes in the bottom exhibit higher light absorption than those with larger particle sizes, as can be seen in Figure 6(a). The TiO_2 layers with larger particle sizes on the top layer exhibit higher light absorption than those with smaller particle sizes, as can be seen in Figure 6(b) [25]. The absorption behaviors in Figures 6(a) and 6(b) are consistent with the observation of photocurrent in Figures 5(a) and 5(b), respectively.

To study the charge transfer effects, electrochemical impedance spectroscopy (EIS) is a useful method for analysis of charge transport process [20–24]. The schematic diagram of the internal resistance related to the charge transfer kinetics

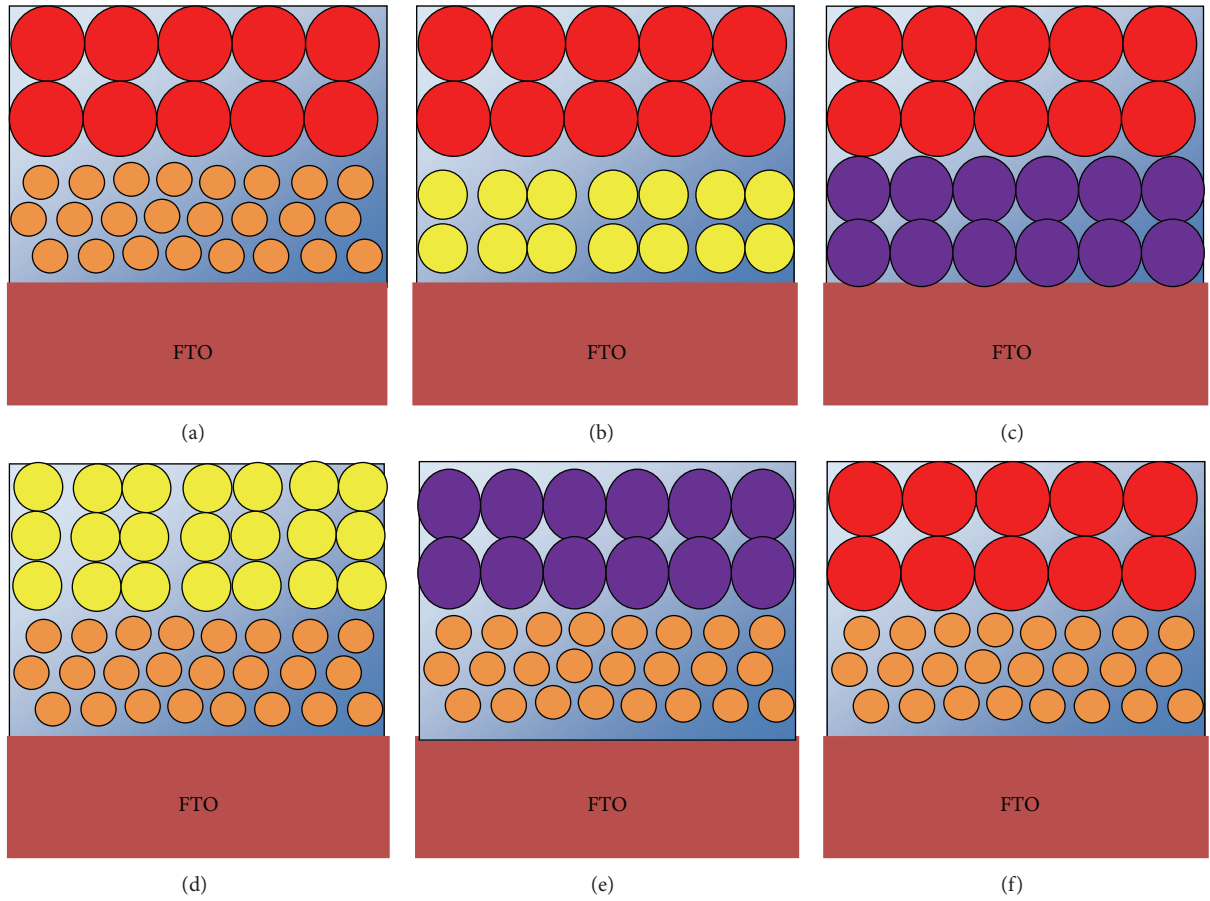


FIGURE 3: The schematic diagrams of double-layer structures with the different particle sizes in the top and bottom layers.

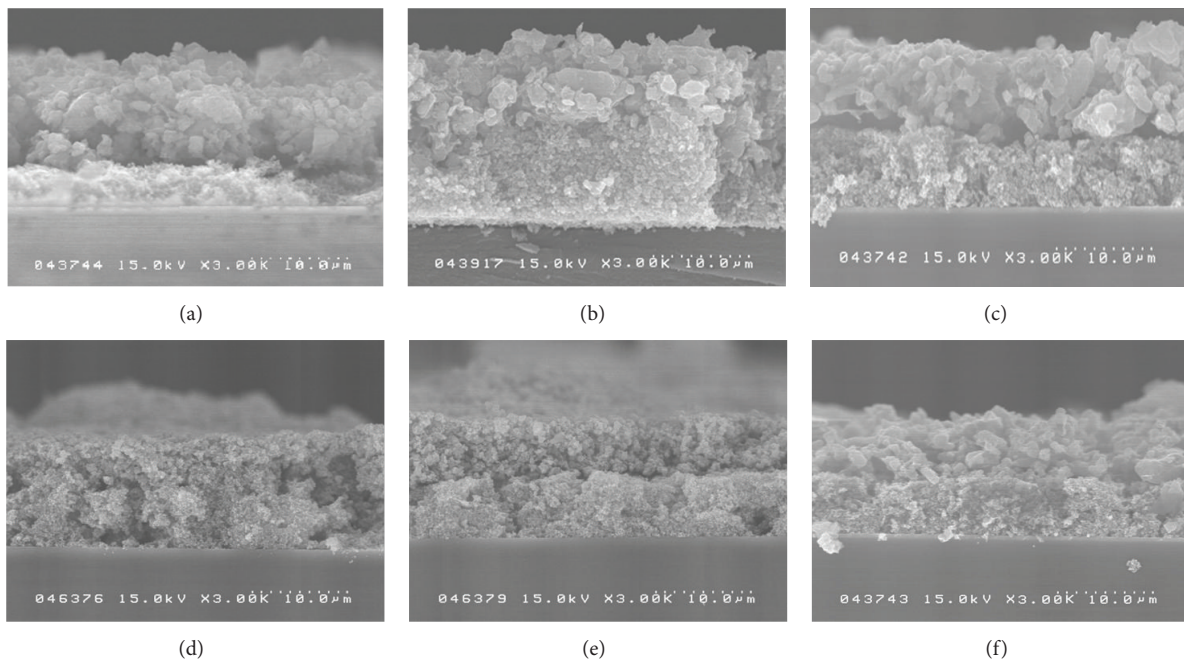


FIGURE 4: The cross section FESEM images of double TiO_2 layers with (a) 400 nm/5 nm/FTO, (b) 400 nm/100 nm/FTO, (c) 400 nm/200 nm/FTO, (d) 100 nm/10 nm/FTO, (e) 200 nm/10 nm/FTO, and (f) 400 nm/10 nm/FTO.

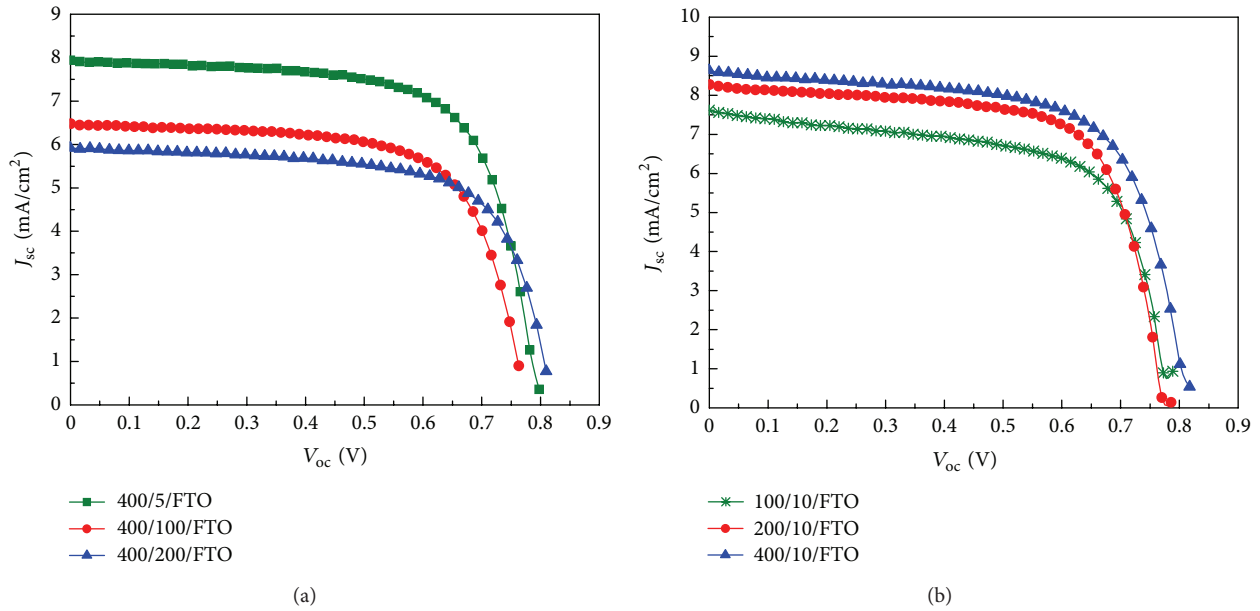


FIGURE 5: The photocurrent-voltage curves of DSSCs with double-layer structures of different TiO_2 particle sizes in the (a) bottom and (b) top layers, respectively.

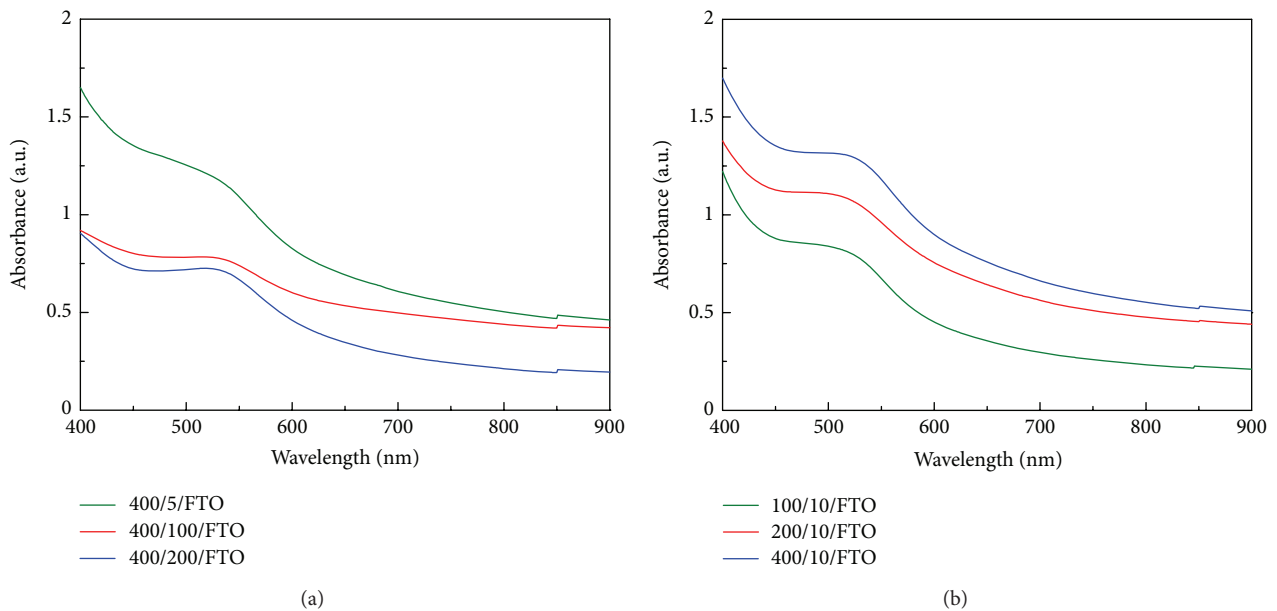


FIGURE 6: The light absorption of double-layer structures with different TiO_2 particle sizes in the (a) bottom and (b) top layers, respectively.

in the DSSCs is shown in Figure 7. In general, the Nyquist plots exhibit three semicircles. The three semicircles are attributed to the redox reaction at the platinum counter electrode (Z1) in the high-frequency region, the electron transfer at the $\text{TiO}_2/\text{dye}/\text{electrolyte}$ interface (Z2) in the middle-frequency region, and carrier transport by ions within the electrolytes (Z3) in the low-frequency region. The resistance elements R1, R2, and R3 are described as the real parts of Z1, Z2, and Z3, respectively [26]. Figures 8(a) and 8(b) show the EIS curves of the DSSCs prepared by double-layer structures

with different TiO_2 particle sizes in the bottom and top, respectively, in the form of the Nyquist plots. Two semicircles are observed in these two figures. The semicircle at low-frequency region merged with the semicircle at the middle-frequency region due to the weak resistance of ions transport in the electrolytes. The charge transfer resistance of the large semicircle in the middle-frequency region may include the extent of electron transport in the photoanode [27]. It was explained that the back-transport of electrons from the FTO electrode to the I_3^- was suppressed by the introduction of

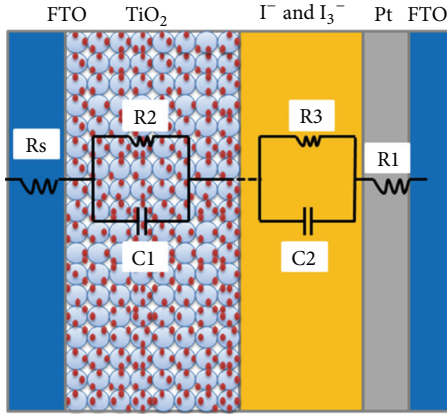


FIGURE 7: The schematic diagram of the internal resistance related to the charge transfer kinetics in the DSSCs.

small particle sizes in TiO_2 layers. During the deposition of Pt as a counter electrode, there were some slight differences such as the Pt crystallites contacting and the thickness of Pt layer between the counter electrodes. These differences caused the resistance for these two cells in the high frequency to be inconsistent [28]. The charge transport resistance parameters of EIS measurement for double TiO_2 layers are listed in Table 3. The charge transport resistance R_2 is 13.40, 18.10, and 44.33 Ω for double layers with 400/5/FTO, 400/100/FTO, and 400/200/FTO structures, respectively. The DSSCs with smaller particle size of TiO_2 layers in the bottom exhibit the lower charge transport resistance. The charge transport resistance R_2 is 18.67, 12.98, and 12.28 Ω for the double layers with 100/10/FTO, 200/10/FTO, and 400/10/FTO structures, respectively. The DSSCs with larger particle size of TiO_2 on the top exhibit the lower charge transport resistance. It is noted that the charge transport resistance in the DSSCs with 400/10/FTO structures is lower than that with 400/5/FTO structures. It means that the interface between layers with different particle sizes will be an important factor to affect the solar performance except for considering back-scattering light and surface area.

It is known that the path-depth length of light increases with wavelength. If a better solar performance is obtained, the back-scattering particles will be gradually increased. Therefore, a triple-layer structure with gradually increasing the particle size was examined. Figure 9 shows the schematic diagrams of triple-layer structures with the different particle sizes in the first (bottom), second (middle), and third (top) layers. When the light is gradually scattered with wavelength, the smaller particle underlayer will recapture the scattering light gradually from the above scattering layer. Figure 10 shows the photocurrent-voltage curves of DSSCs with triple-layer structure of TiO_2 layers. The solar performance parameters of these DSSCs are listed in Table 4. The DSSCs with 40 nm particle size in second layer exhibit higher solar efficiency than the other two of 10 and 100 nm. The fill factor degrades with the increasing particle size in the second layer due to small particle size having larger surface contact area. However, the DSSCs with 40 nm particle size in second layer

TABLE 2: Solar performance parameters of DSSCs with double-layer structure of different TiO_2 particle sizes in the bottom and top layers.

Double layers (nm)	J_{sc} (mA/cm ²)	V_{oc} (V)	Fill factor	Efficiency (%)
400/5/FTO	7.94	0.80	0.68	4.31
400/100/FTO	6.47	0.78	0.65	3.42
400/200/FTO	5.92	0.81	0.67	3.22
100/10/FTO	7.62	0.78	0.63	3.76
200/10/FTO	8.28	0.78	0.66	4.29
400/10/FTO	8.63	0.81	0.66	4.63

TABLE 3: The parameters of charge transfer resistance in double-layer structures by EIS measurements.

Double layers (nm)	R_s (Ω)	R_1 (Ω)	R_2 (Ω)
400/5/FTO	29.18	10.29	13.40
400/100/FTO	20.77	21.34	18.10
400/200/FTO	20.67	20.48	44.33
100/10/FTO	14.62	21.27	18.67
200/10/FTO	16.41	8.81	12.98
400/10/FTO	13.81	17.74	12.28

present a maximal photocurrent. It possibly indicates that if the underlayer particle wants to effectively recapture the scattering light from the above scattering layer, the particle size ratio of layer by layer should not vary too much. There exists discontinuity interface between layer and layer. This discontinuity interface cannot be neglected for multiple-layer structures. The choice of the particle sizes in the middle layer will depend on the particle sizes in the bottom and top layers. In addition, the DSSCs with larger particle sizes in the top layer exhibit higher solar efficiency due to strong back-scattering light. Figure 11 shows the photocurrent-voltage curves of DSSCs prepared by triple layers with different particle sizes and the mixing of particle sizes in TiO_2 layers. The solar performance parameters of these DSSCs are listed in Table 5. It is noted that the solar efficiency of the DSSCs in Figure 11 is higher than that in Figure 10 due to different TiO_2 thicknesses in these DSSCs. The DSSCs with smaller particle sizes of TiO_2 in the bottom layer exhibit higher solar efficiency than those with larger particle sizes of TiO_2 . The mixing of the particle sizes in the middle layers can achieve higher solar efficiency. Figure 12 shows the EIS curves of DSSCs with the triple-layer structures with different particle sizes of TiO_2 layers. The charge transport resistance parameters of EIS measurement are listed in Table 6. The DSSCs with larger particle sizes in the top layer (400 nm/200 nm/10 nm) exhibit smaller charge transfer resistance than the other two of 400 nm/100 nm/10 nm and 200 nm/100 nm/10 nm. It indicates that the choice of the particle sizes in the middle layer will affect the charge transfer resistance of TiO_2 layer. This behavior is consistent with the observation in Figure 10.

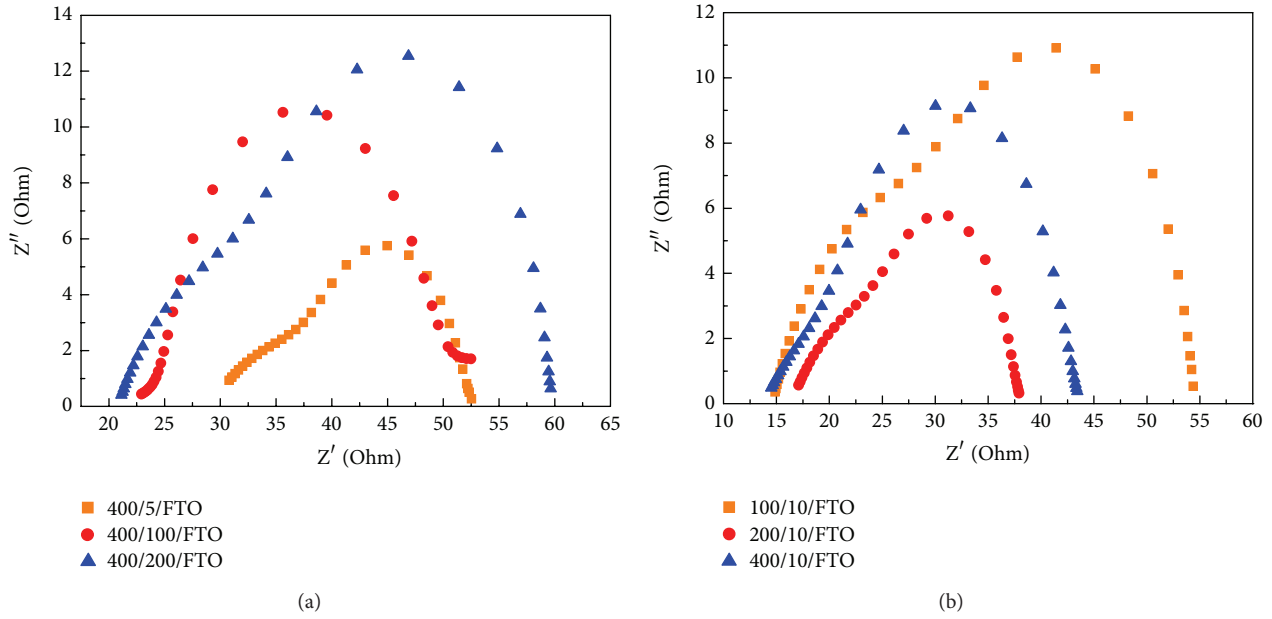


FIGURE 8: The EIS curves of the DSSCs prepared by double-layer structures with different TiO₂ particle sizes in the (a) bottom and (b) top layers, respectively, in the form of the Nyquist plots.

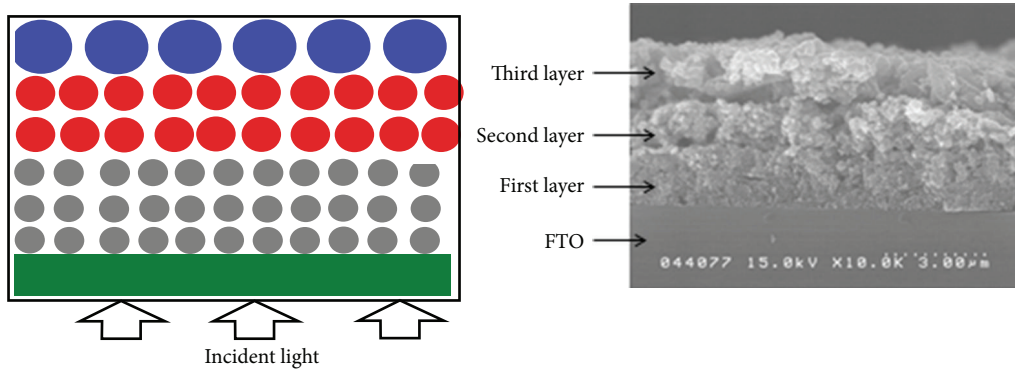


FIGURE 9: The schematic diagrams of triple-layer structures with the different particle sizes in the first (bottom), second (middle), and third (top) layers.

TABLE 4: Solar performance parameters of DSSCs with triple-layer structures of different TiO₂ particle sizes in the first (bottom), second (middle), and third (top).

Triple layers (nm)	J_{sc} (mA/cm ²)	V_{oc} (V)	Fill factor	Efficiency (%)
200/21/10	7.45	0.81	0.68	4.15
200/40/10	8.92	0.81	0.67	4.82
200/100/10	8.94	0.79	0.66	4.71
400/100/10	9.49	0.80	0.67	5.14
400/200/10	9.64	0.80	0.68	5.32

TABLE 5: Solar performance parameters of the DSSCs with triple-layer structures of different TiO₂ particle sizes in the first (bottom), second (middle), and third (top).

Triple layers (nm)	J_{sc} (mA/cm ²)	V_{oc} (V)	Fill factor	Efficiency (%)
200/100/9/FTO	10.08	0.78	0.67	5.26
200/9/100/FTO	8.46	0.77	0.65	4.28
200/9 + 100/9/FTO	10.72	0.77	0.65	5.38

4. Conclusions

The solar performance of DSSCs with different particle sizes in single, double, and triple TiO₂ layers has been investigated.

For single layer, the DSSCs with larger particle size of TiO₂ layers have lower solar efficiency than those with smaller particle size of TiO₂. The lower solar efficiency in larger particle sizes of TiO₂ can be attributed to a strong back-scattering light and less dye adsorption. In addition, the optimal TiO₂ thickness for achieving the maximum efficiency

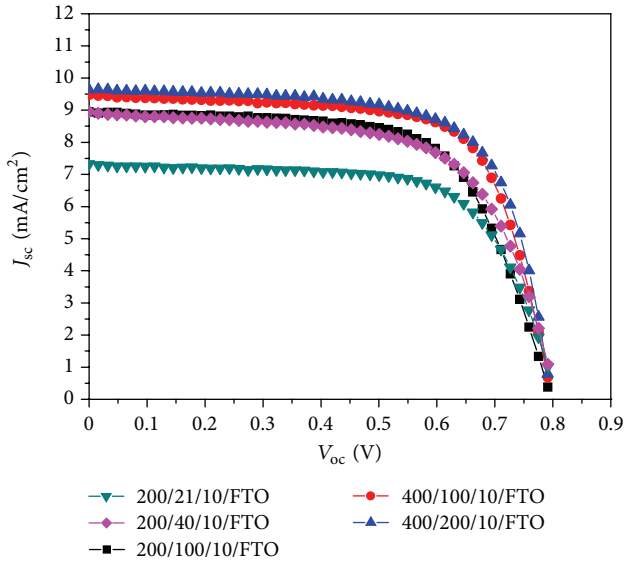


FIGURE 10: The photocurrent-voltage curves of DSSCs with triple-layer structure of TiO_2 layers.

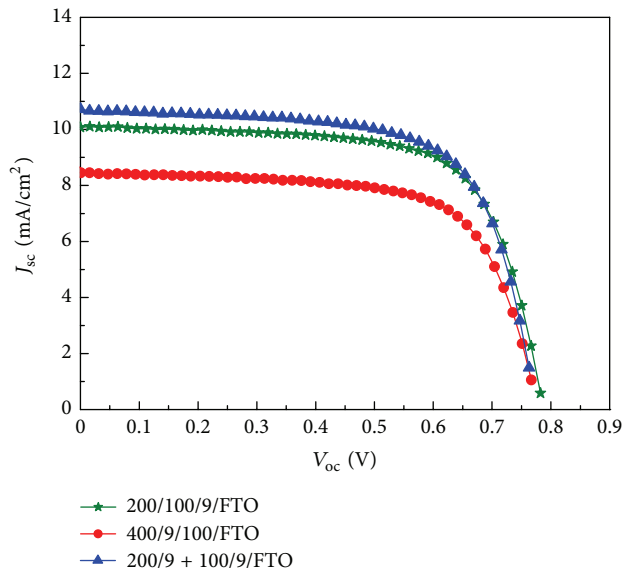


FIGURE 11: The photocurrent-voltage curves of DSSCs prepared by triple-layers with different particle sizes and the mixing of particle size in TiO_2 layers.

TABLE 6: The parameters of charge transfer resistance in triple-layer structures by EIS measurements.

Triple layers (nm)	R_s (Ω)	R_1 (Ω)	R_2 (Ω)
200/100/10/FTO	13.28	14.65	12.01
400/100/10/FTO	18.77	15.76	11.71
400/200/10/FTO	14.64	13.03	10.01

depends on the particle sizes of TiO_2 . The larger the particle sizes of TiO_2 , the shorter the optimal TiO_2 thickness. For double layers, the DSSCs with larger particle sizes in the top layer and smaller particle sizes in the bottom layer can obtain

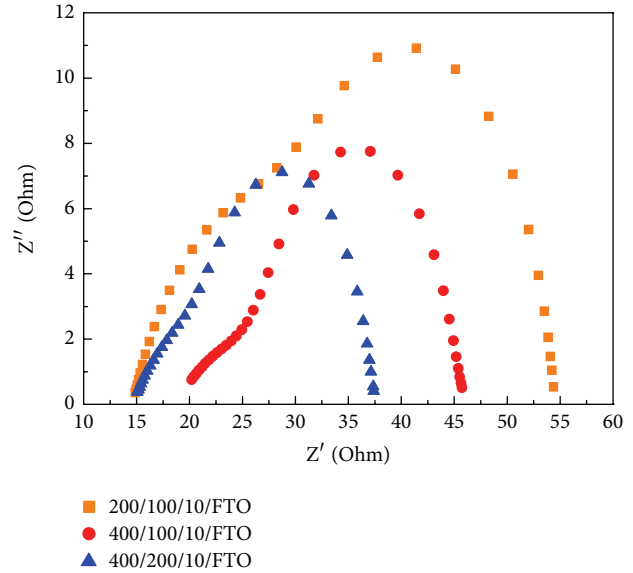


FIGURE 12: The EIS curves of DSSCs with the triple layer structures with different particle sizes of TiO_2 layers.

higher solar efficiency due to stronger back-scattering light and large surface area, respectively. The experimental results indicate that the choice of particle size in the bottom layer is more important than that in the top layer for achieving higher solar efficiency. For triple layers, the DSSCs with larger particle sizes in the top layer and smaller particle sizes on the bottom layer can also obtain higher solar efficiency. However, the choice of the particle sizes in the middle layer will depend on the particle sizes in the bottom and top layers. The mixing of the particle sizes in the middle layer is a good choice for achieving higher solar efficiency.

Acknowledgment

This work was supported by the National Science Council of Taiwan (Project no. NSC100-2221-E-182-037).

References

- [1] B. O'Regan and M. Gratzel, "A low-cost, high-efficiency solar cell based on dye-sensitized colloidal TiO_2 films," *Nature*, vol. 353, pp. 737–740, 1991.
- [2] M. Gratzel, "Conversion of sunlight to electric power by nanocrystalline dye-sensitized solar cells," *Journal of Photochemistry and Photobiology A*, vol. 164, pp. 3–14, 2004.
- [3] Q. F. Zhang, C. S. Dandeneau, X. Y. Zhou, and G. Z. Cao, "ZnO nanostructures for dye-sensitized solar cells," *Advanced Materials*, vol. 21, pp. 4087–4108, 2009.
- [4] S. Ito, T. N. Murakami, P. Comte et al., "Fabrication of thin film dye sensitized solar cells with solar to electric power conversion efficiency over 10%," *Thin Solid Films*, vol. 516, no. 14, pp. 4613–4619, 2008.
- [5] D. B. Kuang, S. Ito, B. Wenger et al., "High molar extinction coefficient heteroleptic ruthenium complexes for thin film dye-sensitized solar cells," *Journal of the American Chemical Society*, vol. 128, no. 12, pp. 4146–4154, 2006.

- [6] Q. F. Zhang and G. Z. Cao, "Nanostructured photoelectrodes for dye-sensitized solar cells," *Nano Today*, vol. 6, no. 1, pp. 91–109, 2011.
- [7] Y. Aswani, H. W. Lee, H. N. Tsao et al., "Porphyrin-sensitized solar cells with cobalt (II/III)-based redox electrolyte exceed 12 percent efficiency," *Science*, vol. 334, pp. 629–634, 2011.
- [8] Q. F. Zhang and G. Z. Cao, "Nanostructured photoelectrodes for dye-sensitized solar cells," *Nano Today*, vol. 6, no. 1, pp. 91–109, 2011.
- [9] J. S. Im, S. K. Lee, and Y. S. Lee, "Cocktail effect of Fe_2O_3 and TiO_2 semiconductors for a high performance dye-sensitized solar cell," *Applied Surface Science*, vol. 257, no. 6, pp. 2164–2169, 2011.
- [10] J. Ferber and J. Luther, "Computer simulations of light scattering and absorption in dye-sensitized solar cells," *Solar Energy Materials and Solar Cells*, vol. 54, no. 1–4, pp. 265–275, 1998.
- [11] G. Rothenberger, P. Comte, and M. Grätzel, "A contribution to the optical design of dye-sensitized nanocrystalline solar cells," *Solar Energy Materials and Solar Cells*, vol. 58, pp. 321–336, 1999.
- [12] M. Wei, Y. Konishi, H. Zhou, M. Yanagida, H. Sugihara, and H. Arakawa, "Highly efficient dye-sensitized solar cells composed of mesoporous titanium dioxide," *Journal of Materials Chemistry*, vol. 16, no. 13, pp. 1287–1293, 2006.
- [13] W. G. Yang, F. R. Wan, Q. W. Chen, J. J. Li, and D. S. Xu, "Controlling synthesis of well-crystallized mesoporous TiO_2 microspheres with ultrahigh surface area for high-performance dye-sensitized solar cells," *Journal of Materials Chemistry*, vol. 20, no. 14, pp. 2870–2876, 2010.
- [14] K. Yan, Y. Qiu, W. Chen, M. Zhang, and S. Yang, "A double layered photoanode made of highly crystalline TiO_2 nanooctahedra and agglutinated mesoporous TiO_2 microspheres for high efficiency dye sensitized solar cells," *Energy and Environmental Science*, vol. 4, no. 6, pp. 2168–2176, 2011.
- [15] D. H. Chen, F. Z. Huang, Y. B. Cheng, and R. A. Caruso, "Mesoporous anatase TiO_2 beads with high surface areas and controllable pore sizes: a superior candidate for high-performance dye-sensitized solar cells," *Advanced Materials*, vol. 21, no. 21, pp. 2206–2210, 2009.
- [16] Y. J. Kim, M. H. Lee, H. J. Kim et al., "Formation of highly efficient dye-sensitized solar cells by hierarchical pore generation with nanoporous TiO_2 spheres," *Advanced Materials*, vol. 21, no. 36, pp. 3618–3673, 2009.
- [17] I. G. Yu, Y. J. Kim, H. J. Kim, C. Lee, and W. I. Lee, "Size-dependent light-scattering effects of nanoporous TiO_2 spheres in dye-sensitized solar cells," *Journal of Materials Chemistry*, vol. 21, no. 2, pp. 532–538, 2011.
- [18] F. Sauvage, D. Chen, P. Comte et al., "Dye-sensitized solar cells employing a single film of mesoporous TiO_2 beads achieve power conversion efficiencies over 10%," *ACS Nano*, vol. 4, no. 8, pp. 4420–4425, 2010.
- [19] Y. C. Park, Y. J. Chang, B. G. Kum et al., "Size-tunable mesoporous spherical TiO_2 as a scattering overlayer in high-performance dye-sensitized solar cells," *Journal of Materials Chemistry*, vol. 21, no. 26, pp. 9582–9586, 2011.
- [20] M. J. Ross and K. R. William, *Impedance Spectroscopy: Emphasizing Solid Materials and Systems*, John Wiley & Sons, New York, NY, USA, 1987.
- [21] A. Hauch and A. Georg, "Diffusion in the electrolyte and charge-transfer reaction at the platinum electrode in dye-sensitized solar cells," *Electrochimica Acta*, vol. 46, no. 22, pp. 3457–3466, 2001.
- [22] Q. Wang, J. E. Moser, and M. Grätzel, "Electrochemical impedance spectroscopic analysis of dye-sensitized solar cells," *The Journal of Physical Chemistry B*, vol. 109, pp. 14945–14953, 2005.
- [23] N. Papageorgiou, W. F. Maier, and M. Grätzel, "An iodine/triiodide reduction electrocatalyst for aqueous and organic media," *Journal of the Electrochemical Society*, vol. 144, no. 3, pp. 876–884, 1997.
- [24] J. Bisquert, "Theory of the impedance of electron diffusion and recombination in a thin layer," *Journal of Physical Chemistry B*, vol. 106, no. 2, pp. 325–333, 2002.
- [25] K. Kalyanasundaram and M. Grätzel, "Applications of functionalized transition metal complexes in photonic and optoelectronic devices," *Coordination Chemistry Reviews*, vol. 177, pp. 347–414, 1998.
- [26] N. Koide, A. Islam, Y. Chiba, and L. Han, "Improvement of efficiency of dye-sensitized solar cells based on analysis of equivalent circuit," *Journal of Photochemistry and Photobiology A*, vol. 182, no. 3, pp. 296–305, 2006.
- [27] L. Han, N. Koide, Y. Chiba, and T. Mitate, "Modeling of an equivalent circuit for dye-sensitized solar cells," *Applied Physics Letters*, vol. 84, no. 13, pp. 2433–2435, 2004.
- [28] D. Qian, Y. Li, Q. Zhang, G. Shi, and H. Wang, "Anatase TiO_2 sols derived from peroxotitanium acid and to form transparent TiO_2 compact film for dye-sensitized solar cells," *Journal of Alloys and Compounds*, vol. 509, pp. 10121–10126, 2011.

Research Article

Integration of High-Performance Nanocrystalline TiO₂ Photoelectrodes for N719-Sensitized Solar Cells

Ke-Jian Jiang,¹ Jin-Ming Zhou,¹ Kazuhiro Manseki,² Qi-Sheng Liu,¹ Jin-Hua Huang,¹ Yan-lin Song,¹ and Shozo Yanagida³

¹Laboratory of New Materials, Institute of Chemistry, Chinese Academy of Sciences, Beijing 100190, China

²Graduate School of Engineering, Environmental and Renewable Energy System (ERES) Division, Gifu University, 1-1, Yanagido, Gifu 501-1193, Japan

³ISIR, Osaka University, 2-1, Mihoga-oka, Ibaraki, Osaka 567-0047, Japan

Correspondence should be addressed to Shozo Yanagida; yanagida@mls.eng.osaka-u.ac.jp

Received 12 February 2013; Accepted 21 April 2013

Academic Editor: Theodoros Dimopoulos

Copyright © 2013 Ke-Jian Jiang et al. This is an open access article distributed under the Creative Commons Attribution License, which permits unrestricted use, distribution, and reproduction in any medium, provided the original work is properly cited.

We report on enhanced performance of N719-sensitized TiO₂ solar cells (DSCs) incorporating size and photoelectron diffusion-controlled TiO₂ as sensitizer-matched light-scatter layers on conventional nanocrystalline TiO₂ electrodes. The double-layered N719/TiO₂ composite electrode with a high dye-loading capacity exhibits the diffused reflectance of more than 50% in the range of $\lambda = 650\text{--}800\text{ nm}$, even when the films are coupled with the titania nanocrystalline underlayer in the device. As a result, the increased near-infrared light-harvesting produces a high light-to-electricity conversion efficiency of over 9% mainly due to the significant increase of J_{sc} . Such an optical effect of the NIR-light scattering TiO₂ electrodes will be beneficial when the sensitizers with low molar extinction coefficients, such as N719, are introduced in the device.

1. Introduction

Dye-sensitized solar cells (DSCs) have been explored from both academic and industry world as a promising alternative to the conventional silicon-based photovoltaic devices [1–3], and efficiencies of over 12% have been achieved [4]. In this cell, a wide band-gap nanostructured semiconductor electrode (typically, TiO₂) is employed to support a large surface area, on which dye molecules are assembled to improve the light harvesting of the dyed electrode. A great deal of effort has been focused on the development of effective panchromatic sensitizers or cosensitizers for efficient solar light harvesting in DSC devices. On the other hand, the light-harvesting efficiency of DSC can be promoted by introducing a sophisticated structure in the photoelectrode, in which the photon path length is increased by the confinement of incident solar energy light. Usami made the theoretical finding that lightscattering in DSCs will be optimized if the diameter of TiO₂ nanocrystals is twice the size of the wavelength of incident light [5]. The effect has been verified in the DSCs, in which a TiO₂ layer built from

submicrometer-sized TiO₂ particles was employed in combination with a transparent nanostructured TiO₂ layer [6–8]. In addition, TiO₂ (or ZnO) photoelectrodes with submicrometer-sized beads, hollow spheres, and tubes have been widely investigated [9–15].

As an alternative to such a large particle light-scattering material, TiO₂ layers with periodic pore structures exhibiting photonic band gaps have been applied for DSCs to enhance light harvesting efficiency [16–21]. Such light scattering TiO₂ layers, however, required an elaborate multistep synthesis. On the other hand, Hore et al. reported scattering of light on disordered spherical voids in TiO₂ electrodes for enhanced DSC performance. The DSC with 400 nm void layers gave a higher efficiency (6.7%) as compared to the cavity-free layer (5.4%) [22]. While the overall efficiency was improved, a slight increase of J_{sc} was observed and the appreciable increase of fill factors resulted in the 18% increment of conversion efficiency. Despite a number of nanostructured TiO₂ photoelectrodes reported as mentioned previously, the cell performance originated from spherical void-centered TiO₂ has still been poorly understood. Most importantly,

little has been reported on an enhancement of near-infrared-(NIR-) light response in IPCE [22, 23]. As organic dye molecules with large extinction coefficients even in the red region were used, the results represent a compromise between slight light scattering and enhanced mobility of viscous electrolytes in the large hollow cavities [23]. In this paper we demonstrate optimized effects of scattering on submicron TiO_2 particles with spherical cavities on quantum efficiencies of light-to-electricity conversion of N719-sensitized solar cells at a NIR region, where the N719 dye has a low extinction coefficient. Accordingly, we prepared a TiO_2 layer containing 600 nm large spherical cavities and combined successively with the conventional nanocrystalline TiO_2 layer. We then applied the hollow-cavity-based TiO_2 /nanocrystalline TiO_2 double composite electrodes to N719-sensitized DSC. The DSC exhibited a maximum conversion efficiency of 9.25% versus 6.38% for the reference cell with single conventional TiO_2 electrodes. We demonstrated that the hollow-cavity-based TiO_2 contributes not only to the enhanced absorption of near-infrared photons but also to effective dye sensitization as evidenced by the remarkable enhancement of J_{sc} in the performance. It should be noted that the effective electron diffusion coefficient of the dye-coated light-scattering TiO_2 layer also plays a crucial role in the improved DSC performance.

2. Materials and Methods

Polyethyleneglycol (PEG, $M_w = 20,000$) was purchased from Fluka Co. The Ru dye, N719 (cis-bis(isothiocyanato) bis(2,2'-bipyridyl-4,4'-dicarboxylato)-ruthenium (II) bis-tetrabutylammonium) was purchased from Solaronix S.A. Iodine, 1-propyl-3-methylimidazolium iodide, valeronitrile, lithium iodide, and *tert*-butylpyridine were purchased from Aldrich without purification.

2.1. Preparation of DSCs. A 60 nm dense TiO_2 layer was deposited on a patterned ITO-coated glass substrates ($10 \Omega/\square$, Nippon Sheet Glass) by spin coating technique with tetraisopropyl orthotitanate in ethanol, as reported previously [24]. The TiO_2 films, served as a blocking layer in DSCs, were annealed in air at 500°C for 30 minutes. Following this, a TiO_2 paste with 20 nm particle size was deposited by doctor blade technique on the blocking layer, where the TiO_2 paste was prepared according to the previous report [25]. A transparent TiO_2 underlayer was achieved after the calcination at 500°C for 30 minutes. Functional polystyrene spheres (PS) (560 nm in size) were synthesized according to our previous method [26]. The resulting latex spheres were used directly without purification. The polystyrene spheres (PS) were fabricated via batch emulsion polymerization, where styrene was mixed with methyl methacrylate (MMA) and acrylic acid (AA). For the preparation of the spherical cavity-based light-scattering TiO_2 layer, as prepared spheres were dispersed in the TiO_2 colloid with the particle size of about 20 nm as a coating paste for the preparation of the overlayer. The PS sphere, the previously mentioned TiO_2 colloid, and PEG were mixed in water with ratio of 1/0.5/0.3 (TiO_2 /PS/PEG, by weight) and homogenized with a stirring bar and ultrasonication. The

resulting paste was deposited as a light-scattering layer on the underlayer, followed by the same calcination procedure mentioned previously. Finally, the double-layered TiO_2 film was impregnated with 0.2 M TiCl_4 aqueous solution at room temperature overnight and then calcinated again at 500°C for 30 minutes. After cooling to about 120°C , the films were emerged overnight in 1:1 v/v acetonitrile and *tert*-butyl alcohol solvent mixture containing N719 dye at a concentration of 0.3 mM. A Pt-sputtered FTO glass was used as a counter electrode. The electrolyte was composed of 0.6 M 1-propyl-3-methylimidazolium iodide, 0.1 M LiI, 0.04 M I_2 , and 0.5 M *tert*-butylpyridine in the mixture of acetonitrile and valeronitrile (1:1, by volume).

2.2. Characterization and Photoelectric Measurements. The SEM images of titania films were obtained with a field-emission SEM (JEOL JSM-4800, Japan). The optical reflection measurement was performed using an UV-vis spectrophotometer (U-3010, HITACHI) equipped with an integrating sphere.

The incident photon-to-current conversion efficiency (IPCE) for solar cells was measured by using a commercial setup (PV-25 DYE, JASCO) equipped with a monochromator. A 300 W Xenon lamp was employed as a light source for the generation of a monochromatic beam. Calibrations were performed with a standard silicon photodiode. IPCE is defined by $\text{IPCE}(\lambda) = hc J_{sc} / e\phi\lambda$, where h is Planck's constant, c is the speed of light in a vacuum, e is the electronic charge, λ is the wavelength in meters (m), J_{sc} is the short-circuit photocurrent density (A m^{-2}), and ϕ is the incident radiation flux (W m^{-2}). The photocurrent-voltage (*I-V*) characteristics were recorded using a computer-controlled Keithley 2400 source meter under air mass (AM) 1.5 simulated illumination (100 mW cm^{-2} , Oriel, 67005). The active area of the samples was about 0.2 cm^2 , controlled by an aperture mask to prevent extra light from coming through the lateral space. *I-V* data were well within experimental error.

3. Results and Discussion

As shown in Figure 1(a), the latex PS sphere holds a hard PS core with an elastomeric PMMA/PAA shell and presents a monodispersity with the size of about 560 nm (Figure 1(b)). The TiO_2 overlayer was prepared through a simple mixing of submicrometer-size polystyrene (PS) spheres and nano sized TiO_2 particles, followed by subsequent coating and calcinations on a transparent TiO_2 underlayer. The PS spheres vanish during the calcination process.

The SEM image in Figure 2(a) shows a top surface image of the TiO_2 overlayer. It is very clear that homogeneous spherical voids spread on the whole surface with the size of around 600 nm. Figure 2(b) shows a top surface image of the TiO_2 transparent layer, which presents a porous structure comprised of 20 nm sized TiO_2 particles. The cross-sectional image of the corresponding double-layer electrode is shown in Figure 2(c), where the $8 \mu\text{m}$ thick transparent nanoporous TiO_2 underlayer and the $6 \mu\text{m}$ thick TiO_2 overlayer are formed without cracks.

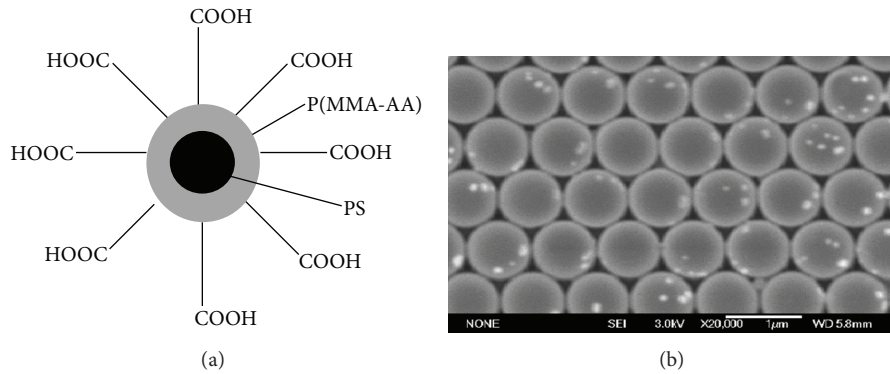


FIGURE 1: (a) A schematic structure of the functionalized polystyrene spheres. (b) A SEM image of the PS spheres with a diameter of 560 nm.

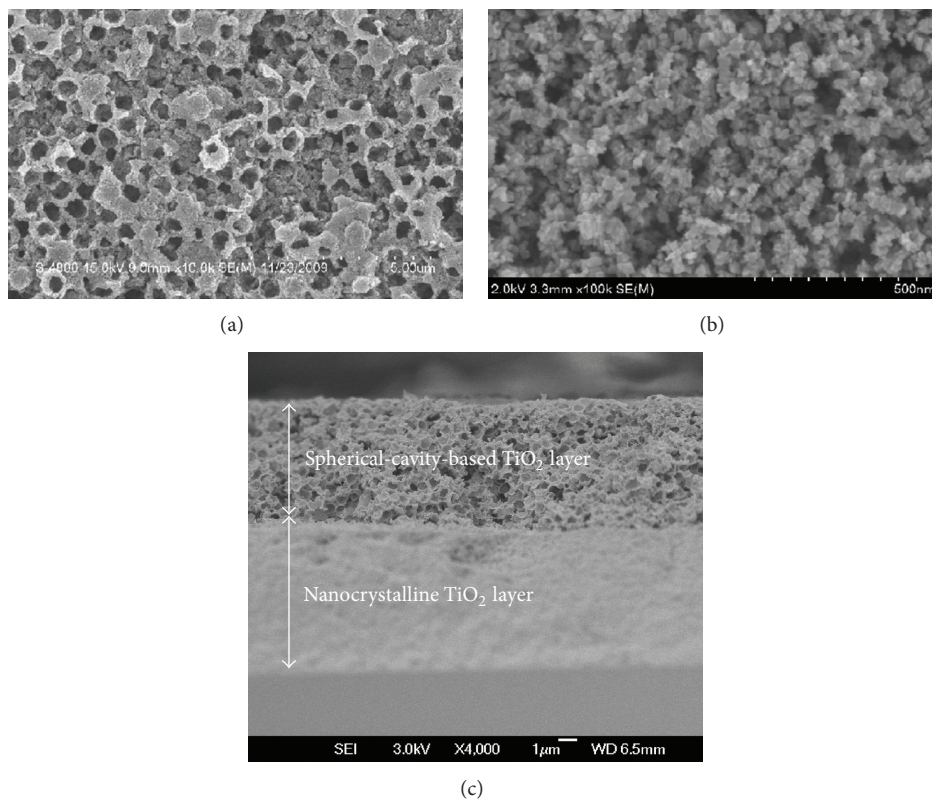


FIGURE 2: Scanning electron micrographs of (a) the top view of a spherical-cavity-based TiO_2 film, (b) the top view of a nanocrystalline TiO_2 film, (c) cross-sectional view of the double-layer TiO_2 film with a nanocrystalline TiO_2 layer and a spherical-cavity-based TiO_2 layer.

In order to investigate the light-scattering ability of the overlayer, UV-vis reflectance spectra were recorded for a $6\ \mu\text{m}$ thick spherical-cavity-based TiO_2 film with and without sensitization by using a standard N719 dye, and an $8\ \mu\text{m}$ -thick nanostructured TiO_2 film was employed for comparison, as shown in Figure 3. For the film without the dye loading, the reflectance of the overlayer is more than 70% in the whole UV-vis region, indicating that more than 90% of the light reflecting efficiency can be achieved by the overlayer when considering the absorption and reflection by the FTO glass substrate. By contrast the reflectance of the transparent nanostructured TiO_2 underlayer is less than 30%. After the

dye adsorption, the reflectance was significantly decreased in the spectral range by around 535 nm for both the layers, where N719 dye has the maximum absorption, indicating that the reduction is mainly ascribed to the light absorption by the dye. Most importantly, the diffused reflectance of the TiO_2 /dye composite film is found to be more than 50% in the range of $\lambda = 650\text{--}800\ \text{nm}$ after the dye loading for the overlayer.

We tested the double composite films as DSC photoelectrodes (denoted as sample 1) consisting of a $8\ \mu\text{m}$ thick nanostructured TiO_2 underlayer and a $6\ \mu\text{m}$ thick overlayer, in which a single-layer TiO_2 electrode only with the $8\ \mu\text{m}$

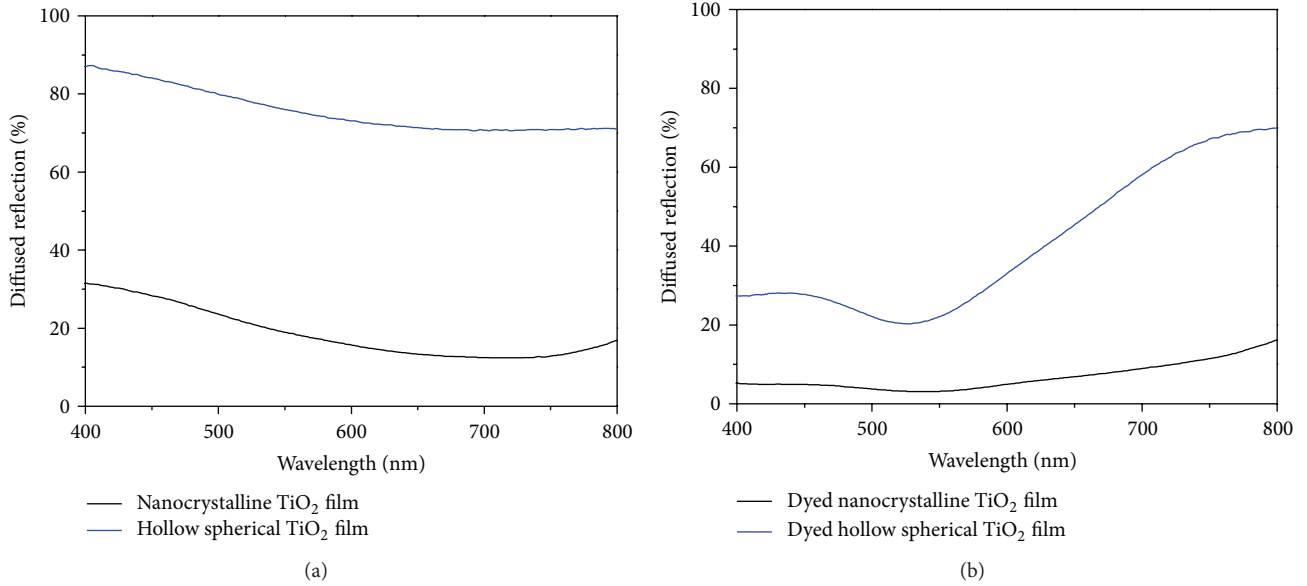


FIGURE 3: Diffused reflectance spectra of a nanocrystalline TiO_2 film ($8 \mu\text{m}$ thick) and a spherical-cavity-based TiO_2 film ($6 \mu\text{m}$ thick) without (a) and with (b) N719 dye loading.

TABLE 1: Photovoltaic characteristics of samples 1, 2, and 3 measured under AM1.5 illumination (100 mW cm^{-2}). Each data represents the average of three cells with active area of 0.2 cm^2 .

Sample	Thickness [μm]	J_{sc} [mA/cm^2]	V_{oc} [V]	FF	η [%]	Adsorbed dye [$\mu \text{ mol cm}^{-2}$]
1	8 + 6	18.40 ± 0.05	0.73 ± 0.02	0.69 ± 0.01	9.25 ± 0.05	1.163
2	8	13.04 ± 0.03	0.73 ± 0.02	0.67 ± 0.01	6.38 ± 0.05	1.012
3	10	14.86 ± 0.03	0.70 ± 0.02	0.68 ± 0.01	7.07 ± 0.05	1.171

thick TiO_2 underlayer (sample 2) was used for comparison. The current-voltage characteristics are shown in Figure 4 and Table 1. The conversion efficiency (η) was improved from 6.38% for sample 2 to 9.25% for sample 1, corresponding to the 45% increment. The improved efficiency was mainly caused by the increase of the short-circuit current density (J_{sc}) from 13.04 mA cm^{-2} to 18.40 mA cm^{-2} , while the V_{oc} s and fill factors are the same or comparable for the two samples. It should be noted that, in the overlayer, the submicro-meter sized voids are surrounded by the nanostructured TiO_2 film with the TiO_2 particles of 20 nm. The dye molecules can be absorbed on the overlayer to contribute to the increment of J_{sc} in the double layer. In order to evaluate the effect of dye absorption in the overlayer on J_{sc} , the one-layer nanostructured TiO_2 electrode with a thickness of $10 \mu\text{m}$ was prepared (sample 3), by considering the amount of the dye loading for fair comparison (the porosity of TiO_2 overlayer : $\sim 80\%$). The amounts of the absorbed dyes were determined for the three different electrodes by measuring the eluted dye concentration from the TiO_2 electrodes as shown in Table 1. The dye adsorption capacity was comparable for samples 1 and 3, suggesting that the scattering layer maintains a high dye-adsorption capacity. As shown in Table 1, sample 3 with the $10 \mu\text{m}$ thick TiO_2 electrode gave 14.86 mA cm^{-2} of J_{sc} , which was much lower than that of sample 1. A further comparison between sample 2 and sample 3 showed only

a slight increase (1.82 mA cm^{-2}) in J_{sc} . On the other hand, the reflectance for sample 1 was significantly higher across the visible part of the spectrum than that of a single-layer TiO_2 cell as mentioned previously. Therefore, these results indicated that the marked increment in J_{sc} for sample 1 as compared to 3 is ascribed to the stronger light scattering, particularly at a red to near-infrared light region. It is thus postulated that both the light-scattering property and high dye-loading capacity from the integrated nanocrystalline composite electrodes resulted in the significant increase of IPCE as shown in Figure 5. In addition, it should be noted that the unaffected and effective electron diffusion coefficient in the double-layered TiO_2 is essential for the improved IPCE in sample 1.

4. Conclusions

We applied a facile colloidal template method for the preparation of spherical-cavity-based TiO_2 /nanocrystalline TiO_2 double composite layers as a strong near-infrared light-scattering layer for N719-sensitized solar cells, which is particularly useful for the significant gain of photocurrents. The DSC fabricated by using double-layered electrodes composed of the scattering layer and the nanocrystalline TiO_2 layer produced a higher conversion efficiency of 9.25% versus 6.38% for the reference cell with a single TiO_2 electrode

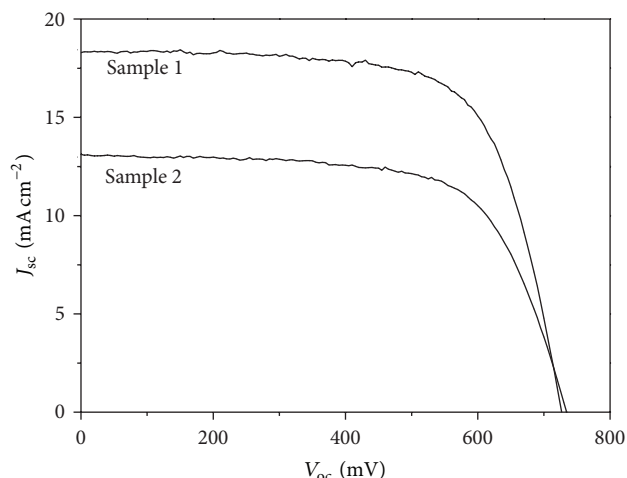


FIGURE 4: Photocurrent and voltage curves for samples 1 and 2. Both measurements were performed under AM 1.5 G with the active area of 0.2 cm^2 .

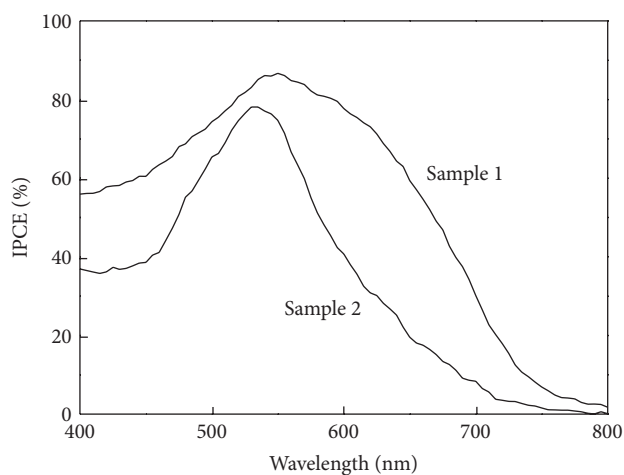


FIGURE 5: Incident monochromatic photon-to-current conversion efficiency (IPCE) as a function of excitation wavelength for samples 1 and 2.

with the comparable thickness. The results obtained from our facile photon capture approach could open up new perspectives of exploiting low-cost and high-efficiency DSCs with a wide range of newly developed dye molecules and electrolytes.

Conflict of Interests

The authors declare that there is no conflict of interests.

Acknowledgments

The authors would like to acknowledge the National 863 Program (no. 2011AA050521) and 973 Program (no. 2006CB806200), National Science Foundation of China (nos. 20774103, 50625312, 60601027, 20421101, and U0634004), (No. 50973105), and the Koshiyama Research Grant in Japan for financial support.

References

- [1] B. O'Regan and M. Grätzel, "A low-cost, high-efficiency solar cell based on dye-sensitized colloidal TiO_2 films," *Nature*, vol. 353, pp. 737–740, 1991.
- [2] S. Yanagida, Y. You, and K. Manseki, "Iodine/Iodide-Free Dye-Sensitized Solar Cells," *Accounts of Chemical Research*, vol. 42, no. 11, pp. 1827–1838, 2009.
- [3] J. Xia and S. Yanagida, "Strategy to improve the performance of dye-sensitized solar cells: Interface engineering principle," *Solar Energy*, vol. 85, no. 12, pp. 3143–3159, 2011.
- [4] A. Yella, H. W. Lee, H. N. Tsao et al., "Porphyrin-sensitized solar cells with cobalt (II/III)-based redox electrolyte exceed 12 percent efficiency," *Science*, vol. 334, no. 6056, pp. 629–634, 2011.
- [5] A. Usami, "Theoretical simulations of optical confinement in dye-sensitized nanocrystalline solar cells," *Solar Energy Materials and Solar Cells*, vol. 64, no. 1, pp. 73–83, 2000.
- [6] C. J. Barbé, F. Arendse, P. Comte et al., "Nanocrystalline titanium oxide electrodes for photovoltaic applications," *Journal of the American Ceramic Society*, vol. 80, no. 12, pp. 3157–3171, 1997.
- [7] S. Ito, P. Comte, P. Chen et al., "Fabrication of screen-printing pastes from TiO_2 powders for dye-sensitized solar cells," *Progress in Photovoltaics*, vol. 15, no. 7, pp. 603–612, 2007.
- [8] Y. Chiba, A. Islam, Y. Watanabe, R. Komiya, N. Koide, and L. Han, "Dye-sensitized solar cells with conversion efficiency of 11.1%," *Japanese Journal of Applied Physics*, vol. 45, no. 24-28, pp. L638–L640, 2006.
- [9] T. P. Chou, Q. Zhang, G. E. Fryxell, and G. Cao, "Hierarchically structured ZnO film for dye-sensitized solar cells with enhanced energy conversion efficiency," *Advanced Materials*, vol. 19, no. 18, pp. 2588–2592, 2007.
- [10] D. H. Chen, F. Z. Huang, Y. -B. Cheng, and R. A. Caruso, "Mesoporous anatase TiO_2 beads with high surface areas and controllable pore sizes: a superior candidate for high-performance dye-sensitized solar cells," *Advanced Materials*, vol. 21, no. 21, pp. 2206–2210, 2009.
- [11] I. G. Yu, Y. J. Kim, H. J. Kim, C. Lee, and W. I. Lee, "Size-dependent light-scattering effects of nanoporous TiO_2 spheres in dye-sensitized solar cells," *Journal of Materials Chemistry*, vol. 21, no. 2, pp. 532–538, 2011.
- [12] H. J. Koo, Y. J. Kim, Y. H. Lee, W. I. Lee, K. Kim, and N. G. Park, "Nano-embossed Hollow Spherical TiO_2 as Bifunctional Material for High-Efficiency Dye-Sensitized Solar Cells," *Advanced Materials*, vol. 20, no. 1, pp. 195–199, 2008.
- [13] S. C. Yang, D. J. Yang, J. Kim et al., "Hollow TiO_2 Hemispheres Obtained by Colloidal Templating for Application in Dye-Sensitized Solar Cells," *Advanced Materials*, vol. 20, no. 5, pp. 1059–1064, 2008.
- [14] D. Li, P. C. Chang, C. J. Chien, and J. G. Lu, "Applications of tunable TiO_2 nanotubes as nanotemplate and photovoltaic device," *Chemistry of Materials*, vol. 22, no. 20, pp. 5707–5711, 2010.
- [15] J. Yu, J. Fan, and L. Zhan, "Dye-sensitized solar cells based on hollow anatase TiO_2 spheres prepared by self-transformation method," *Electrochimica Acta*, vol. 55, no. 3, pp. 597–602, 2010.
- [16] S. H. A. Lee, N. M. Abrams, P. G. Hoertz, G. D. Barber, L. I. Halaoui, and T. E. Mallouk, "Coupling of titania inverse opals to nanocrystalline titania layers in dye-sensitized solar cells," *Journal of Physical Chemistry B*, vol. 112, no. 46, pp. 14415–14421, 2008.
- [17] A. Mihi, M. E. Calvo, J. A. Anta, and H. Miguez, "Spectral response of opal-based dye-sensitized solar cells," *Journal of Physical Chemistry C*, vol. 112, pp. 13–17, 2008.

- [18] S. Nishimura, N. Abrams, B. A. Lewis et al., "Standing wave enhancement of red absorbance and photocurrent in dye-sensitized titanium dioxide photoelectrodes coupled to photonic crystals," *Journal of the American Chemical Society*, vol. 125, no. 20, pp. 6306–6310, 2003.
- [19] L. J. Diguna, Q. Shen, J. Kobayashi, and T. Toyoda, "High efficiency of CdSe quantum-dot-sensitized TiO₂ inverse opal solar cells," *Applied Physics Letters*, vol. 91, no. 2, Article ID 023116, 2007.
- [20] S. Guldin, S. Hüttner, M. Kolle et al., "Dye-sensitized solar cell based on a three-dimensional photonic crystal," *Nano Letters*, vol. 10, no. 7, pp. 2303–2309, 2010.
- [21] S. Colodrero, A. Mihi, L. Hnggman et al., "Porous one-dimensional photonic crystals improve the power-conversion efficiency of dye-sensitized solar cells," *Advanced Materials*, vol. 21, no. 7, pp. 764–770, 2009.
- [22] S. Hore, P. Nitz, C. Vetter, C. Prah, M. Niggemann, and R. Kern, "Scattering spherical voids in nanocrystalline TiO₂ —Enhancement of efficiency in dye-sensitized solar cells," *Chemical Communications*, no. 15, pp. 2011–2013, 2005.
- [23] T. T. T. Pham, T. Bessho, N. Mathews et al., "Light scattering enhancement from sub-micrometer cavities in the photoanode for dye-sensitized solar cells," *Journal of Materials Chemistry*, vol. 22, no. 32, Article ID 16201, 2012.
- [24] P. Wang, S. M. Zakeeruddin, P. Comte, R. Charvet, R. Humphry-Baker, and M. Gratzel, "Enhance the performance of dye-sensitized solar cells by co-grafting amphiphilic sensitizer and hexadecylmalonic acid on TiO₂ nanocrystals," *Journal of Physical Chemistry B*, vol. 107, no. 51, pp. 14336–14341, 2003.
- [25] K. Manseki, W. Jarernboon, Y. Youhai et al., "Solid-state dye-sensitized solar cells fabricated by coupling photoelectrochemically deposited poly(3,4-ethylenedioxythiophene) (PEDOT) with silver-paint on cathode," *Chemical Communications*, vol. 47, no. 11, pp. 3120–3122, 2011.
- [26] J. X. Wang, Y. Q. Wen, H. Ge et al., "Simple Fabrication of Full Color Colloidal Crystal Films with Tough Mechanical Strength," *Macromolecular Chemistry and Physics*, vol. 207, no. 6, pp. 596–604, 2006.

Research Article

A Facile Synthesis of Granular ZnO Nanostructures for Dye-Sensitized Solar Cells

Md. Mahbubur Rahman,¹ Narayan Chandra Deb Nath,¹
Kwang-Mo Noh,² Jaecheon Kim,³ and Jae-Joon Lee^{1,3}

¹ Department of Advanced Technology Fusion, Konkuk University, Seoul 143-701, Republic of Korea

² Nanotechnology Research Center and Department of Nano Science and Mechanical Engineering, Konkuk University, Chungju 380-701, Republic of Korea

³ Nanotechnology Research Center and Department of Applied Chemistry, Konkuk University, Chungju 380-701, Republic of Korea

Correspondence should be addressed to Jae-Joon Lee; jjlee@kku.ac.kr

Received 15 February 2013; Accepted 5 April 2013

Academic Editor: Theodoros Dimopoulos

Copyright © 2013 Md. Mahbubur Rahman et al. This is an open access article distributed under the Creative Commons Attribution License, which permits unrestricted use, distribution, and reproduction in any medium, provided the original work is properly cited.

Granular ZnO nanostructures of single-crystalline wurtzite hexagonal phases were synthesized by a facile and low-cost chemical method in aqueous condition. The average size of ZnO nanograin increased with reflux time, and it significantly affected the open circuit potential (V_{oc}) while the short circuit current density (J_{sc}) was not changed much. The overall energy conversion efficiency was 1.82% with the smaller grain size of *ca.* 250 nm when it was used as photoelectrode of DSSCs. The positive shifting of the Fermi energy (E_F) and low density of surface states (DOS) were consistent with the reduction of the recombination of excited electron with electrolyte for smaller grains.

1. Introduction

Zinc oxide (ZnO) is unique in exhibiting both semiconducting and piezoelectric properties [1]. Bulk ZnO is a direct and a wide band gap semiconductor ($E_g \sim 3.2$ eV at 25°C) with high excitation binding energy (~ 0.06 eV), large saturation velocity (3.2×10^7 cm s⁻¹), and high optical gain (300 cm⁻¹) [2]. The high excitation binding energy leads to excitonic transitions ($\sim 25^\circ\text{C}$), high radiative recombination efficiency for spontaneous emission, and a low threshold voltage for laser emission. The quantum confinement effect of photo-generated electron-hole pairs and the tunability of optical and electronic properties of ZnO nanoparticles (~ 10 nm) [3, 4] allowed them to be used in various nanodevices such as information storage, sensing, and surface acoustic wave devices [5–7].

ZnO is potentially useful in dye-sensitized solar cells (DSSCs) because it has a similar band gap to TiO₂ and shows lower electron-hole (e^- - h^+) recombination probability due to its filled valence band (E_{VB})($3d^{10}$) and *s-p* hybridization

properties of conduction band (E_{CB}) [2]. The less population of deep traps in ZnO nanostructures compared with TiO₂ nanoparticles induced the longer electron lifetime [2]. In spite of these superior physical properties of ZnO, the photoconversion efficiency of TiO₂-based DSSC is generally much higher than ZnO. This was mainly attributed to the acidity of the binding groups of dyes (e.g., N719, N3, and black dyes, etc.), which reduced the chemical stability of ZnO by dissolving it to form a precipitation of dye-Zn²⁺ complexes to lead electron injection and dye regeneration inefficiently [8]. In general, it is known that nanostructures, such as nanorods, nanofibers, and nanowires, induce less recombination to improve the charge collection efficiency [9–11]. This work reports the synthesis of granular ZnO nanostructures by simple hydrothermal reactions of zinc nitrate and KOH in the presence of tetra butyl ammonium hexafluorophosphate (TBAPF₆). The effects of the size of ZnO nanograin on the photovoltaic performances of DSSCs were studied in conjunction with their morphology as well as the optical and the electronic properties.

2. Experimental

Zinc nitrate [$\text{Zn}(\text{NO}_3)_2 \cdot 6\text{H}_2\text{O}$] (0.01 mol) and KOH (0.02 mol) were dissolved in 20 mL of distilled water to form a white flocculate, which was then diluted to 100 mL. After the addition of 5×10^{-3} mol TBAPF₆ while stirring, it was refluxed for 30, 60, and 120 min to obtain white precipitates. The samples, being collected by centrifuge and dried for 30 hours at room temperature after washing with water and ethanol, were sintered in an electric muffle furnace at 500°C for 30 min in ambient condition before further characterization. They were denoted as Z1, Z2, and Z3, respectively, depending on the reflux time.

Scanning electron microscopy (SEM, Hitachi S-3000N, Japan) was used to investigate the ZnO nanograin's surface morphologies. X-ray diffractometry (Philips, X'pert, Netherland) was conducted using Cu K α radiation ($\lambda = 0.15406$ nm) over a 2θ scan range of 20°–80°. Optical absorption and photoluminescence emission spectra of the ZnO dispersed in ethanol were obtained using a UV-Vis spectrophotometer (Scinco, S-3100, Republic of Korea) and spectrofluorometer (Horiba, Fluorolog-3, USA). The amount of dye adsorptions on photoelectrodes was measured from the absorption spectra of desorbed-dye solutions as reported in the literature [12].

ZnO paste was prepared by mixing ZnO powder, which was pretreated by acetyl-acetone to minimize aggregation with ethanol, terpineol, and 10% ethyl cellulose as reported elsewhere [10, 11]. The ZnO films on FTO (Pilkington, 8 Ω /sq) were prepared by doctor blading and were sintered in an electric muffle furnace at 500°C under ambient condition. They were immersed in ethanolic solution of 0.4 mM *cis*-diisothiocyanato-bis (2,2'-bipyridyl-4,4'-dicarboxylato) ruthenium(II) bis-tetrabutylammonium (N719) for 12 h. Counter electrodes were prepared by spin coating of 5 mM chloroplatinic acid hexahydrate ($\text{H}_2\text{PtCl}_6 \cdot 6\text{H}_2\text{O}$) in ethanol on FTO and by sintering it in an electric muffle furnace at 380°C for 20 min. The dye-loaded photoelectrodes (active area *ca.* 0.2 cm²) and platinumized counter electrodes were sandwiched with 50 μm thick surlyn film as a spacer and sealing agent at 110°C for 10 min. The electrolyte solution composed of 0.6 M 1,2-dimethyl-3-propylimidazolium iodide (DMPII), 0.1 M LiI, 0.1 M I₂, and 0.5 M 4-*tert*-butylpyridine (*t*BP) in 3-methoxypropionitrile (MPN) was injected into the cell through the drilled holes on the counter electrode. They were sealed with a transparent scotch tape for temporal sealing.

An AM1.5 solar simulator with a 200 W Xenon lamp (Polaronix K201, McScience, Republic of Korea) was used to illuminate the cells, whose current density-voltage (*J-V*) properties were measured using a photovoltaic power meter (Polaronix K101 LAB20, McScience, Republic of Korea). The incident light intensity was adjusted to 100 mWcm⁻² (1 sun) by a standard mono-Si solar cell (PVM 396, PV Measurement Inc., USA) certified by the US National Renewable Energy Laboratory. Cyclic voltammetric (CV) experiment was performed with a CHI430A electrochemical workstation (CH instruments, Inc., USA). ZnO nanograins on FTO, a platinum wire, and a Ag/Ag⁺ electrode were used as working,

counter, and reference electrodes, respectively. Electrochemical impedance spectra (EIS) were obtained under open circuit and dark conditions at frequencies of 10⁵–0.1 Hz with a 5 mV ac amplitude (IM6ex, Zahner-Elektrik GmbH & Co. KG, Germany). The measured spectra were fitted to an equivalent circuit appropriate for DSSCs using Zview software (version 3.1, Scribner Associates Inc., USA).

3. Results and Discussion

The SEM images showed that the average size of ZnO nanograins increased slowly with reflux time by reducing the population of smaller size grains, while the aspect ratio (*ca.* 1.75) was almost unchanged. The lengths of the grains ranged from *ca.* 50 to 750 nm, while the upper limit of the grain length was *ca.* 350, 500, and 750 nm for Z1, Z2, and Z3, respectively (Figure 1(a)). The XRD patterns of all the synthesized ZnO nanograins were consistent with the single-crystalline wurtzite (hexagonal-phase) with no impurities such as Zn and Zn(OH)₂. All the diffraction peaks were well indexed to the hexagonal phase of ZnO reported in JCPDS card (no. 36-1451) (Figure 1(b)(A)).

All the absorption maxima (λ_{max}), observed at *ca.* 362, 376, and 378 nm for Z1, Z2, and Z3, respectively, were blue-shifted relative to the bandgap energy (E_g) of bulk ZnO [2] with the much broader absorption edges for Z1 (Inset, Figure 1(b)(B)). The lowest value of the λ_{max} of Z1 indicated the larger E_g and the positive shift of quasi-Fermi level ($E_{F,q}$) compared to those of Z2 and Z3 [13]. Photoluminescence emission spectra, recorded at room temperature under excitation at 350 nm for Z1 and 360 nm for Z2 and Z3, clearly showed the strong UV emissions peaked at *ca.* 368 nm (Z1) and *ca.* 385 nm (both Z2 and Z3) (Figure 1(b)(B)) which could be attributed to the direct and instant radiative recombination of excitons (RR0) (Scheme 1). The very broad and weak emission observed at *ca.* 565 nm for Z1 was attributed to the other radiative recombination (RR1) through the defect levels possibly caused by vacancies in the interstitial site of zinc and oxygen [14] as described in Scheme 1. Holes form the valence band edge ($E_{V,B}$) of ZnO recombined with electron by tunneling through these defect levels. The significantly low emission intensities in the visible range indicated little density of defect levels for Z2 and Z3 compared with Z1 [15–18]. It indicated that the Z1 has the high probability of recombination of excitons under UV illumination. Nevertheless, the photoelectrode constructed with Z1 showed the better performance in DSSCs as shown in the photocurrent density-voltage (*J-V*) characteristics (Figure 2(a) and Table 1). It was partly because there was no exciton generation in Z1 nanograins during the operation of DSSC and the source of electron was from dyes, which were mostly excited by visible light under AM 1.5 condition. Therefore, the existence of these intrinsic defect levels of Z1 nanograins did not contribute much to reduce the cell performance because the recombination of these electros was more significantly involved with the highest occupied molecular orbital (HOMO) of dye, which is energetically

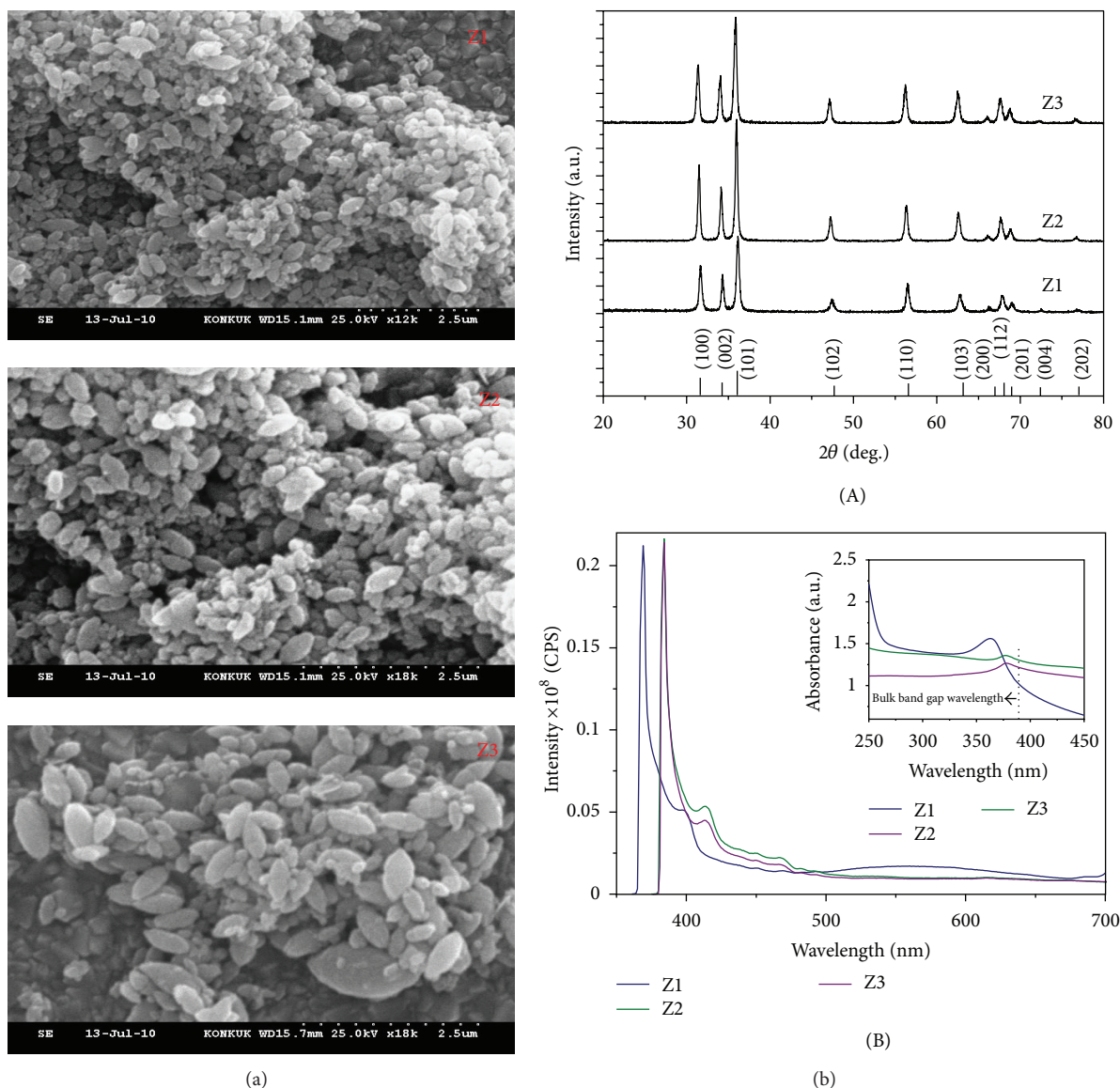


FIGURE 1: (a) Scanning electron microscopic (SEM) images (on FTO) and (b) X-ray diffraction (XRD) pattern (A) and photoluminescence spectra in ethanol (inset, the corresponding UV-visible absorption spectra) (B) of Z1, Z2, and Z3 grains.

much more closer to the conduction band edge (E_{CB}) of ZnO than these intrinsic defect levels of Z1 nanograins (Scheme 1).

The overall energy conversion efficiency with Z1 was *ca.* 1.82% and it was up to 11% and 15.2% higher than that of Z2 and Z3, respectively. The higher efficiency for Z1 was mainly attributed to the higher open circuit potential (V_{oc}) compared to Z2 and Z3. Meanwhile, the short circuit current density (J_{sc}) was not affected significantly even though the dye loading for Z1 was higher up to *ca.* 26.8 and 41.42% than those of Z2 and Z3, respectively (Table 1). It could be attributed to the scattering effect with bigger grains [19]. The variation of V_{oc} in DSSC was known to be dependent significantly on the distribution and density of surface states in the mesoporous structure of photoelectrode, which was

investigated by monitoring the nonfaradic capacitive current flow at these electrodes. The capacitive charging current appeared in the forward scans in CVs (Figure 2(b)) could be interpreted as the filling of these surface trap states as previously studied in similar systems based on TiO_2 nanoparticles [20–22] and the current essentially reached zero during reverse scans to sufficiently positive potentials because of the regeneration of these surface states by discharging. The higher values of capacitive currents for Z2 and Z3 compared to those of the Z1 indicated the higher density of such trap states as described in Scheme 1. It was found, from the density of states (DOS) calculation [22], that they distributed exponentially with the onset potential being dependent on the size of ZnO grain (Figure 2(c), Table 1). The downshift of the onset of the

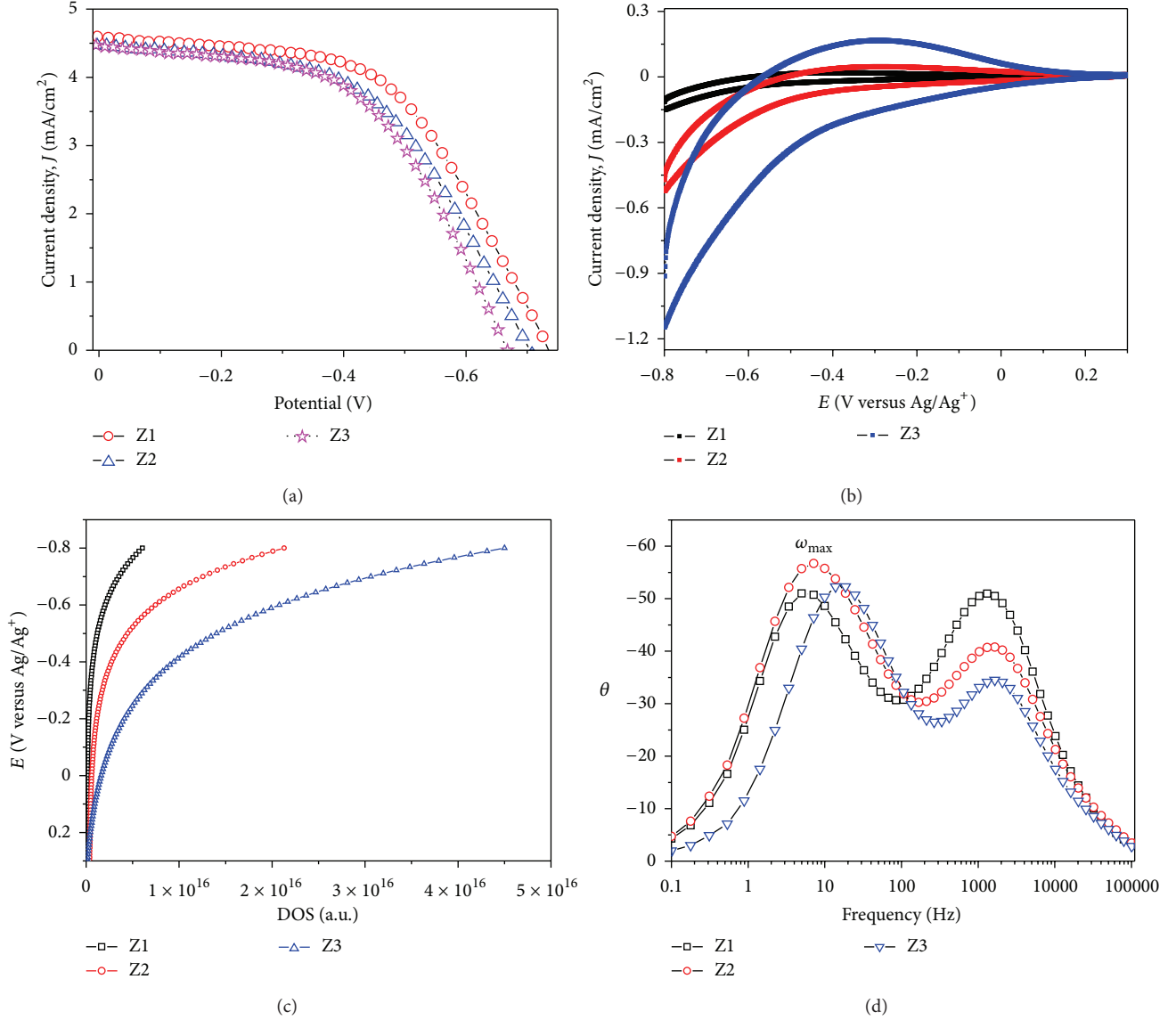


FIGURE 2: (a) Current density-voltage (J - V) characteristics of DSSCs with photoelectrodes of Z1, Z2, and Z3 grains. (b) Cyclic voltammograms (CVs) of the photoelectrodes in 0.5 M LiClO_4 dissolved in acetonitrile at a scan rate of 50 mV/s . (c) The exponential distribution of the density of states (DOS) of different ZnO nanograins was deduced by capacitive charging of electrons into the surface states versus applied potential and (d) the Bode plots from electrochemical impedance spectroscopy of DSSCs.

TABLE 1: Photovoltaic and kinetic parameters of Z1, Z2, and Z3 DSSCs photoelectrodes along with their amounts of adsorbed dye and the onset potential for exponential distribution of the density of states (DOS).

Electrode	J_{sc} (mA/cm^2)	V_{oc} (V)	FF (%)	η (%)	Adsorbed dye (mol/cm^2)	$k_{Z/E}$ (s^{-1})	Onset potential (eV versus Vacuum)
Z1	4.6	0.73	54.08	1.82	5.77×10^{-7}	5.58	4.45
Z2	4.46	0.70	52.17	1.64	4.55×10^{-7}	7.10	4.76
Z3	4.44	0.66	53.08	1.58	4.08×10^{-7}	16.85	4.87

state distribution was consistent with the tendency of the negative shift of the pseudo-Fermi level of the photoelectrode (Scheme 1) [23], which was responsible for the higher recombination rate to induce the decrease of V_{oc} . The electron transfer kinetics, measured by electrochemical impedance

spectroscopy (EIS) at the $\text{ZnO}|$ electrolyte interface under dark condition (Figure 2(d)), was also consistent with this trend by showing the lowest value of the back electron transfer rate to I_3^- ($k_{Z/E}$) for Z1 as summarized in Table 1.

- the photoelectrode of dye sensitized solar cells," in *Composite Materials for Medicine and Nanotechnology*, B. Attaf, Ed., pp. 181–210, InTech, Rijeka, Croatia, 2011.
- [3] M. Makkar and H. S. Bhatti, "Inquisition of reaction parameters on the growth and optical properties of ZnO nanoparticles synthesized via low temperature reaction route," *Chemical Physics Letters*, vol. 507, no. 1–3, pp. 122–127, 2011.
 - [4] Y. P. Du, Y. W. Zhang, L. D. Sun, and C. H. Yan, "Efficient energy transfer in monodisperse Eu-doped ZnO nanocrystals synthesized from metal acetylacetonates in high-boiling solvents," *Journal of Physical Chemistry C*, vol. 112, no. 32, pp. 12234–12241, 2008.
 - [5] M. M. Rahman, A. J. S. Ahammad, J. H. Jin, S. J. Ahn, and J. J. Lee, "A comprehensive review of glucose biosensors based on nanostructured metal-oxides," *Sensors*, vol. 10, no. 5, pp. 4855–4886, 2010.
 - [6] J. I. Sohn, S. S. Choi, S. M. Morris et al., "Novel nonvolatile memory with multibit storage based on a ZnO nanowire transistor," *Nano Letters*, vol. 10, no. 11, pp. 4316–4320, 2010.
 - [7] V. Chivukula, D. Ciplys, M. Shur, and P. Dutta, "ZnO nanoparticle surface acoustic wave UV sensor," *Applied Physics Letters*, vol. 96, no. 23, Article ID 233512, 2010.
 - [8] M. Quintana, T. Edvinsson, A. Hagfeldt, and G. Boschloo, "Comparison of dye-sensitized ZnO and TiO₂ solar cells: studies of charge transport and carrier lifetime," *Journal of Physical Chemistry C*, vol. 111, no. 2, pp. 1035–1041, 2007.
 - [9] M. H. Lai, A. Tubtintae, M. W. Lee, and G. J. Wang, "ZnO-nanorod dye-sensitized solar cells: new structure without a transparent conducting oxide layer," *International Journal of Photoenergy*, vol. 2012, Article ID 497095, 5 pages, 2012.
 - [10] M. M. Rahman, H. S. Son, S. S. Lim, K. H. Chung, and J. J. Lee, "Effect of the TiO₂ nanotubes in the photoelectrode on efficiency of dye-sensitized solar cell," *Journal of Electrochemical Science and Technology*, vol. 2, pp. 110–115, 2011.
 - [11] K. H. Chung, M. M. Rahman, H. S. Son, and J. J. Lee, "Development of well-aligned TiO₂ nanotube arrays to improve electron transport in dye-sensitized solar cells," *International Journal of Photoenergy*, vol. 2012, Article ID 215802, 6 pages, 2012.
 - [12] H. S. Uam, Y. S. Jung, Y. Jun, and K. J. Kim, "Relation of Ru(II) dye desorption from TiO₂ film during illumination with photocurrent decrease of dye-sensitized solar cells," *Journal of Photochemistry and Photobiology A*, vol. 212, no. 2–3, pp. 122–128, 2010.
 - [13] N. S. Pesika, K. J. Stebe, and P. C. Searson, "Relationship between absorbance spectra and particle size distributions for quantum-sized nanocrystals," *Journal of Physical Chemistry B*, vol. 107, no. 38, pp. 10412–10415, 2003.
 - [14] Y. S. Kim and C. H. Park, "Rich variety of defects in ZnO via an attractive interaction between O vacancies and Zn interstitials: origin of *n*-type doping," *Physical Review Letters*, vol. 102, no. 8, Article ID 086403, 2009.
 - [15] T. Tatsumi, M. Fujita, N. Kawamoto, M. Sasajima, and Y. Horikoshi, "Intrinsic defects in ZnO films grown by molecular beam epitaxy," *Japanese Journal of Applied Physics A*, vol. 43, no. 5, pp. 2602–2606, 2004.
 - [16] F. Wen, W. Li, J. H. Moon, and J. H. Kim, "Hydrothermal synthesis of ZnO:Zn with green emission at low temperature with reduction process," *Solid State Communications*, vol. 135, pp. 34–37, 2005.
 - [17] K. Vanheusden, W. L. Warren, C. H. Seager, D. R. Tallant, J. A. Voigt, and B. E. Gnade, "Mechanisms behind green photoluminescence in ZnO phosphor powders," *Journal of Applied Physics*, vol. 79, no. 10, pp. 7983–7990, 1996.
 - [18] B. K. Sharma, N. Khare, and D. Haranath, "Photoluminescence lifetime of Al-doped ZnO films in visible region," *Solid State Communications*, vol. 150, pp. 2341–2345, 2010.
 - [19] H. Park, W. R. Kim, H. T. Jeong, J. J. Lee, H. G. Kim, and W. Y. Choi, "Fabrication of dye-sensitized solar cells by transplanting highly ordered TiO₂ nanotube arrays," *Solar Energy Materials & Solar Cells*, vol. 95, pp. 184–189, 2011.
 - [20] A. Hagfeldt and M. Grätzel, "Light-induced redox reactions in nanocrystalline systems," *Chemical Reviews*, vol. 95, pp. 49–68, 1995.
 - [21] J. Moser, S. PUNCHIHEWA, P. P. Infelta, and M. Grätzel, "Surface complexation of colloidal semiconductors strongly enhances interfacial electron-transfer rates," *Langmuir*, vol. 7, no. 12, pp. 3012–3018, 1991.
 - [22] N. C. D. Nath, S. Sarker, A. J. S. Ahammad, and J. J. Lee, "Spatial arrangement of carbon nanotubes in TiO₂ photoelectrodes to enhance the efficiency of dye-sensitized solar cells," *Physical Chemistry Chemical Physics*, vol. 14, pp. 4333–4338, 2012.
 - [23] J. Bisquert, F. Fabregat-Santiago, I. Mora-Seró, G. Garcia-Belmonte, E. M. Barea, and E. Palomares, "A review of recent results on electrochemical determination of the density of electronic states of nanostructured metal-oxide semiconductors and organic hole conductors," *Inorganica Chimica Acta*, vol. 361, no. 3, pp. 684–698, 2008.
 - [24] J. B. Baxter and E. S. Aydil, "Nanowire-based dye-sensitized solar cells," *Applied Physics Letters*, vol. 86, no. 5, Article ID 053114, 2005.
 - [25] A. Umar, "Growth of comb-like ZnO nanostructures for Dye-sensitized solar cells applications," *Nanoscale Research Letters*, vol. 4, no. 9, pp. 1004–1008, 2009.
 - [26] J. J. Wu, G. R. Chen, H. H. Yang, C. H. Ku, and J. Y. Lai, "Effects of dye adsorption on the electron transport properties in ZnO nanowire dye-sensitized solar cells," *Applied Physics Letters*, vol. 90, no. 21, Article ID 213109, 2007.
 - [27] A. Pandikumar, K. M. Saranya, and R. Ramaraj, "Sheaf-like-ZnO Ag nanocomposite materials modified photoanode for low-cost metal-free organic dye-sensitized solid-state solar cells," *Applied Physics Letters*, vol. 101, no. 9, Article ID 093112, 2012.

Research Article

DFT Study of Binding and Electron Transfer from a Metal-Free Dye with Carboxyl, Hydroxyl, and Sulfonic Anchors to a Titanium Dioxide Nanocluster

Corneliu I. Oprea,¹ Petre Panait,¹ Jeanina Lungu,¹ Daniela Stamate,² Anca Dumbravă,² Fanica Cimpoesu,³ and Mihai A. Gîrțu¹

¹ Department of Physics, Ovidius University of Constanța, 900527 Constanța, Romania

² Department of Chemistry, Ovidius University of Constanța, 900527 Constanța, Romania

³ Department of Theoretical Chemistry, Institute of Physical Chemistry, 060021 Bucharest, Romania

Correspondence should be addressed to Mihai A. Gîrțu; girtu@univ-ovidius.ro

Received 14 February 2013; Accepted 9 April 2013

Academic Editor: Theodoros Dimopoulos

Copyright © 2013 Corneliu I. Oprea et al. This is an open access article distributed under the Creative Commons Attribution License, which permits unrestricted use, distribution, and reproduction in any medium, provided the original work is properly cited.

We report results of density functional theory (DFT) calculations of a metal-free dye, 5-(4-sulfophenylazo)salicylic acid disodium salt, known as Mordant Yellow 10 (MY-10), used as sensitizer for TiO₂ dye-sensitized solar cells (DSSCs). Given the need to better understand the behavior of the dyes adsorbed on the TiO₂ nanoparticle, we studied various single and double deprotonated forms of the dye bound to a TiO₂ cluster, taking advantage of the presence of the carboxyl, hydroxyl, and sulfonic groups as possible anchors. We discuss various binding configurations to the TiO₂ substrate and the charge transfer from the pigment to the oxide by means of DFT calculations. In agreement with other reports, we find that the carboxyl group tends to bind in bidentate bridging configurations. The salicylate uses both the carboxyl and hydroxyl substituent groups for either a tridentate binding to adjacent Ti(IV) ions or a bidentate Ti-O binding together with an O-H-O binding, due to the rotation of the carboxyl group out of the plane of the dye. The sulfonic group prefers a tridentate binding. We analyze the propensity for electron transfer of the various dyes and find that for MY-10, as a function of the anchor group, the DSSC performance decreases in the order hydroxyl + carboxyl > carboxyl > sulfonate.

1. Introduction

Dye-sensitized solar cells (DSSCs) have attracted considerable interest over the last years, as they offer the advantages of low fabrication costs, transparency, and flexibility, when desired [1]. For such reasons, DSSCs may constitute a choice for affordable low-power generation in urban areas and in particular a possibility of producing power generating windows [2, 3].

The working principle of the DSSCs is based on light absorption in a dye anchored on TiO₂ anatase nanoparticles, followed by transfer of the photoelectron from the dye to the wide bandgap semiconductor and through the transparent conducting oxide to the external load; at the counter electrode, the redox electrolyte facilitates the transport of the electron back to the dye and the regeneration of the sensitizer,

through reduction of the triiodide ion at the counter electrode, followed by oxidation of the iodide ion at the dye [1, 4]. The efficiency of the photovoltaic device depends strongly upon the dye and electrolyte used [5–7]. The highest efficiencies, of over 12%, have been obtained using metal complexes [8], and values above 9% have been obtained also with organic dyes [9–11].

An efficient solar cell sensitizer should demonstrate (i) strong adsorption to the semiconductor surface through anchoring groups, (ii) intense absorption in the visible part of the spectrum, (iii) proper energy level alignment of the excited state of the dye and the conduction band edge of the semiconductor, as well as the redox level of the electrolyte and the ground state of the dye, (iv) fast charge transfer from the dye to the substrate, with low loss of photoelectrons, and (v) electrochemical and thermal stability [1, 4, 12].

The anchoring modes of the dye to the TiO₂ surface are of crucial importance, the bonding type and the extent of electronic coupling between the dye excited state and the semiconductor unoccupied states influencing directly the overall cell performance [1, 4, 13]. Anchoring to TiO₂ has been achieved through a number of functional groups [14–16], such as carboxylic acid, sulfonic acid, phosphonic acid, acetylacetonate derivatives, and salicylate the most widely used and successful to date being the carboxylic acid [4]. Some derivatives of carboxylic acid, such as ester, acid chloride, acetic anhydride, carboxylate salt, amide, or silane have also been used as anchoring groups [4, 17].

The standard anchoring group for sensitizers is carboxylic acid (–COOH) [4, 11], as so far the best photovoltaic conversion efficiencies have been obtained with dyes bound to the substrate through carboxylic acid groups [5, 8]. The carboxylic acid groups, while ensuring efficient adsorption of the dye on the surface, also promote electronic coupling between the donor levels of the excited chromophore and the conduction band of the TiO₂ nanoparticles. Early experimental studies indicated various anchoring configurations, ranging from monodentate ester-like binding [18], bidentate bridging [19], or both bidentate chelate and bridging [20]. More sensitive experiments [21] showed that 63% of surface binding arises from ester formation, 34% from chelating and bridging, and 3% from anion and hydrogen bonding.

Efficient anchoring with phosphonic acid has been obtained for a ruthenium(II) complex with terpyridine [22], which allowed for a binding to TiO₂ stronger than the typical N3 dye [5] with carboxylic acid groups. The sulfonic group was used as anchor for several porphyrin- and phthalocyanine-based dyes [23] as well as for some polypyridyl complexes [24] but it has been systematically outperformed by the carboxyl group.

The salicylate has been reported in several studies [25, 26] regarding adsorption to TiO₂. A comparative study of the surface complexation of colloidal titanium dioxide by monodentate and bidentate benzene derivatives (benzoic acid, phthalic acid, isophthalic acid, terephthalic acid, salicylic acid, and catechol) [25] showed that there is a sharp acceleration of the electron transfer in the presence of the bidentate ligands salicylate and phthalate, whereas the monodentate complexant benzoate exhibits practically no effect.

Another interesting experimental study [27] introduced carboxyl, hydroxyl, and/or sulfonate anchoring groups onto the skeletons of some hemicyanine-based organic dyes. It was shown that the incident photon-to-current conversion efficiencies (IPCE) for the photoelectrodes and the overall photovoltaic conversion efficiencies of the DSSCs depended strongly on the anchoring group types and decreased in the order carboxyl + hydroxyl > carboxyl > sulfonate + hydroxyl [27].

The fast electron transfer in the case of bidentate salicylate ligand [25] and the higher performance of the dyes with both carboxyl and hydroxyl anchoring groups [27] has led us to revisit an earlier study [28] of a 5-(4-sulfophenylazo)salicylic acid disodium salt dye, known as Mordant Yellow 10 (MY-10). Based on a combined experimental and theoretical approach, we explained puzzling results regarding the correlation

between the pH of the solution and the photovoltaic conversion efficiency of the device. Despite the relatively low efficiency, initially attributed to the weak optical absorption in the visible range and the unoptimized fabrication procedures, MY-10 provides an interesting opportunity for the study of the role of dye deprotonation on the device efficiency as well as the influence of the energy difference between the excited state of the dye and the conduction band edge of the oxide on the short circuit current of the DSSC. More importantly, on the topic of adsorption to the substrate, MY-10 offers a chance to study the various ways of binding to the TiO₂ and compare, for that purpose, the –OH, –CO₂H, and –SO₃H groups.

Our approach is inspired by the early theoretical studies on dyes with –COOH anchors [29], which showed by means of density functional theory (DFT) calculations that the preferred binding configuration of the carboxyl group is bidentate bridging. More recently extended theoretical modeling [30] demonstrated that for the dyes bearing a carboxylic acid as anchoring group, the preferred adsorption mode is bidentate bridging, with one proton transferred to a nearby surface oxygen, while the monodentate anchoring is usually predicted to be less stable [31–33]. Moreover, DFT and time-dependent DFT (TD-DFT) methods allowed for the description not only of the absorption spectrum of the dye but also of the more complex system consisting of the dye, and the TiO₂ cluster. The bonding of the dye on the nanoparticle, the alignment of the energy levels of the two subsystems, and the transfer of the electron from the dye to the cluster have all been successfully calculated by means of a DFT approach [34, 35].

We report here results of DFT and TD-DFT calculations performed on complex systems consisting of the MY-10 dye and a TiO₂ nanocluster. Our present computational studies provide the electronic structure and the optical spectra of the dye-TiO₂ nanocluster system. We analyze various binding configurations of the dye to the cluster and discuss the energy level alignment with the semiconducting oxide and the electrolyte as well as the charge transfer from the pigment to the oxide. We compare our theoretical results with the experimental data available and explain the puzzling behavior of the short-circuit current.

2. Computational Details

The structures of all dyes were optimized in their various forms, including protonated and/or deprotonated correspondents, using the density functional theory (DFT) [36–38], with the B3LYP exchange-correlation functional [39, 40] and the 6-31G(d) basis set [41] for the free dyes or the less demanding 3-21G(d) basis set for the adsorbed dyes on the anatase cluster model. Vibrational analysis was performed at the same level of theory to check the stability of all optimized structures and to obtain the zero-point corrections to the total electronic energies.

The molecular orbitals and electronic transitions were calculated in solvent (water) employing the polarizable continuum model (PCM) [42, 43], by TD-DFT [44] using the same B3LYP functional. The cavity used in the PCM calculation was built from spheres centered on heavy nuclei,

based on the United Atom for Hartree-Fock procedure described in [42, 43]. The basis sets on the heavier atoms were augmented by diffuse functions via 6-31+G(d) [41] for better evaluation of electronic states of the free dyes. In the case of the dyes adsorbed on the cluster, the electronic states were accurately computed using the double- ζ quality DZVP basis sets including polarization functions for the valence electrons [45]. All calculations were performed with the GAUSSIAN03 package [46].

3. Results and Discussion

This section is divided in five parts. The first two subsections refer to the independent dye, dealing with the proton affinity and the electron transfer. The third subsection treats the TiO_2 nanocluster, whereas the last two deal with the more complex system consisting of the dye-oxide couple.

3.1. Dye Deprotonation. In a previous study [28] we reported extensive experimental and theoretical studies of DSSCs sensitized with Mordant Yellow 10, 5-(4-sulfophenylazo)salicylic acid disodium salt, $\text{C}_{13}\text{H}_8\text{N}_2\text{Na}_2\text{O}_6\text{S}$. The dye has the structural pattern of salicylic acid, having three functional groups: one of them ($-\text{SO}_3^-$) ensures its solubility in water and the others ($-\text{COO}^-$, $-\text{OH}$) act as chelating groups. MY-10 may also be viewed as the product of the double deprotonation of an organic acid, 5-(4-sulfophenylazo)salicylic acid, which for convenience will be labeled here as H_3ACY (acid chrome yellow). Consequently, we further label H_2ACY^- , HACY^{2-} , and ACY^{3-} , the various partially and fully deprotonated species.

One of the key factors required for an efficient operation of the DSSCs is the ability of the dye molecules to adsorb onto the semiconductor surface. This condition is uniquely fulfilled by H_3ACY , which offers the ground for comparing some of the most important anchoring groups: $-\text{COOH}$, $-\text{OH}$, and $-\text{SO}_3\text{H}$, all present in the same simple pigment. Upon adsorption of the dye on the substrate, the proton of the anchoring group is lost by the pigment. In order to identify the most probable deprotonation site, and thus which group is energetically favored to act as anchor, we computed the proton affinities of the dyes, in water solvent, as energy difference between the various deprotonated species and the protonated form.

The deprotonation of H_3ACY was performed at sites labeled as H1, H2, and H3 in Figure 1. Vibration analysis was performed on all optimized structures to ensure their stable character and to provide zero-point corrections to proton affinities. The results are presented in Table 1.

Based on the results shown in Table 1, the first proton to go is H1, the one that belongs to the $-\text{SO}_3\text{H}$ group. The energy required for the deprotonation increases for the hydroxyl group and even more so for the carboxyl group. However, the deprotonation at the H2 and H3 sites is almost as likely to occur, the difference in energy being very small.

Considering next the double deprotonation, we note that once the first proton is gone from the sulfonic group, the next proton that can leave the molecule is at the $-\text{OH}$ group. Again, the difference in energy being so small, it is almost as

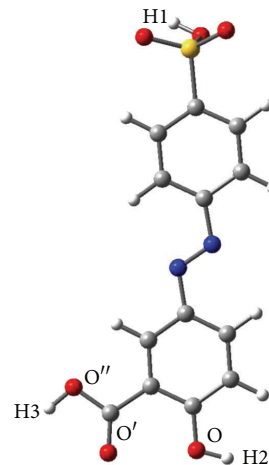


FIGURE 1: Optimized geometry of the dye, in its protonated form, as acid chrome yellow (H_3ACY), calculated at DFT/B3LYP/6-31G(d) level. The atom labeling is used in Table 1.

TABLE 1: Proton affinities (PA) of H_3ACY in water solution using the PCM approach [42, 43].

Dye (deprotonation site)	Energy (hartree)	Proton affinity (eV)
ACY^{3-} (missing all three: H1, H2, and H3)	-1459.0783688	36.97
H1-ACY^{2-} (missing H2 and H3)	-1459.5074405	25.29
H2-ACY^{2-} (missing H1 and H3)	-1459.5449373	24.27
H3-ACY^{2-} (missing H1 and H2)	-1459.5473253	24.21
H1H2-ACY^- (missing H3)	-1459.9751650	12.57
H1H3-ACY^- (missing H2)	-1459.9792599	12.45
H2H3-ACY^- (missing H1)	-1460.0061527	11.72
H_3ACY	-1460.4369320	—

likely for the proton to leave the $-\text{CO}_2\text{H}$ group. Unlikely is the deprotonation at the hydroxyl and carboxyl groups leaving the proton on the sulfonic group. Finally, the loss of all three protons comes at a higher price.

3.2. Electron Transfer for the Free Dye. Based on the experimental and theoretical results reported in our earlier paper [28], we exclude the case of ACY^{3-} , as it led to poor energy level alignment and small photovoltaic conversion efficiency. Also, the case of the fully protonated dye, H_3ACY , is not of real interest, as the binding to the substrate only through H-bonds is unlikely [15, 21] and unappealing. As we shall demonstrate in Section 3.4, the H-bonds may strengthen mechanically the anchoring to the substrate when other binding pathways exist. However, in the absence of π binding pathways, the presence of an intermediate H atom can harm the charge injection. It is the presence of conjugated bonds, allowing for π electron delocalization, that facilitates the electron transfer [47].

We assume that the energy level alignment is appropriate, allowing for the electron injection into the conduction

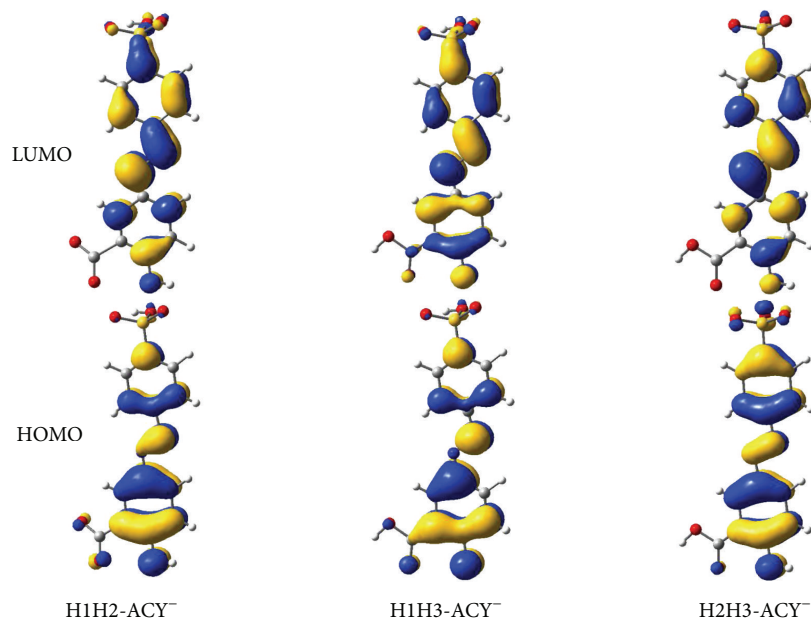


FIGURE 2: Isodensity surfaces ($0.03 e/\text{bohr}^3$) of the key molecular orbitals of the single deprotonated forms of the dye calculated at DFT/B3LYP/6-31+G(d) level in water.

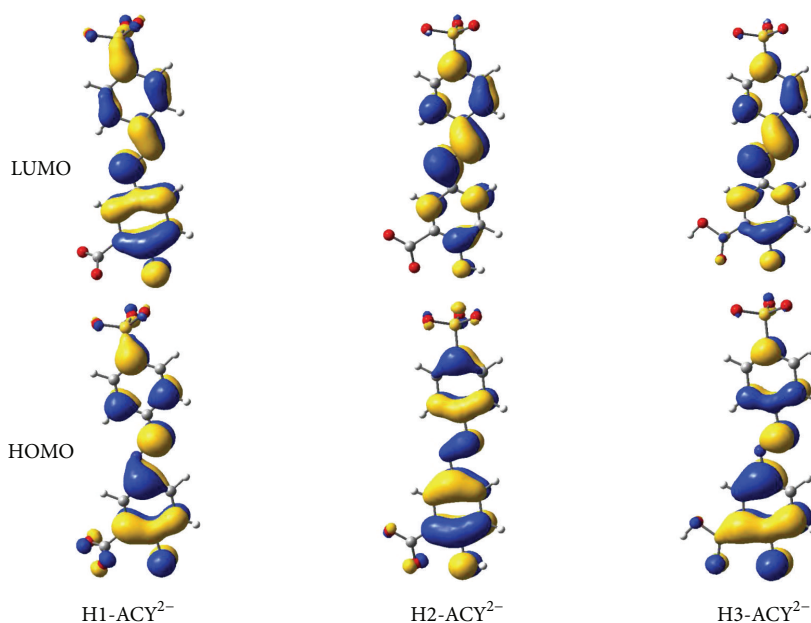


FIGURE 3: Isodensity surfaces ($0.03 e/\text{bohr}^3$) of the key molecular orbitals of the double deprotonated forms of the dye calculated at DFT/B3LYP/6-31+G(d) level in water.

band of the oxide, and the regeneration of the sensitizer is possible. This requirement is verified by the single and double deprotonated forms of the dye, as shown earlier for two particular cases [28]. To also explore the likelihood of the electron transfer processes, it is useful to also look at the electron densities of the highest occupied (HO) and lowest unoccupied (LU) molecular orbitals (MO) of the single and double deprotonated forms of the dye (see Figures 2 and 3, resp.). A quantitative measure of the propensity for electron

transfer of the dyes can be obtained by calculating the contribution to the electron density of each atom and adding these weights for three units, considered as donor, bridge, and acceptor. The three distinct units that we considered are benzenesulfonic acid, azo group, and salicylic acid. The values are reported in Table 2.

As it can be seen in Figures 2 and 3, the azo group plays an important role in the molecule as the nature of the bonding between the two nitrogen atoms correlates

TABLE 2: Contributions of various groups, in %, to the electron density of the HOMO and LUMO, calculated at DFT/B3LYP/6-31+G(d) level.

Dye	MO	BSA	-N=N-	SA
H2-ACY ²⁻ (missing H1 and H3)	HOMO	26.73	7.80	65.46
	LUMO	33.96	38.52	27.51
H1H2-ACY ⁻ (missing H3)	HOMO	37.75	7.84	54.41
	LUMO	52.70	19.93	27.37
H1-ACY ²⁻ (missing H2 and H3)	HOMO	49.81	6.72	43.47
	LUMO	46.20	7.20	46.60
H3-ACY ²⁻ (missing H1 and H2)	HOMO	49.80	6.72	43.48
	LUMO	48.43	11.27	40.30
H1H3-ACY ⁻ (missing H2)	HOMO	44.46	11.53	44.01
	LUMO	53.20	21.18	25.62
H2H3-ACY ⁻ (missing H1)	HOMO	38.24	11.49	50.27
	LUMO	38.42	38.08	23.49

BSA: benzenesulfonic acid, SA: salicylic acid.

well with the character of the entire molecular orbital. The HOMO is an π orbital and corresponds to an -N=N- double bond, whereas the LUMO is an π^* orbital, matching the antibonding between the nitrogen atoms.

The propensity for electron transfer of the dyes can be correlated with the variation in electron density following the photoexcitation of the dye from the ground to the excited state. The push-pull concept [11] expresses the tendency of a donating part of the dye to transfer an electron, through an π bridge, to an accepting unit.

In this context, looking at the values reported in Table 2, we note that for all forms of dye, the azo group has a higher electron density in the LUMO than in the HOMO. This increase comes from the decrease of electron density on the salicylic acid, with only one exception, H1-ACY²⁻, for which the variation is in case very small. Therefore, with one exception, when it is a very poor acceptor, the salicylic acid tends to act like an electron donor.

Looking carefully at the benzenesulfonic acid, we observe that it acts as a poor donor in the case of H1-ACY²⁻ and H3-ACY²⁻. More often it tends to be an acceptor, a poor one in the case of H2H3-ACY²⁻ and a much better one in the other instances, particularly for H1H2-ACY²⁻.

The electron transfer from the dye to the oxide also depends on the matrix element connecting the two states [48], which is correlated with the orbital overlap between the π^* orbital of the dye and the d orbitals of the Ti(IV) ion [49]. In turn, the overlap depends on the relative symmetry of the orbitals and on the electron density localized on the binding atoms [17]. Qualitatively, the electron density of the key atoms can be seen in Figures 2 and 3. However, for a more quantitative approach, we display in Table 3 the electron density on the key oxygen atoms from the -OH group, the -COOH group (the one situated closer to the hydroxyl group), and from the -SO₃H group (considered all together).

As it can be seen from Table 3, the electron density is consistently high on the oxygen atom of the -OH group for the HOMOs of all forms of dye. In the case of the LUMOs there are some significant variations between the various dye species, the electron density being slightly larger than for the

HOMO of H1-ACY²⁻ but significantly smaller in the rest. This result suggests that if the dye binds to the titania substrate through the oxygen of the -OH group, the higher electron transfer rate would occur in the case of the H1-ACY²⁻ dye.

The oxygen atom on the -COOH group has, consistently, a smaller electron density than the oxygen of the -OH group, for all the key MOs. These small values of the electron densities on the -COOH suggest that, if the binding was through that oxygen atom, the electron injection rate would be relatively low. The two cases for which the electron density is more significant are when the H3 proton is present, H3-ACY²⁻ and H1H3-ACY⁻, but even in these instances, the LUMOs have lower charge than the corresponding HOMOs. Therefore, if the dye binds to the titania substrate through the oxygen of the -COOH group, one would expect a relatively low transfer rate.

The electron density present on the three oxygen atoms of the sulfonic group is smaller or comparable to the one localized on the hydroxyl group. However, the charge is slightly larger in the LUMOs of the single deprotonated dyes that preserve the H1 proton: H1H2-ACY⁻ and H1H3-ACY⁻. The charge increases from HOMO to LUMO in the cases when the H1 proton is present, but in such cases, the binding to the titania cluster would be hindered. Hence, we are led to think that if the dye binds through the sulfonic group, the electron transfer rate would be relatively small.

To summarize the analysis of this section, none of the forms of the dye is optimized for the use in DSSCs, as the push-pull effects and the charge on the binding atoms are far from being competitive. However, these systems provide an interesting laboratory for the analysis of some of the key DSSC sensitizer design criteria. Taking each form of dye one by one, based on the limited information provided by Tables 2 and 3, we can speculate the following:

- (i) H1-ACY²⁻: there is a slight push-pull effect from the benzenesulfonic acid to the azo bridge and the salicylic acid, and the electron density on the peripheral oxygen atom is high. Binding through the oxygen of the -OH group might lead to a sizeable electron transfer;

TABLE 3: Contributions of the oxygen atoms (O from the –OH group, O' from the –COOH group, and all from the –SO₃H group, considered together), in %, to the electron density of the HOMO and LUMO, calculated at DFT/B3LYP/6-31+G(d) level.

Dye	MO	O (–OH)	O' (–COOH)	3 × O (–SO ₃ H)
H2-ACY ²⁻ (missing H1 and H3)	HOMO	9.48	0.99	1.82
	LUMO	1.99	0.02	1.67
H1H2-ACY ⁻ (missing H3)	HOMO	8.21	0.84	0.89
	LUMO	1.40	0.01	2.31
H1-ACY ²⁻ (missing H2 and H3)	HOMO	3.28	0.65	1.07
	LUMO	3.75	0.08	2.49
H3-ACY ²⁻ (missing H1 and H2)	HOMO	14.05	6.62	1.34
	LUMO	3.11	0.40	1.33
H1H3-ACY ⁻ (missing H2)	HOMO	8.86	1.37	1.22
	LUMO	3.20	0.47	3.52
H2H3-ACY ⁻ (missing H1)	HOMO	10.33	0.87	4.29
	LUMO	2.20	0.07	1.58

- (ii) H2-ACY²⁻: there is a clear push effect from the salicylic group, but the charge remains localized on the azo group, with a slight pull effect from the benzenesulfonic acid. Under these circumstances, the transfer through the carboxyl group is likely to be small due to both the reverse push-pull and the small electron density. The binding through the sulfonic group might be advantageous due to the push-pull and the charge density on the peripheral oxygen atoms but remains questionable due to the symmetry of the binding orbitals;
- (iii) H3-ACY²⁻: both acids push the charge to the azo bridge group located in the middle of the molecule. Binding through the oxygen of the hydroxyl seems more desirable;
- (iv) H2H3-ACY⁻: fairly similar to H3-ACY²⁻;
- (v) H1H2-ACY⁻: there is a significant push-pull effect from the salicylic acid to the benzenesulfonic acid. The binding through the oxygen atoms of the sulfonic group seems more likely to allow for charge transfer (provided that) but the H1 proton may hinder such binding;
- (vi) H1H3-ACY⁻: a case relatively similar to H1H2-ACY⁻.

3.3. Titania Nanocluster. TiO₂ anatase nanoparticles are modeled by a geometry optimized cluster with the molecular formula Ti₂₄O₅₀H₄, originating from the experimental structure of (101) surface, which is most common in the anatase form of TiO₂ [50]. To avoid the problem of the surface states in the gap, we performed geometry optimization of model clusters with a slight deviation from the TiO₂ stoichiometry and introduced four hydrogen atoms to terminate the dangling bonds at the periphery. This approach resulted in compact structures with 4-, 5-, and 6-fold coordinated Ti ions, together with 2- and 3-fold coordinated oxygen atoms.

Following the geometry optimization, the structure is slightly distorted (see Figure 4) to minimize the surface stresses. Other clusters of larger sizes have also been studied

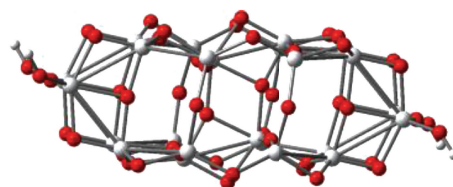


FIGURE 4: Lateral view of the optimized structures of the Ti₂₄O₅₀H₄ nanocluster modeling the anatase titania (101) surface. The geometry optimization was performed at DFT/B3LYP/3-21G(d) level.

[51] but when dealing with relatively small molecules, such as MY-10, the Ti₂₄O₅₀H₄ cluster provides a reasonable compromise between accuracy and computational costs. Larger clusters, such as (TiO₂)₈₂, might be more appropriate when dealing with larger dye molecules, particularly the typical ruthenium(II) complexes [52].

The average value of the Ti-O distance was 1.909 Å, smaller than the experimental value of 1.950 Å, valid for the bulk oxide. The distribution of these distances widens significantly compared to the bulk, with the standard deviation of the Ti-O distance being 0.133 Å for the cluster and 0.022 Å for the bulk. The deformation of the structure changes angles and distances such that the increase in the length of the cluster from 12.04 Å in the bulk to 12.12 Å in the cluster is opposite to the decrease in width, from 7.59 Å to 7.21 Å. The relative variation of the cluster distances compared to the values in the bulk, is less than 5%. We note that the values reported earlier [51] have slight deviations from those presented here, due to the different DFT functional and basis set used.

The geometry relaxation led to band gaps of 4.24 eV significantly larger than the experimental value of ~3.2 eV for anatase titania [1]. We modeled TiO₂ anatase nanoparticles by means of geometry-optimized clusters with molecular formulae Ti₂₄O₅₀H₄, Ti₃₄O₇₀H₄, and Ti₄₄O₉₀H₄. [51]. The resulting bandgaps were 4.24, 4.36, and 4.26 eV, respectively, sensitive to the DFT functional and basis sets used. The differences from the experimental value of the bulk are likely due to the size effects, demonstrated [53] for (TiO₂)_n (with n

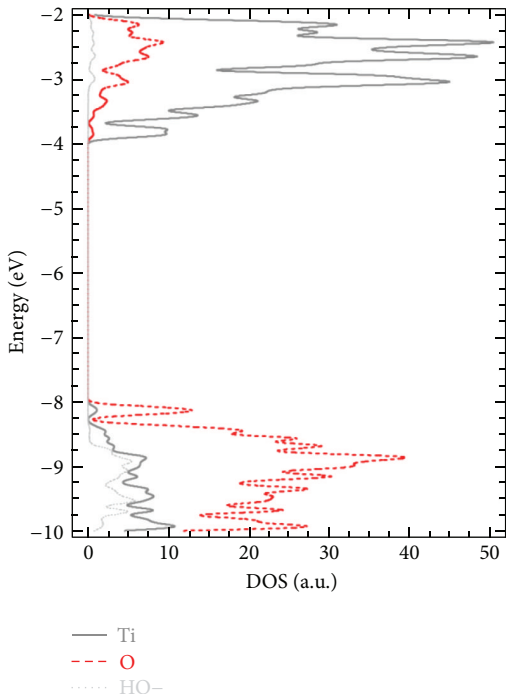


FIGURE 5: Density of states of the $\text{Ti}_{24}\text{O}_{50}\text{H}_4$ cluster calculated at DFT/B3LYP/DZVP level in water. The contributions of the orbitals to Ti and O atoms as well as to the $-\text{OH}$ groups are shown separately.

being between 1 and 68). Moreover, for $n < 60$, the bandgap has a nonmonotonous variation with n [53].

A quantity that crucially influences the performance of DSSCs is the position of the conduction band edge, which can be determined by DFT calculations, E_{CB} , or based on the energy of the electronic transition, as an oxidation potential [35], CBOP: -4.62 eV.

The nature of the states in the valence and conduction band can be more easily identified from Figure 4, which displays the density of states (DOS), and Figure 5, which illustrates the electron density of the key molecular orbitals. The valence band is dominated by the contributions from the O p orbitals, whereas the conduction band is dominated by the d orbitals of the Ti atoms. The introduction of the hydrogen atoms that end the four dangling bonds has a minor contribution to the key regions of the DOS (near the edges of the valence and particularly conduction bands) but plays an important role in removing any surface states from the gap.

The electronic structure of the $\text{Ti}_{24}\text{O}_{50}\text{H}_4$ cluster is shown in Figure 6. The highest occupied valence band (VB) state consists mostly of oxygen $2p$ atomic orbitals, whereas the lowest unoccupied state of the conduction band is formed by titanium $3d$ atomic orbitals.

3.4. Dye Adsorption: Binding Configurations. The anchoring modes of the dye to the TiO_2 surface are of crucial importance, the bonding type and the extent of electronic coupling between the dye excited state and the semiconductor unoccupied states influencing directly the overall cell performance

TABLE 4: Distances, in Å, and angles, in $^\circ$, relevant to the binding through the $-\text{COOH}$ group of the dye to the nanocluster. The geometry was optimized at DFT/B3LYP/3-21G(d) level.

	H2-ACY $^{2-}$	HIH2-ACY $^-$
$r(\text{Ti}-\text{O})$	1.949	1.980
$r(\text{Ti}-\text{O}')$	2.038	2.059
ψ	39.10	32.41
θ	13.14	8.82
φ	-4.31	-3.83

[1, 4, 30]. As discussed in the Introduction, a number of theoretical studies have approached the adsorption of the dye on the titania surface [5, 29–33, 51]. The calculations show that for the organic dyes bearing a carboxylic acid as anchoring group, the preferred adsorption mode is bidentate bridging, with one proton transferred to a nearby surface oxygen, while the monodentate anchoring is usually predicted to be less stable [52].

In contrast to the usual dyes, MY-10 provides an unusually rich ground for exploration of the various binding configurations, as it offers $-\text{SO}_3\text{H}$, $-\text{COOH}$, and $-\text{OH}$ anchoring groups. We start our analysis with the dyes anchored to the substrate in the familiar way, through the carboxyl group. The optimized geometries are shown in Figure 7 whereas the distances and angles relevant to the binding of the dye to the $\text{Ti}_{24}\text{O}_{50}\text{H}_4$ cluster are presented in Table 4.

In Table 4, the angle ψ was chosen between the dye axis (the direction joining the S atom and the C atom bound to the hydroxyl group) and the direction of the two binding Ti atoms. This way, the angle ψ is sensitive to the difference between the two bond lengths and correlates to the mechanical strength of the anchoring of the dye to the substrate. The angle θ is made by the plane of the dye with the direction of the Ti-O bond. Finally, the angle φ is measured between the plane of the dye and the direction defined by the two titanium ions bound to the dye. Both θ and φ angles affect the orbital overlap between the π^* of the dye and the d orbitals of the Ti(IV) ion, influencing the electron transfer.

The first thing to note for both the HIH2-ACY $^-$ and the H2-ACY $^{2-}$ dyes is the bidentate bridging binding configuration, in agreement with other reports, either experimental [14–21] or theoretical [29, 30] for dyes with carboxyl group anchors. It is worth mentioning that starting the optimization from other initial geometries (monodentate ester-like or bidentate chelating) eventually leads to the same bidentate bridging configuration.

The two Ti-O bond lengths are different by less than 5% for both dyes. The shorter distances suggest a stronger binding for H2-ACY $^{2-}$. The angle ψ is well correlated with the relative difference between the Ti-O distances, being larger for H2-ACY $^{2-}$. The small values for the θ and φ angles may suggest a weaker orbital overlap with the d_{z^2} and a stronger overlap with d_{xz} .

We continue our analysis with the dyes anchored to the substrate, through the hydroxyl group. The optimized geometries are displayed in Figure 8. The bond lengths and

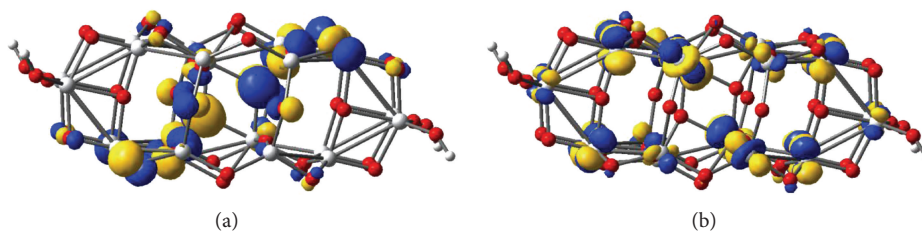


FIGURE 6: Isodensity surfaces ($0.03 \text{ e}/\text{bohr}^3$) of the key molecular orbitals of the $\text{Ti}_{24}\text{O}_{50}\text{H}_4$ cluster, calculated at DFT/B3LYP/DZVP level in water: (a) highest occupied valence band orbital, (b) lowest unoccupied conduction band orbital.

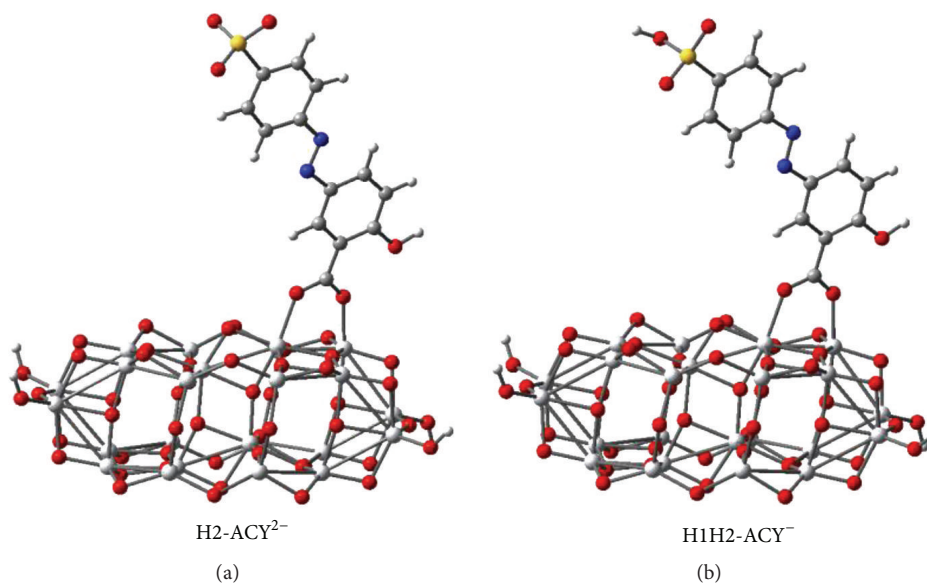


FIGURE 7: Optimized structure of complex dye-oxide systems with anchoring through the carboxyl group, calculated at DFT/B3LYP/3-21G(d) level.

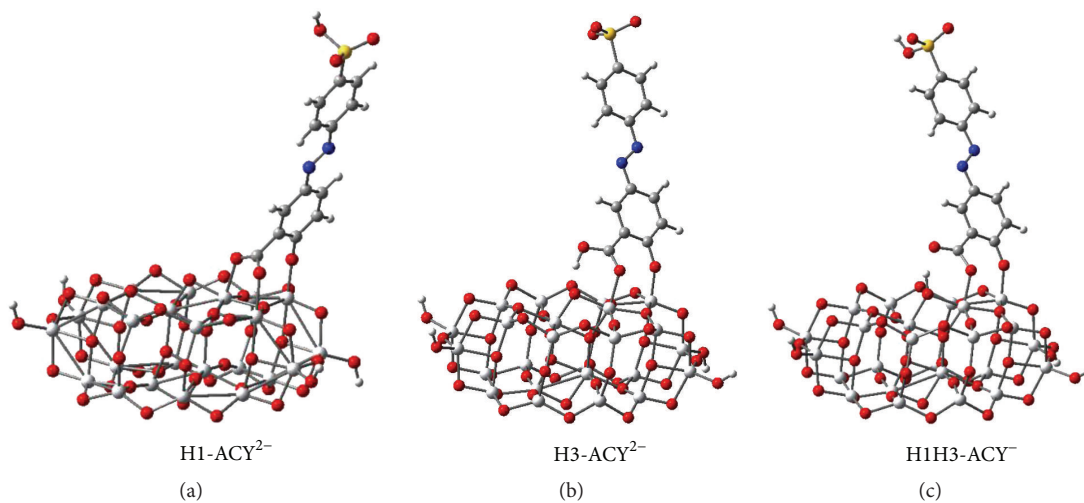


FIGURE 8: Optimized structure of complex dye-oxide systems with anchoring primarily through the hydroxyl group, calculated at DFT/B3LYP/3-21G(d) level.

TABLE 5: Distances, in Å, and angles, in °, relevant to the binding primarily through the -OH group of the dye to the nanocluster. O_D-H and $H-O_S$ refer to the distances between the H3 proton and the adjacent oxygen atom on the dye and on the substrate, respectively. The geometry was optimized at DFT/B3LYP/3-21G(d) level.

	H1-ACY ²⁻	H3-ACY ²⁻	HIH3-ACY ⁻
$r(\text{Ti}-\text{O})$	1.880	1.832	1.855
$r(\text{Ti}-\text{O}')$	2.063	2.020	1.932
$r(\text{Ti}-\text{O}'')$	2.029	—	—
$r(O_D-H)$	—	1.082	1.504
$r(H-O_S)$	—	1.462	1.060
ψ	89.54	95.17	92.49
θ	16.96	29.35	33.58
φ	28.12	11.53	10.45

angles relevant to the binding of the dye to the nanocluster are reported in Table 5.

We note that for all three dyes, binding through the oxygen of the hydroxyl group is accompanied by supplementary binding through the adjacent carboxyl group. Also, for all three dyes, the shortest bond length is the one to the oxygen of the hydroxyl group, revealing the strongest bond. Moreover, the lengths of the shortest Ti-O bonds are smaller in this case than in the previous case of binding through a carboxyl anchor.

The similarities stop here as for the H1-ACY²⁻ dye, the binding is tridentate, through both oxygen atoms of -COO⁻. In this case, the group twists away from the plane of the dye allowing the two oxygen atoms to bind to the neighboring Ti(IV) ions. The axis of the dye suffers a large inclination, ψ , within its plane, while the plane of the pigment is rotated with respect to the Ti-Ti direction leading to a large φ angle of 28.12°.

When the carboxyl group is protonated, the binding configuration remains bidentate, the difference arising from the supplementary hydrogen bond. In the case of H3-ACY²⁻ the proton remains bound in the carboxyl group, whereas for HIH3-ACY⁻, the situation is reversed, the proton binding to an oxygen atom from the substrate. The large differences between the O-H distances clearly show that in the latter case the proton leaves the dye and binds to the substrate. The value close to 90° of θ in the case of H1-ACY²⁻ suggests that that the dye is supported in a balanced way by its two pillars, the hydroxyl and the carboxyl groups. In the case of the other two dyes, H3-ACY²⁻ and HIH3-ACY⁻, the values in excess of 90° indicate that the axis is inclined due to shorter bond lengths with the oxygen of the hydroxyl group. Also, for these two pigments, the carboxyl group remains in the plane of the molecule, which suffers smaller deviations, φ , from the Ti-Ti direction.

The early work on surface complexation of colloidal titanium dioxide by various benzene derivatives [25, 26] suggested that the salicylate complex formed involves both substituent groups and leads to the formation of a six-atom ring with a chelating type of bonding to the same Ti(IV) ion (see Figure 9(a)). Our results confirm the involvement

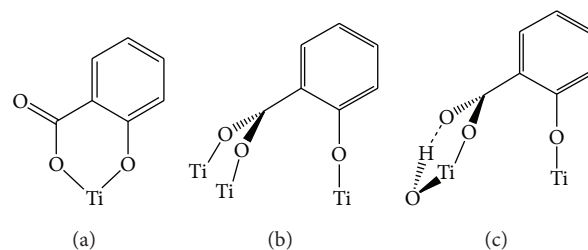


FIGURE 9: Binding schemes for the salicylate unit to the TiO₂ substrate.

of both substituent groups but clearly demonstrate that the main binding configuration is bridging, engaging at least two adjacent titanium ions (Figures 9(b) and 9(c)). Moreover, a third bond, either a covalent O-Ti bond or a hydrogen bond, strengthens mechanically the anchoring to the substrate.

We end our analysis of the optimized geometry of the sensitizers adsorbed to the substrate with H2H3-ACY⁻, for which the anchor is the sulfonic group. The optimized geometry is presented in Figure 10.

The geometry optimization of the complex system consisting of the H2H3-ACY⁻ sensitizer bound to the Ti₂₄O₅₀H₄ cluster through the sulfonic group indicates tridentate binding to three adjacent Ti(IV) ions. The bond lengths are different, 2.155, 2.167, and 2.152 Å, longer than the typical values obtained in the previous cases. The angle ψ is 83.21°, showing that the dye is not supported in a balanced way by its three pillars. The other angles are $\theta = 13.75^\circ$ and $\varphi = 6.26^\circ$, indicating a relatively small tilt of the plan of the dye with respect to the direction of the shortest Ti-O bond and also a fairly small rotation of that plan with respect to the Ti-Ti axis.

3.5. Electron Transfer for the Adsorbed Dye. In Section 3.2, we analyzed the propensity for charge transfer of the various free dyes. We return to the topic, this time treating the entire dye-substrate system. Following a similar procedure, we look at the key molecular orbitals, particularly at the one that corresponds to the excited state of the dye and the one that matches to the conduction band edge of the semiconductor.

As already mentioned, although the key information regarding the electron transfer rate may be provided by the matrix element connecting these two states [48], a simpler and still useful indication of the likelihood of the transfer may be offered by the overlap between the π^* orbital of the dye and the d orbitals of the Ti(IV) ion [49]. In turn, the overlap depends strongly on the electron density localized on the binding atoms. Qualitatively, the electron density of the key atoms can be seen in Figures 11 and 12, whereas some quantitative measures are reported in Tables 6 and 7, in the form of electron densities of the TiO₂ nanocluster, on the entire dye as well as on its main three parts (benzenesulfonic acid, azo group, and salicylic acid), and on the peripheral oxygen atoms bound to titanium. The actual overlaps between the key orbitals involved in the charge transfer are reported in Table 8.

The key molecular orbitals of H2-ACY²⁻ and HIH2-ACY⁻ are qualitatively similar in the sense that the HOMOs

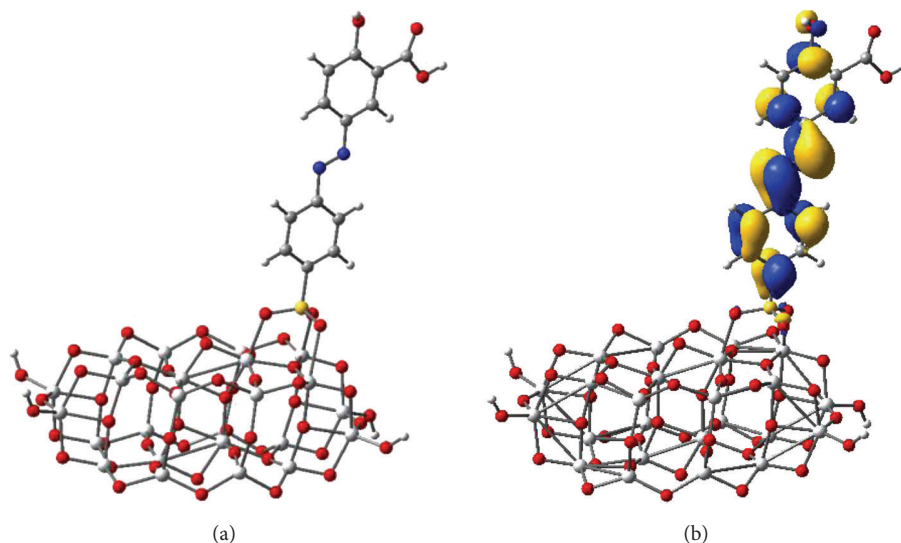


FIGURE 10: (a) Optimized structure of the H2H3-ACY⁻-oxide system, with anchoring through the sulfonic group, calculated at DFT/B3LYP/3-21G(d) level. (b) Isodensity surfaces (0.03 e/bohr³) of the MO corresponding to the excited state of the sensitizer key molecular orbitals of the H2H3-ACY⁻ dye adsorbed on the TiO₂ nanocluster calculated at DFT/B3LYP/DZVP level in water.

TABLE 6: Contributions of various groups, in %, to the electron density of the MO corresponding to the excited state of the sensitizer, calculated at DFT/B3LYP/DZVP level.

Dye	TiO ₂	Dye	BSA	-N=N-	SA	O'	O''	O
H2-ACY ²⁻	18.74	81.26	22.46	39.82	18.98	0.031	0.106	2.008
HIH2-ACY ⁻	9.23	90.77	28.65	39.98	22.14	0.025	0.118	2.772

BSA: benzenesulfonic acid, SA: salicylic acid.

and the LUMOs have π and d characters, respectively. Moreover, the HOMOs and LUMOs are strongly localized on the dye and on the substrate, respectively, whereas the MO corresponding to the excited state of the sensitizer has a mixed character, being delocalized also on the titania cluster.

When looking at the free H2-ACY²⁻ dye, we noticed a sizeable push effect from the salicylic group and a slight pull effect from the benzenesulfonic acid, with the charge localized on the azo group. In the case of the interacting sensitizer, binding through the carboxyl group, where the charge is negligible, leads to almost 19% delocalization of the electron over the substrate. The higher electron density on the oxygen of the hydroxyl group remains unused.

In the case of HIH2-ACY⁻, there is a significant change between the noninteracting and the interacting sensitizers. In the free case, we found a clear push-pull effect from the salicylic to the benzenesulfonic acid but when the dye is adsorbed on the substrate, the charge tends to localize more on the azo group, and about 9% leaks to the cluster. Similar to the previous case, the charge on the carboxyl group is negligible and the high density on the hydroxyl group substrate stays trapped.

We now move further to the dyes bound through the oxygen of the hydroxyl group. The HOMOs and the LUMOs have, as expected, π and d characters, respectively, and are strongly localized on the dye or on the substrate. The MO

TABLE 7: Contributions of various groups, in %, to the electron density of the HOMO and LUMO, calculated at DFT/B3LYP/DZVP level.

Dye	TiO ₂	Dye	BSA	-N=N-	SA	O'	O''	O
HI-ACY ²⁻	29.37	70.63	21.43	30.21	18.99	0.042	0.133	0.830
H3-ACY ²⁻	70.83	29.17	6.58	12.32	10.28	0.256	0.194	0.280
HIH3-ACY ⁻	79.42	20.58	5.05	7.70	7.83	0.084	0.521	0.211

BSA: benzenesulfonic acid, SA: salicylic acid.

corresponding to the excited state of the sensitizer has a mixed character, being delocalized also on the titania cluster.

In the case of HI-ACY²⁻, almost 30% of the electron density is distributed over the cluster, whereas the percentages are significantly larger, for both H3-ACY²⁻ and HIH3-ACY⁻, of more than 70% and 79%, respectively. The much larger charge distributed on the titania, reflecting the higher likelihood of charge transfer, may be correlated with the strong binding through both salicylate substituents. We note, as it can be seen from Figure 12, that the main pathway for charge transfer is through the oxygen atom of the hydroxyl group.

The free HI-ACY²⁻ dye showed a slight push-pull effect from the benzenesulfonic acid towards the azo bridge and the salicylic acid. Also, the electron density on the peripheral oxygen atom was high. The interacting dye tends, again, to accumulate more charge on the azo group but passes more of it to the substrate, by taking advantage of the higher orbital overlap.

In the case of the noninteracting H3-ACY²⁻ sensitizer, both acids push the charge to the azo bridge group located in the middle of the molecule, whereas the high electron density on the oxygen atom makes the binding through the corresponding hydroxyl more desirable. This tendency is preserved for the interacting sensitizer, whose electron density is

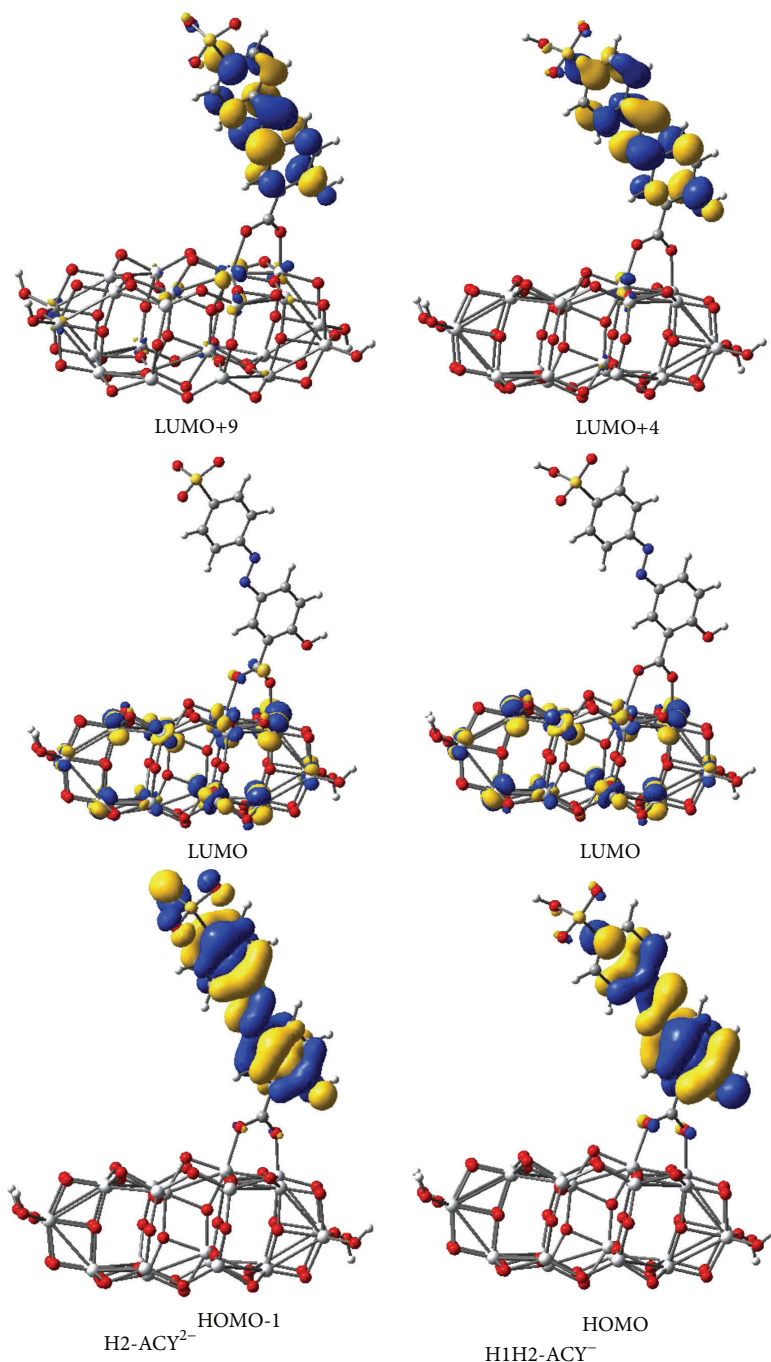


FIGURE 11: Isodensity surfaces ($0.03 e/\text{bohr}^3$) of the key molecular orbitals of the dyes adsorbed on the TiO_2 nanocluster calculated at DFT/B3LYP/DZVP level in water.

now more significantly pushed from the benzenesulfonic acid through the median azo group towards the salicylic group and the substrate.

The single deprotonated dye H1H3-ACY^{2-} displayed a clear push-pull effect from the salicylic to the benzenesulfonic acid, but when the pigment is adsorbed on the substrate the charge tends to transfer in the opposite direction towards the cluster.

We note for the last two dyes that the presence of the intermediate H atom does not create a significant pathway for charge injection, the H-bonding having a more important role in the mechanical adherence to the oxide.

The orbital overlap between the MOs corresponding to the excited state of the dye and the conduction band edge of the substrate is correlated, as expected, with the electron densities on the peripheral, contact atoms. The overlap is

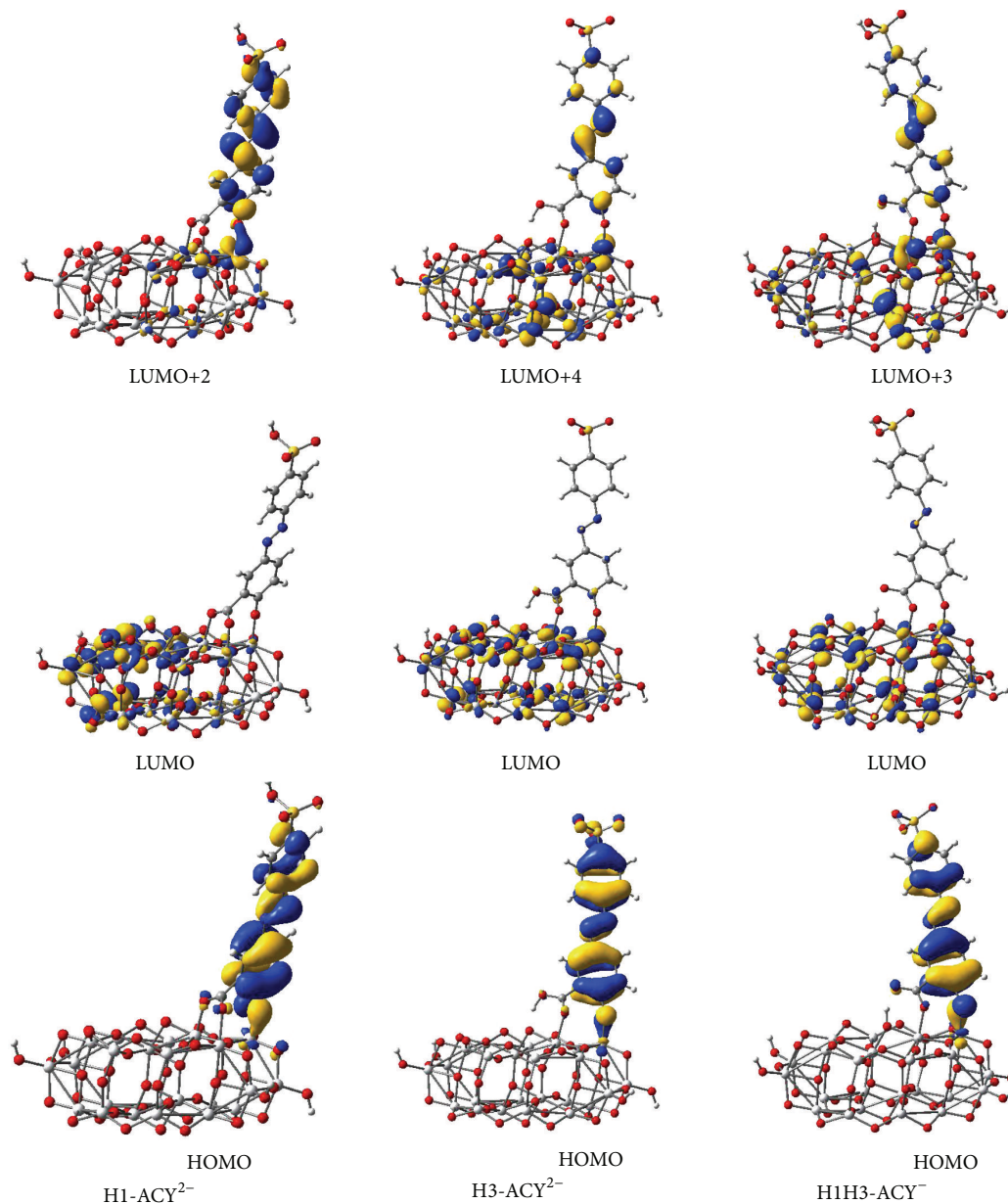


FIGURE 12: Isodensity surfaces ($0.03 e/\text{bohr}^3$) of the key molecular orbitals of the dyes adsorbed on the TiO_2 nanocluster calculated at DFT/B3LYP/DZVP level in water.

TABLE 8: Orbital overlap between the key molecular orbitals (the excited state of the dye and the conduction band edge of the substrate), calculated at DFT/B3LYP/DZVP level.

H2-ACY ²⁻	H1H2-ACY ⁻	H1-ACY ²⁻	H3-ACY ²⁻	H1H3-ACY ⁻	H2H3-ACY ⁻
0.0061	0.0097	0.0294	0.0199	0.0424	0.0042

very small for the cases of anchoring through the carboxyl group (H2-ACY²⁻ and H1H2-ACY⁻) and larger in the cases of binding through the hydroxyl group.

As early as 1979, Goodenough and coworkers suggested that the π^* orbitals of the dicarboxy-bipyridine ligand of the ruthenium(II) dye would promote rapid excited-state electron injection into the conduction band of TiO_2 but not that of SnO_2 or ZnO [49]. The reason originated in the difference

of symmetry, as the TiO_2 conduction band is comprised mainly of unfilled d orbitals where that of SnO_2 and ZnO possesses predominantly s -orbital character. The coupling would be optimal when the carboxyl group and the bipyridine are close to coplanarity. In fact, it was shown computationally that the planar geometry enhances the injection [54].

Our results, so far, have shown that the oxygen of the hydroxyl group offers, in the context of a salicylate, a good

electron transfer pathway, as it preserves the π^* nature of the dye MO. In contrast, in the case of the adhesion through the sulfonic group, the tetrahedral anchor does not preserve the planar symmetry of the dye. By twisting the lobes of the p orbitals of the oxygen atoms away from the plane of the dye, to insure the proper binding to the neighboring Ti(IV) ions, the electron transfer pathway is affected, likely causing the lower photovoltaic conversion performance of the actual devices [24]. Although the dyes studied are different from those reported by Chen et al. [27], our results are consistent with theirs in the sense that the DSSC performance depends strongly on the anchoring group types and likely decreases in the order hydroxyl + carboxyl > carboxyl > sulfonate.

4. Conclusions

The anchoring modes of the dye onto the TiO₂ surface are of crucial importance to the DSSC performance through the bonding type and the extent of electronic coupling between the dye excited state and the conduction band edge of the semiconductor. As most of the theoretical studies so far have focused on sensitizers with carboxyl groups as anchors, we took advantage of the opportunity offered by the protonated form of the Mordant Yellow 10 dye, which has a -OH, -CO₂H and -SO₃H groups, to perform a comparative study of the various anchors, binding configurations as well as propensity for electron transfer.

We studied the dye in various single and double deprotonated forms both free and anchored to a TiO₂ nanocluster in various binding configurations. First, we determined the proton affinity to identify the way the dye would tend to deprotonate. Then we studied the distribution of charge on the dye for the key MOs to analyze the intramolecular charge transfer, following a push-pull approach. We also determined the distribution of charge on the anchoring oxygen atoms to get an indication of the likelihood of the transfer to the substrate.

After optimizing the Ti₂₄O₅₀H₄ nanocluster, we studied the interacting dye-substrate system. The geometry optimization showed, in agreement with other reports, that the carboxyl group tends to bind in bidentate bridging configurations. The salicylate uses both the carboxyl and hydroxyl substituent groups to form either a tridentate binding to adjacent Ti(IV) ions or a bidentate Ti-O binding together with a O-H-O binding, due to the rotation out of the plane of the dye of the carboxyl group. The H-bonds strengthen mechanically the anchoring to the substrate when other binding pathways exist. However, in the absence of π binding pathways, the presence of an intermediate H atom can harm the charge injection. It is the presence of conjugated bonds, allowing for π electron delocalization, that facilitates the electron transfer. The sulfonic group prefers a tridentate binding.

To better understand the electron transfer process, we studied the distribution of charge on the cluster, on the entire sensitizer as well as on the various parts of the dye, and on the peripheral oxygen atoms. Inspired by the ideas of Goodenough and coworkers, we discussed the orbital overlap between the π^* orbital of the dye and the d orbitals of Ti(IV) ion. We showed that the oxygen of the hydroxyl group offers

in the context of a salicylate, a good electron transfer pathway, as it preserves the π^* nature of the dye MO. In contrast, in the case of the anchoring through the sulfonic group, the p orbitals of the oxygen atoms are moved away from the plane of the dye, to insure the proper binding to the neighboring metal ions, affecting the electron transfer pathway. Based on our computational results and analyses, we suggest that the DSSC performance decreases in the order hydroxyl + carboxyl > carboxyl > sulfonate.

Acknowledgments

The authors acknowledge the financial support from SNSF and UEFISCDI through the joint Grants RSRP IZERO-142144/1 and PN-II-Idei-RSRP-1/2012.

References

- [1] M. Grätzel, "Photoelectrochemical cells," *Nature*, vol. 414, no. 6861, pp. 338–344, 2001.
- [2] K. S. Ahn, S. J. Yoo, M. S. Kang, J. W. Lee, and Y. E. Sung, "Tandem dye-sensitized solar cell-powered electrochromic devices for the photovoltaic-powered smart window," *Journal of Power Sources*, vol. 168, no. 2, pp. 533–536, 2007.
- [3] R. Baetens, B. P. Jelle, and A. Gustavsen, "Properties, requirements and possibilities of smart windows for dynamic daylight and solar energy control in buildings: a state-of-the-art review," *Solar Energy Materials and Solar Cells*, vol. 94, no. 2, pp. 87–105, 2010.
- [4] A. Hagfeldt, G. Boschloo, L. Sun, L. Kloo, and H. Pettersson, "Dye-sensitized solar cells," *Chemical Reviews*, vol. 110, pp. 6595–6663, 2010.
- [5] M. K. Nazeeruddin, F. De Angelis, S. Fantacci et al., "Combined experimental and DFT-TDDFT computational study of photoelectrochemical cell ruthenium sensitizers," *Journal of the American Chemical Society*, vol. 127, no. 48, pp. 16835–16847, 2005.
- [6] L. M. Peter, "The Grätzel cell: where next?" *Journal of Physical Chemistry Letters*, vol. 2, no. 15, pp. 1861–1867, 2011.
- [7] B. E. Hardin, H. J. Snaith, and M. D. McGehee, "The renaissance of dye-sensitized solar cells," *Nature Photonics*, vol. 6, pp. 162–169, 2012.
- [8] A. Yella, H. W. Lee, H. N. Tsao et al., "Porphyrin-sensitized solar cells with cobalt (II/III)-based redox electrolyte exceed 12 percent efficiency," *Science*, vol. 334, pp. 629–634, 2011.
- [9] S. Ito, S. M. Zakeeruddin, R. Humphry-Baker et al., "High-efficiency organic-dye-sensitized solar cells controlled by nanocrystalline-TiO₂ electrode thickness," *Advanced Materials*, vol. 18, no. 9, pp. 1202–1205, 2006.
- [10] S. Hwang, J. H. Lee, C. Park et al., "A highly efficient organic sensitizer for dye-sensitized solar cells," *Chemical Communications*, no. 46, pp. 4887–4889, 2007.
- [11] A. Mishra, M. K. R. Fischer, and P. Büuerle, "Metal-Free organic dyes for dye-sensitized solar cells: from structure: property relationships to design rules," *Angewandte Chemie International Edition*, vol. 48, no. 14, pp. 2474–2499, 2009.
- [12] T. W. Hamann, R. A. Jensen, A. B. F. Martinson, H. Van Ryswyk, and J. T. Hupp, "Advancing beyond current generation dye-sensitized solar cells," *Energy and Environmental Science*, vol. 1, no. 1, pp. 66–78, 2008.

- [13] J. Lungu, C. I. Oprea, A. Dumbrava et al., "Heterocyclic azodyes as pigments for dye sensitized solar cells—a combined experimental and theoretical study," *Journal of Optoelectronics and Advanced Materials*, vol. 12, no. 9, pp. 1969–1975, 2010.
- [14] K. Kalyanasundaram and M. Grätzel, "Applications of functionalized transition metal complexes in photonic and optoelectronic devices," *Coordination Chemistry Reviews*, vol. 177, no. 1, pp. 347–414, 1998.
- [15] W. M. Campbell, A. K. Burrell, D. L. Officer, and K. W. Jolley, "Porphyrins as light harvesters in the dye-sensitized TiO₂ solar cell," *Coordination Chemistry Reviews*, vol. 248, no. 13-14, pp. 1363–1379, 2004.
- [16] E. Galoppini, "Linkers for anchoring sensitizers to semiconductor nanoparticles," *Coordination Chemistry Reviews*, vol. 248, no. 13-14, pp. 1283–1297, 2004.
- [17] S. Ardo and G. J. Meyer, "Photodriven heterogeneous charge transfer with transition-metal compounds anchored to TiO₂ semiconductor surfaces," *Chemical Society Reviews*, vol. 38, no. 1, pp. 115–164, 2009.
- [18] P. Falaras, "Synergetic effect of carboxylic acid functional groups and fractal surface characteristics for efficient dye sensitization of titanium oxide," *Solar Energy Materials and Solar Cells*, vol. 53, no. 1-2, pp. 163–175, 1998.
- [19] N. W. Duffy, K. D. Dobson, K. C. Gordon, B. H. Robinson, and A. J. McQuillan, "In situ infrared spectroscopic analysis of the adsorption of ruthenium(II) bipyridyl dicarboxylic acid photosensitizers to TiO₂ in aqueous solutions," *Chemical Physics Letters*, vol. 266, no. 5-6, pp. 451–455, 1997.
- [20] T. Ma, K. Inoue, K. Yao et al., "Photoelectrochemical properties of TiO₂ electrodes sensitized by porphyrin derivatives with different numbers of carboxyl groups," *Journal of Electroanalytical Chemistry*, vol. 537, no. 1-2, pp. 31–38, 2002.
- [21] Y. X. Weng, L. Li, Y. Liu, L. Wang, and G. Z. Yang, "Surface-binding forms of carboxylic groups on nanoparticulate TiO₂ surface studied by the interface-sensitive transient triplet-state molecular probe," *Journal of Physical Chemistry B*, vol. 107, no. 18, pp. 4356–4363, 2003.
- [22] P. Péchy, F. P. Rotzinger, M. K. Nazeeruddin et al., "Preparation of phosphonated polypyridyl ligands to anchor transition-metal complexes on oxide surfaces: application for the conversion of light to electricity with nanocrystalline TiO₂ films," *Journal of the Chemical Society, Chemical Communications*, no. 1, pp. 65–66, 1995.
- [23] H. Deng, Y. Zhou, H. Mao, and Z. Lu, "The mixed effect of phthalocyanine and porphyrin on the photoelectric conversion of a nanostructured TiO₂ electrode," *Synthetic Metals*, vol. 92, no. 3, pp. 269–274, 1998.
- [24] O. Schwarz, D. Van Loyen, S. Jockusch, N. J. Turro, and H. Dürr, "Preparation and application of new ruthenium(II) polypyridyl complexes as sensitizers for nanocrystalline TiO₂," *Journal of Photochemistry and Photobiology A*, vol. 132, no. 1-2, pp. 91–98, 2000.
- [25] J. Moser, S. PUNCHIHewa, P. P. Infelta, and M. Grätzel, "Surface complexation of colloidal semiconductors strongly enhances interfacial electron-transfer rates," *Langmuir*, vol. 7, no. 12, pp. 3012–3018, 1991.
- [26] S. Tunesi and M. A. Anderson, "Surface effects in photochemistry: an in situ cylindrical internal reflection-Fourier transform infrared investigation of the effect of ring substituents on chemisorption onto TiO₂ ceramic membranes," *Langmuir*, vol. 8, no. 2, pp. 487–495, 1992.
- [27] Y. S. Chen, C. Li, Z. H. Zeng, W. B. Wang, X. S. Wang, and B. W. Zhang, "Efficient electron injection due to a special adsorbing group's combination of carboxyl and hydroxyl: dye-sensitized solar cells based on new hemicyanine dyes," *Journal of Materials Chemistry*, vol. 15, no. 16, pp. 1654–1661, 2005.
- [28] C. I. Oprea, A. Dumbrava, I. Enache et al., "Role of energy level alignment in solar cells sensitized with a metal-free organic dye: a combined experimental and theoretical approach," *Physica Status Solidi A*, vol. 208, pp. 2467–2477, 2011.
- [29] A. Vittadini, A. Selloni, F. P. Rotzinger, and M. Grätzel, "Formic acid adsorption on dry and hydrated TiO₂ anatase (101) surfaces by DFT calculations," *Journal of Physical Chemistry B*, vol. 104, no. 6, pp. 1300–1306, 2000.
- [30] M. Pastore and F. De Angelis, "Computational modelling of TiO₂ surfaces sensitized by organic dyes with different anchoring groups: adsorption modes, structure and implication for electron injection/recombination," *Physical Chemistry Chemical Physics*, vol. 14, pp. 920–928, 2012.
- [31] K. Srinivas, K. Yesudas, K. Bhanuprakash, V. J. Rao, and L. Giribabu, "A combined experimental and computational investigation of anthracene based sensitizers for DSSC: comparison of cyanoacrylic and malonic acid electron withdrawing groups binding onto the TiO₂ anatase (101) surface," *Journal of Physical Chemistry C*, vol. 113, no. 46, pp. 20117–20126, 2009.
- [32] C. Férez León, L. Kador, B. Peng, and M. Thelakkat, "Characterization of the adsorption of Ru-bpy dyes on mesoporous TiO₂ films with UV-Vis, Raman, and FTIR spectroscopies," *Journal of Physical Chemistry B*, vol. 110, no. 17, pp. 8723–8730, 2006.
- [33] N. Martsinovich and A. Troisi, "High-throughput computational screening of chromophores for dye-sensitized solar cells," *The Journal of Physical Chemistry C*, vol. 115, pp. 11781–11792, 2011.
- [34] S. J. Moon, J. H. Yum, R. Humphry-Baker et al., "Highly efficient organic sensitizers for solid-state dye-sensitized solar cells," *Journal of Physical Chemistry C*, vol. 113, no. 38, pp. 16816–16820, 2009.
- [35] F. De Angelis, S. Fantacci, and A. Selloni, "Alignment of the dye's molecular levels with the TiO₂ band edges in dye-sensitized solar cells: a DFT-TDDFT study," *Nanotechnology*, vol. 19, no. 42, Article ID 424002, 2008.
- [36] P. Hohenberg and W. Kohn, "Inhomogeneous electron gas," *Physical Review*, vol. 136, pp. B864–B871, 1964.
- [37] W. Kohn and L. J. Sham, "Self-consistent equations including exchange and correlation effects," *Physical Review*, vol. 140, pp. A1133–A1138, 1965.
- [38] R. G. Parr and W. Yang, *Density-Functional Theory of Atoms and Molecules*, Oxford University Press, New York, NY, USA, 1989.
- [39] A. D. Becke, "Density-functional thermochemistry. III. The role of exact exchange," *The Journal of Chemical Physics*, vol. 98, no. 7, pp. 5648–5652, 1993.
- [40] C. Lee, W. Yang, and R. G. Parr, "Development of the Colle-Salvetti correlation-energy formula into a functional of the electron density," *Physical Review B*, vol. 37, no. 2, pp. 785–789, 1988.
- [41] V. A. Rassolov, M. A. Ratner, J. A. Pople, P. C. Redfern, and L. A. Curtiss, "6-31G* basis set for third-row atoms," *Journal of Computational Chemistry*, vol. 22, no. 9, pp. 976–984, 2001.
- [42] V. Barone and M. Cossi, "Quantum calculation of molecular energies and energy gradients in solution by a conductor solvent model," *The Journal of Physical Chemistry A*, vol. 102, pp. 1995–2001, 1998.

- [43] J. Tomasi, B. Mennucci, and R. Cammi, "Quantum mechanical continuum solvation models," *Chemical Reviews*, vol. 105, pp. 2999–3093, 2005.
- [44] M. E. Casida, C. Jamorski, K. C. Casida, and D. R. Salahub, "Molecular excitation energies to high-lying bound states from time-dependent density-functional response theory: characterization and correction of the time-dependent local density approximation ionization threshold" *Journal of Chemical Physics*, vol. 108, no. 11, pp. 4439–4449, 1998.
- [45] N. Godbout, D. R. Salahub, J. Andzelm, and E. Wimmer, "Optimization of Gaussian-type basis sets for local spin density functional calculations. Part I. Boron through neon, optimization technique and validation," *Canadian Journal of Chemistry*, vol. 70, no. 2, pp. 560–571, 1992.
- [46] M. J. Frisch, G. W. Trucks, H. B. Schlegel et al., *Gaussian 03, Revision C.02*, Gaussian Inc., Wallingford, Conn, USA, 2004.
- [47] F. De Angelis, "Direct vs. indirect injection mechanisms in perylene dye-sensitized solar cells: a DFT/TDDFT investigation," *Chemical Physics Letters*, vol. 493, no. 4-6, pp. 323–327, 2010.
- [48] D. Matthews, P. Infelta, and M. Grätzel, "Calculation of the photocurrent-potential characteristic for regenerative, sensitized semiconductor electrodes," *Solar Energy Materials and Solar Cells*, vol. 44, no. 2, pp. 119–155, 1996.
- [49] S. Anderson, E. C. Constable, M. P. Dare-Edwards et al., "Chemical modification of a titanium (IV) oxide electrode to give stable dye sensitisation without a supersensitiser," *Nature*, vol. 280, no. 5723, pp. 571–573, 1979.
- [50] A. Selloni, "Crystal growth: anatase shows its reactive side," *Nature Materials*, vol. 7, no. 8, pp. 613–615, 2008.
- [51] C. I. Oprea, P. Panait, F. Cimpoesu, M. Ferbinteanu, and M. A. Girtu, "Density functional theory (DFT) study of coumarin-based dyes adsorbed on TiO₂ nanoclusters—applications to dye-sensitized solar cells," *Materials*, 2013.
- [52] F. De Angelis, S. Fantacci, A. Selloni, M. K. Nazeeruddin, and M. Grätzel, "First-principles modeling of the adsorption geometry and electronic structure of Ru(II) dyes on extended TiO₂ substrates for dye-sensitized solar cell applications," *Journal of Physical Chemistry C*, vol. 114, no. 13, pp. 6054–6061, 2010.
- [53] M. J. Lundqvist, M. Nilsing, P. Persson, and S. Lunell, "DFT study of bare and dye-sensitized TiO₂ clusters and nanocrystals," *International Journal of Quantum Chemistry*, vol. 106, no. 15, pp. 3214–3234, 2006.
- [54] P. Persson, S. Lunell, and L. Ojamäe, "Electronic interactions between aromatic adsorbates and metal oxide substrates calculated from first principles," *Chemical Physics Letters*, vol. 364, no. 5-6, pp. 469–474, 2002.

Research Article

Theoretical Study of Copper Complexes: Molecular Structure, Properties, and Its Application to Solar Cells

Jesus Baldenebro-Lopez,^{1,2} Norma Flores-Holguin,¹ Jose Castorena-Gonzalez,² Jorge Almaral-Sanchez,² and Daniel Glossman-Mitnik¹

¹ NANOCOSMOS Virtual Lab, Centro de Investigación en Materiales Avanzados, S.C., Miguel de Cervantes 120, Complejo Industrial Chihuahua, 31190 Chihuahua, CHIH, Mexico

² Facultad de Ingeniería Mochis, Universidad Autónoma de Sinaloa, Prol. Ángel Flores y Fuente de Poseidón, S.N., 81223 Los Mochis, SIN, Mexico

Correspondence should be addressed to Daniel Glossman-Mitnik; daniel.glossman@cimav.edu.mx

Received 13 October 2012; Revised 26 January 2013; Accepted 3 February 2013

Academic Editor: Theodoros Dimopoulos

Copyright © 2013 Jesus Baldenebro-Lopez et al. This is an open access article distributed under the Creative Commons Attribution License, which permits unrestricted use, distribution, and reproduction in any medium, provided the original work is properly cited.

We present a theoretical investigation of copper complexes with potential applications as sensitizers for solar cells. The density functional theory (DFT) and time-dependent DFT were utilized, using the M06 hybrid meta-GGA functional with the LANL2DZ (D95V on first row) and DZVP basis sets. This level of calculation was used to find the optimized molecular structure, the absorption spectra, the molecular orbitals energies, and the chemical reactivity parameters that arise from conceptual DFT. Solvent effects have been taken into account by an implicit approach, namely, the polarizable continuum model (PCM), using the nonequilibrium version of the IEF-PCM model.

1. Introduction

A survey of our energy supply options reveals that the sun is the only clean energy source in sufficiently abundant supply to meet global demand, yet less than 0.1% of our energy needs are met through the direct conversion of sunlight [1]. For this reason, considerable attention and extensive research efforts have been devoted over the last years to dye-sensitized solar cells (DSSCs) as valuable and low-cost alternatives to silicon and other inorganic semiconductor-based photovoltaic devices [2–4]. The DSSC devices are composed of a nanocrystalline TiO₂ film adsorbed by organic or inorganic dyes as the sensitizer. When the dye molecule is excited by the absorption of sunlight, an electron is readily injected into the conduction band of TiO₂. The electron is then transported to the external circuit, and the dye molecule is regenerated by redox reaction coupled to ion pair in electrolyte [5].

One of the key components of a DSSC is the sensitizer [6], which is responsible for light absorption and the generation of electric charges [7], thus exerting a significant

influence on the power conversion efficiency (η) [8]. The most common sensitizers are Ru(II) complexes based on 2,2'-bipyridine (bpy) ligands, such as cis-di(thiocyanato) bis(bpy-4,4'-dicarboxylate)ruthenium(II) (N3 [9] and N719 [10]). These complexes have reached over 11% power conversion efficiency [11]; but the rarity and high cost of the Ru may limit their practical usage. Alonso-Vante and coworkers [12] discovered that copper(I) complexes have similar photophysical properties with Ru complexes, indicating that the iterative chemical optimization of common metal complexes sensitizers can be comparable to that of Ru complexes [13]. Copper(I) complexes display a wide variety of excited states and especially photophysical and photochemical processes; particularly, copper(I)-polypyridine complexes exhibit low-lying MLCT transitions that can participate, among others, in electron transfer processes [14]. Copper-based dye sensitizers might be good substitutes to meet the requirements for next-generation DSSC devices. However, only a few studies have reported work on DSSCs coupled with copper-based dye sensitizers [15–18]. In this research, we propose the study of five molecular systems of the type [CuL₂]⁺ with bipyridine

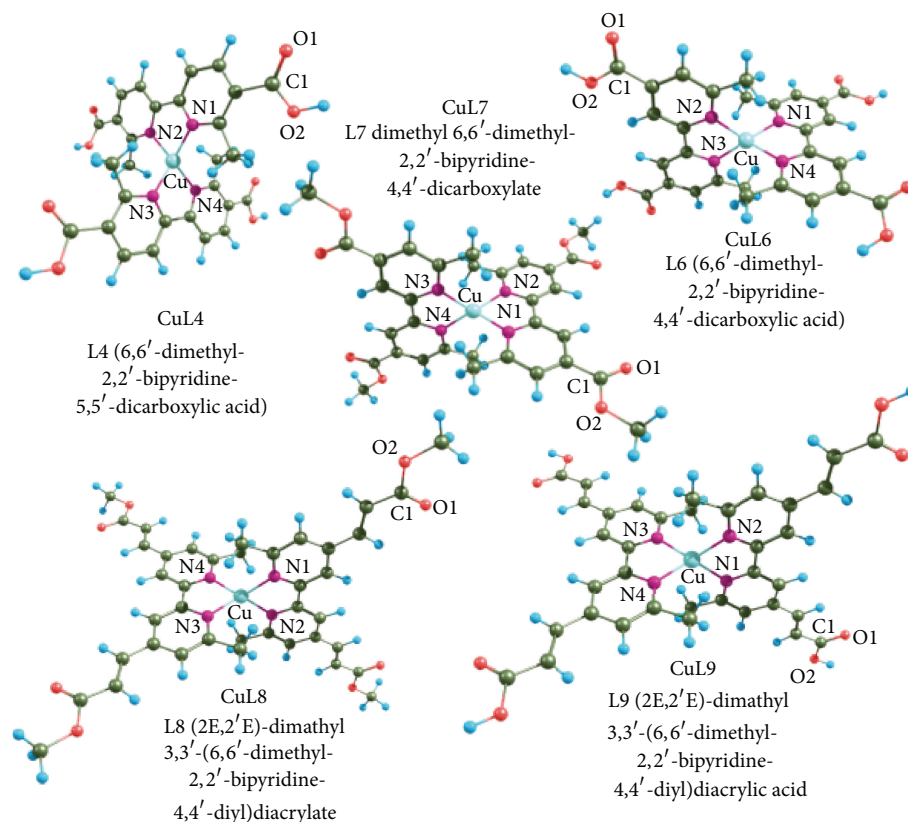


FIGURE 1: Optimized molecular structures of copper complexes in solution at the M06/LANL2DZ + DZVP level of theory.

ligands; in order to calculate from the theoretical point of view their geometric and spectroscopic properties, as well as chemical reactivity.

2. Molecular Modeling

Molecular calculations were carried out with density functional theory (DFT) [19–21] and time-dependent (TD) DFT [22–24] in the Gaussian09 program [25]. The hybrid-meta-GGA functional considered in this study is the M06 [26] due to the ability to study properties of organometallic compounds; our group has done a preliminary study [27]. The LANL2DZ (D95V on first row) for C, H, O, and N atoms [28] and DZVP for Cu atom [29] basis sets were used for the geometrical optimizations, as well as electrical and optical properties of all of the copper-based dye sensitizers considered, both in the gas phase and in solution. Ultraviolet-visible spectra (UV-Vis) have been simulated using the TD-DFT approach and analyzed through the SWizard program [30, 31], through pseudo-Voigt band shape with relative weight of Gaussian functions; solvent effects have been taken into account by an implicit approach, namely, the polarizable continuum model (PCM) [32] using the nonequilibrium version of the IEF-PCM model [33]; the equations were solved for 20 excited states.

Using the DFT framework makes it possible to find the chemical reactivity descriptors values, such as electron affinity (A), ionization potential (I), electronegativity (χ), hardness (η), and electrophilic index (ω); all these values were obtained using system energy calculations. The electronegativity, hardness, and electrophilic index are defined as

$$\chi = -\frac{(I + A)}{2},$$

$$\eta = \frac{(I - A)}{2}, \quad (1)$$

$$\omega = \frac{\mu^2}{2\eta},$$

where μ denotes the chemical potential and is calculated as $-\chi$.

3. Results and Discussion

Optimized molecular structures of copper complexes in the presence of solvent are shown in Figure 1. A selection of geometric parameters of these five molecules is listed in Table 1 (for more details, see supplementary material available online at <http://dx.doi.org/10.1155/2013/613064>). The molecular structures in gas phase and in solution are

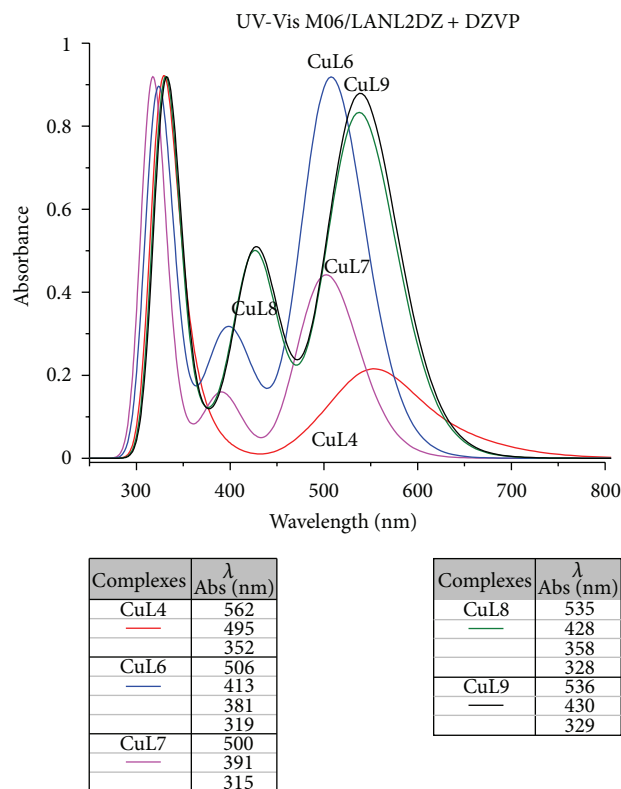


FIGURE 2: Ultraviolet-visible (UV-Vis) spectra of copper complexes analyzed in this study.

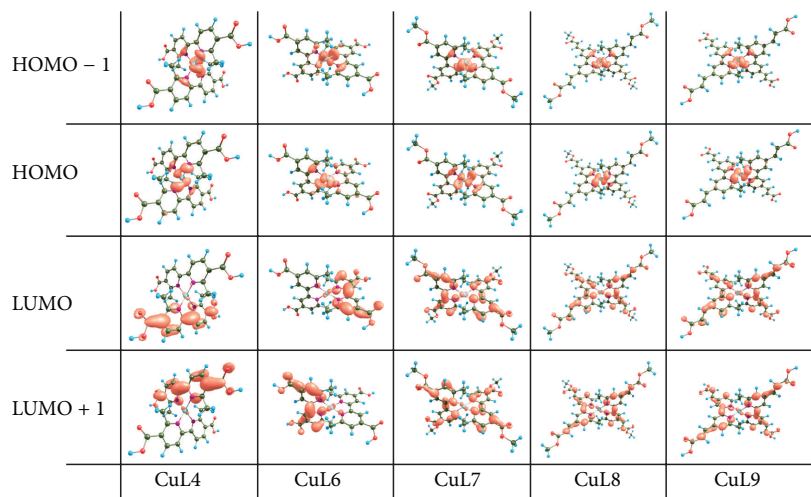


FIGURE 3: Molecular orbitals for Cu complexes calculated at the M06/LANL2DZ + DZVP level of theory.

qualitatively similar; however, the greatest change is observed in bond angles and dihedral angles. The 5,5' position of the carboxylic acid on the bipyridine ligands for CuL4 copper complex favors the increase of distance between the copper atom and the nitrogen atoms with respect to 4,4' positions of the other complexes, because of the position of the acceptor. Substitution of the carboxylic acid with methyl ester groups do not change radically the distance of the metal center to the ligand.

Absorption spectra for the proposed copper complexes are shown in Figure 2. These spectra were performed in the presence of solvent, under the same optimization conditions. The calculated value of the absorption wavelength (λ) is an important parameter, which indicates that these molecular systems should be considered for use as a functional material (as dye in this case) in a DSSC, the value of this parameter meets the requirement of the absorption property whose wavelength of maximum absorption (λ_{\max}) should not be

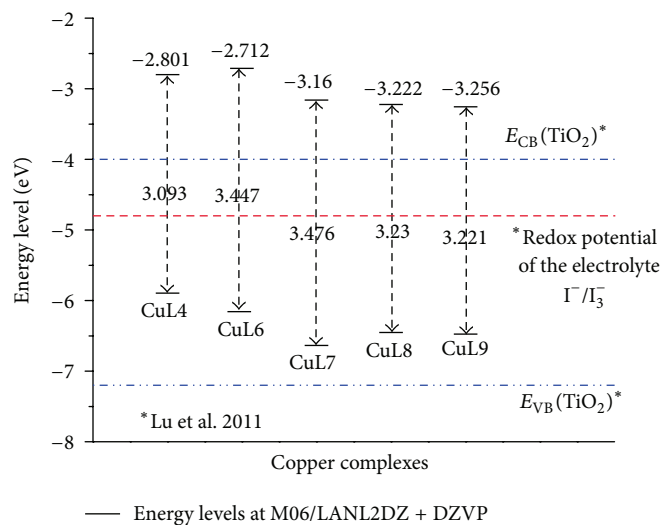


FIGURE 4: Molecular orbitals energy levels diagram.

greater than 920 nm as established in the literature [34]. All studied sensitizers reach their λ_{\max} above 500 nm, the largest value corresponds to the CuL4 sensitizer with 562 nm.

Table 2 shows the results of TD-DFT calculations performed using the M06 functional and the LANL2DZ+DZVP basis sets; including the corresponding wavelengths (in nm), the energies (in eV), the oscillator strength (f), and the orbitals involved in the transitions. This information shows that the peak of the wavelength of maximum absorption is due to charge transfer between the metal atom and the ligand molecule, which may be explained more clearly in Figure 3. The excitation contains a mixture of HOMO \rightarrow LUMO, HOMO - 1 \rightarrow LUMO, and HOMO - 1 \rightarrow LUMO + 1, this leads to consider them as degenerate orbitals.

The charge transfer efficiency from the sensitizer to the nanocrystalline oxide is extremely important in the solar cell design. Since the crucial electronic excitations occur from the highest occupied molecular orbitals (HOMO) to the lowest unoccupied molecular orbitals (LUMO), it is, therefore, important to form efficient charge-separated states with the HOMO localized on the donor subunit and the LUMO on the acceptor subunit. Figure 3 shows as the HOMO orbital density is located over around the copper atom in complexes; meanwhile, the density of the LUMO orbital is in the ligand, tending to move toward the carboxyl acid and methyl ester groups. This is beneficial in accordance with the above mentioned.

Figure 4 shows the HOMO-LUMO molecular orbitals' energetic position. These results are of great importance, since they can be used during synthesis to determine the solubility and chemical reactivity of the molecule, as reported in different studies [35, 36]. Additional factors to consider is the sensitizer LUMO level that is greater than the conduction band level of nanocrystalline oxides that are commonly used in such devices, also the HOMO level can be observed below the redox potential of the electrolyte [37]; both considerations

are important to the design of the sensitizer. The CuL4 complex has the smaller energy gap (3.093 eV); however, the values for the other complexes studied are close to this. Molecular orbitals energy levels were calculated in the presence of solvent.

Chemical reactivity parameters such as ionization potential (I), electron affinity (A), electronegativity (χ), chemical hardness (η), and electrophilicity index (ω) for the studied molecular systems (Table 3) were obtained by energy calculations (neutral and ionic state), taking into account the ground state geometry optimization.

According to Table 3, complexes with carboxylic acid as anchor groups exhibit greater electron affinity, electronegativity, and electrophilicity index than those containing methyl ester groups. The trend in ionization potential for the copper complexes is CuL8 < CuL9 < CuL7 < CuL4 < CuL6. The results indicate that CuL6 and CuL7 copper complexes are harder than the rest of the systems studied; this can be interpreted as systems with greater resistance to change with the number of electrons.

4. Conclusions

In this work, the molecular structure and properties of five molecular systems proposed as sensitizers in dye-sensitized solar cells have been calculated. The applied methodology for this study is based on the density functional theory, using the M06 hybrid meta-GGA functional and the LANL2DZ and DZVP basis sets.

The molecular systems characterization includes the calculation of geometric parameters, ultraviolet-visible spectra, electronic excited states, molecular orbitals, and chemical reactivity parameters. The longer wavelength of maximum absorption and the smallest energy gap is for the CuL4 complex. For all cases, the HOMO orbital density is located over around the copper atom; meanwhile, the density of

TABLE 1: Selected bond lengths (angstroms), bond angles, and dihedral angles (degrees) for copper complexes.

Parameter	Gas phase					In presence of solvent				
	CuL4	CuL6	CuL7	CuL8	CuL9	CuL4 ^a	CuL6 ^a	CuL7 ^b	CuL8 ^b	CuL9 ^b
Cu-N1	2.0459	2.0310	2.0318	2.0321	2.0320	2.0445	2.0250	2.0289	2.0299	2.0300
Cu-N2	2.0493	2.0282	2.0318	2.0321	2.0320	2.0364	2.0274	2.0290	2.0300	2.0301
Cu-N3	2.0475	2.0332	2.0318	2.0321	2.0320	2.0427	2.0243	2.0289	2.0300	2.0301
Cu-N4	2.0481	2.0284	2.0318	2.0321	2.0320	2.0386	2.0261	2.0289	2.0299	2.0300
Cl-O1	1.2342	1.2314	1.2355	1.2383	1.2359	1.2468	1.2444	1.2408	1.2446	1.2453
Cl-O2	1.3691	1.3675	1.3586	1.3647	1.3706	1.3509	1.3502	1.3555	1.3649	1.3636
N1-Cu-N2	81.67	81.87	81.92	81.56	81.58	81.87	81.85	81.97	81.72	81.77
N1-Cu-N3	129.67	124.35	124.78	124.99	124.98	127.57	125.02	125.37	125.56	125.53
N3-Cu-N4	81.47	81.80	81.91	81.56	81.58	81.87	81.93	81.97	81.72	81.77
N2-Cu-N4	129.16	124.99	124.78	124.99	124.98	132.13	125.26	125.37	125.56	125.53
N1-N2-N3-N4	-73.96	-81.11	-80.87	-80.97	-80.97	-73.13	-81.47	-79.85	-79.85	-79.84

^aMeOH solution, ^bChloroform solution.

TABLE 2: Copper complexes electronic excited states, showing wavelengths (nm), energies (eV), oscillator strength (f), and the orbitals involved in the transitions. Only excited states with $f > 0.02$ are shown.

Copper complex	λ (nm)	E (eV)	f	Assignment; H = HOMO, L = LUMO, and L + 1 = LUMO + 1
CuL4	562	2.21	0.048	H-1 \rightarrow L (61%) H \rightarrow L (26%) H-1 \rightarrow L + 1 (10%)
	495	2.51	0.026	H-1 \rightarrow L + 1 (75%) H \rightarrow L + 1 (17%)
	352	3.52	0.057	H-1 \rightarrow L + 3 (51%) H \rightarrow L + 3 (29%) H-1 \rightarrow L + 4 (11%) H \rightarrow L + 4 (7%)
CuL6	505	2.45	0.243	H \rightarrow L (66%) H-1 \rightarrow L + 1 (29%)
	413	3.00	0.030	H \rightarrow L + 2 (54%) H-2 \rightarrow L (21%) H-1 \rightarrow L + 2 (16%) H \rightarrow L + 3 (6%)
	381	3.25	0.028	H-1 \rightarrow L + 3 (78%) H-2 \rightarrow L + 1 (7%) H-3 \rightarrow L (7%)
	319	3.89	0.092	H-4 \rightarrow L (52%) H-3 \rightarrow L (21%) H-6 \rightarrow L (18%)
CuL7	500	2.48	0.267	H-1 \rightarrow L + 1 (+52%) H \rightarrow L (+47%)
	391	3.17	0.045	H \rightarrow L + 3 (65%) H-1 \rightarrow L + 2 (32%)
	315	3.94	0.285	H-4 \rightarrow L + 1 (46%) H-6 \rightarrow L (43%)
CuL8	535	2.32	0.391	H-1 \rightarrow L + 1 (52%) H \rightarrow L (45%)
	428	2.90	0.112	H \rightarrow L + 3 (60%) H-1 \rightarrow L + 2 (37%)
	358	3.46	0.025	H-1 \rightarrow L + 4 (56%) H \rightarrow L + 5 (40%)
	328	3.78	0.303	H-5 \rightarrow L (47%) H-6 \rightarrow L + 1 (40%) H-7 \rightarrow L (5%)
CuL9	536	2.31	0.376	H-1 \rightarrow L + 1 (52%) H \rightarrow L (45%)
	430	2.88	0.102	H \rightarrow L + 3 (61%) H-1 \rightarrow L + 2 (37%)
	329	3.77	0.280	H-5 \rightarrow L (48%) H-6 \rightarrow L + 1 (39%)

TABLE 3: Chemical reactivity parameters using DFT descriptors.

Copper complex	Chemical reactivity descriptors (eV)				
	I	A	χ	η	ω
CuL4	9.79	4.47	7.13	2.66	9.55
CuL6	10.15	4.53	7.34	2.81	9.58
CuL7	9.74	4.13	6.94	2.80	8.58
CuL8	9.35	4.26	6.80	2.54	9.10
CuL9	9.57	4.44	7.01	2.56	9.58

the LUMO orbital is in the ligand. Moreover, the molecular orbitals levels are appropriate considering the position of the conduction band of nanocrystalline oxides and the redox

potential of the electrolyte. Analyzing these data makes it possible to find potential applications for these copper complexes in photovoltaic devices.

Acknowledgments

This work has been supported by Consejo Nacional de Ciencia y Tecnología (CONACYT), Centro de Investigación en Materiales Avanzados, S.C. (CIMAV), Universidad Autónoma de Sinaloa, and Dirección de Investigación y Posgrado by PROFAPI 2012/040. J. Baldenebro-Lopez gratefully acknowledges a fellowship from CONACYT. D. Glossman-Mitnik and N. Flores-Holguin are researchers of CIMAV and CONACYT.

References

- [1] P. G. Bomben, K. C. D. Robson, B. D. Koivisto, and C. P. Berlinguette, "Cyclometalated ruthenium chromophores for the dye-sensitized solar cell," *Coordination Chemistry Reviews*, vol. 256, pp. 1438–1450, 2012.
- [2] F. De Angelis, S. Fantacci, and R. Gebauer, "Simulating dye-sensitized TiO₂ heterointerfaces in explicit solvent: absorption spectra, energy levels, and dye desorption," *Journal of Physical Chemistry Letters*, vol. 2, no. 7, pp. 813–817, 2011.
- [3] Y. Shibano, T. Umeyama, Y. Matano, and H. Imahori, "Electron-donating perylene tetracarboxylic acids for dye-sensitized solar cells," *Organic Letters*, vol. 9, no. 10, pp. 1971–1974, 2007.
- [4] Y. Wang, M. Wu, X. Lin, A. Hagfeldt, and T. Ma, "Optimization of the performance of dye-sensitized solar cells based on Pt-like TiC counter electrodes," *The European Journal of Inorganic Chemistry*, vol. 2012, no. 22, pp. 3557–3561, 2012.
- [5] S.-H. Liu, H. Fu, Y.-M. Cheng et al., "Theoretical study of N749 dyes anchoring on the (TiO₂)₂₈ surface in DSSCs and their electronic absorption properties," *The Journal of Physical Chemistry C*, vol. 116, no. 31, pp. 16338–16345, 2012.
- [6] C. Dragonetti, A. Valore, A. Colombo et al., "A new thiocyanate-free cyclometalated ruthenium complex for dye-sensitized solar cells: beneficial effects of substitution on the cyclometalated ligand," *Journal of Organometallic Chemistry*, vol. 714, pp. 88–93, 2012.
- [7] M. Katono, T. Bessho, M. Wielopolski et al., "Influence of the anchoring modes on the electronic and photovoltaic properties of D- π -A dyes," *The Journal of Physical Chemistry C*, vol. 116, no. 32, pp. 16876–16884, 2012.
- [8] X. Lu, Q. Feng, T. Lan, G. Zhou, and Z.-S. Wang, "Molecular engineering of quinoxaline-based organic sensitizers for highly efficient and stable dye-sensitized solar cells," *Chemistry of Materials*, vol. 24, no. 16, pp. 3179–3187, 2012.
- [9] M. K. Nazeeruddin, A. Kay, I. Rodicio et al., "Conversion of light to electricity by cis-X₂bis(2,2'-bipyridyl-4,4'-dicarboxylate)ruthenium(II) charge-transfer sensitizers (X = Cl-, Br-, I-, CN-, and SCN-) on nanocrystalline TiO₂ electrodes," *Journal of the American Chemical Society*, vol. 115, no. 14, pp. 6382–6390, 1993.
- [10] M. K. Nazeeruddin, F. de Angelis, S. Fantacci et al., "Combined experimental and DFT-TDDFT computational study of photoelectrochemical cell ruthenium sensitizers," *Journal of the American Chemical Society*, vol. 127, no. 48, pp. 16835–16847, 2005.
- [11] G. C. Vougioukalakis, A. I. Philippopoulos, T. Stergiopoulos, and P. Falaras, "Contributions to the development of ruthenium-based sensitizers for dye-sensitized solar cells," *Coordination Chemistry Reviews*, vol. 255, no. 21–22, pp. 2602–2621, 2011.
- [12] N. Alonso-Vante, J.-F. Nierengarten, and J.-P. Sauvage, "Spectral sensitization of large-band-gap semiconductors (thin films and ceramics) by a carboxylated bis(1,10-phenanthroline)copper(I) complex," *Journal of the Chemical Society, Dalton Transactions*, no. 11, pp. 1649–1654, 1994.
- [13] J. Deng, Q. Xiu, L. Guo, L. Zhang, G. Wen, and C. Zhong, "Branched chain polymeric metal complexes containing Co(II) or Ni(II) complexes with a donor- π -acceptor architecture: synthesis, characterization, and photovoltaic applications," *Journal of Materials Science*, vol. 47, no. 7, pp. 3383–3390, 2012.
- [14] L. Barrientos, C. Araneda, B. Loeb, and I. G. Crivelli, "Synthesis, spectroscopic and electrochemical characterization of copper(I) complexes with functionalized pyrazino[2,3-f]-1,10-phenanthroline," *Polyhedron*, vol. 27, no. 4, pp. 1287–1295, 2008.
- [15] S. Sakaki, T. Kuroki, and T. Hamada, "Synthesis of a new copper(I) complex, [Cu(tmdcbpy)₂]⁺ (tmdcbpy = 4,4',6,6'-tetramethyl-2,2'-bipyridine-5,5'-dicarboxylic acid), and its application to solar cells," *Journal of the Chemical Society, Dalton Transactions*, no. 6, pp. 840–842, 2002.
- [16] S. Hattori, Y. Wada, S. Yanagida, and S. Fukuzumi, "Blue copper model complexes with distorted tetragonal geometry acting as effective electron-transfer mediators in dye-sensitized solar cells," *Journal of the American Chemical Society*, vol. 127, no. 26, pp. 9648–9654, 2005.
- [17] T. Bessho, E. C. Constable, M. Graetzel et al., "An element of surprise-efficient copper-functionalized dye-sensitized solar cells," *Chemical Communications*, pp. 3717–3719, 2008.
- [18] Y.-Y. Lin, T.-H. Chu, S.-S. Li et al., "Interfacial nanostructuring on the performance of polymer/TiO₂ nanorod bulk heterojunction solar cells," *Journal of the American Chemical Society*, vol. 131, no. 10, pp. 3644–3649, 2009.
- [19] P. Hohenberg and W. Kohn, "Inhomogeneous electron gas," *Physical Review*, vol. 136, no. 3B, pp. B864–B871, 1964.
- [20] W. Kohn and L. J. Sham, "Self-consistent equations including exchange and correlation effects," *Physical Review*, vol. 140, no. 4A, pp. A1133–A1138, 1965.
- [21] R. G. Parr and W. Yang, *Density-Functional Theory of Atoms and Molecules*, Oxford University Press, New York, NY, USA, 1989.
- [22] K. Burke, J. Werschnik, and E. K. U. Gross, "Time-dependent density functional theory: past, present, and future," *Journal of Chemical Physics*, vol. 123, no. 6, 9 pages, 2005.
- [23] R. E. Stratmann, G. E. Scuseria, and M. J. Frisch, "An efficient implementation of time-dependent density-functional theory for the calculation of excitation energies of large molecules," *Journal of Chemical Physics*, vol. 109, no. 19, pp. 8218–8224, 1998.
- [24] R. Bauernschmitt and R. Ahlrichs, "Treatment of electronic excitations within the adiabatic approximation of time dependent density functional theory," *Chemical Physics Letters*, vol. 256, no. 4–5, pp. 454–464, 1996.
- [25] F. Gaussian 09 Revision A. 02, M. J., G. W. Trucks, H. B. Schlegel et al., Gaussian, Inc., Wallingford CT, 2009.
- [26] Y. Zhao and D. G. Truhlar, "The M06 suite of density functionals for main group thermochemistry, thermochemical kinetics, noncovalent interactions, excited states, and transition elements: two new functionals and systematic testing of four M06-class functionals and 12 other functionals," *Theoretical Chemistry Accounts*, vol. 120, no. 1–3, pp. 215–241, 2008.
- [27] J. Baldenebro-López, J. Castorena-González, N. Flores-Holguín, J. Almaral-Sánchez, and D. Glossman-Mitnik, "Computational molecular nanoscience study of the properties of copper complexes for dye-sensitized solar cells," *International Journal of Molecular Sciences*, vol. 13, no. 12, pp. 16005–16019, 2012.
- [28] T. H. Dunning Jr. and P. J. Hay, *Methods of Electronic Structure Theory*, Plenum, New York, NY, USA, 1976.
- [29] C. Sosa, J. Andzelm, B. C. Elkin, E. Wimmer, K. D. Dobbs, and D. A. Dixon, "A local density functional study of the structure and vibrational frequencies of molecular transition-metal compounds," *The Journal of Physical Chemistry*, vol. 96, no. 16, pp. 6630–6636, 1992.
- [30] S. I. Gorelsky, "Swizard program," 2012, University of Ottawa, Ottawa, Canada, <http://www.sg-chem.net/>.

- [31] S. I. Gorelsky and A. B. P. Lever, "Electronic structure and spectra of ruthenium diimine complexes by density functional theory and INDO/S. Comparison of the two methods," *Journal of Organometallic Chemistry*, vol. 635, no. 1-2, pp. 187-196, 2001.
- [32] J. Tomasi, B. Mennucci, and R. Cammi, "Quantum mechanical continuum solvation models," *Chemical Reviews*, vol. 105, no. 8, pp. 2999-3094, 2005.
- [33] M. Cossi and V. Barone, "Time-dependent density functional theory for molecules in liquid solutions," *The Journal of Chemical Physics*, vol. 115, no. 10, pp. 4708-4717, 2001.
- [34] M. A. Green, *Solar Cells: Operating Principles, Technology and Systems Applications*, Prentice-Hall, Englewood Cliffs, New Jersey, USA, 1982.
- [35] F. de Angelis, S. Fantacci, and A. Sgamellotti, "An integrated computational tool for the study of the optical properties of nanoscale devices: application to solar cells and molecular wires," *Theoretical Chemistry Accounts*, vol. 117, no. 5-6, pp. 1093-1104, 2007.
- [36] Y.-X. Weng, Y.-Q. Wang, J. B. Asbury, H. N. Ghosh, and T. Lian, "Back electron transfer from TiO₂ nanoparticles to Fe^{III}(CN)₆³⁻: origin of non-single-exponential and particle size independent dynamics," *Journal of Physical Chemistry B*, vol. 104, no. 1, pp. 93-104, 2000.
- [37] X. Lu, S. Wei, C.-M. L. Wu, S. Li, and W. Guo, "Can polypyridyl Cu(I)-based complexes provide promising sensitizers for dye-sensitized solar cells? A theoretical insight into Cu(I) versus Ru(II) sensitizers," *Journal of Physical Chemistry C*, vol. 115, no. 9, pp. 3753-3761, 2011.

Research Article

Computational Nanochemistry Study of the Molecular Structure and Properties of Chlorophyll a

Mónica Alvarado-González,¹ Norma Flores-Holguín,² and Daniel Glossman-Mitnik²

¹ Centro de Investigación en Alimentación y Desarrollo (CIAD), Avenida Cuarta sur No. 3820, Fracc. Vencedores del Desierto Unidad Delicias, 33089 Delicias, CHIH, Mexico

² Laboratorio Virtual NANOCOSMOS, Centro de Investigación en Materiales Avanzados, Miguel de Cervantes 120, Complejo Industrial Chihuahua, 31109 Chihuahua, CHIH, Mexico

Correspondence should be addressed to Daniel Glossman-Mitnik; daniel.glossman@cimav.edu.mx

Received 10 October 2012; Accepted 23 December 2012

Academic Editor: Theodoros Dimopoulos

Copyright © 2013 Mónica Alvarado-González et al. This is an open access article distributed under the Creative Commons Attribution License, which permits unrestricted use, distribution, and reproduction in any medium, provided the original work is properly cited.

The M06 family of density functionals has been assessed for the calculation of the molecular structure and properties of the chlorophyll a molecule. Besides the determination of the molecular structures, the UV-Vis spectra have been computed using TD-DFT in the presence of a solvent, and the results were compared with the experimental data available. The chemical reactivity descriptors have been calculated through conceptual DFT. The active sites for nucleophilic and electrophilic attacks have been chosen by relating them to the Fukui function indices. A comparison between the descriptors calculated through vertical energy values and those arising from the Koopmans' theorem approximation have been performed in order to check for the validity of the last procedure.

1. Introduction

The sun has been shining for some four and half a billion years and is expected to do so for as long again. It is the earth's only truly sustainable source of energy. Photosynthesis, the process by which the energy of sunlight absorbed in the chlorophyll pigments of green plants fixes atmospheric carbon dioxide (CO₂) to carbohydrates, supplies us directly or indirectly with all our food. The oxygen discarded by plants as part of this process replenishes the atmosphere with the oxygen humans and animals need for survival [1]. Photosynthesis is by far the most spectacular physiological process in plant growth and productivity. Due to this fact, the study of photosynthesis has captivated plant physiologists, botanists, plant biologists, horticulturalists, agronomists, agriculturalists, crop growers, and, most recently, plant molecular and cellular biologists around the world [2].

A fundamental principle of photochemistry—photosynthesis is partly a photochemical reaction—is that, for light to drive a reaction, it must first be absorbed. This means that there must be a pigment, which is any molecule that

absorbs light. Chlorophyll a serves a dual role in oxygenic photosynthesis: in light harvesting as well as in converting energy of absorbed photons to chemical energy [3]. The biological importance of chlorophyll a seems obvious because it is necessary for the photochemistry in oxygenic photosynthetic organisms, with the only known exception of *A. marinus* which utilizes both chlorophyll d and chlorophyll a for the photochemistry [4].

The aim of this work is to test the performance of the M06 family of density functionals [5–7] for the prediction of the infrared (IR) and ultraviolet-visible (UV-vis) spectra, the dipole moment, polarizability, and the chemical reactivity descriptors that arise from conceptual density functional theory (DFT) [8, 9] for the chlorophyll a molecule. A comparison between the descriptors calculated through vertical energy values and those arising from the Koopmans' theorem approximation will be performed in order to check for the validity of the last procedure within DFT. The results will be compared with the empirical evidence available in the literature.

2. Theory and Computational Details

All computational studies were performed with the Gaussian 09 [10] series of programs with density functional methods as implemented in the computational package. The equilibrium geometries of the molecules were determined by means of the gradient technique. The force constants and vibrational frequencies were determined by computing analytical frequencies on the stationary points obtained after the optimization to check if there were true minima. The basis sets used in these work were MIDIY, which is the same basis set as MIDI! with a polarization function added to the hydrogen atoms, and the DGDZVP basis set for Mg. The MIDI! basis is a small double-zeta basis with polarization functions on N-F, Si-Cl, Br, and I [11–16].

For the calculation of the molecular structure and properties of the studied systems, we have chosen the hybrid meta-GGA density functionals: M06, M06L, M06-2X, and M06HF [5], which consistently provide satisfactory results for several structural and thermodynamic properties. Solvation energies were computed by the integral equation formalism polarizable continuum model (IEF-PCM) [17], including the UAKS model and methanol as a solvent.

The calculation of the ultraviolet (UV-Vis) spectra of the studied systems has been performed by solving the time-dependent DFT (TD-DFT) equations according to the method implemented in Gaussian 09 [13, 18–20]. The equations have been solved for 10 excited states.

The infrared (IR) and ultraviolet (UV-Vis) spectra were calculated using the SWizard program [21, 22] and visualized with Gabedit [23]. In all cases the displayed spectra show the calculated frequencies and absorption or emission wavelengths.

The highest-occupied molecular orbital (HOMO) and lowest-occupied molecular Orbital (LUMO) were extracted from the calculations and visualized using the Chemcraft Program Revision 1.6 [24].

Within the conceptual framework of DFT [8, 9], the chemical potential μ , which measures the escaping tendency of electron from equilibrium is defined as

$$\mu = \left(\frac{\partial E}{\partial N} \right)_{v(\vec{r})} = -\chi, \quad (1)$$

where χ is the electronegativity.

The global hardness η can be seen as the resistance to charge transfer:

$$\eta = \frac{1}{2} \left(\frac{\partial^2 E}{\partial N^2} \right)_{v(\vec{r})}. \quad (2)$$

Using a finite difference approximation and Koopmans' theorem [13–16], the above expressions can be written as

$$\begin{aligned} \mu &\approx -\frac{1}{2}(I + A) \approx \frac{1}{2}(\epsilon_L + \epsilon_H), \\ \eta &\approx \frac{1}{2}(I - A) \approx \frac{1}{2}(\epsilon_L - \epsilon_H), \end{aligned} \quad (3)$$

where ϵ_H and ϵ_L are the energies of the highest occupied and the lowest unoccupied molecular orbitals: HOMO and LUMO, respectively.

The electrophilicity index ω represents the stabilization energy of the systems when it gets saturated by electrons coming from the surrounding:

$$\omega = \frac{\mu^2}{2\eta} \approx \frac{(I + A)^2}{2(I - A)} \approx \frac{(\epsilon_L + \epsilon_H)^2}{2(\epsilon_L - \epsilon_H)}. \quad (4)$$

The condensed Fukui functions can also be employed to determine the reactivity of each atom in the molecule. The corresponding condensed functions are given by $f_k^+ = q_k(N+1) - q_k(N)$ (for nucleophilic attack), $f_k^- = q_k(N) - q_k(N-1)$ (for electrophilic attack), and $f_k^0 = [q_k(N+1) - q_k(N-1)]/2$ (for radical attack), where q_k is the gross charge of atom k in the molecule.

It is possible to evaluate condensed Fukui functions from single-points calculations directly, without resorting to additional calculations involving the systems with $N-1$ and $N+1$ electrons:

$$\begin{aligned} f_k^+ &= \sum_{a \in k} \left[c_{ai}^2 + c_{ai} \sum_{b \neq a} c_{bi} S_{ab} \right] \quad (\text{where } i = \text{LUMO}), \\ f_k^- &= \sum_{a \in k} \left[c_{ai}^2 + c_{ai} \sum_{b \neq a} c_{bi} S_{ab} \right] \quad (\text{where } i = \text{HOMO}) \end{aligned} \quad (5)$$

with c_{ai} being the LCAO coefficients and S_{ab} the overlap matrix. The condensed Fukui functions are normalized, thus $\sum_k f_k = 1$ and $f_k^0 = [f_k^+ + f_k^-]/2$.

The electrodonating (ω^-) and electroaccepting (ω^+) powers have been defined as [25]:

$$\begin{aligned} \omega^- &= \frac{(3I + A)^2}{16(I - A)}, \\ \omega^+ &= \frac{(I + 3A)^2}{16(I - A)}. \end{aligned} \quad (6)$$

It follows that a larger ω^+ value corresponds to a better capability of accepting charge, whereas a smaller value of ω^- value of a system makes it a better electron donor. In order to compare ω^+ with $-\omega^-$, the following definition of net electrophilicity has been proposed [26]:

$$\Delta\omega^\pm = \omega^+ - (-\omega^-) = \omega^+ + \omega^-, \quad (7)$$

that is, the electroaccepting power relative to the electrodonating power.

Indeed, there exist in the literature many other methods for the computation of the chemical reactivity descriptors considered in this work [27–29].

3. Results and Discussion

The molecular structure of chlorophyll a was preoptimized by starting with the readily available PDB structure, and finding

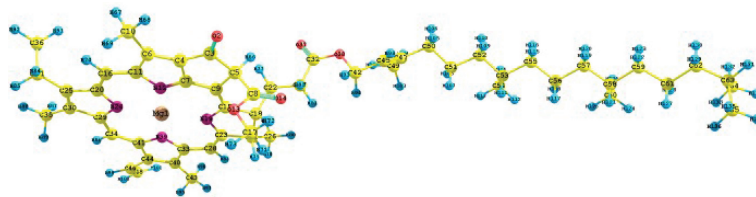


FIGURE 1: Optimized molecular structure of the chlorophyll a molecule.

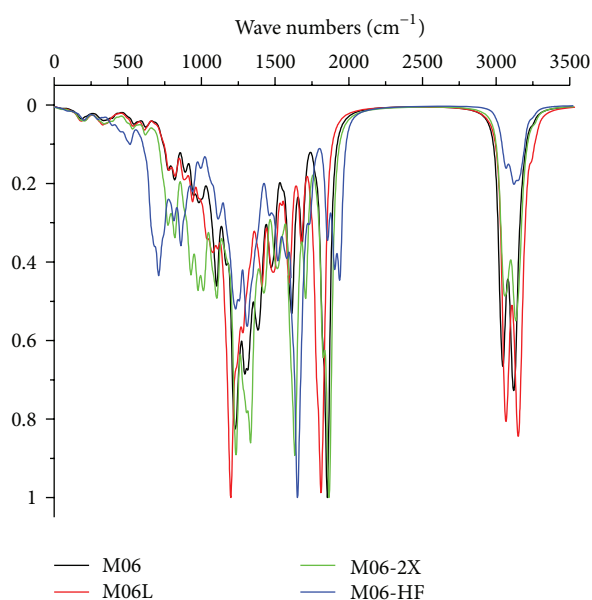


FIGURE 2: Infrared spectra of the chlorophyll a molecule calculated with the M06, M06L, M06-2X, and M06-HF density functionals and the MIDIY and DGDZVP basis sets.

the most stable conformer by means of the conformers module of materials studio through a random sampling with molecular mechanics techniques and a consideration of all the torsional angles. The structure of the resulting conformer was then optimized with the M06, M06L, M06-2X, and M06-HF density functionals in conjunction with the MIDIY and DGDZVP basis sets. The optimized molecular structure of the chlorophyll a molecule (with the M06 density functional) is shown in Figure 1, while the bond distances (in Å) and the bond angles (in degrees) calculated with the M06, M06L, M06-2X and M06-HF functionals in conjunction with the MIDIY and DGDZVP basis sets are presented in Tables A.1 and A.2 of the Supplementary Materials available online at <http://dx.doi.org/10.1155/2013/424620>, respectively. It is not the objective of this study to analyze in detail the results predicted by the different functionals for the optimized structure of the chlorophyll a molecule. However, a comparison of the results by superimposing structures reveals that there are not important differences between them. This is not surprising because modern density functionals are able to predict molecular structures with a good degree of accuracy and using low-cost basis sets. These results are an

improvement over those obtained with other low-level older density functionals [30].

The situation is quite different for the prediction of the IR and UV-Vis spectra, and this could be ascribed to the different functional form of the density functionals. The infrared spectra of the chlorophyll a molecule calculated with the M06, M06L, M06-2X, and M06-HF density functionals and the MIDIY and DGDZVP basis sets are shown in Figure 2. Indeed, we should note that none of the IR spectra display a frequency value below zero or imaginary, and this means that the structures predicted by all the functionals are a minimum on the potential energy surface. The IR spectrum of chlorophyll a has been measured and elucidated more than 60 years ago [31]. A comparison of the results shown in Figure 2 with those reported in Figure 1 of the mentioned article reveals that the overall shape is more or less the same, with significant differences for the M06-2X and M06-HF spectra. It is well known that calculated Hartree-Fock (HF) IR spectra must be scaled to account for the effects of anharmonicity and correlation. With modern density functionals that explicitly include correlation, this scaling factor is close to 1, and this can be an indication of the goodness of a given functional. For the results presented here, it is remarkable that the M06 and the local M06L predict so well the IR spectrum of chlorophyll a. Notwithstanding, these results should be taken with care because the experimental spectrum in that paper (and also in later works) has been taken from the solid, while the present calculations have been done in the presence of methanol simulated through a polarized continuum method. It should be noticed that a recent work on the estimation of scaling factors for a large number of density functionals have shown that functionals with low percentages of HF exchange tend to predict more accurate frequencies [32].

The molecular dipole moment is perhaps the simplest experimental measure of charge distribution in a molecule. The accuracy of the overall distribution of electrons in a molecule is hard to quantify, since it involves all the multipoles. The polarizability α contributes to the understanding of the response of the system when the external field is changed, while the number of electrons N is kept fixed. The polarizability is calculated as the average of the polarizability tensor $\langle \alpha \rangle = (1/3)(\alpha_{xx} + \alpha_{yy} + \alpha_{zz})$.

The molecular dipole moments μ (in Debye) and global polarizabilities α (in Bohr³) of the chlorophyll a molecule calculated with the M06, M06L, M06-2X and M06-HF density functionals and the MIDIY and DGDZVP basis sets are shown in Table 1.

TABLE 1: Molecular dipole moments μ (in Debye) and global polarizabilities α (in Bohr³) of chlorophyll a calculated with the M06, M06L, M06-2X, and M06-HF density functionals and the MIDIY and DGDZVP basis sets.

Property	M06	M06L	M06-2X	M06-HF
μ	5.574	5.498	6.074	7.584
α	761.74	786.94	754.28	744.11

The visible part of the electronic absorption spectrum is one of the more fascinating features of chlorophyll molecules [30]. For this reason, there is a great interest in the study of photosynthetic materials for their application in organic solar cells. First, we can refer to a theoretical study of the excited states of chlorophyll a and pheophytin a using a combination of density functional theory and the multireference configuration interaction method (DFT/MRCI) [33]. In a second place, there has been several interesting experimental and theoretical studies on photosynthetic materials: (i) chlorophyll a derivatives with various hydrocarbon ester groups for efficient dye-sensitized solar cells [34]; (ii) natural chlorophyll-related porphyrins and chlorins for dye-sensitized solar cells [35] and (iii) to a significant enhancement in the power-conversion efficiency of chlorophyll cosensitized solar cells by mimicking the principles of natural photosynthetic light-harvesting complexes. Indeed, this is a very enlightenment work, but in this study we only want to compare our results with the available experimental data for the absorption spectrum of chlorophyll a in methanol. There is also a recent DFT benchmark calculation on the performance of density-functional-based methods in the description of some biological systems, chlorophyll a among them [36].

The absorption or UV-Vis spectra of the chlorophyll a molecule calculated with the M06, M06L, M06-2X, and M06-HF density functionals and the MIDIY and DGDZVP basis sets are presented in Figure 3. The experimental absorption spectrum of chlorophyll a in methanol has been reported [37] and displays the characteristic bands at 432 and 665 nm. All the calculated spectra have the same shape, and it is the same as for the experimental absorption spectrum. However, there is a shift in each one of the spectrum that can be related to the amount of HF exchange that it is included for every density functional considered in this study. The functional form of the M06, M06-2X and M06-HF functionals is the same, with the only difference given by the aforementioned amount of HF exchange. It is evident from the results in Figure 3 that a larger amount of HF exchange included leads to larger shifts of the peaks when compared with the experimental spectrum. Notwithstanding, only the M06L density functional results are able to reproduce the experimental spectrum with a very small error for the blue band (437.4 nm) and of 38 nm for the band belonging to the maximum wavelength (627 nm). The results for the orbital transition assignments for each one of the calculations are given in Tables A3, A4, A5, and A6 of the Supplementary Materials for the interested reader.

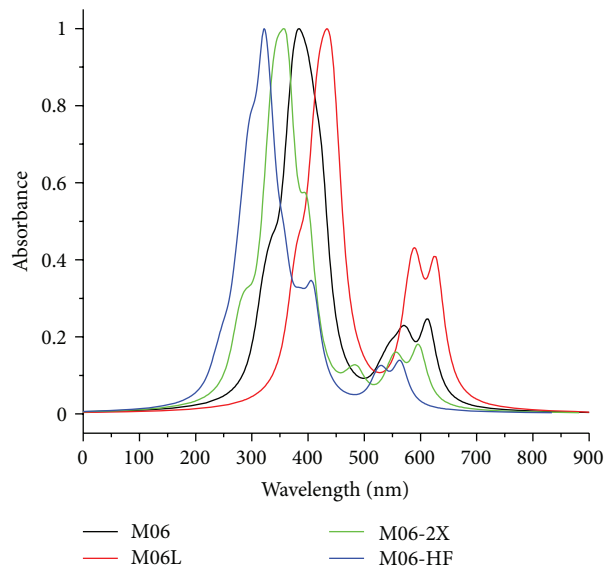


FIGURE 3: Absorption spectra of the chlorophyll a molecule calculated with the M06, M06L, M06-2X, and M06-HF density functionals and the MIDIY and DGDZVP basis sets.

The HOMO and LUMO orbitals of the chlorophyll a molecule calculated with the M06, M06L, M06-2X, and M06-HF density functionals and the MIDIY and DGDZVP basis sets are shown in Figure 4.

The validity of the Koopmans' theorem within the DFT approximation is controversial. However, it has been shown [38] that although the KS orbitals may differ in shape and energy from the HF orbitals, and the combination of them produces conceptual DFT reactivity descriptors that correlate quite well with the reactivity descriptors obtained through Hartree-Fock calculations. Thus, it is worth to calculate the electronegativity, global hardness, and global electrophilicity for the studied systems using both approximations in order to verify the quality of the procedures.

The HOMO and LUMO orbital energies (in eV), ionization potentials I and electron affinities A (in eV), and global electronegativity χ , total hardness η , and global electrophilicity ω of the chlorophyll a molecule calculated with the M06, M06L, M06-2X, and M06-HF density functionals and the MIDIY and DGDZVP basis sets are presented in Table 2. The upper part of the table shows the results derived assuming the validity of Koopmans' theorem, and the lower part shows the results derived from the calculated vertical I and A .

The condensed Fukui functions have been calculated using the AOMix molecular analysis program [22, 39] starting from single-point energy calculations. We have presented, discussed, and successfully applied the described procedure in our previous studies on different molecular systems [40–43].

The condensed dual descriptor has been defined as $\Delta f_k = f_k^+ - f_k^-$ [44, 45]. From the interpretation given to the Fukui function, one can note that the sign of the dual descriptor is very important to characterize the reactivity of a site within a molecule toward a nucleophilic or an electrophilic attack.

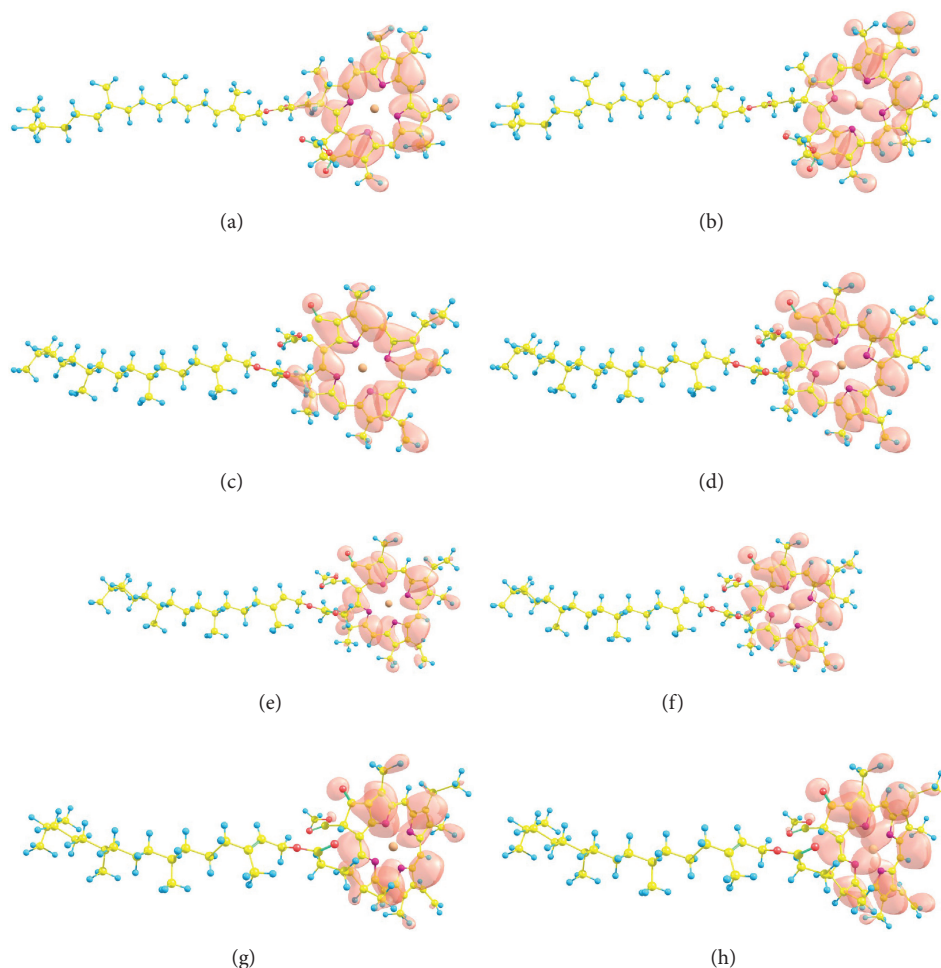


FIGURE 4: HOMO and LUMO orbitals of the chlorophyll a molecule calculated with the M06, M06L, M06-2X, and M06-HF density functionals and the MIDIY and DGDZVP basis sets.

TABLE 2: HOMO and LUMO orbital energies (in eV), ionization potentials I and electron affinities A (in eV), and global electronegativity χ , total hardness η , and global electrophilicity ω of chlorophyll a calculated with the M06, M06L, M06-2X, and M06-HF density functionals and the MIDIY and DGDZVP basis sets. The upper part of the table shows the results derived assuming the validity of Koopmans' theorem and the lower part shows the results derived from the calculated vertical I and A .

Property	M06	M06L	M06-2X	M06-HF
HOMO	5.221	4.680	5.897	7.076
LUMO	2.466	2.989	1.973	0.892
χ	3.8435	3.8344	3.9349	3.9839
η	2.7550	1.6912	3.9240	6.1840
ω	2.6810	4.3468	1.9729	1.2833
I	6.196	6.145	6.361	6.522
A	1.442	1.479	0.056	1.453
χ	3.8190	3.8121	3.2084	3.9874
η	4.7540	4.6660	6.3058	5.0684
ω	1.5339	1.5572	0.8162	1.5685

That is, if $\Delta f_k > 0$, then the site is favored for a nucleophilic attack, whereas if $\Delta f_k < 0$, then the site may be favored for an electrophilic attack [44–46].

The electrophilic f^+ and nucleophilic f^- condensed Fukui functions and Δf over the atoms of the chlorophyll a molecule calculated with the M06, M06L, M06-2X and M06-HF density functionals and the MIDIY and DGDZVP basis sets are shown in Table 3. The actual values have been multiplied by 100 for an easier comparison.

The electrodonating (ω^-) and electroaccepting (ω^+) powers and net electrophilicity $\Delta\omega^\pm$ of the chlorophyll a molecule calculated with the M06, M06L, M06-2X and M06-HF density functionals and the MIDIY and DGDZVP basis sets are presented in Table 4. The upper part of the table shows the results derived assuming the validity of Koopmans' theorem and the lower part shows the results derived from the calculated vertical I and A .

The results from Table 4 clearly indicate that chlorophyll a is an electrodonating molecule, with the same result predicted by all the four density functionals considered in this study.

TABLE 3: Electrophilic f^+ and nucleophilic f^- condensed Fukui functions and Δf over the atoms of the chlorophyll a molecule calculated with the M06, M06L, M06-2X, and M06-HF density functionals and the MIDIY and DGDZVP basis set. The actual values have been multiplied by 100 for an easier comparison.

Atom	M06			M06L			M06-2X			M06-HF		
	f^+	f^-	Δf	f^+	f^-	Δf	f^+	f^-	Δf	f^+	f^-	Δf
1 Mg	0.63	0.04	0.59	0.61	0.05	0.56	0.80	0.03	0.77	1.15	0.07	-0.45
2 O	3.32	1.29	2.03	4.22	1.45	3.77	2.83	1.30	1.53	1.82	1.37	0.45
3 C	2.46	0.26	2.20	2.99	0.32	2.67	2.09	0.22	1.87	1.36	0.16	1.20
4 C	3.97	2.78	1.19	3.97	2.40	1.57	3.88	3.43	0.45	2.88	4.71	-1.83
6 C	9.62	4.74	5.88	10.15	5.45	4.70	9.33	4.29	5.04	8.31	4.32	3.99
7 C	2.46	6.68	-4.22	2.03	6.37	-4.34	2.79	7.00	-4.21	3.16	8.70	-5.54
9 C	4.42	0.83	3.59	4.89	0.90	3.99	3.73	0.95	2.78	1.85	0.73	1.12
11 C	2.89	10.28	-7.39	2.71	9.25	-6.54	2.81	11.62	-8.81	1.83	14.90	-13.07
15 C	1.29	8.03	-6.74	1.34	8.47	-7.13	1.20	7.59	-6.39	0.98	6.66	-5.68
16 C	10.30	0.14	10.16	9.33	0.14	9.19	11.31	0.10	11.21	14.50	0.30	14.20
19 N	7.08	0.16	6.92	7.46	0.18	7.28	6.60	0.12	6.48	5.44	0.10	5.34
20 C	0.52	11.11	-10.59	0.48	9.72	-9.24	0.41	12.70	-12.29	0.01	15.67	-15.66
23 C	2.67	8.08	-5.41	2.77	8.79	-6.02	2.62	6.96	-4.34	2.36	4.59	-2.23
24 N	5.77	0.24	5.53	5.45	0.25	5.20	5.96	0.22	5.74	6.48	0.27	6.21
25 C	1.33	2.17	0.84	1.13	2.14	-0.99	1.73	2.31	-0.58	3.31	1.71	1.60
28 C	4.73	1.69	3.04	4.92	1.84	3.08	4.45	1.27	3.18	4.29	1.37	2.92
29 C	2.29	9.54	-7.25	1.91	8.55	-6.64	2.99	10.49	-7.50	5.46	10.18	-4.72
30 C	0.25	3.62	-3.37	0.23	3.23	-3.00	0.18	3.98	-3.80	0.01	5.22	-5.21
33 C	5.55	6.72	-1.17	5.11	6.98	-1.87	5.96	6.08	-0.12	6.33	0.34	5.99
34 C	7.17	0.64	6.53	6.57	0.60	5.97	7.24	0.62	6.62	6.50	1.49	5.01
40 C	5.65	3.07	-2.58	5.78	2.70	3.08	5.53	2.93	2.60	5.49	2.12	3.37
41 C	4.65	9.53	-4.88	4.04	9.08	-5.04	5.32	9.42	-4.10	6.96	7.60	-0.64
44 C	4.85	1.54	3.31	4.67	2.19	2.48	4.96	1.14	3.82	4.74	0.31	4.43
48 C	2.53	1.07	1.46	3.53	2.13	1.40	1.97	0.62	1.35	1.18	0.13	1.05

TABLE 4: Electrodonating (ω^-) and electroaccepting (ω^+) powers and net electrophilicity $\Delta\omega^\ddagger$ of chlorophyll a calculated with the M06, M06L, M06-2X, and M06-HF density functionals and the MIDIY and DGDZVP basis sets. The upper part of the table shows the results derived assuming the validity of Koopmans' theorem, and the lower part shows the results derived from the calculated vertical I and A .

Property	M06	M06L	M06-2X	M06-HF
ω^-	7.4560	10.7165	6.1585	4.9450
ω^+	3.6125	6.8821	2.2236	0.9611
$\Delta\omega^\ddagger$	11.0685	17.5986	8.3821	5.9061
ω^-	5.2745	5.3121	3.6307	5.4474
ω^+	1.4547	1.5000	0.4224	1.4600
$\Delta\omega^\ddagger$	6.7292	6.8121	4.0531	6.9074

However, only the results obtained through the calculations with the M06 and M06L density functionals are in fairly agreement between those from vertical calculations of I and A and those coming from the assumption of the validity of the Koopmans' theorem in DFT.

4. Conclusions

From the whole of the results presented in this contribution it has been clearly demonstrated that the sites of interaction of the chlorophyll a molecule can be predicted by using DFT-based reactivity descriptors such as the hardness, softness, and electrophilicity, as well as Fukui function calculations. These descriptors were used in the characterization and successful description of the preferred reactive sites and provide a firm explanation for the reactivity of the chlorophyll a molecule.

The M06 family of density functionals (M06, M06L, M06-2X, and M06-HF) used in the present work leads to the same qualitatively and quantitatively similar description of the chemistry and reactivity of the chlorophyll a molecule, yielding reasonable results. However, for the case of the M06 and M06L functionals, the agreement between the results obtained through energy calculations and those that assume the validity of the Koopmans' theorem is fairly good.

Acknowledgments

This work has been partially supported by CIMAV, SC, and Consejo Nacional de Ciencia y Tecnología (CONACYT,

Mexico). N. Flores-Holguín and D. Glossman-Mitnik are researchers of CONACYT and CIMAV. MAG is a researcher of CONACYT and CIAD.

References

- [1] M. D. Archer and J. Barber, Eds., *Molecular to Global Photosynthesis*, vol. 2 of *Series on Photoconversion of Solar Energy*, Imperial College Press, London, UK, 2004.
- [2] M. Pessaraki, *Handbook of Photosynthesis*, Books in Soils, Plants and the Environment, Taylor & Francis, New York, NY, USA, 2nd edition, 2005.
- [3] L. O. Bjorn, G. C. Papageorgiu, R. E. Blankenship, and Govindjee, "A view-point: why chlorophyll a?" *Photosynthesis Research*, vol. 99, no. 2, pp. 85–98, 2009.
- [4] R. Tanaka and A. Tanaka, "Chlorophyll cycle regulates the construction and destruction of the light-harvesting complexes," *Biochimica et Biophysica Acta*, vol. 1807, no. 8, pp. 968–976, 2011.
- [5] Y. Zhao and D. G. Truhlar, "Density functionals with broad applicability in chemistry," *Accounts of Chemical Research*, vol. 41, no. 2, pp. 157–167, 2008.
- [6] Y. Zhao and D. G. Truhlar, "The M06 suite of density functionals for main group thermochemistry, thermochemical kinetics, noncovalent interactions, excited states, and transition elements: two new functionals and systematic testing of four M06-class functionals and 12 other functionals," *Theoretical Chemistry Accounts*, vol. 120, no. 1–3, pp. 215–241, 2008.
- [7] Y. Zhao and D. G. Truhlar, "Applications and validations of the Minnesota density functionals," *Chemical Physics Letters*, vol. 502, no. 1–3, pp. 1–13, 2011.
- [8] R. G. Parr and W. Yang, *Density Functional Theory of Atoms and Molecules*, Oxford University Press, New York, NY, USA, 1989.
- [9] P. Geerlings, F. De Proft, and W. Langenaeker, "Conceptual density functional theory," *Chemical Reviews*, vol. 103, no. 5, pp. 1793–1873, 2003.
- [10] M. J. Frisch, G. W. Trucks, H. B. Schlegel et al., *Gaussian 09 Revision A.1*, Gaussian Inc., Wallingford, Conn, USA, 2009.
- [11] S. Huzinaga, J. Andzelm, M. Klobukowski, E. Radzio-Audzelm, Y. Sakai, and H. Tatewaki, *Gaussian Basis Sets for Molecular Calculations*, Elsevier, Amsterdam, The Netherlands, 1984.
- [12] R. E. Easton, D. J. Giesen, A. Welch, C. J. Cramer, and D. G. Truhlar, "The MIDI basis set for quantum mechanical calculations of molecular geometries and partial charges," *Theoretical Chemistry Accounts*, vol. 93, no. 5, pp. 281–301, 1996.
- [13] E. Lewars, *Computational Chemistry—Introduction to the Theory and Applications of Molecular and Quantum Mechanics*, Kluwer Academic Publishers, Dordrecht, The Netherlands, 2003.
- [14] D. C. Young, *Computational Chemistry—A Practical Guide for Applying Techniques to Real-World Problems*, John Wiley & Sons, New York, NY, USA, 2001.
- [15] F. Jensen, *Introduction to Computational Chemistry*, John Wiley & Sons, Chichester, UK, 2nd edition, 2007.
- [16] C. J. Cramer, *Essentials of Computational Chemistry—Theories and Models*, John Wiley & Sons, Chichester, UK, 2nd edition, 2004.
- [17] J. Tomasi, B. Mennucci, and E. Cancès, "The IEF version of the PCM solvation method: an overview of a new method addressed to study molecular solutes at the QM ab initio level," *Journal of Molecular Structure: THEOCHEM*, vol. 464, no. 1–3, pp. 211–226, 1999.
- [18] R. E. Stratmann, G. E. Scuseria, and M. J. Frisch, "An efficient implementation of time-dependent density-functional theory for the calculation of excitation energies of large molecules," *Journal of Chemical Physics*, vol. 109, no. 19, pp. 8218–8224, 1998.
- [19] R. Bauernschmitt and R. Ahlrichs, "Treatment of electronic excitations within the adiabatic approximation of time dependent density functional theory," *Chemical Physics Letters*, vol. 256, no. 4–5, pp. 454–464, 1996.
- [20] M. E. Casida, C. Jamorski, K. C. Casida, and D. R. Salahub, "Molecular excitation energies to high-lying bound states from time-dependent density-functional response theory: characterization and correction of the time-dependent local density approximation ionization threshold," *Journal of Chemical Physics*, vol. 108, no. 11, pp. 4439–4449, 1998.
- [21] S. Gorelsky, *Swizard Program Revision 4.6*, University of Ottawa, Ottawa, Canada, 2010, <http://www.sg-chem.net/>.
- [22] S. Gorelsky and A. Lever, "Electronic structure and spectra of ruthenium diimine complexes by density functional theory and INDO/S. Comparison of the two methods," *Journal of Organometallic Chemistry*, vol. 635, no. 1–2, pp. 187–196, 2001.
- [23] A. Allouche, "Gabedit—a graphical user interface for computational chemistry softwares," *Journal of Computational Chemistry*, vol. 32, no. 1, pp. 174–182, 2011.
- [24] G. Zhurko and D. Zhurko, *Chemcraft Program Revision 1.6*, Grigoriy A. Zhurko, Ivanovo, Russia, 2012, <http://www.chemcraft.com/>.
- [25] J. L. Gázquez, A. Cedillo, and A. Vela, "Electrodonating and electroaccepting powers," *The Journal of Physical Chemistry A*, vol. 111, no. 10, pp. 1966–1970, 2007.
- [26] P. K. Chattaraj, A. Chakraborty, and S. Giri, "Net electrophilicity," *The Journal of Physical Chemistry A*, vol. 113, no. 37, pp. 10068–10074, 2009.
- [27] G. De Luca, E. Sicilia, N. Russo, and T. Mineva, "On the hardness evaluation in solvent for neutral and charged systems," *Journal of the American Chemical Society*, vol. 124, no. 7, pp. 1494–1499, 2002.
- [28] T. Mineva, E. Sicilia, and N. Russo, "Density-functional approach to hardness evaluation and its use in the study of the maximum hardness principle," *Journal of the American Chemical Society*, vol. 120, no. 35, pp. 9053–9058, 1998.
- [29] T. Mineva, V. Parvanov, I. Petrov, N. Neshev, and N. Russo, "Fukui indices from perturbed kohn-sham orbitals and regional softness from mayer atomic valences," *The Journal of Physical Chemistry A*, vol. 105, no. 10, pp. 1959–1967, 2001.
- [30] D. Sundholm, "Density functional theory calculations of the visible spectrum of chlorophyll a," *Chemical Physics Letters*, vol. 302, no. 5–6, pp. 480–484, 1999.
- [31] J. W. Weigl and R. Livingston, "Infrared spectra of chlorophyll and related compounds," *Journal of the American Chemical Society*, vol. 75, no. 9, pp. 2173–2176, 1953.
- [32] I. M. Alecu, J. Zheng, Y. Zhao, and D. G. Truhlar, "Computational thermochemistry: scale factor databases and scale factors for vibrational frequencies obtained from electronic model chemistries," *Journal of Chemical Theory and Computation*, vol. 6, no. 9, pp. 2872–2887, 2010.
- [33] A. B. J. Parusel and S. Grimme, "A theoretical study of the excited states of chlorophyll a and pheophytin a," *Journal of Physical Chemistry B*, vol. 104, no. 22, pp. 5395–5398, 2000.

- [34] X. F. Wang, H. Tamiaki, L. Wang et al., "Chlorophyll-a derivatives with various hydrocarbon ester groups for efficient dye-sensitized solar cells: static and ultrafast evaluations on electron injection and charge collection processes," *Langmuir*, vol. 26, no. 9, pp. 6320–6327, 2010.
- [35] X.-F. Wang and O. Kitao, "Natural chlorophyll-related porphyrins and chlorins for dye-sensitized solar cells," *Molecules*, vol. 17, no. 4, pp. 4484–4497, 2012.
- [36] M. Alberto, T. Marino, N. Russo, E. Sicilia, and M. Toscano, "The performance of density functional based methods in the description of selected biological systems and processes," *Physical Chemistry Chemical Physics*, vol. 14, no. 43, pp. 14943–14953, 2012.
- [37] H. Lichtenthaler and C. Buchman, *Chlorophylls and Carotenoids: Measurement and Characterization by UV-Vis Spectroscopy*, vol. F4.3.1–F4.3.8 of *Current Protocols in Food Analytical Chemistry*, John Wiley & Sons, Inc., New York, NY, USA, 2001.
- [38] J. Zevallos and A. Toro-Labbé, "A theoretical analysis of the Hohn-Sham and Hartree-Fock orbitals and their use in the determination of electronic properties," *Journal of the Chilean Chemical Society*, vol. 48, no. 4, pp. 39–47, 2003.
- [39] S. Gorelsky, *AOMix: Program for Molecular Orbital Analysis—Version 6.5*, University of Ottawa, Ottawa, Canada, 2011, <http://www.sg-chem.net/>.
- [40] T. Ruiz-Anchondo and D. Glossman-Mitnik, "Computational characterization of the β,β -carotene molecule," *Journal of Molecular Structure: THEOCHEM*, vol. 913, no. 1–3, pp. 215–220, 2009.
- [41] D. Glossman-Mitnik, "Computational study of 3,4-diphenyl-1,2,5-thiadiazole 1-oxide for organic photovoltaics," *International Journal of Photoenergy*, vol. 2009, Article ID 806714, 8 pages, 2009.
- [42] D. Glossman-Mitnik, "Computational molecular characterization of Coumarin-102," *Journal of Molecular Structure: THEOCHEM*, vol. 911, no. 1–3, pp. 105–108, 2009.
- [43] T. Ruiz-Anchondo, N. Flores-Holguín, and D. Glossman-Mitnik, "Natural carotenoids as nanomaterial precursors for molecular photovoltaics: a computational DFT study," *Molecules*, vol. 15, no. 7, pp. 4490–4510, 2010.
- [44] C. Morell, A. Grand, and A. Toro-Labbé, "New dual descriptor for chemical reactivity," *The Journal of Physical Chemistry A*, vol. 109, no. 1, pp. 205–212, 2005.
- [45] C. Morell, A. Grand, and A. Toro-Labbé, "Theoretical support for using the $\Delta f(r)$ descriptor," *Chemical Physics Letters*, vol. 425, no. 4–6, pp. 342–346, 2006.
- [46] J. L. G. Gázquez, "Chemical reactivity concepts in density functional theory," in *Chemical Reactivity Theory: A Density Functional View*, P. K. Chattaraj, Ed., chapter 2, pp. 7–21, CRC Press, Taylor & Francis Group, Boca Raton, Fla, USA, 2009.